Development of Bore Reconstruction Techniques Applied to the Study of Brass Wind Instruments

Darren Alexander Hendrie

A thesis submitted in fulfilment of the requirements
for the degree of Doctor of Philosophy
to the
University of Edinburgh

Ph.D
University of Edinburgh
2007

Declaration

I declare that this thesis is composed by myself, and that the work therein is my own, except where explicitly stated otherwise.

Signature.....

Date.....

Darren Hendrie

Abstract

The acoustic impedance is a valuable parameter in musical acoustics. Information contained within this frequency-domain parameter can be used to determine the acoustical behaviour of a musical wind instrument: the notes at which the instrument will play; the ease with which a particular note can be played; and the timbre of the instrument. The time-domain version of acoustic impedance - the *input impulse response* - gives us information on how sound waves propagate within an instrument under playing conditions and how sound is radiated from the open end or from other holes in the bore. Acoustic impedance data can also be used to calculate an accurate profile of the internal structure of the instrument - referred to as a *bore reconstruction*. This is very useful as the main bore is usually coiled and difficult to measure mechanically. An accurate reconstruction, however, is only possible if the impedance is measured over a large range of frequencies, typically of the order of tens of hertz up to many kilohertz.

The bulk of this work follows on from research where the impedance of a short, closed, cylindrically-symmetric tube has been measured experimentally at high frequencies - 1 kHz up to 20 kHz - and compared with theory. The technique used is known as the *Two-Microphone-Four-Calibration* system, or *TMFC* system: two microphones are used to monitor the air pressure in the system, and measurement of four closed tubes of different length are required for calibration. The TMFC system has been modified so that impedance data far below 1 kHz (down to 10 Hz) can be attained for a full instrument as well as instrument components - for example trombone mouthpieces or French horn crooks. Suitable algorithms have been developed for processing the impedance data.

Obtaining large bandwidth impedance data has allowed the possibility of accurate reconstructions of an instrument's internal profile. The results are compared with plane-wave theoretical models, which are derived in detail, and other well-documented methods of bore and impedance analysis: the acoustic pulse reflectometer *(APR)*, and the brass instrument analysis system *(BIAS)*.

An in-depth discussion and analysis of the TMFC results for test objects and instruments of various lengths are presented. Simulations, whereby bore profiles are artificially altered, and a post-processing method utilising *transmission matrix theory (TMT)*, are explored.

A variety of orchestral French horn crooks dating from as early as the 18th-Century have been measured using APR and TMFC. A comparison is made between the capabilities of the two systems. Conclusions - of interest from a historical and manufacturing perspective - are drawn.

The BIAS has been used to investigate how changes to the bore profile affect the behaviour of trumpets. The impedance of the trumpet is measured using a variety of leadpipes and mouthpieces.

Acknowledgements

Many thanks to my supervisor, Murray Campbell whom - despite a heavy workload - has always had, or made time for me; to my second supervisor Clive Greated; to Maarten van Walstijn who helped me a great deal during, not only my PhD, but my Master's dissertation; and to Jonathan Kemp for help with computational and pulse reflectometry issues.

A sincere thank you to the people of the Acoustics and Fluid Dynamics group who made the postgraduate experience so enjoyable: Michael Newton, Rob MacDonald, Sam Stevenson, Juliette Paris (honorary member), David Skulina, Seona Bromage, Alistair Braden, Alan Wooley, Steven Tonge, Lin Zhang, John Cosgrove, Calum Gray, and Sandra Carral.

Thank you again to Alistair Braden for permission to use his BIES algorithms.

Thanks to John Chick with whom I collaborated for the ICA conference in Madrid.

Thanks to Arnold Myers for supplying instruments for analysis, and for his accurate calliper measurements.

Many thanks to the technical staff of Edinburgh University for their precise manufacturing and excellent craftsmanship: Vince Devine, Andrew Downie, Derek Low, and Ronnie Proc.

Thanks to all the other wonderful people I have met along the way during my time at Edinburgh University.

Thank you to Andrew Lafong and Steven Plank for taking the photos used in this thesis.

Finally, a big thank you to my parents Alex and Sylvia Hendrie who have continually supported me throughout my life and academic career.

This research was funded by E.P.S.R.C.

Contents

List of Figures

List of Tables

List of Abbreviations

APR	Acoustic Pulse Reflectometry/Reflectometer
BIAS	Brass Instrument Analysis System
BIES	Brass Instrument Evolution Software
DFT	Discrete Fourier Transform
FFT	Fast Fourier Transform
IFFT	Inverse Fast Fourier Transform
IIR	Input Impulse Response
SBW	Suitable Bandwidth
SFR	Singularity-Free Region
TMFC	Two-Microphone-Four-Calibration
TMTC	Two-Microphone-Three-Calibration
TMT	Transmission Matrix Theory

List of Symbols

a	measurement duct radius
a_0	constant
A,B,C	coefficients
$\mathcal{A},\mathcal{B},\mathcal{C}$	calibration parameters
A_n, B_n	Fourier coefficients
$\mathcal{B}_\mathcal{M}$	bulk modulus
c	speed of sound
C_p, (C_V)	specific heat capacity at constant pressure(/volume)
d	microphone separation distance
$(f_{\text{cut on}}), f$	(cut on) frequency
f_s	first non-zero singular frequency
$f_{\max}$, $f_{\min}$	maximum and minimum frequency data components
G	ratio of microphone transducing characteristics
$\mathbf{H}$	transmission matrix
H_1, H_2	microphone transducing characteristics
i	imaginary unit ($i = \sqrt{-1}$)
I	current
J	Bessel function of the first kind
k, (k_{mn})	wavenumber (associated with mnth mode)
$\mathcal{L}$	length of pipe
m	mass of 1 mole of ideal gas/flare constant/number of nodal diameters
M	mass of ideal gas
n	number of moles/number of nodal circles/integer value
N	number of data points in data set
p	acoustic pressure
$p_{\text{meas}}(x,t)$	physically measurable pressure
P_0	equilibrium pressure
P	absolute pressure
$P_n(x)$	pressure profile of the nth mode along the x direction
$p^+(x,t)$, $p^-(x,t)$	forward and backward-propagating pressure waves
r	radial coordinate
r_v, (r_t)	pipe radius to viscous(/thermal) boundary layer thickness ratio
R	real part of complex impedance/resistance
(R_π), $R(\omega)$	(power) reflection coefficient
$\mathcal{R}$	ideal gas constant
s	microphone signal
S	surface area
$\mathcal{S}$	fractional condensation
t	time

T	total sample time
Δt	temporal resolution of input impulse response
T_{IIR}	duration of input impulse response
T_π	transmission coefficient
$\mathcal{T}_{\text{abs}}$	absolute temperature
$\mathcal{T}$	curvature
ΔT	change in temperature
$(U), u$	(volume) velocity
$U_n(x)$	axial volume velocity of the nth mode
$U^+(x,t)$, $U^-(x,t)$	forward and backward-propagating volume velocity waves
$\vec{v} = (v_x, v_y, v_z)$	velocity vector
V	voltage
Δx	axial resolution of bore reconstruction
x_0	constant
x, y, z	Cartesian coordinates
X	imaginary part of complex impedance/reactance
$\mathcal{Y}$	microphone signal ratio
$\mathcal{Y}_0$	microphone signal ratio (closed at reference plane)
$\mathcal{Y}_{\text{neg}}$	microphone signal ratio (closed at -$\mathcal{L}$)
$\mathcal{Y}_{\text{pos}}$	microphone signal ratio (closed at +$\mathcal{L}$)
$\mathcal{Y}_{\text{2pos}}$	microphone signal ratio (closed at +2$\mathcal{L}$)
Y	Bessel function of the second kind
(z), Z	(specific) acoustic impedance
Z_c	characteristic impedance
Z_{IN}	input impedance
$Z_{\mathcal{L}}$	load impedance
$\bar{Z}$	normalised impedance
Z_r	radiation impedance
Z_{flanged}, $(Z_{\text{unflanged}})$	radiation impedance of a flanged(/unflanged) pipe
$Z_{\text{IN}}^{\text{open}}$, $(Z_{\text{IN}}^{\text{closed}})$	input impedance of an ideally open(/closed) pipe
$Z_{\text{IN}}^{\text{conical}}$, $(Z_{\text{IN}}^{\text{open conical}})$	input impedance of an (ideally open) conical horn
$Z_{\text{IN}}^{\text{exponential}}$, $(Z_{\text{IN}}^{\text{open exponential}})$	input impedance of an (ideally open) exponential horn
α, (α_{mn})	attenuation constant (associated with mnth mode)
γ	ratio of specific heats
Γ	complex wavenumber/propagation constant
ξ	small displacement in the x direction
κ	thermal conductivity
λ	wavelength
ϕ	azimuthal angle
$\psi_n(y,z)$	pressure profile in the y-z plane for the nth mode
(ρ_0), ρ	(mean) density
θ	polar angle
Θ_n^m	Legendre function
(ν), η	(kinematic) viscosity
ω	angular frequency

Chapter 1

Introduction

1.1 Thesis Outline

The main aims of this thesis are as follows:

Aim I. To give a good foundation on the background theory of acoustics, in particular impedance theory, and to develop theoretical models with which to compare experimental results.

Aim II. To develop a technique - known as the Two-Microphone-Four-Calibration (TMFC) method - capable of measuring the input impedance of musical instruments and instrument components at *low* frequencies - below 1 kHz.

Aim III. To develop algorithms for the handling and post-processing of impedance data, involving the calculation of the input impulse response and bore reconstruction for musical instruments and their components.

Aim IV. To use the TMFC technique, Acoustic Pulse Reflectometer (APR), and Brass Instrument Analysis System (BIAS) to solve design problems and investigate how instruments - historical and contemporary - have been manufactured. This will also involve giving a comparison between the three methods in terms of advantages/disadvantages and limitations.

Aim V. To suggest future work in terms of improvements to the TMFC method, algorithms to be developed, and instruments of interest to be studied.

In this chapter, we hope to address the following points:

A. To explain why this research is relevant to not only the academic community, but also to musical instrument manufacturers and historians, as well as the industrial, commercial, and medical sectors.

B. To demonstrate how the work in this thesis fits in with the body of work that has been, or is currently being, done in the field.

1.2 Overview of Thesis

A summary of the issues covered in each subsequent chapter is given here to clarify the flow of the thesis.

1.2.1 Chapter 2: Background Acoustics Theory

This chapter starts by outlining the basics of acoustics theory: derivation of the wave equation and its solutions in Cartesian, spherical polar, and cylindrical polar co-ordinate systems; the definition of a fluid; the approximation of air to an ideal gas, and the behaviour of sound in these gases.

Core to this thesis is the understanding of three main acoustic parameters:

i. *Acoustic impedance*

ii. *Input impulse response*

iii. *Bore reconstruction*

A theoretical expression is derived for the input impedance of a cylindrical duct terminated with a general impedance load. This is done for both lossy and lossless propagation. We start by looking at some simple examples of cylindrically-symmetric objects: open and closed cylinders; cones; and Bessel curves. We can then develop accurate impedance curves for an instrument by approximating its profile to a concatenation of these objects.

The input impedance, which is a frequency-domain parameter, can be converted to its corresponding time-domain version - this is known as the input impulse response.

From the input impulse response, the internal profile of the object can be deduced. This is referred to as the bore reconstruction. The chapter finishes with a simple example to illustrate how the impedance, impulse response, and bore reconstruction are related and how they are deduced.

1.2.2 Chapter 3: The Two-Microphone-Four-Calibration System

This chapter explains the workings of the *Two-Microphone-Four-Calibration (TMFC)* method which is designed to calculate the acoustic input impedance of musical instruments. A general expression for the experimental impedance of the instrument to be studied is derived in terms of the ratio of the pressures measured by two microphones and three complex calibration coefficients. For frequencies above 1 kHz a calibration procedure is used in which theory and experiment are fully decoupled. For frequencies below 1 kHz a partial calibration technique is used in which theory and experimental are not fully separated since knowledge of the propagation constant is required. A comparison with the other bore reconstruction methods of APR and BIAS is given. Advantages and disadvantages of the TMFC technique relative to these methods are highlighted. There is some lengthy discussion on pitfalls that must be avoided to obtain accurate and complete data over a large bandwidth. This includes: higher-modal propagation - since most of the algorithms used assume plane-wave propagation; singularity effects - in which the ratio of the pressures at the microphones is undefined; calibration of two microphones - since the response of each microphone is not identical; upper frequency limitations - dictated by the cut-on frequency at which higher modes begin to propagate; and lower frequency limitations - dictated by the finite separation of the microphones. At the end of this chapter some preliminary impedance results are given, compared with the plane-wave theoretical prediction, and discussed.

1.2.3 Chapter 4: Impedance Measurement of Trumpets Using BIAS

This results chapter is concerned with research on the Smith-Watkins trumpet. Expert trumpet players were invited - under strict playing test conditions - to play a Smith-Watkins '464R-25' trumpet with (i) a 'symphonic' set-up consisting of a 1.5C mouthpiece and wide '36' leadpipe, and (ii) A 'screamer' set-up consisting of a screamer

mouthpiece - developed by Smith - and a narrow '12' leadpipe. Players found, as expected, that the two set-ups behaved in a similar manner but with one noticeable exception: for the screamer set-up, there was a small, but definite resonance at approximately 2 kHz. For the traditional set-up there was no such observation. These observations are investigated experimentally using the *Brass-Instrument-Analysis-System (BIAS)* and conclusions are drawn.

1.2.4 Chapter 5: Bore Reconstruction via the TMFC Method

In this chapter, the TMFC system is used to measure the impedance and calculate bore reconstructions for a set of test objects for which the impedance is simple and accurately known. These include cylindrical and stepped tubes, and horns. Once we have established that the system is capable of giving accurate results we can start measuring musical instruments for which the profile, in general, is complicated and not known accurately. This includes the study of samples from a set of French horn crooks: a comparison is made between two F-crooks in the set. One is perceived by an expert to play 'well', and another is perceived to play 'poorly'. The system is used to determine scientifically why these observations are so. An adaptor allowing the measurement of instruments plus their mouthpieces was designed. An example result is given for a Dennis Wick trombone mouthpiece. Coupling issues between the system and an instrument are discussed. Due to the nature of acoustic propagation, a small section of cylindrical tubing must always be used as part of the coupler. This however, alters the measured impedance and so must be removed via a post-processing technique. This frequency-domain technique is discussed.

1.2.5 Chapter 6: Bore Reconstruction of French Horn Crooks

This final results chapter investigates the behaviour and design of some traditional and contemporary horn crooks. The bore profiles of a sizable sample of terminally-fitting crooks are derived from the TMFC method. Bore profiles were also derived from time-domain pulse reflectometry measurements for comparison. The results for both methods are presented with their advantages and disadvantages being discussed. Comments are also made on how the crooks were manufactured.

1.2.6 Chapter 7: Conclusions and Future Work

The final chapter serves two purposes. One, to review the main results and findings that can be drawn from the thesis and demonstrate that the original aims have indeed been satisfied. A discussion of the experimental obstacles, difficulties with computational analysis, and how these problems were overcome to achieve these aims are outlined.

The second purpose is to suggest future work, with regards to the study of a wider range of instruments and improvements to the TMFC system.

1.3 Past and Present Research in the Field

Similar methods to that of the TMFC technique have been utilised in the past, whereby a varying number of microphones and a varying number of calibration procedures (usually closed tubes) are used to determine the input impedance or related parameters. These methods are outlined in the following examples.

Single and multiple microphone techniques have been widely used to measure the characteristic impedance of porous materials - for such applications as turbo-machinery noise control and room acoustics[1, 2, 3, 4, 5, 6, 7]. Other papers of interest can be found in the literature[8, 9, 10, 11, 12, 13, 14].

Dalmont et al[15, 16] developed a two microphone method at the start of the 21st Century in which two calibration measurements are made. The first involves a long closed tube for which an approximate expression for the impedance is determined. The second is a measurement of a shorter closed tube. This allows an accurate determination of the propagation constant. Errors appear in the results as complex amplitude oscillations. These errors can be partially removed by applying a low pass filter to the data. Then expressions for the calibration parameters can be deduced and improved via an iterative process. A sine wave source is used as the excitation.

In the early Nineties the *Two-Microphone-Three-Calibration (TMTC)* system by Gibiat, Laloë et al[17] was developed. The method requires the determination of three complex calibration parameters. This is achieved by making use of three cylindrical calibration tubes. Despite yielding accurate results at low frequencies this method has the disadvantage that experiment and theory cannot be fully decoupled since the

propagation constant is obtained using a theoretical model rather than being accounted for in the calibration. At very high frequencies - many kilohertz - it is found that the errors in the propagation constant model grow large thus the method is limited to low frequencies. For this reason, van Walstijn developed the Two-Microphone-Four-Calibration[18, 19, 20, 21] technique which can measure from 1 kHz up to 20 kHz and requires no knowledge of the propagation constant.

Other types of acoustic excitation used in the field include that used by Seybert and Ross[22] in the late Nineties in which a two microphone measurement column is acoustically driven by a Gaussian white noise sample producing a randomly fluctuating pressure field.

Acoustic Pulse Reflectometry (APR) is an example of a single microphone technique that has had a lot of success in the field of bore reconstruction[23, 24, 25, 26, 27, 28, 29, 30, 31, 32, 33, 34, 35, 36, 37, 38]. It was originally designed for the purpose of seismological studies[39, 40] in the Sixties for determining the thickness and type of various rock layers (stratification) within the crust of the Earth. The excitation mechanism was in the form of a pulse and was generated by detonating dynamite. This method, unlike the previous methods, uses only a single microphone and is a time-domain rather than frequency-domain technique in which the bore reconstruction is obtained from directly measuring the input impulse response (IIR). This method is limited by the bandwidth over which it can yield results; this is currently tens of Hz to 15 kHz[24]. The upper frequency limit restricts the axial resolution of the reconstruction. The lower limit can cause the reconstructed profile to be underestimated. Due to the nature of the excitation signal, losses are an important problem for APR, especially when attempting to reconstruct long instruments[33, 41, 42].

Another example of a single microphone technique is that developed by Keefe et al[43] in the early Nineties intended for the impedance measurement of human ear canals. The method uses a variety of calibration tubes and a chirp as the excitation signal. This system not only measures the impedance but also the reflection coefficient. Then the Fourier transform is taken to obtain the time-domain response.

Both time-domain and frequency-domain methods have been used to study the airway dimensions of patients[44, 45, 46, 47, 48, 49, 50, 51, 52]. Canine tracheas were

originally measured in the Seventies[53], and human vocal tracts were first studied later in the Eighties[54]. More contemporary studies with relevance to the medical field include the work by Gray et al in 2005[55, 56].

Fault finding and leak detection in musical instruments and ducts is another area of interest[57, 58, 59, 60, 61]. Many musical wind instruments are constructed from thin pipes that are curled round into complicated shapes. This means that access to the inside of the object is very difficult with, say, callipers if we wanted to assess the internal bore for imperfections. However, described in this thesis are non-invasive methods of studying the desired object. A bore reconstruction can be generated by the acquired data and any cracks, dents or anomalies can be identified and hence corrected.

A very successful technique developed by Kausel et al is the commercially available *Brass-Instrument-Analysis-System (BIAS)*[62, 63]. This is a device in which a feedback loop ensures a constant volume velocity hence the impedance becomes a monotonic function of pressure which is measured by a single microphone situated in the measurement head.

Work done by Forbes et al [64, 65, 66, 67, 68, 69, 70] approaches bore reconstruction in the context of pulse reflectometry from a slightly different, and very mathematical, angle. Their method is to measure the radiated wave from the open end of the study object. From this information the reflectance can be derived. The impedance follows trivially from this. Once obtained, the IIR and bore profile can be found. An advantage of this method is that there is no need to couple the study object to a measurement duct, and so there is no need for the long source tube normally used by APR to eliminate secondary reflections interfering with the pre-deconvolved impulse response signal.

Wolfe et al have successfully measured a clarinet with the impedance measured at the reed of the instrument[71]. This was done using a three microphone technique measuring as high as 4 kHz. The flute has also been investigated by measuring the impedance at the embouchure[71, 72, 73, 74, 75].

Research by Braden et al[76, 77, 78, 79] has involved the determination of the input impedance from a known profile via the Brass-Instrument-Evolution-Software (BIES) developed by the author[80]. The experimental impedance has been obtained using the BIAS for comparison, mainly for Rath trombones. The inverse problem is also

considered: calculating a bore profile from knowledge of the impedance. This is done using an optimisation technique: the known impedance is used as a 'target' for the software. The algorithm divides the profile into many small cylindrical sections. The radii of the profile for each section is iteratively adjusted until its associated impedance matches that of the target impedance. The code explores both genetic algorithms, and the Rosenbrock direct-search method. Higher-mode propagation and the effect of bends in an instrument are also highlighted.

1.4 Applications

1.4.1 The 'Virtual Work Bench'

The bore profile of an instrument is very important in determining the sound produced by that instrument. Information about the sound is contained within the instrument's impedance curve - the positions of the impedance peaks determine the obtainable notes; the magnitude and Q-factor determine how easily a note can be played; and the relative magnitudes of the impedance peaks strongly influence the timbre. It is possible to calculate the impedance curve for a known profile, then changes can be made to the profile to see how they affect the impedance and hence determine how they affect the sound[81]. This is much less time consuming and less costly than producing many instruments with slightly different bores and comparing them by ear.

1.4.2 Example of Problem Solving in Musical Acoustics: The Cornetto

As well as being able to calculate an experimental expression for the input impedance, impulse response and bore profile, it is a very important ability in musical acoustics to be able to convert between all three parameters. A good example of this is work carried out by Campbell and van Walstijn on the intonation of cornetti[81]. Two 'identical' cornetti were found to play differently. One played 'well', while one played 'poorly' at certain notes. On inspection of the bore profile it was found that in fact the instruments did not have exactly the same profile. The 'poor' instrument varied significantly in profile from the 'well-playing' instrument at two main points: one at the

throat of the instrument; and one close to the mouth. The next question was: which deviation was causing the instrument to be musically different? Was it the former, the latter, or a combination of both? To answer this question, two theoretical bore profiles were generated: one with the profile of the poor instrument but with the deviation at the mouth artificially removed; and one with the deviation at the throat artificially removed. The impedance curves were then obtained for both of these artificial profiles and compared with the impedance curve of the well behaved instrument. The artificial impedance curve with the deviation at the mouth had a similar impedance curve to the well behaved curve; the deviation at the mouth has no significant effect on the musicality of the instrument. The artificial impedance curve with the deviation at the throat showed a different impedance curve to that of the well behaved instrument curve, so the deviation at the throat was almost fully responsible for the discrepancies between the two instruments.

Chapter 2

Background Acoustics Theory

This chapter starts with a basic discussion of the properties of fluids and the propagation of sound in such media[82, 83, 84, 85, 86]. Air will be considered to be a 'perfect fluid' obeying the equation of state for an ideal gas allowing us to yield some useful theoretical equations for modelling the behaviour of sound in air. Since the work in this thesis deals with relatively low amplitudes of sound it is reasonable to assume wave propagation in the air is linear. This allows us to use the linearised version of the wave equation which we will derive, along with its solutions in various coordinate systems. Some time will be spent looking at an important frequency-domain parameter: the *acoustic impedance*. We will discuss theoretical impedance models for three simple objects: the cylinder, the cone, and the horn. The profile of a real musical instrument can then be theoretically decomposed into a specified number of sections with the internal profile of each section being modelled by an appropriate approximate curve. From this approach an accurate impedance model can be derived for the instrument. The model will however assume that only the planar mode propagates in the acoustic space of the instrument since the algorithms developed do not take account of higher modal propagation. Losses incurred by the acoustic waves at the walls of the instrument and at the open end will be considered. We will look at two useful properties that can be derived from the impedance: the input impulse response, and the bore reconstruction. Finally, there will be a short discussion on the APR and BIAS equipment.

2.1 Fluid Dynamics

The term 'fluid' refers to a substance that will deform when acted upon by a shear force i.e. a fluid has an ability to flow. Both liquids and gases come under the heading of a fluid, but there is an important difference between the two: liquids can generally be considered incompressible - unless subjected to extreme pressures - whereas gases can be either[87]. For example, when considering the flow of air over an aerofoil it is acceptable to assume that air is incompressible and has a constant density throughout. However, it is the ability to compress and decompress (rarefy) that allows air, in the appropriate conditions, to store and release energy.

2.2 Sound in a Fluid

Sound waves are pressure oscillations occurring in a fluid. The resulting vibrations of the fluid particles are parallel to the direction of travel of the wave. This is known as a *longitudinal wave*. If the fluid happens to be air and the propagating wave reaches the ear, the eardrum is also set into a vibrational pattern. This results in a signal being sent to the brain via the *cochlear* or *auditory nerve* where it is interpreted as sound[82], provided the frequency of the wave lies in the audible range (for humans this is 20 Hz to 20 kHz)[85]. If a gas, which is an example of a fluid, can be considered as ideal then many useful theoretical models can be derived for the propagation of sound in this medium.

2.3 Air: The Ideal Gas

Air, to a good approximation can be considered as an *ideal gas* meaning that the particles constituting the gas behave like point masses of zero volume, collide elastically, and obey the equation of state[85]

$$pV = n\mathcal{R}\mathcal{T}_{\text{abs}} \tag{2.1}$$

where p is the air pressure, V is the volume of the gas, n is the number of moles, $\mathcal{R}$ is the gas constant and $\mathcal{T}_{\text{abs}}$ is the absolute temperature (in K).

2.3.1 Speed of Sound in an Ideal Gas

The speed of sound in an ideal gas, found in standard physics text[85], is proportional to the square root of the temperature

$$v = \sqrt{\frac{\gamma \mathcal{R} \mathcal{T}_{\text{abs}}}{m}} \tag{2.2}$$

where γ is the ratio of the specific heat capacity at constant pressure to the specific heat capacity at constant volume

$$\gamma = \frac{C_p}{C_V} \tag{2.3}$$

and m is the mass of one mole of the gas. For this thesis the air temperature could be assumed to be constant for the duration of any one experiment. There was, of course, significant fluctuation from day to day. The effect this temperature variation would have on the sound propagation was accounted for in the algorithms.

2.4 Derivation of the Linear Acoustic Wave Equation

Consider a small mass of ideal gas. When it experiences a small pressure increase, p, its volume will decrease slightly according to how compressible the gas is. This property is represented by the *bulk modulus,* $\mathcal{B}_{\mathcal{M}}$, defined as the ratio of the change in pressure from equilibrium to the fractional change in volume[85]

$$\mathcal{B}_{\mathcal{M}} = -\frac{P - P_0}{(V - V_0)/V} \tag{2.4}$$

where P_0 and V_0 are the pressure and volume of the mass at equilibrium respectively. The small pressure fluctuation causes the absolute pressure and volume to change respectively to P and V. Note that the pressure difference is

$$p = P - P_0. \tag{2.5}$$

During the compression (or expansion) the mass, M, of the gas remains constant i.e. mass is neither created or destroyed, hence

$$M = \rho_0 V_0 = \rho V \tag{2.6}$$

where ρ_0 is the air density at equilibrium and ρ is the new air density caused by the pressure fluctuation. Combining equation (2.4) and (2.5) with equation (2.6) we find that

$$\rho = \rho_0 \left(\frac{p}{\mathcal{B}_\mathcal{M}} + 1 \right). \tag{2.7}$$

If the fluctuations in pressure are small then we can assume that

$$\frac{p}{\mathcal{B}_\mathcal{M}} \ll 1 \tag{2.8}$$

and so

$$\rho \approx \rho_0. \tag{2.9}$$

Newton's second law applied to fluid mechanics[87] states that a lump of gas situated in a pressure gradient will accelerate according to

$$-\nabla p = \rho \frac{\mathrm{D}\vec{v}}{\mathrm{Dt}} \tag{2.10}$$

where $\vec{v} = (v_x, v_y, v_z)$ is the velocity vector with components in the x, y, and z-direction. ∇ is the gradient operator and D/Dt is the *material derivative* or *substantive derivative*

$$\frac{\mathrm{D}}{\mathrm{Dt}} = \frac{\partial}{\partial t} + v_x \frac{\partial}{\partial x} + v_y \frac{\partial}{\partial y} + v_z \frac{\partial}{\partial z}. \tag{2.11}$$

Again, since the pressure fluctuations are small we can assume that the terms containing a component of velocity are negligible[88]

$$\frac{\mathrm{D}}{\mathrm{Dt}} \approx \frac{\partial}{\partial t} \tag{2.12}$$

and since the density is approximately constant equation (2.10) becomes

$$\rho_0 \frac{\partial \vec{v}}{\partial t} = -\nabla p. \tag{2.13}$$

This is known as *Euler's linear force equation*[83],[85],[87].

Another standard result from fluid dynamics theory is the *continuity equation*[85]

$$\frac{\partial \rho}{\partial t} + \nabla \cdot (\rho \vec{v}) = 0. \tag{2.14}$$

This equation, like (2.6), states that the mass of the fluid must be conserved. Substituting equation (2.7) into equation (2.14) and taking ρ outside of the divergence term we find

$$\frac{1}{\mathcal{B}_\mathcal{M}} \frac{\partial p}{\partial t} + \nabla \cdot \vec{v} = 0. \tag{2.15}$$

Taking the partial time derivative of the above equation yields

$$\frac{1}{\mathcal{B}_\mathcal{M}} \frac{\partial^2 p}{\partial t^2} = -\frac{\partial}{\partial t} \nabla \cdot \vec{v}. \tag{2.16}$$

Taking the divergence of Euler's equation gives

$$\frac{1}{\rho_0} \nabla^2 p = -\nabla \cdot \frac{\partial \vec{v}}{\partial t} \tag{2.17}$$

where ∇^2 is the Laplacian operator. The right hand side of the two equations above are equivalent since the order of the operations ∇ and $\partial/\partial t$ does not matter, thus

$$\nabla^2 p = \frac{1}{c^2} \frac{\partial^2 p}{\partial t^2} \tag{2.18}$$

where c is the speed of sound in the medium

$$c = \sqrt{\frac{\mathcal{B}_\mathcal{M}}{\rho_0}}. \tag{2.19}$$

This is the linear acoustic wave equation. Obtaining this equation has required us to make some approximations. It is these approximations that make the wave equation valid only for linear behaviour of the air particles i.e. the restoring force acting on the particle varies linearly with position. The foundational theory of *nonlinear* acoustics

can be found in various textbooks[85], [89].

Note that from this point on the subscript in the expression for density ρ_0 is dropped and replaced simply by ρ .

2.4.1 Solution to the Wave Equation in Cartesian Coordinates

Consider an acoustic wave propagating in the x-direction. The complex solution to the one dimensional equivalent of the wave equation (2.18) in Cartesian coordinates

$$\frac{\partial^2 p}{\partial x^2} = \frac{1}{c^2}\frac{\partial^2 p}{\partial t^2} \tag{2.20}$$

is a plane wave of the form

$$p(x,t) = [A\exp(-ikx) + B\exp(ikx)]\exp(i\omega t) \tag{2.21}$$

where k is the wavenumber and ω is the angular frequency. This can be verified by substitution of (2.21) into the wave equation and noting that

$$c = f\lambda = \frac{\omega}{k}. \tag{2.22}$$

The true pressure that we actually measure, $p_{\text{meas}}(x,t)$, is obtained by taking the *real part* of the complex pressure

$$p_{\text{meas}}(x,t) = \text{Re}\{A\exp[-i(kx-\omega t)] + B\exp[i(kx+\omega t)]\} \tag{2.23}$$

hence

$$p_{\text{meas}}(x,t) = A\cos(kx-\omega t) + B\cos(kx+\omega t). \tag{2.24}$$

So the term containing the amplitude, A, corresponds to the component of the wave travelling in the positive x-direction and the term containing B corresponds to the component in the negative direction.

The x-component of the volume velocity can be obtained by substituting our solution into Euler's linear equation (2.13) giving

$$v_x = \frac{k}{\rho\omega}[A\exp(-ikx) - B\exp(ikx)]\exp(i\omega t). \tag{2.25}$$

This result will be useful when considering the theory of acoustic impedance.

2.4.2 Spherical Polar Coordinates

The wave equation in spherical polar coordinates (r, θ, ϕ) is given by

$$\frac{1}{r^2}\frac{\partial}{\partial r}\left(r^2\frac{\partial p}{\partial r}\right) + \frac{1}{r^2\sin\theta}\frac{\partial}{\partial\theta}\left(\sin\frac{\partial p}{\partial\theta}\right) + \frac{1}{r^2\sin^2\theta}\frac{\partial^2 p}{\partial\phi^2} = \frac{1}{c^2}\frac{\partial^2 p}{\partial t^2} \tag{2.26}$$

where r is the *radial* coordinate, θ is the *polar* or *zenith* angle and ϕ is the *azimuthal* angle. The full solution for the pressure associated with the mnth mode is given by[88],[86]

$$p(r,\theta,\phi) = p_0\sum_{m=0}^{\infty}\sum_{n=0}^{\infty}\exp(-im\phi)\cdot\Theta_n^m(\cos\theta)\cdot\left(\frac{\alpha_{mn}r}{a}\right)\cdot\frac{J_{n+1/2}(kx)}{(kx)^{1/2}} \tag{2.27}$$

where p_0 is the pressure amplitude, a is the transverse radius, m represents the number of nodal pressure diameters in the (r, ϕ) plane and n corresponds to the number of nodal circles. α_{mn} is the attenuation constant associated with mode (m,n) and $\Theta_n^m(\cos\theta)$ represents the Legendre function. For the case of spherically-symmetric waves there is no dependence on θ and ϕ. The Laplacian in equation (2.26) then reduces to[90]

$$\nabla^2 \equiv \frac{1}{r^2}\frac{\partial}{\partial r}\left(r^2\frac{\partial}{\partial r}\right) \tag{2.28}$$

allowing the wave equation to be written as

$$\frac{\partial^2 p}{\partial r^2} + \frac{2}{r}\frac{\partial p}{\partial r} = \frac{1}{c^2}\frac{\partial^2 p}{\partial t^2} \tag{2.29}$$

for which a solution is

$$p(r,t) = \frac{A}{r}\exp[-i(kr-\omega t)] + \frac{B}{r}\exp[i(kr+\omega t)]. \tag{2.30}$$

This can be verified by direct substitution. We can treat the wavefronts in a *conical bore* in this manner i.e. as sections of a spherical wave with no dependence on θ or ϕ.

2.4.3 Cylindrical Polar Coordinates

In the cylindrical polar coordinate system we use (r, ϕ, x), where r is the radial coordinate, ϕ is the transverse concentric coordinate, and x is the axial coordinate. Using the wave equation (2.18) and the expression for the Laplacian in cylindrical polar coordinates (A.11) we find that

$$\frac{1}{r}\frac{\partial}{\partial r}\left(r\frac{\partial p}{\partial r}\right) + \frac{1}{r^2}\frac{\partial^2 p}{\partial \phi^2} + \frac{\partial^2 p}{\partial x^2} = \frac{1}{c^2}\frac{\partial^2 p}{\partial t^2}. \tag{2.31}$$

The full solution to the above equation is given by[86], [88]

$$p(r, \phi, x) = p_0 \sum_{m=0}^{\infty}\sum_{n=0}^{\infty} \exp(-im\phi) \cdot J_m\left(\frac{\alpha_{mn} r}{r_0}\right) \cdot \exp[-i(k_{mn}x + \omega t)] \tag{2.32}$$

where r_0 is the radius of the bore, α_{mn} is the attenuation constant associated with mode (m, n) and

$$k_{mn} = \sqrt{k^2 - \left(\frac{\alpha_{mn}}{r_0}\right)^2} \tag{2.33}$$

where J_m represents the Bessel function of the first kind. If we consider the pressure variation from the axial term by setting the first two terms on the right hand side of equation (2.32) as a constant, A, then we have

$$p(x, t) = A \exp[-i(k_{mn}x + \omega t)]. \tag{2.34}$$

For the plane wave component $(m, n) = (0, 0)$ and so

$$k_{mn} = k_{00} = \frac{\omega}{c} \tag{2.35}$$

and the pressure reduces to

$$p(x, t) = A \exp[-i(kx + \omega t)] \tag{2.36}$$

which is the simplest solution to the one dimensional wave equation in the Cartesian basis.

2.5 Acoustic Impedance

2.5.1 Impedance Definitions

The *specific acoustic impedance, z,* is the ratio of the pressure to the particle speed, u, at a particular point in the space through which the acoustic wave propagates

$$z = p/u. \tag{2.37}$$

The *acoustic impedance, Z,* is similar to the specific acoustic impedance but takes into account the area, S, of the plane (perpendicular to the direction of propagation) through which the wave passes

$$Z = p/uS = p/U = z/S \tag{2.38}$$

where U is the *volume velocity* which is just the particle velocity multiplied by the surface area S.

In general, a phase difference occurs between the applied pressure and the particle's velocity. To account for this we define the *complex impedance*

$$Z = R + iX \tag{2.39}$$

where R is the real resistive part. This term accounts for dissipative processes that the particles experience - for example, losses incurred at the wall of the instrument. X is the imaginary reactive part of the impedance and accounts for mechanisms that transform the kinetic energy of the particles into potential energy and vice versa.

The magnitude of the impedance is

$$|Z| = \sqrt{R^2 + X^2} \tag{2.40}$$

and the phase is given by

$$\angle Z = \tan^{-1}\left(\frac{X}{R}\right). \tag{2.41}$$

2.5.2 Electrical Impedance

As with many acoustical systems, it is sometimes instructive to consider their electrical analogy. Electrical impedance (also usually denoted Z) is defined as the response of an electric circuit to an oscillatory excitation i.e. an alternating current. Mathematically it is defined as the ratio of voltage, V, to current, I. Note that V and I are analogous to p and U respectively. In some ways the electrical impedance of an LCR (Inductor-Capacitor-Resistor) circuit is similar to the acoustic impedance of say, a closed cylindrical tube. Resonance behaviour is observed in both cases. Both systems suffer from losses (wall and thermal losses in the acoustic case, thermal dissipation in the resistor for the electrical case). The ability of air to store and release energy is analogous to the capacitor's ability to store and release the charge on its plates, hence the potential energy stored in the electric field between the two plates is varied. The fact that air has mass (i.e. inertia) is likened to the properties of an inductor. An inductor acts in such a way as to oppose a change in current flow - the inductor applies an electromotive force (e.m.f) opposing the direction of the source voltage. This, like the capacitor results in energy being stored and released in the inductor (but with a phase shift relative to the a.c. source). When an oscillating pressure wave impinges on an air particle, the particle will oppose the change in velocity (momentum) and will gain and lose kinetic energy but with a phase difference relative to the applied pressure. For more on electrical impedance see some standard text books[91].

2.6 Input Impedance Equation and Characteristic Impedance

Consider an acoustic wave propagating in the positive x-direction inside an infinitely long cylindrical tube of constant cross-sectional area S. The solution to the wave equation in Cartesian coordinates was given in equation (2.21) and can be applied to this example. Since the tube is infinitely long there is no reflected wave hence the B coefficient is zero. The complex pressure of the forward propagating wave is then described by

$$p^+(x,t) = A\exp(-ikx)\exp(i\omega t). \tag{2.42}$$

From equation (2.25) we saw that the x-component of velocity was

$$v_x = \frac{k}{\rho\omega}[A\exp(-ikx) - B\exp(ikx)]\exp(i\omega t). \tag{2.43}$$

Setting B to zero and noting that $U(x,t) = v_x S$, the forward propagating component of the complex volume velocity is now

$$U^+(x,t) = \frac{S}{\rho c}[A\exp(-ikx)]\exp(i\omega t) = \frac{S}{\rho c}p^+(x,t). \tag{2.44}$$

The impedance is the magnitude of the ratio of pressure to volume velocity and for this special case is referred to as the *characteristic impedance*

$$Z_c = \frac{\rho c}{S}. \tag{2.45}$$

At high frequencies, the acoustic waves inside the tube are diffracted less, becoming highly directional. As a result the reflection coefficient tends towards zero i.e the B coefficient tends towards zero. For this reason, the impedance tends towards Z_c in the high frequency limit.

For a backward propagating wave the A coefficient must be zero. The complex pressure for the backward propagating wave is described by

$$p^-(x,t) = B\exp(ikx)\exp(i\omega t) \tag{2.46}$$

and the backward component of the complex volume velocity is

$$U^-(x,t) = \frac{S}{\rho c}[-B\exp(ikx)]\exp(i\omega t) = -\frac{S}{\rho c}p^-(x,t) \tag{2.47}$$

and so the characteristic impedance for a backward travelling wave is $-Z_c = -\rho c/s$.

In general, when both forward and backward propagating waves are present the impedance is

$$Z = \frac{p(x,t)}{U(x,t)} = Z_c \left[\frac{A\exp(-ikx) + B\exp(ikx)}{A\exp(-ikx) - B\exp(ikx)} \right]. \tag{2.48}$$

Let us define the plane at $x = 0$ as the *input plane* or *reference plane*. The impedance at this plane is referred to as the *input impedance*, Z_{IN}, where

$$Z_{\text{IN}} = \frac{p(0,t)}{U(0,t)} = Z_c \left[\frac{A+B}{A-B} \right]. \tag{2.49}$$

At a general point along the axis , $x = \mathcal{L}$, the impedance is given by

$$Z_{\mathcal{L}} = \frac{p(\mathcal{L},t)}{U(\mathcal{L},t)} = Z_c \left[\frac{A\exp(-ik\mathcal{L}) + B\exp(ik\mathcal{L})}{A\exp(-ik\mathcal{L}) - B\exp(ik\mathcal{L})} \right]. \tag{2.50}$$

We can rearrange (2.50) to obtain A and B in terms of $Z_{\mathcal{L}}$ and Z_c

$$\frac{B}{A} = \exp(-2ik\mathcal{L}) \left[\frac{Z_{\mathcal{L}} - Z_c}{Z_{\mathcal{L}} + Z_c} \right] \tag{2.51}$$

and substitute this into (2.49). After substantial rearranging this gives

$$Z_{\text{IN}} = Z_c \left[\frac{Z_{\mathcal{L}} + iZ_c \tan(k\mathcal{L})}{iZ_{\mathcal{L}} \tan(k\mathcal{L}) + Z_c} \right] \tag{2.52}$$

or

$$Z_{\text{IN}} = Z_c \left[\frac{Z_{\mathcal{L}} \cos(k\mathcal{L}) + iZ_c \sin(k\mathcal{L})}{iZ_{\mathcal{L}} \sin(k\mathcal{L}) + Z_c \cos(k\mathcal{L})} \right]. \tag{2.53}$$

This equation will be referred to as the *input impedance equation* from here.

2.7 Reflection Coefficient and Power Reflection Coefficient

The *reflection coefficient* (or *reflectance*), $R(\omega)$, is defined as the ratio of the backward and forward propagating pressure waves at the input plane[88]

$$R(\omega) = \frac{p(0,t)^-}{p(0,t)^+} = \frac{B}{A}. \tag{2.54}$$

By rearranging (2.49), we find

$$\frac{B}{A} = \frac{Z_{\text{IN}} - Z_c}{Z_{\text{IN}} + Z_c} \tag{2.55}$$

hence

$$R(\omega) = \frac{Z_{\text{IN}} - Z_c}{Z_{\text{IN}} + Z_c}. \tag{2.56}$$

The *power reflection coefficient* is defined as[92]

$$R_\pi = \left|\frac{B}{A}\right|^2 = \left(\frac{B}{A}\right)\left(\frac{B}{A}\right)^* \tag{2.57}$$

where the $*$ denotes the complex conjugate. Noting that the input impedance can be written as

$$Z_{\text{IN}} = R_{\text{IN}} + iX_{\text{IN}} \tag{2.58}$$

allows us to write

$$R_\pi = \frac{Z_{\text{IN}}Z_{\text{IN}}^* - (Z_{\text{IN}} + Z_{\text{IN}}^*)Z_c + Z_c^2}{Z_{\text{IN}}Z_{\text{IN}}^* + (Z_{\text{IN}} + Z_{\text{IN}}^*)Z_c + Z_c^2} \tag{2.59}$$

and

$$R_\pi = \frac{|Z_{\text{IN}}|^2 - 2R_{\text{IN}}Z_c + Z_c^2}{|Z_{\text{IN}}|^2 + 2R_{\text{IN}}Z_c + Z_c^2}. \tag{2.60}$$

We can also define the *power transmission coefficient* as

$$T_\pi = 1 - R_\pi = \frac{4R_{\text{IN}}Z_c}{|Z_{\text{IN}}|^2 + 2R_{\text{IN}}Z_c + Z_c^2}. \tag{2.61}$$

The power reflection/transmission coefficients are useful when, for example considering the high/low pass filtering effect in a cylindrical tube with an open/closed tone hole[92].

2.8 Acoustic Impedance of Elementary Objects

The following section derives the theoretical impedance of some simple cylindrically symmetric objects. We will start with a closed cylindrical pipe and assume the propagation is lossless. Then we will look at how to incorporate losses experienced by the propagating wave into the model and see how the impedance is modified accordingly. The majority of wind instruments are open at the far end rather than closed so we will consider open pipes with and without a flanged end. Then we will go on to look at multiple cylinder objects, cones and horns and see how an instrument can be represented as a concatenation of the various components.

2.9 Deriving an Accurate Impedance Model

First, we consider the simplest case: a lossless pipe of constant radius closed at the far end. Next, we include losses. We subsequently consider a lossy open ended cylindrical pipe, then conical, exponential and catanoidal horns.

2.9.1 Lossless Closed Pipe

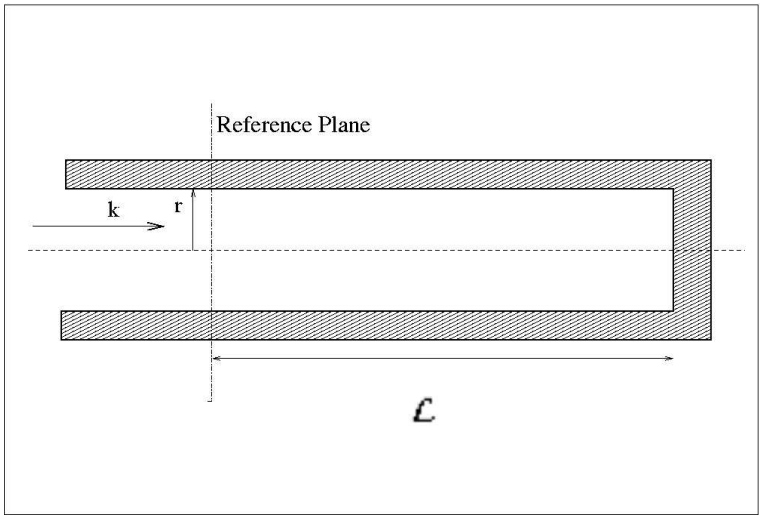

Figure 2.1: A lossless closed pipe of length $\mathcal{L}$ and radius r. In general, the reference plane can be chosen at any point along the pipe.

For the lossless closed pipe we will assume the pipe is of a constant radius, r, and is

closed at the far end, a distance, $\mathcal{L}$, from the plane at which the impedance is calculated, referred to as the *input plane* or *reference plane*. The propagating wave experiences no losses. This means that no energy is lost to the walls via wall vibrations, given to the air as random thermal motion or lost through radiative mechanisms.

For a pipe closed at the far end $Z_{\mathcal{L}} = \infty$. The particle velocity at the wall must be zero irrespective of the applied pressure implying the terms containing Z_c in equation (2.53) become negligible relative to the terms containing $Z_{\mathcal{L}}$. Hence the complex input impedance simplifies to

$$Z_{\text{IN}}^{\text{closed}} = -iZ_c \cot(k\mathcal{L}) \tag{2.62}$$

where

$$Z_c = \frac{\rho c}{\pi r^2}. \tag{2.63}$$

Since the wavenumber k and the rest of the parameters in equation (2.62) are purely real and multiplied by the imaginary unit the real part is zero

$$\text{Re}\left\{\frac{Z_{\text{IN}}^{\text{closed}}}{Z_c}\right\} = 0 \tag{2.64}$$

and the imaginary part is simply

$$\text{Im}\left\{\frac{Z_{\text{IN}}^{\text{closed}}}{Z_c}\right\} = -\cot(k\mathcal{L}). \tag{2.65}$$

It follows trivially that the magnitude of the impedance is

$$\left|\frac{Z_{\text{IN}}^{\text{closed}}}{Z_c}\right| = |\cot(k\mathcal{L})| \tag{2.66}$$

and the phase is given by

$$\angle Z_{\text{IN}}^{\text{closed}} = \tan^{-1}\left(\frac{\text{Im}\{Z_{\text{IN}}^{\text{closed}}\}}{\text{Re}\{Z_{\text{IN}}^{\text{closed}}\}}\right) = \tan^{-1}\left(-\frac{1/\tan(k\mathcal{L})}{\text{Re}\{\text{Z}\}}\right). \tag{2.67}$$

These functions are plotted in Figure 2.2 and Figure 2.3 for a closed pipe of radius 2 cm and length 1 m. The speed of sound is taken as 345 m/s.

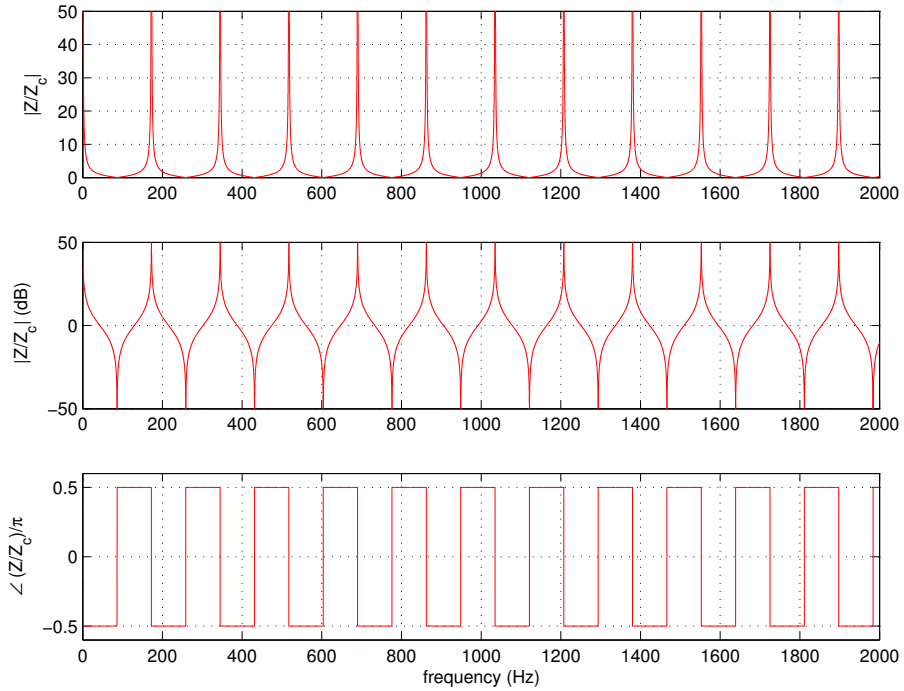

Figure 2.2: Absolute impedance magnitude, impedance magnitude in decibels and impedance phase for the lossless closed pipe of radius 2 cm and length 1 m.

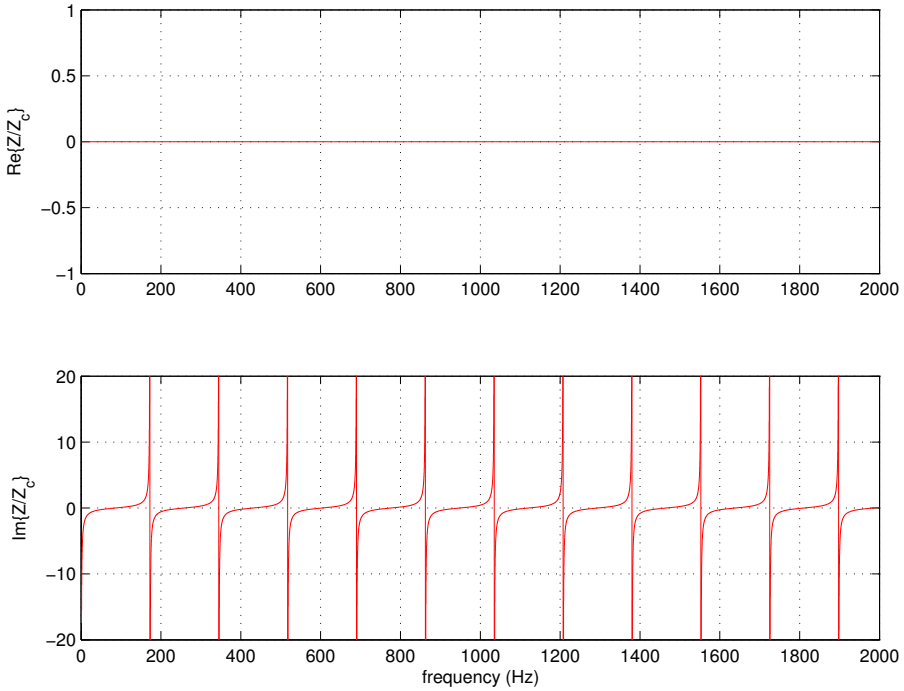

Figure 2.3: Real and imaginary part of the impedance for a lossless closed pipe of radius 2 cm and length 1 m.

Notice that the expression for the absolute impedance magnitude and the imaginary part of the impedance are the same in magnitude. The graphs appear different since the imaginary plot allows negative values whereas the impedance magnitude does not.

The magnitude of the impedance has also been plotted on a decibel scale and has been normalised relative to the characteristic impedance Z_c. Hence

$$\left|\frac{Z_{\text{IN}}}{Z_c}\right|(\text{dB}) = 20\log_{10}\left(\left|\frac{Z_{\text{IN}}}{Z_c}\right|\right). \tag{2.68}$$

Since there are no losses the impedance peaks and troughs in the magnitude plots actually tend to plus and minus infinity respectively.

For the phase of the impedance note that $\tan(k\mathcal{L})$ can take positive or negative values. Since the denominator of (2.67) is the real part of the impedance and equal to zero, the bracketed term can be either $+\infty$ or $-\infty$ thus giving a phase of either $+\pi/2$ or $-\pi/2$. Thus the graph has a square wave type appearance. The phase is positive when

$$\frac{\pi}{2} + n\pi < k\mathcal{L} < (n+1)\pi \tag{2.69}$$

where $n = 0, 1, 2, 3...$, and negative when

$$n\pi < k\mathcal{L} < (n+1)\frac{\pi}{2}. \tag{2.70}$$

As stated in equation (2.54), the reflection coefficient is the ratio of the pressures for the forward and backward propagating waves. For this simple case the forward propagating wave is fully reflected at the closed end back towards the plane at $x = 0$. A simple standing wave is set up. Since the backward travelling wave has the same energy as the forward travelling wave the reflection coefficient is $+1$.

2.9.2 Including Losses in the Model

Consider Figure 2.1. As a wave propagates through the pipe it will lose energy i.e. it will be attenuated because of losses experienced at the interface between the air in the pipe and the wall. The three main causes of losses (not including radiative processes) are wall vibrations, viscous dissipation and thermal dissipation[86]. We do not attempt to model losses via wall vibrations as it is assumed the walls of the aluminium and brass used in the experiments are rigid enough that this effect can be ignored. Viscous dissipation results from the viscous boundary layer formed at the walls as the wave propagates. The ratio of the pipe radius to the thickness of the viscous boundary layer is given by[86]

$$r_v = \left(\frac{\omega\rho}{\eta}\right)^{1/2} a \tag{2.71}$$

where η is the viscosity. The ratio of the pipe radius to the thickness of the thermal boundary layer is given by

$$r_t = \left(\frac{\omega\rho C_p}{\kappa}\right)^{1/2} a \tag{2.72}$$

where κ is the thermal conductivity. At temperatures close to 300 K (within $\pm$10 K) expressions for ρ, η, and κ as a function of temperature, T, can be inserted into the above equations[88] giving

$$r_v \approx 632.8a\sqrt{\omega/2\pi}(1 - 0.0031\Delta T) \tag{2.73}$$

and

$$r_t \approx 532.8a\sqrt{\omega/2\pi}(1 - 0.0031\Delta T) \tag{2.74}$$

where $\Delta T = T - 300$. Fletcher and Rossing[86] state the speed of sound in a lossy pipe as

$$v \approx c\left[1 - \frac{1}{\sqrt{2}r_v} - \frac{(\gamma - 1)}{\sqrt{2}r_t}\right] \tag{2.75}$$

and they define the attenuation constant as

$$\alpha \approx \frac{\omega}{c}\left[\frac{1}{\sqrt{2}r_v} + \frac{(\gamma-1)}{\sqrt{2}r_t}\right]. \tag{2.76}$$

Substituting equations (2.71) and (2.72) into (2.75) and (2.76) and writing γ and ΔT explicitly gives

$$v \approx c\left[1 - \frac{1.65\times10^{-3}}{a\sqrt{\omega/2\pi}}\right] \tag{2.77}$$

and

$$\alpha \approx \frac{3\times10^{-5}\sqrt{\omega/2\pi}}{a}. \tag{2.78}$$

For lossy propagation in the closed pipe the wavenumber k for the lossless case is simply replaced by the *propagation constant*

$$\Gamma = \frac{\omega}{v} - i\alpha. \tag{2.79}$$

Notice that the attenuation constant is proportional to the square root of the frequency so losses are greater at high frequencies.

2.9.3 Lossy Closed Pipe

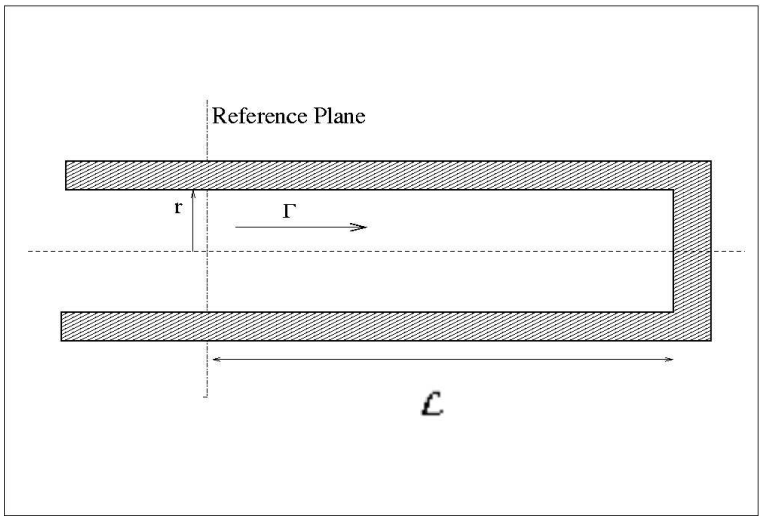

Figure 2.4: A lossy closed pipe of length $\mathcal{L}$ and radius r. For lossy cases the wavenumber k, which is real is replaced by the propagation constant Γ, which is complex.

The complex impedance for the lossy closed pipe is

$$Z_{\mathrm{IN}}^{\mathrm{closed}} = -iZ_c \cot(\Gamma\mathcal{L}). \tag{2.80}$$

The propagation constant now has an imaginary attenuation part as well as a real oscillatory part and so the impedance phase is no longer a square wave function- it is more 'rounded'. Equation (2.80) can be rewritten as

$$\frac{Z_{\mathrm{IN}}^{\mathrm{closed}}}{Z_c} = \frac{\exp(i\omega\mathcal{L}/v)\exp(\alpha\mathcal{L}) + \exp(-i\omega\mathcal{L}/v)\exp(-\alpha\mathcal{L})}{\exp(i\omega\mathcal{L}/v)\exp(\alpha\mathcal{L}) - \exp(-i\omega\mathcal{L}/v)\exp(-\alpha\mathcal{L})}. \tag{2.81}$$

Multiplying the numerator and denominator by the complex conjugate of the denominator allows us to rewrite equation (2.81) in the form of

$$\frac{Z_{\mathrm{IN}}^{\mathrm{closed}}}{Z_c} = R + iX \tag{2.82}$$

and so the complex impedance is

$$\frac{Z_{\mathrm{IN}}^{\mathrm{closed}}}{Z_c} = \left[\frac{\exp(2\alpha\mathcal{L}) - \exp(-2\alpha\mathcal{L})}{2\cosh(2\alpha\mathcal{L}) - 2\cos(2\omega\mathcal{L}/v)}\right] + i\left[\frac{-2\sin(2\omega\mathcal{L}/v)}{2\cosh(2\alpha\mathcal{L}) - 2\cos(2\omega\mathcal{L}/v)}\right]. \tag{2.83}$$

The magnitude of the impedance follows

$$\left|\frac{Z_{\mathrm{IN}}^{\mathrm{closed}}}{Z_c}\right| = \sqrt{\frac{[\exp(2\alpha\mathcal{L}) - \exp(-2\alpha\mathcal{L})]^2 + 4i\sin^2(2\omega\mathcal{L}/v)}{[\exp(2\alpha\mathcal{L}) + \exp(-2\alpha\mathcal{L}) - 2\cos(2\omega\mathcal{L}/v)]^2}} \tag{2.84}$$

and the resultant phase is expressed as

$$\angle Z_{\mathrm{IN}}^{\mathrm{closed}} = \tan^{-1}\left(\frac{\mathrm{Im}\{Z\}}{\mathrm{Re}\{Z\}}\right) = \tan^{-1}\left(\frac{-2\sin(2\omega\mathcal{L}/v)}{\exp(2\alpha\mathcal{L}) - \exp(-2\alpha\mathcal{L})}\right). \tag{2.85}$$

The above results for lossy propagation are plotted in Figure 2.5 and 2.6 for a closed tube of length 1 m and radius 2 cm. The reflection coefficient can also be derived from the impedance using equation (2.56), where Z_{IN} is replaced by $Z_{\mathrm{IN}}^{\mathrm{closed}}$, and is shown in Figure 2.7.

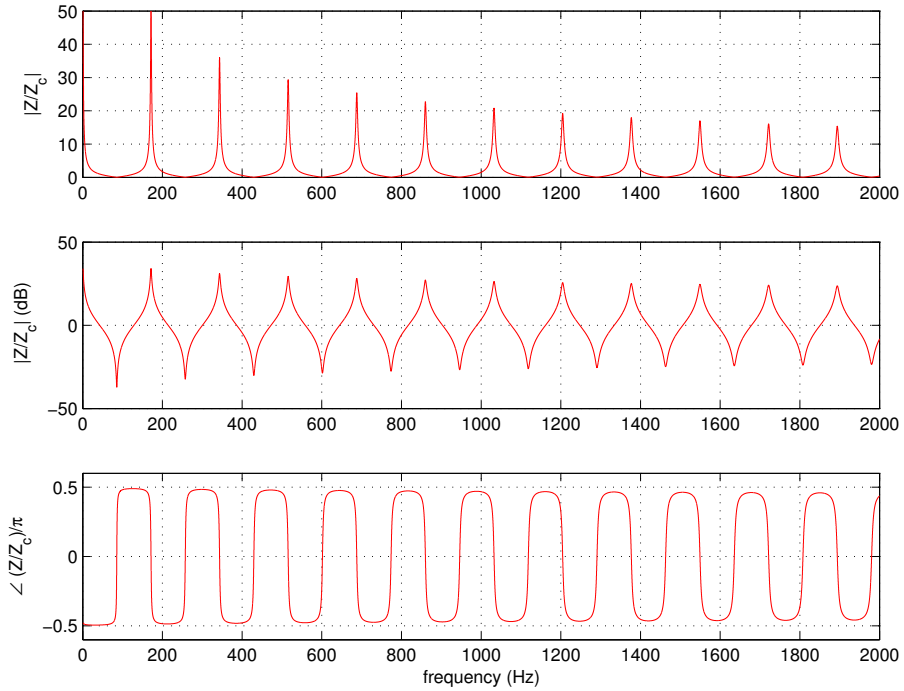

Figure 2.5: Absolute impedance magnitude, impedance in decibels and impedance phase for a lossy closed pipe of radius 2 cm and length 1 m.

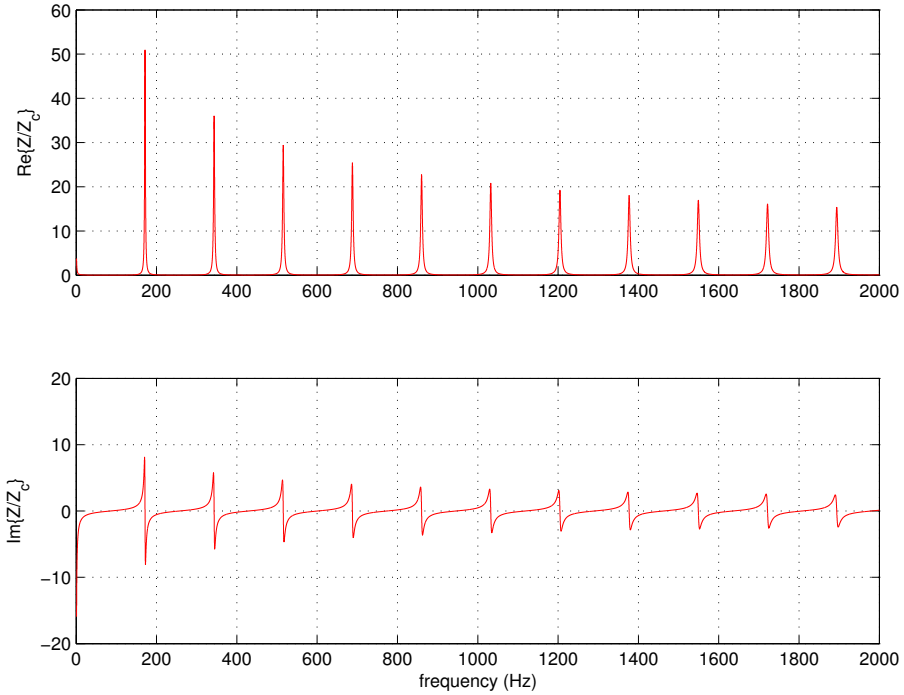

Figure 2.6: Real and imaginary parts of the impedance for a lossy closed pipe of radius 2 cm and length 1 m. For the lossless case the real part is identically zero.

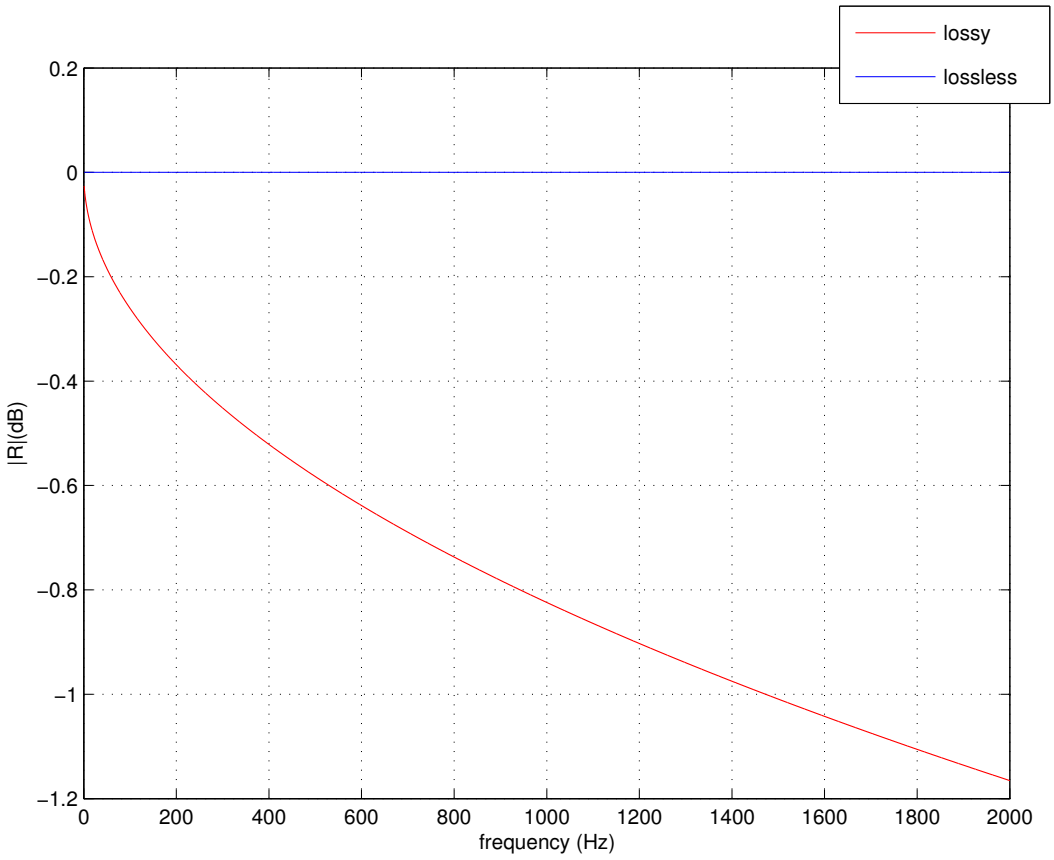

Figure 2.7: Reflection coefficient (in decibels) for a lossy closed pipe of radius 2 cm and length 1 m. For a lossless pipe all the wave energy is reflected and the reflection coefficient is 1 (zero on the dB scale).

2.9.4 Losses in Pipes of Different Width

The losses experienced by a wave in a pipe are related to the diameter of the pipe. The smaller the diameter, the more significant the effects of the wall become, so to minimise losses as large as possible radius of tube should be used. However, the *cut-on frequency* above which higher modes will propagate (see later) is inversely proportional to the radius.

The effect of varying the pipe radius can clearly be seen in the theoretical plots of Figure 2.8.

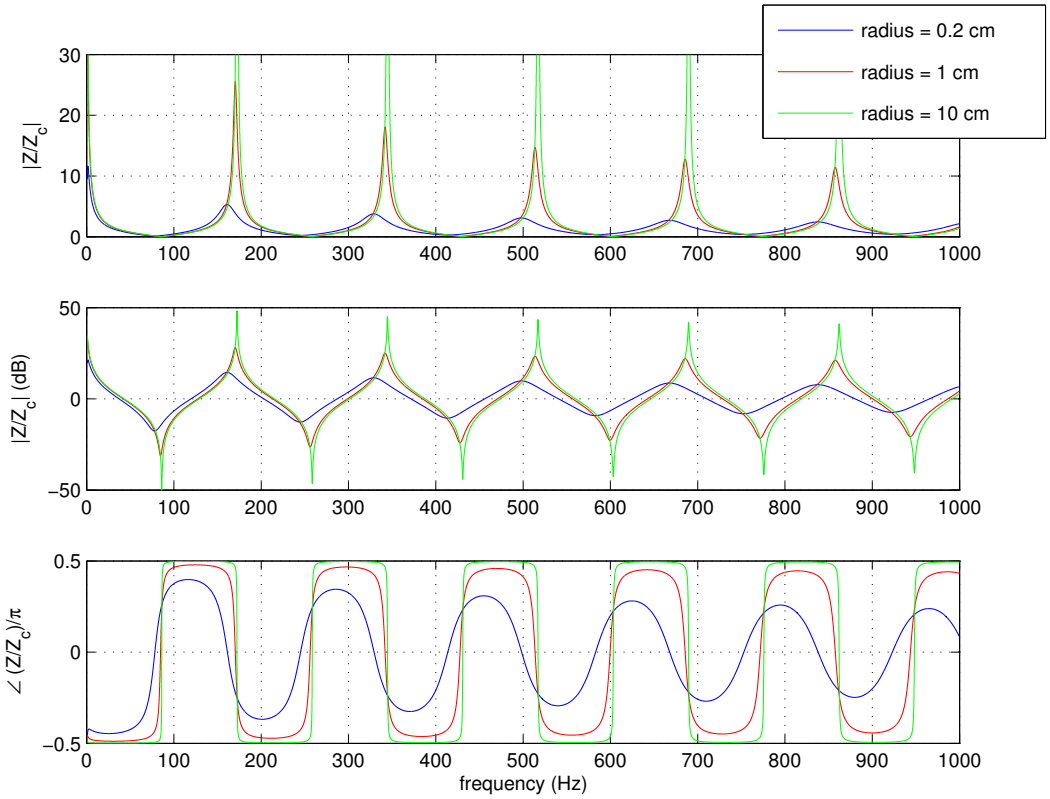

Figure 2.8: Absolute impedance, impedance in decibels and impedance phase for a lossy closed pipe of various diameters.

2.9.5 Open Flanged Pipe

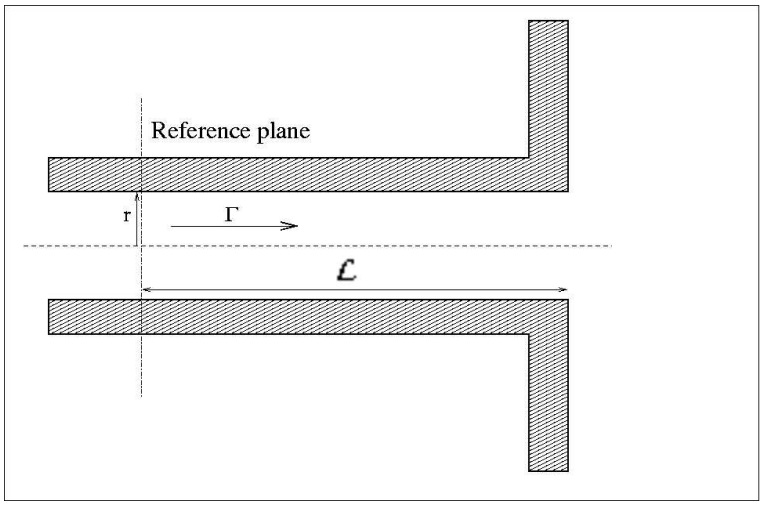

Figure 2.9: A lossy open flanged pipe.

In the low frequency limit ($kr \ll 1$) the radiation impedance for a pipe with a flanged end is given by[85]

$$Z_{\text{flanged}} \approx Z_c \left[\frac{1}{2}(kr)^2 + i \left(\frac{8}{3\pi} \right) kr \right]. \tag{2.86}$$

In fact, a further approximation can be made since, in the low frequency limit, the real part of equation (2.86) is much smaller than the imaginary part[86]

$$Z_{\text{flanged}} \approx iZ_c \left(\frac{8}{3\pi} \right) kr. \tag{2.87}$$

Now, the input impedance of an ideally open lossless flanged pipe is

$$Z_{\text{IN}}^{\text{open}} = iZ_c \tan(k\mathcal{L}). \tag{2.88}$$

In the low frequency limit we can apply the small angle approximation to the above equation to give

$$Z_{\text{IN}}^{\text{open}} = iZ_c k\mathcal{L}. \tag{2.89}$$

Comparing (2.89) and (2.87) we see that equation (2.87) is equivalent to the input

impedance of an open pipe of length $8r/3\pi \approx 0.85r$. For this reason we can replace the flanged pipe of length $\mathcal{L}$ by an 'ideally open' pipe of length $\mathcal{L} + 0.85r$ and ignore the radiation loss when $kr \ll 1$[86]. By ideally open we mean that the pipe opens into another pipe with an infinite radius. Thus the expression for the input impedance becomes

$$Z_{\text{IN}}^{\text{open}} = iZ_c \tan(k[\mathcal{L} + 0.85r]). \tag{2.90}$$

This is called an *end correction* and the new length is known as the *effective length*. Consider the example given in the following figure for an open flanged tube. The radius of the tube is 2 cm and the length is 1 m. We can model this as an open tube with a length of 1.0170 m and radiation impedance of zero for frequencies where the condition $kr \ll 1$ is met - i.e. $f \ll 2.7$ kHz. The impedance for the tube is plotted up to 2 kHz for the lossless and lossy case.

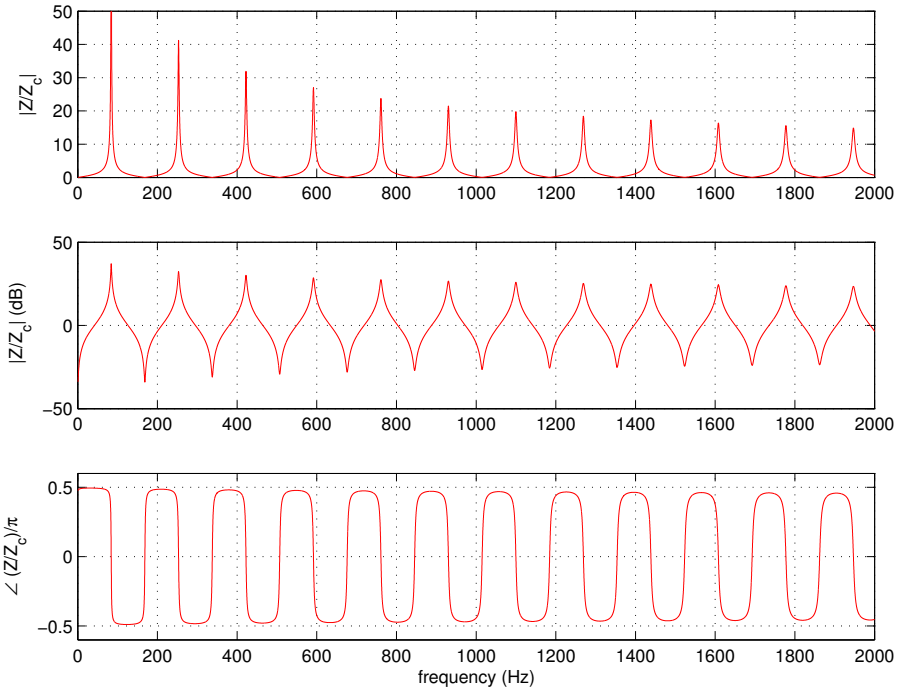

Figure 2.10: Absolute impedance, impedance in decibels, and impedance phase for a pipe of physical length 1 m (effective length 1.017 m) and radius 2 cm with an idealised terminating impedance of zero.

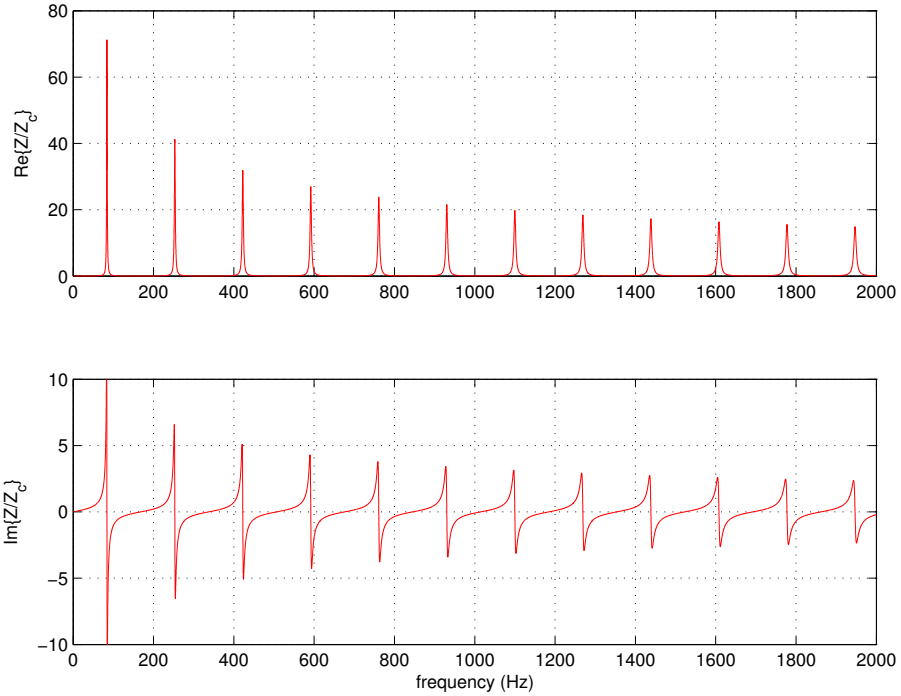

Figure 2.11: Real and imaginary parts of the impedance for a pipe of radius 2 cm and physical length 1 m (effective length 1.017 m) with an idealised terminating impedance of zero.

2.9.6 Open Unflanged Pipe

Consider an unflanged open ended pipe. In the low frequency limit the radiation impedance of the unflanged end[23]

$$Z_{\text{unflanged}} = Z_c \left[\frac{1}{4}(kr)^2 + i(0.6kr) \right]. \tag{2.91}$$

Using the same approximations given for the open flanged case, we can replace the unflanged pipe of length $\mathcal{L}$ by an ideally open pipe of length $\mathcal{L} + 0.6r$ and ignore the radiation loss when $kr \ll 1$. Thus the expression for the input impedance becomes

$$Z_{\text{IN}}^{\text{open}} = iZ_c \tan(k[\mathcal{L} + 0.6r]). \tag{2.92}$$

Figure 2.12 and 2.13 show the impedance in equation (2.92) plotted for a pipe of radius 2 cm and length 1 m. The wavenumber has been replaced by the propagation constant to account for losses in the pipe.

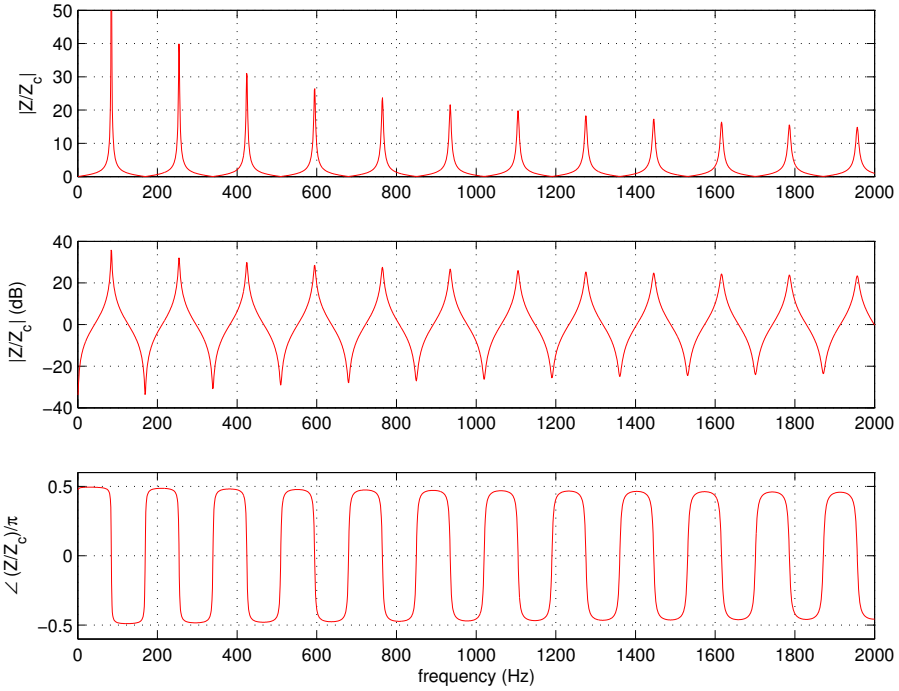

Figure 2.12: Absolute impedance, impedance in decibels and impedance phase for an unflanged open pipe of radius 2 cm and length 1 m.

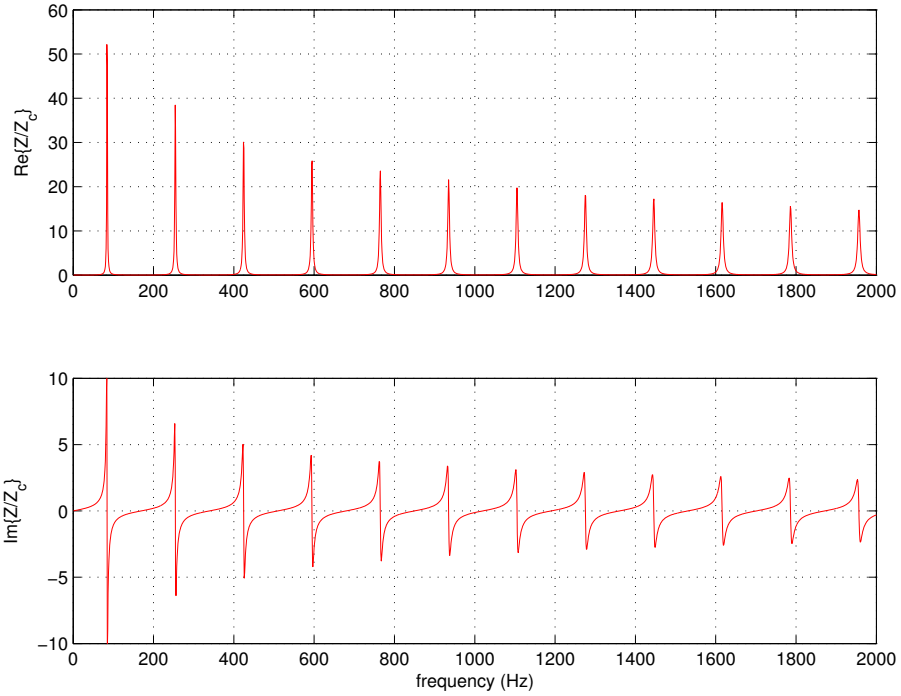

Figure 2.13: Real and imaginary parts of the impedance for an unflanged open pipe of radius 2 cm and length 1 m.

2.10 Multi-Cylinder Pipes

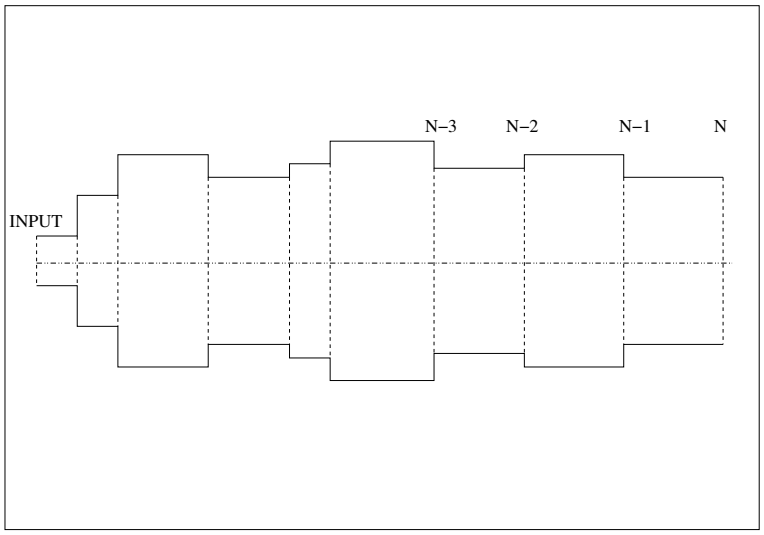

Figure 2.14: A concatenation of cylindrical tubes with various length and radii. The object has an open unflanged end at the Nth plane.

Consider the case where we have a series of thin-walled cylindrical sections of various lengths and radii connected together as shown in Figure 2.14. If we know the load impedance, $Z_{\mathcal{L}}$, at plane N (let us call it Z_{N}) we can deduce the impedance at plane (N-1) using the input impedance equation

$$Z_{\mathrm{N}-1} = Z_{c1}\left[\frac{Z_{\mathrm{N}}\cos(kl_1) + iZ_{c1}\sin(kl_1)}{iZ_{\mathrm{N}}\sin(kl_1) + Z_{c1}\cos(kl_1)}\right] \tag{2.93}$$

where Z_{c1} and l_1 are the characteristic impedance and length of the first cylinder to the left of the Nth plane respectively. The impedance at plane N, denoted Z_{N}, is just the radiation impedance of an unflanged end given previously by equation (2.91)

$$Z_{\mathrm{N}} = Z_{\mathrm{unflanged}} = Z_c\left[\frac{1}{4}(ka)^2 + i(0.6ka)\right]. \tag{2.94}$$

Now that we have an expression for the impedance at plane (N-1) this can be inserted back into the input impedance equation as the load impedance at plane (N-1) to find the impedance at plane (N-2)

$$Z_{\mathrm{N}-2} = Z_{c2}\left[\frac{Z_{\mathrm{N}-1}\cos(kl_2) + iZ_{c2}\sin(kl_2)}{iZ_{\mathrm{N}-1}\sin(kl_2) + Z_{c2}\cos(kl_2)}\right] \tag{2.95}$$

where Z_{c2} and l_2 are the characteristic impedance and length of the second cylinder to the left of the Nth plane respectively. At plane (N-3)

$$Z_{\mathrm{N}-3} = Z_{c3}\left[\frac{Z_{\mathrm{N}-2}\cos(kl_3) + iZ_{c3}\sin(kl_3)}{iZ_{\mathrm{N}-2}\sin(kl_3) + Z_{c3}\cos(kl_3)}\right] \tag{2.96}$$

and so on. If we keep repeating this method we can work our way back to find the impedance at the input. This procedure can be generalised for any number of sections and value of radiation impedance. Hence a good approximation for the profile of a horn can be built up from small pieces of cylinders and the impedance can be determined. The agreement between the experimental and the theoretical approximation improves as a larger number of cylinders are used in the model[93, 94, 95].

Note that the sections do not have to be cylindrical. Conical and Bessel shaped sections are commonly used. This method allows the theoretical impedance for a wind instrument to be accurately calculated.

An example of the impedance of a multi-cylinder pipe is given in Figure 2.15. In this case, we have a concatenation of three cylinders. Starting at the input end the radii of the cylinders are 2 cm, 4 cm, and 8 cm and have length 0.3, 0.6, and 0.9 m respectively. The cylinder at the far end is assumed to be terminated by an unflanged end.

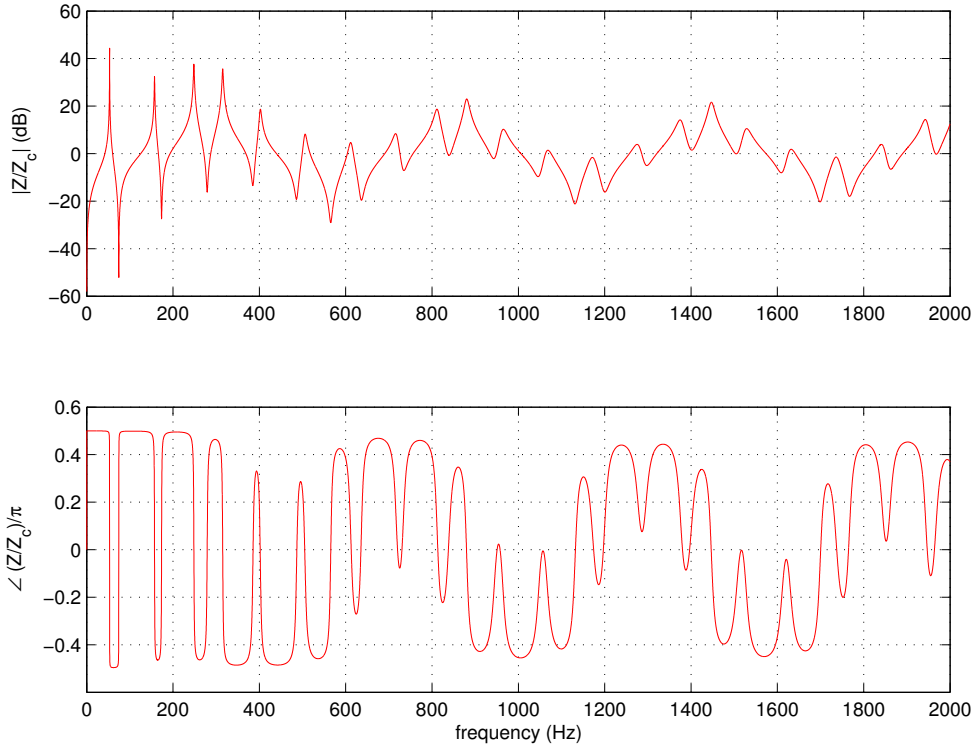

Figure 2.15: Open unflanged pipe comprising three cylindrical sections.

2.11 Cones and Horns

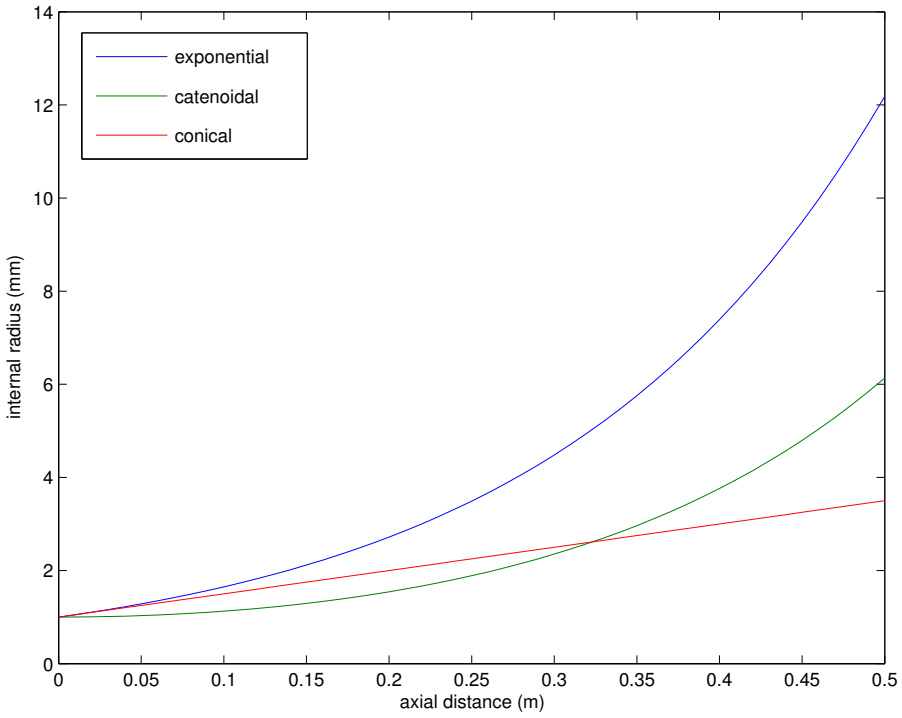

Figure 2.16: Example profiles for the conical, exponential, and catenoidal horn. All profiles have a throat radius of 1 mm and flare constant, $m = 5$.

A common method for modelling a wind instrument is to divide it into a number of small sections. Each section is then approximated to either a cylinder or a horn. Some examples of horn profiles are given in Figure 2.16 for illustration.

For the specific case of wave propagation in a horn the wave equation can be rewritten in the form of *Webster's equation*. In the one dimensional case this is[76]

$$\frac{1}{S}\frac{\partial}{\partial x}\left(S\frac{\partial p}{\partial x}\right) = \frac{1}{c^2}\frac{\partial^2 p}{\partial t^2} \tag{2.97}$$

where S is the area of the propagating wave front. There is class of horn profiles called the *Salmon horns*[86] for which Webster's equation holds. For the Salmon horns

$$a = a_0[\cosh(mx) + \mathcal{T}\sinh(mx)] \tag{2.98}$$

where a is the radius of the horn as a function of position x, m is the *flare constant*,

and a_0 and $\mathcal{T}$ are constants. The Salmon horns can be subdivided into the following categories. If we set $\mathcal{T} = 1$ and rewrite the hyperbolic sine and cosine function in terms of complex exponentials we obtain the profile of an *exponential horn*

$$a = a_0 \exp(mx) \tag{2.99}$$

and if we set $\mathcal{T} = 1/mx_0$ where x_0 is a constant and $m \to 0$ we can rewrite equation (2.98) as

$$a = \frac{a_0}{2}\left[\exp(mx) + \exp(-mx) + \frac{\exp(mx)}{mx_0} - \frac{\exp(-mx)}{mx_0}\right]. \tag{2.100}$$

The first two terms tend to 1 and using the MacLaurin series to expand the exponentials simplifies the equation to

$$a = a_0\left(1 + \frac{x}{x_0}\right) \tag{2.101}$$

thus we simply have the profile of a *conical horn*. Since the theoretical model assumes losses at the wall are dependent on the radius of the object(2.78), the losses will vary axially along the horn. This is not easily accounted for[86]. In the following examples we will consider only lossless propagation.

2.11.1 Conical Horn

The input impedance of a conical horn terminated by a general load impedance $Z_{\mathcal{L}}$ is given by[86]

$$Z_{\text{IN}}^{\text{conical}} = Z_{c1}\left[\frac{iZ_{\mathcal{L}}\left[\sin(k\mathcal{L} - \widehat{kx_2})/\sin(\widehat{kx_2})\right] + Z_{c2}\sin(k\mathcal{L})}{Z_{\mathcal{L}}\left[\sin(k\mathcal{L} + \widehat{kx_1} - \widehat{kx_2})\right] - iZ_{c2}\left[\sin(k\mathcal{L} + \widehat{kx_1})/\sin(\widehat{kx_1})\right]}\right] \tag{2.102}$$

where $\widehat{kx_1} \equiv \tan^{-1}(kx_1)$, $\widehat{kx_2} \equiv \tan^{-1}(kx_2)$, $Z_{c1} = \rho c/(\pi r_1^2)$ and $Z_{c2} = \rho c/(\pi r_2^2)$, the input radius (throat) r_1 is at position x_1, and the far end (mouth) radius r_2 is positioned at x_2. The length $\mathcal{L} = x_2 - x_1$ where x_1 and x_2 are measured from the conical apex. For the special case of the *ideally open-ended conical horn* we have

$$Z_{\text{IN}}^{\text{open conical}} = iZ_{c1}\frac{\sin(k\mathcal{L})\sin[\widehat{kx_1}]}{\sin(k\mathcal{L}+\widehat{kx_1})}. \tag{2.103}$$

Figure 2.17 shows equation (2.103) plotted for the values $\mathcal{L} = 5.2$ cm, $r_1 = 1$ cm, and $r_2 = 10$ cm.

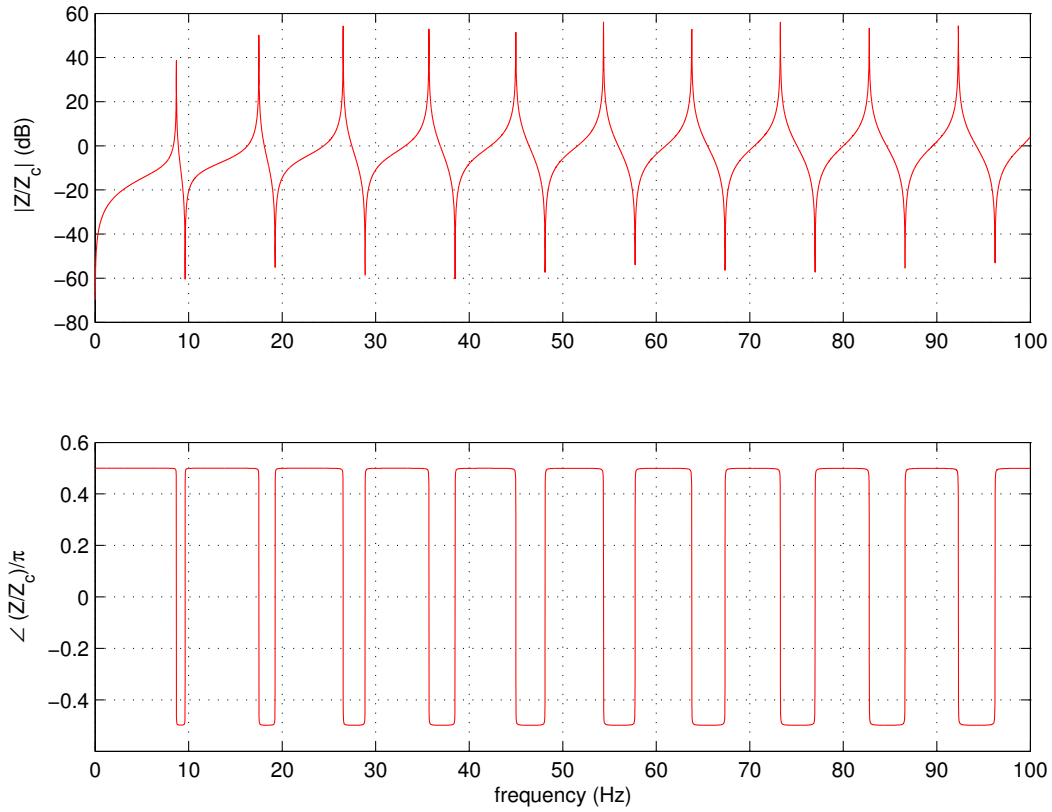

Figure 2.17: Impedance of an ideally open conical horn.

2.11.2 Exponential Horn

For an exponential horn the input impedance is given by

$$Z_{\mathrm{IN}}^{\mathrm{exp}} = Z_{c1}\left[\frac{Z_{\mathcal{L}}\cos(\bar{k}\mathcal{L}+\tan^{-1}(m/\bar{k}))+iZ_{c2}\sin(\bar{k}\mathcal{L})}{iZ_{\mathcal{L}}\sin(\bar{k}\mathcal{L})+Z_{c2}\cos(\bar{k}\mathcal{L}-\tan^{-1}(m/\bar{k}))}\right] \tag{2.104}$$

where $\bar{k} \equiv +\sqrt{k^2-m^2}$. m is the flare constant, $Z_{c1} = \rho c/(\pi r_1^2)$, $Z_{c2} = \rho c/(\pi r_2^2)$ and, as in the previous section, the input radius r_1 is at position x_1, and the far end radius r_2 is positioned at x_2. The length $\mathcal{L} = x_2 - x_1$ where x_1 and x_2 are measured from the apex. For the ideally open exponential horn

$$Z_{\mathrm{IN}}^{\text{open exponential}} = iZ_{c1}\left[\frac{\sin(\bar{k}\mathcal{L})}{\cos(\bar{k}\mathcal{L}-\tan^{-1}(m/\bar{k}))}\right]. \tag{2.105}$$

Figure 2.18 shows equation (2.105) plotted for the values $\mathcal{L}$ = 6.93 cm, m = 5, r_1 = 1 cm, and r_2 = 2 cm.

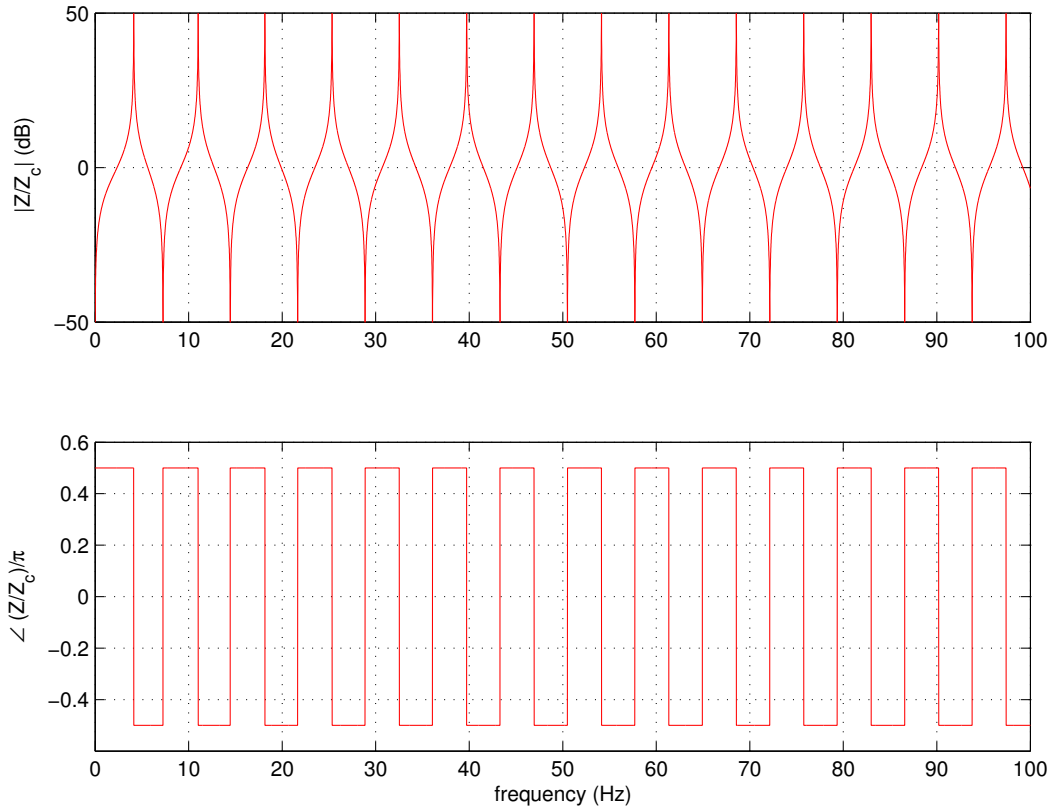

Figure 2.18: The impedance of an ideally open exponential horn.

2.11.3 Bessel Horns

The Bessel horn has the profile

$$a = a_0(-x)^{-m}. \tag{2.106}$$

An example of a Bessel profile (with a throat radius of 1 cm, mouth radius 1.5 cm, length 15 cm, and flare constant of 2.5) and its associated impedance curve is given in Figures 2.19 and 2.20.

The solution for the pressure profile is given by[76] as

$$p(x) = x^{m+1/2}[AJ_{m+1/2}(kx) + BY_{m+1/2}(kx)] \tag{2.107}$$

where A and B are constants, J and Y are Bessel functions of the first and second kind respectively. Using the Euler's linear force equation the particle velocity is

$$v(x) = i\frac{k}{\rho\omega}x^{m+1/2}[AJ_{m-1/2}(kx) + BY_{m-1/2}(kx)] \tag{2.108}$$

from which the impedance can be deduced. For an in depth treatment of Bessel horns see Braden[76]. An advantage of using the Bessel horn over cones or cylinders is that the resulting profile tends to be more smoothly varying.

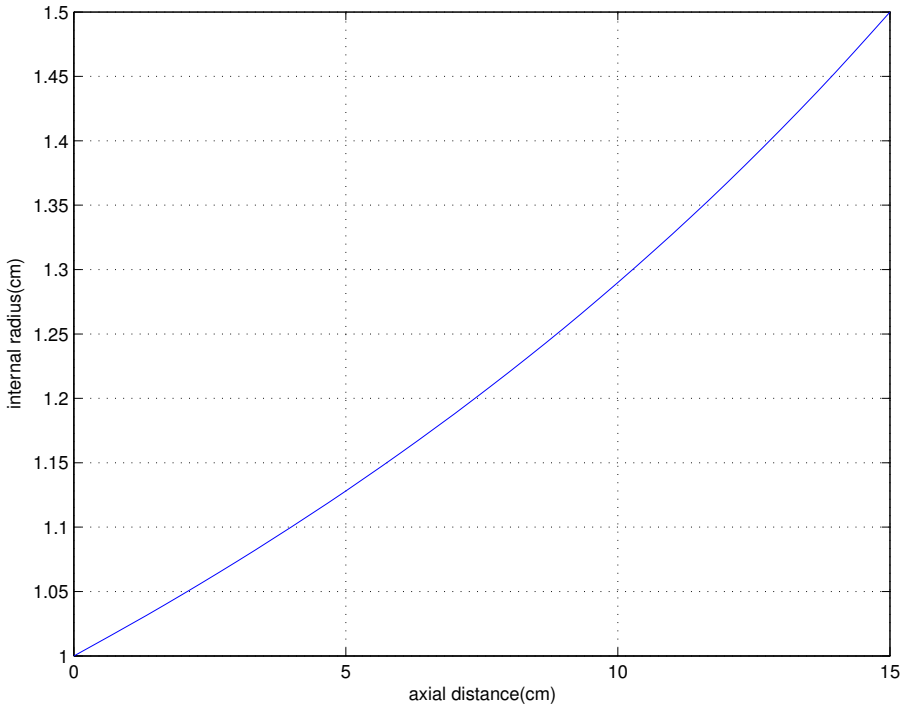

Figure 2.19: The profile for a Bessel horn with a throat radius of 1 cm, mouth radius of 1.5 cm, length of 15 cm and flare constant of 2.5.

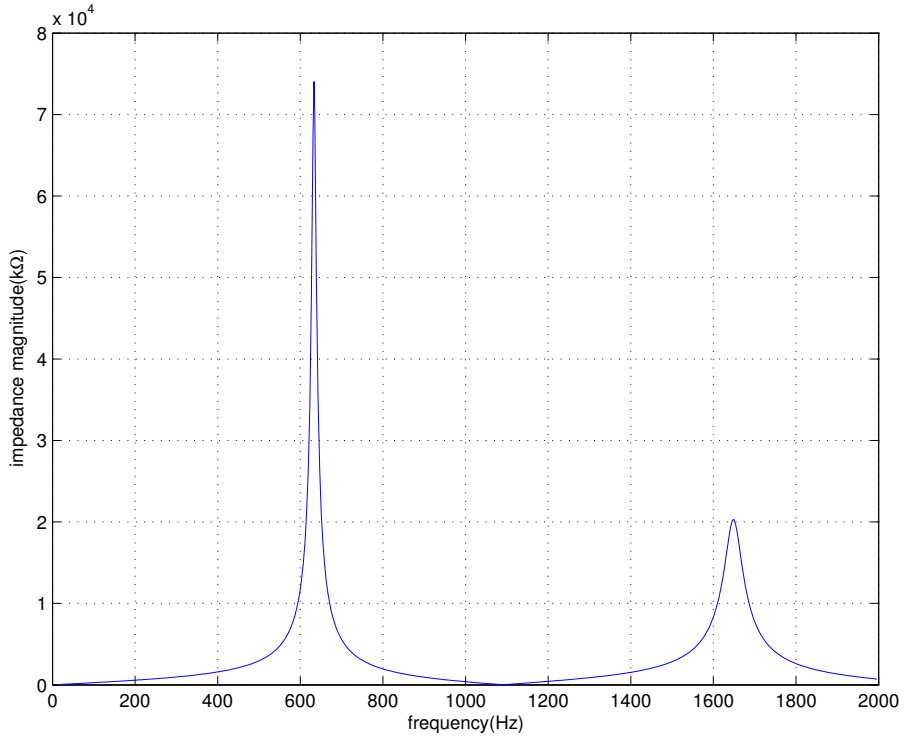

Figure 2.20: Impedance magnitude for the Bessel horn with the profile given in Figure 2.19.

2.12 Modelling

Now we have derived the impedance for a number of different profiles it is possible to decompose the bell of an instrument into a number of these sections and calculate the impedance of the full instrument. A computationally efficient algorithm designed to handle an instrument model with many elements is the Brass Instrument Evolution Software (BIES) developed by Braden which we will use here.

2.12.1 Deriving the Impedance of a Real Horn from the Bore Profile

Figure 2.21: A horn of known geometry.

Figure 2.21 shows a photograph of a horn. The internal radius can be measured at various points along its axial length with callipers. The bell section is modelled using various different methods in Figure 2.22. The simplest being a concatenation of small cylindrical elements (blue line). A more accurate representation can be achieved by using conical elements instead (green line). However, both of these methods have used many sections which is computationally expensive. In this example an equally good result can be obtained using very few Bessel functions. The red line shows the bell modelled by a single Bessel element with a suitably chosen flare constant m = 1.2. The rest of the horn leading back up to the input was modelled simply as a cylinder of

constant radius of 4.6 mm.

The impedance corresponding to each modelling scheme is shown in Figure 2.23. We can see that modelling the horn as a single Bessel function gives an almost identical impedance curve to that obtained by using many concatenated cones, whereas the cylindrical element model gives a substantially different result. This is due to the relatively low number of cylinders used causing the profile to deviate significantly from the true profile.

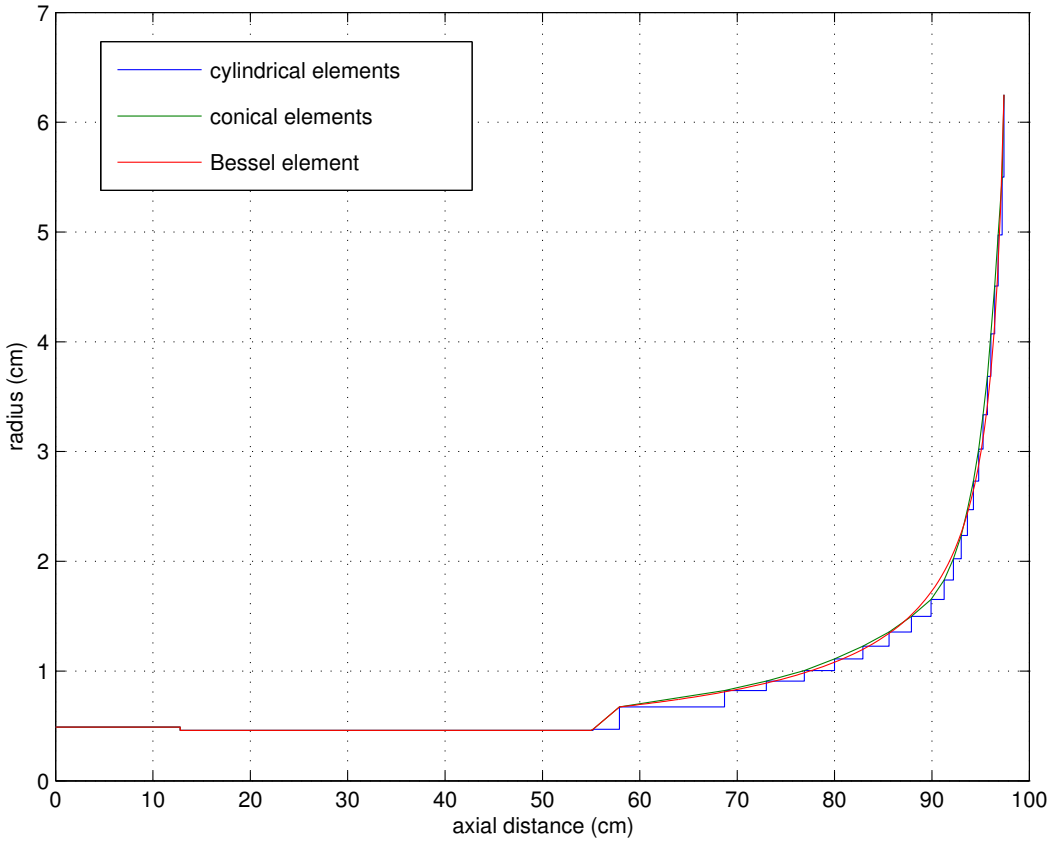

Figure 2.22: Approximate profiles for the horn plus a coupler.

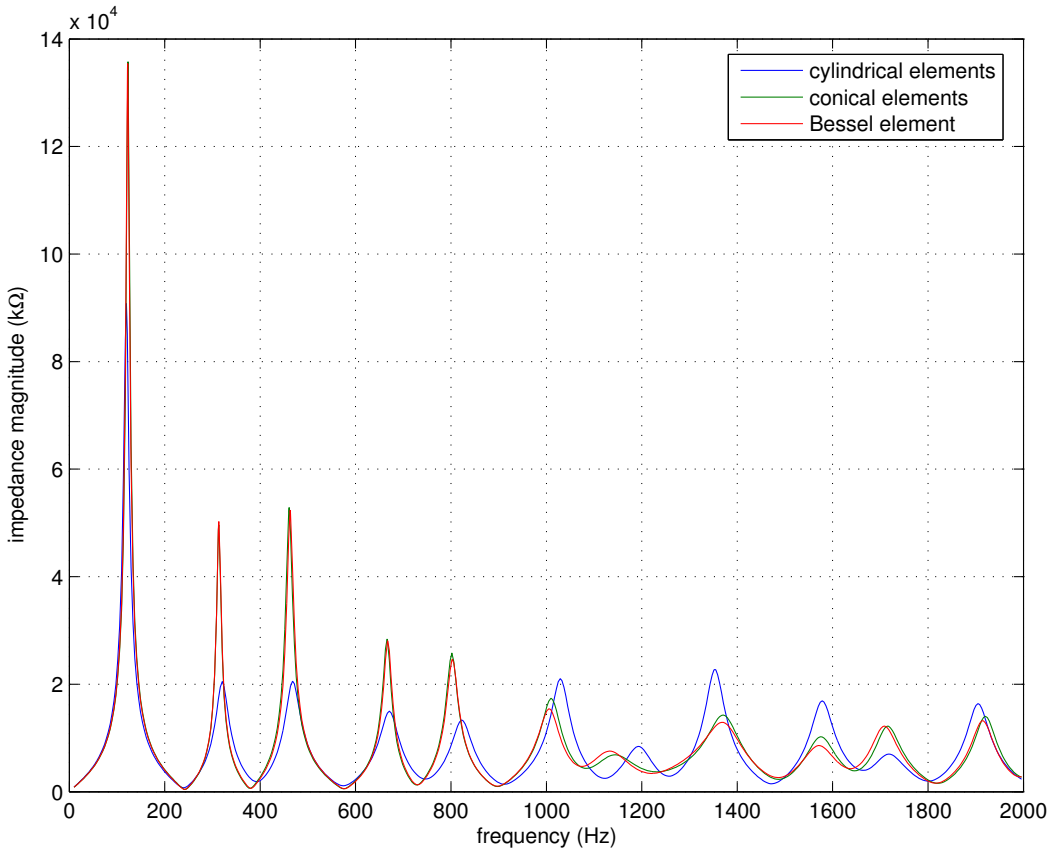

Figure 2.23: Impedance magnitude for the horn using different modelling schemes; cylindrical, conical, and Bessel segments.

2.13 Higher Modes

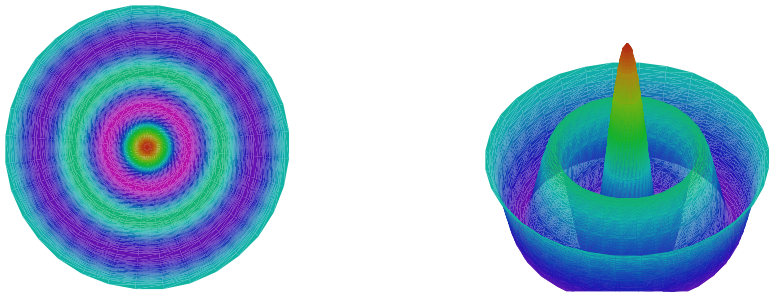

(0,4) **(0,4)**

Figure 2.24: Example of a higher mode - the radially-symmetric (0,4) mode.

So far we have discussed impedance theory based on the assumption that the propagation is of a planar nature. This is generally true for low frequencies. However, higher modes can be excited for a number of reasons[24, 96, 97, 98] - excitation of the bore at frequencies above the cut-on frequency, structural imperfections, or large variations in the bore profile. Higher modes will also arise if the bore contains any non-cylindrical sections. The cut-on frequency for a cylindrically symmetric tube is given by[86]

$$f_{\text{cut on}} = \frac{1.84c}{2\pi a}. \tag{2.109}$$

At frequencies below the cut on frequency the only mode of propagation that occurs is the planar mode. All higher modes are evanescent i.e. their wavenumbers are imaginary hence they are attenuated rapidly and their propagation can be neglected inside the duct.

As we can see from equation (2.109), $f_{\text{cut on}}$ is inversely related to the measurement duct radius so the thinner we make the measurement duct the larger the range of frequencies we can consider, without having to deal with higher modes of excitation. However, this also increases the losses experienced by the wave. For the apparatus used in this system, $a = 4.9$ mm which corresponds to a cut on frequency of about 20.5 kHz. To study close to this frequency regime requires a microphone separation of 7 mm.

Cylindrical polar coordinates (r, ϕ) are the most sensible choice of basis for higher mode analysis in cylindrical ducts. An example is given in Figure 2.24. The (0,4) mode

is radially symmetric and has four (blue) rings of nodal pressure in the figure on the left. On the right we see more clearly the variation in pressure as a function of radius. The study of higher modes is usually referred to as multimodal theory. For a more detailed analysis of this theory see Sharp[23], Kemp[24], and Braden[76].

2.13.1 Higher Mode Effects on the Impedance

As we have seen in Chapter 2, the three dimensional acoustic wave equation is

$$\nabla p = \frac{1}{c^2}\frac{\partial^2 p}{\partial t^2} \tag{2.110}$$

with the Laplacian written in Cartesian coordinates as

$$\nabla = \frac{\partial^2}{\partial x^2} + \frac{\partial^2}{\partial y^2} + \frac{\partial^2}{\partial z^2}. \tag{2.111}$$

Since the x component points in the axial direction and the higher mode components lie in the y-z plane it is convenient to rewrite the above equation as

$$\nabla = \frac{\partial^2}{\partial x^2} + \nabla_\perp \tag{2.112}$$

where

$$\nabla_\perp = \frac{\partial^2}{\partial y^2} + \frac{\partial^2}{\partial z^2}. \tag{2.113}$$

We can then separate the variables into an x part, a y-z part and a temporal part. The pressure and particle velocity are then given by[24]

$$p(x, y, z, t) = \sum_{n=0}^{\infty} P_n(x)\psi_n(y, z)\exp(i\omega t) \tag{2.114}$$

$$u_z(x, y, z, t) = \sum_{n=0}^{\infty} U_n(x)\psi_n(y, z)\exp(i\omega t) \tag{2.115}$$

where $\psi_n(y, z)$ is the pressure profile in the y-z plane for the nth mode, $P_n(x)$ is the pressure profile of the nth mode along the x direction and $U_n(x)$ is the axial volume velocity of the nth mode. Substituting (2.114) into the wave equation gives

$$\frac{1}{\psi_n(y,z)}\nabla_\perp\psi_n(y,z)+\frac{1}{P_n(x)}\frac{\partial^2 P_n(x)}{\partial x^2}=\frac{1}{\exp(i\omega t)}\frac{1}{c^2}\frac{\partial^2}{\partial t^2}\exp(i\omega t)=\text{constant}. \quad (2.116)$$

The temporal part is solved by the dispersion relation $\omega = ck$ with k referred to as the *free space wavenumber*. For the x component

$$P_n(x)=A_n\exp(-ik_nx)+B_n\exp(ik_nx). \quad (2.117)$$

It follows from the Euler force equation that the volume velocity is

$$U_n(x)=\frac{k_nS}{k\rho c}[A_n\exp(-ik_nx)-B_n\exp(ik_nx)] \quad (2.118)$$

and the characteristic impedance is given by

$$Z_c=\frac{k\rho c}{k_nS}. \quad (2.119)$$

The equation for the y-z plane is

$$\nabla_\perp\psi_n(y,z)=-\alpha_n^2\psi_n(y,z) \quad (2.120)$$

where α_n is the wavenumber for the nth mode in the y-z plane. The wavenumbers obey the relation

$$k_n^2=k^2-\alpha_n^2. \quad (2.121)$$

In Chapter 2 we considered the impedance of various objects using plane wave theory (i.e. higher modes were ignored). BIES has the ability to incorporate these modes into the analysis.

Figure 2.25 shows the profile of a short tube of radius 1 cm and length 10 cm, stepping up to 1.5 cm, then followed by a cone of length 15 cm with a final radius of 2.5 cm. We briefly mentioned the BIES software in Chapter 1. A more detailed analysis can be found in Braden's thesis[76], conference papers[77, 78, 79], and tutorial guide[80]. Using BIES, the impedance curve for the simulated duct of Figure 2.25 has

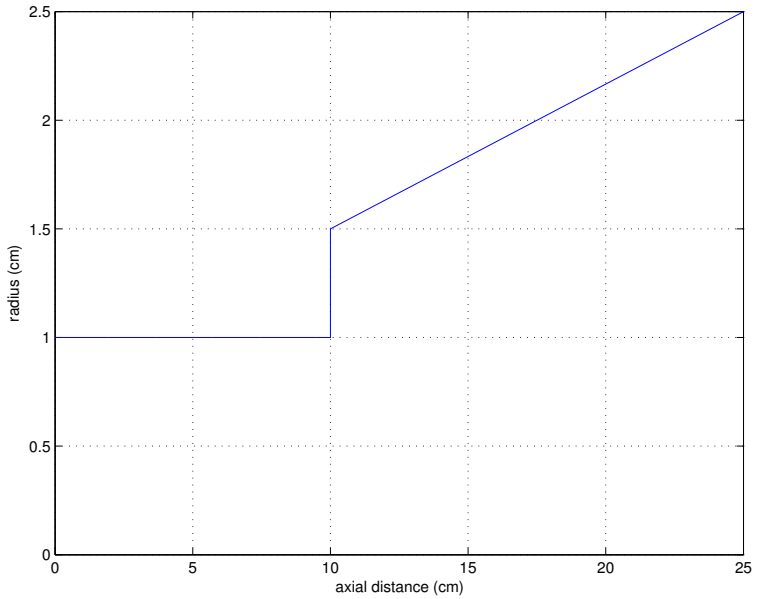

Figure 2.25: Bore profile of simulated test object.

been calculated assuming that only the planar mode is present (red line); the planar mode plus the first (0,1) mode is present (blue line); and the planar, (0,1), and (0,2) mode are present (green line).

We can see, as expected, that all three curves are very similar due to the effects of higher modes generally being small and of a perturbative nature. We also notice that including the first higher modes has the effect of reducing the magnitude of the impedance peaks: this implies that energy is moved from the lower frequencies into the higher ranges. We also note that the inclusion of the second mode makes very little difference to curve- since the blue and green line are almost identical.

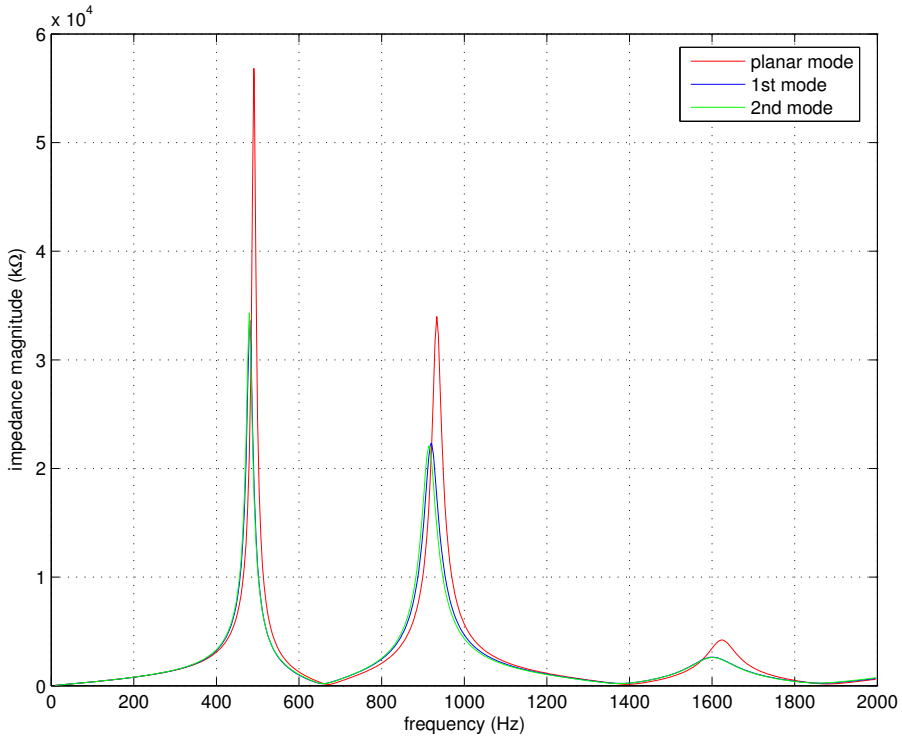

Figure 2.26: Calculated impedance for the profile given in Figure 2.25.

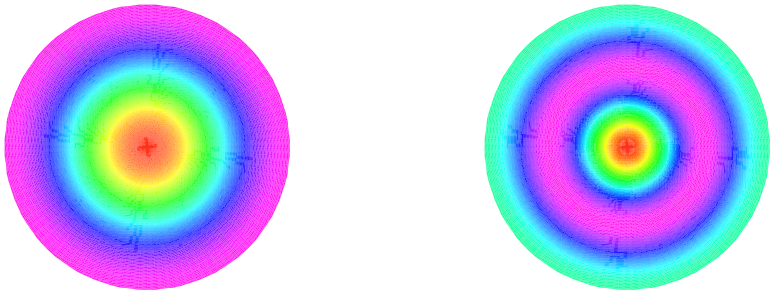

(0,1) **(0,2)**

Figure 2.27: Diagrammatic representation of the higher modes included in calculating the impedance of the object described in Figure 2.25.

2.14 Input Impulse Response and Bore Reconstruction

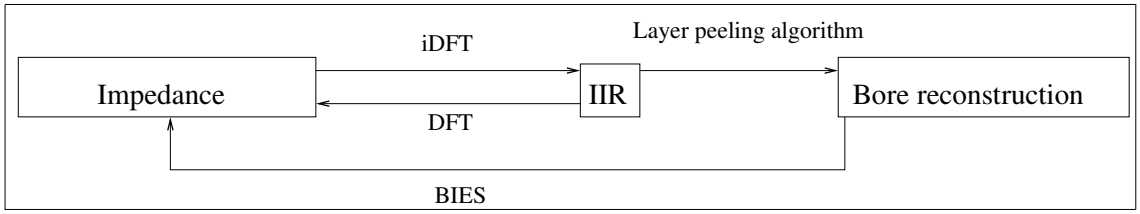

Figure 2.28: Flow chart showing the relationships between the impedance, the input impulse response and the bore reconstruction.

Let us now think about the propagation of sound in the time-domain rather than the frequency-domain. A change in the cross sectional area through which a wave propagates corresponds to a change in impedance causing the wave to be partially reflected[23]. If a microphone is placed in the vicinity of the input plane these reflections can be plotted as a function of time. If the mechanism used to excite the object is a short sharp impulse (ideally a Dirac delta function) the collection of reflections is said to be the input impulse response (IIR). It is effectively the time domain equivalent of the input impedance. More specifically, it is equal to the *real part of the inverse Fourier transform of the reflection function*[17]

$$\mathrm{IIR}(t) = \mathrm{Re}\left[\mathrm{iDFT}\{R(\omega)\}\right]. \tag{2.122}$$

For this operation to work note that we must apply conjugate symmetry to the raw reflection coefficient data (for details of the algorithms see Appendix E). Once acquired, a bore reconstruction algorithm can be applied to the impulse response data[23, 24, 99] and an approximation to the profile of the measured instrument can be obtained.

To calculate the bore reconstruction the input impulse response can be used to determine the reflection coefficients at each boundary along the bore. The reflection coefficient at a boundary between two infinitely long cylinders of cross-sectional area S_1 and S_2 is

$$R(\omega)_{1,2} = \frac{S_1/S_2 - 1}{S_1/S_2 + 1}. \tag{2.123}$$

We can rearrange this equation and define the cross-sectional area for a general boundary $i+1$ as

$$S_{i+1} = S_i \frac{1 - R(\omega)_{i,i+1}}{1 + R(\omega)_{i,i+1}}. \tag{2.124}$$

If the cross-sectional area is known at the input plane, this equation can be applied recursively to obtain the area at each boundary along the bore.

The first attempts at acoustic bore reconstruction utilised the Ware-Aki method[23, 24] which does not account for losses. The layer-peeling method developed by Amir et al[100] does account for losses, gives identical results to the Ware-Aki method when losses are ignored, and was used by Sharp[23] and Kemp[24]. Losses are included in the model by applying a digital filter - which is dependent on the length and the radius of the segment - to the forward propagating waves, and applying the inverse filter to the backward propagating waves.[23]. Various filter models are described by Sharp[23].

Consider the example of the closed tube for which the plane wave impedance was given previously (2.80). Figure 2.29 shows the theoretical impedance of a lossy closed tube of length 12.8 cm and radius 4.9 mm between 50 Hz and 20 kHz. Taking an inverse Fourier transform of the impedance produces the time-domain impulse response. For an object of constant radius and closed at the end we expect the impulse to traverse along the length of the tube and get fully reflected at the closed end i.e. we expect a large single peak in the IIR at a time $t = 2\mathcal{L}/c = 0.8$ ms. A peak is observed in Figure 2.30, but it is not perfectly sharp. An infinitely sharp peak would require an infinite bandwidth of data. A finite bandwidth results in the peak being 'spread out' slightly. Figure 2.31 shows the resultant bore profile when the IIR is used as input for the reconstruction algorithm. The reconstruction maintains a constant radius up to the closed end of the tube where it is accurately predicted to drop to zero at around 128 mm. The reconstruction oscillates about the true profile between 0 and 120 mm. There is a small over-prediction in the reconstructed profile just before the end of the tube. This is known as the Gibbs' phenomenon and is an inherent and unavoidable artifact due to the Fourier nature of the reconstruction algorithm (see Appendix C).

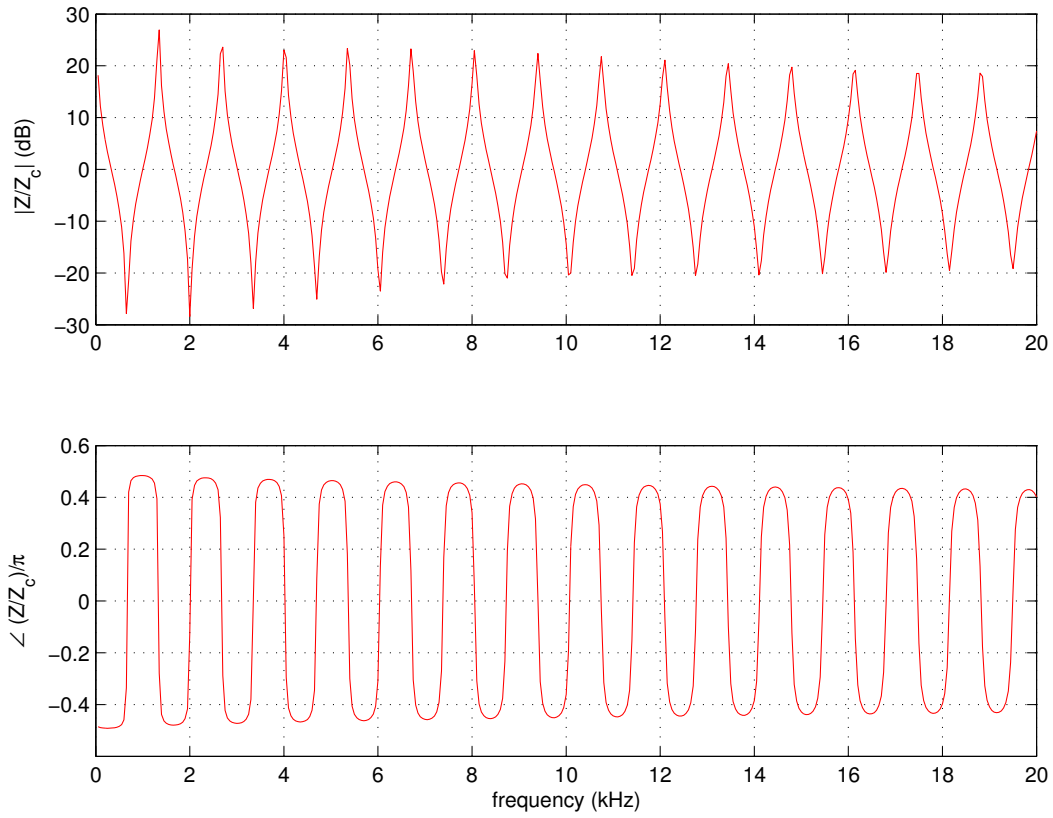

Figure 2.29: The theoretical impedance of a lossy closed tube of length 12.8 cm and radius 4.9 mm over the frequency range 50 Hz to 20 kHz.

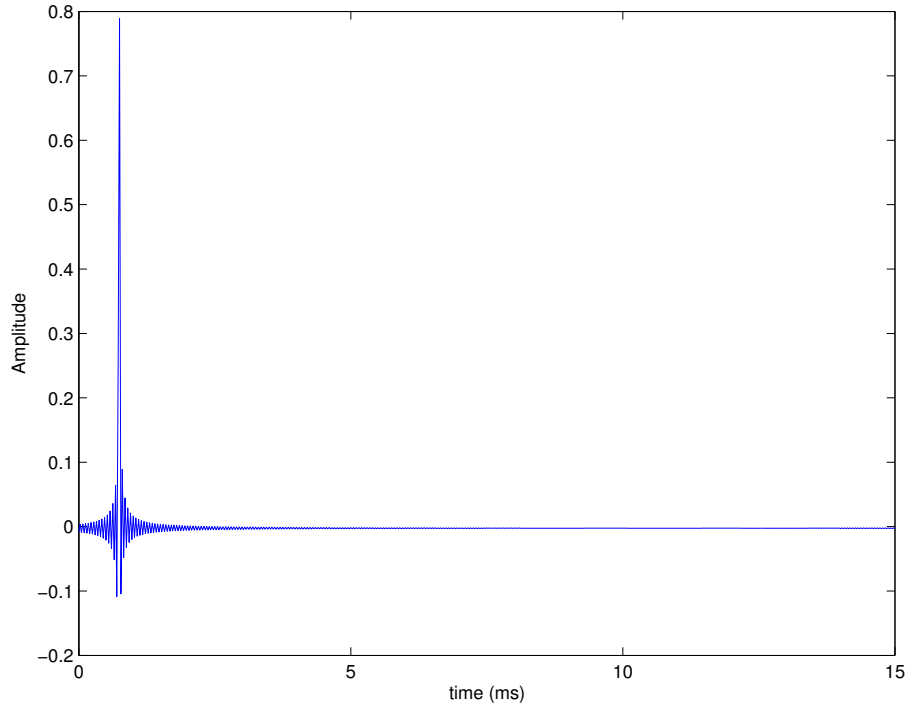

Figure 2.30: Theoretical impulse response for the closed tube.

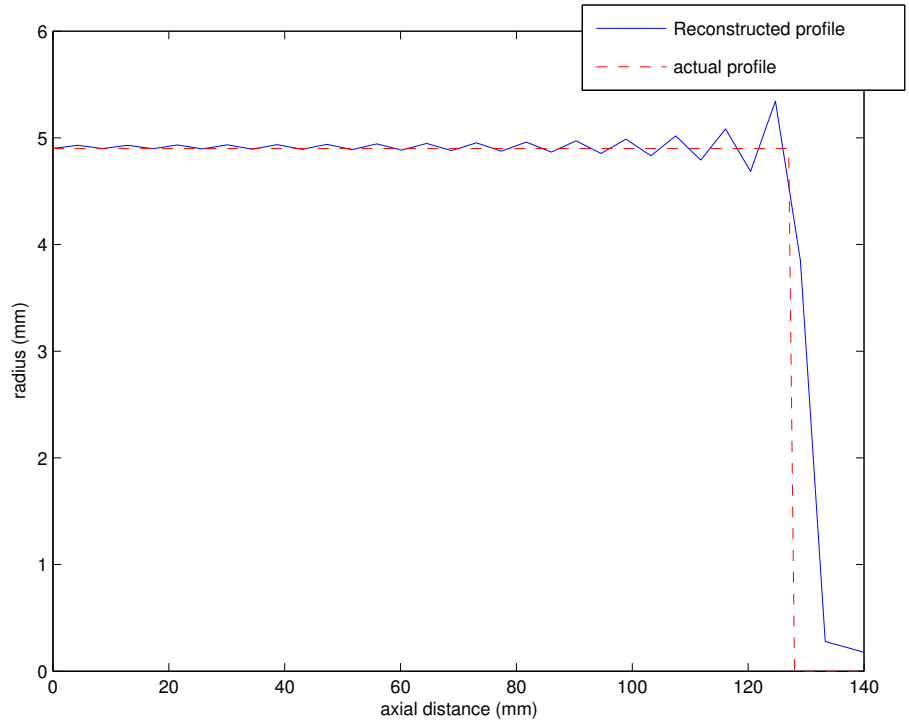

Figure 2.31: Bore reconstruction for the closed tube.

It is important to understand how our choice with regards to sampling the impedance will affect the IIR and the reconstruction. Suppose we have an impedance data set with a minimum frequency $f_{\min}$, where $f_{\min} \neq 0$, a maximum frequency $f_{\max}$, and a frequency resolution of Δf. The number of data points in this set must be

$$N = \frac{f_{\max} - f_{\min}}{\Delta f} + 1 \tag{2.125}$$

provided that $(f_{\max} - f_{\min})/\Delta f$ is an integer. For an even spacing of data points

$$f_{\min} = \Delta f \tag{2.126}$$

must be obeyed. There are $2N$ points in the resulting impulse response when the impedance is transformed. The length of the IIR signal is given by

$$T_{\text{IIR}} = \frac{1}{\Delta f} \tag{2.127}$$

and the temporal resolution of the IIR must then be

$$\Delta t = \frac{T_{\text{IIR}}}{2N}. \tag{2.128}$$

In general, the spatial resolution of the bore reconstruction is

$$\Delta \text{x} = \frac{c\Delta t}{2}. \tag{2.129}$$

For the impedance of the closed tube given in Figure 2.29: $f_{\min} = 50$ Hz, $f_{\max} = 20$ kHz, and $\Delta f = 50$ Hz. This gives an IIR signal length of 20 ms, a temporal resolution of 0.025 ms, and an axial bore resolution of 4.3 mm.

On inspection of equation (2.125) we see that increasing the maximum measured frequency $f_{\max}$ (keeping all other variables constant) will result, of course, in the number of data points increasing. The length of the IIR signal will be *unchanged* since it only depends on the frequency spacing Δf. The temporal resolution Δt of the IIR will improve i.e. Δt *decreases*, and so will the axial resolution, Δx, of the bore reconstruction.

If we increase the frequency resolution i.e. Δf decreases, the number of data points

will again increase. The length of the IIR increases since it is defined as the reciprocal of the lowest frequency measured - which in turn must equal the frequency spacing (2.126). The longer the instrument to be measured, the longer it will take for all the primary reflections to travel back from the end of the instrument to the input plane, thus the longer the impulse response must be to accommodate all these reflections. Thus the frequency resolution determines the maximum length of instrument that can be measured. Note that the temporal resolution of the IIR remains unchanged when altering the frequency resolution - the number of points increases but the length of the signal also increases so the two effects cancel out.

2.15 Outline of Other Systems

2.15.1 Acoustic Pulse Reflectometry

A brief description of Acoustic Pulse Reflectometry and its applications has been given in Chapter 1. A thorough explanation of the APR apparatus can be found in Sharp or Kemp's thesis[23, 24]. This method involves using a short acoustic pulse wave (a 'click') composed of a range of frequencies as the excitation signal. It is a time-domain technique which directly measures the input impulse response. Since the pulse must have a finite duration it must also have a finite width. The input impulse response however is defined as the time-domain response to an ideal pulse of infinitesimal width - a Dirac delta function. To obtain the input impulse response the reflections from the object under study must be deconvolved with the non-ideal excitation pulse. Via the layer-peeling algorithm outlined in Chapter 2 a bore profile can be obtained. However, the system has its limitations. The excitation pulse is composed of a relatively small bandwidth of frequencies (from close to zero up to 15 kHz)[24]. Attenuation losses experienced by the propagating pulse are great when measuring long instruments and so a low signal is returned to the microphone. These main factors reduce the quality of reconstruction and set an upper bound on the length of instrument that can be measured.

Recent improvements to APR have been made by Kemp which involve using a two microphone technique to improve the data obtained at low frequencies - this is outlined in the literature[41].

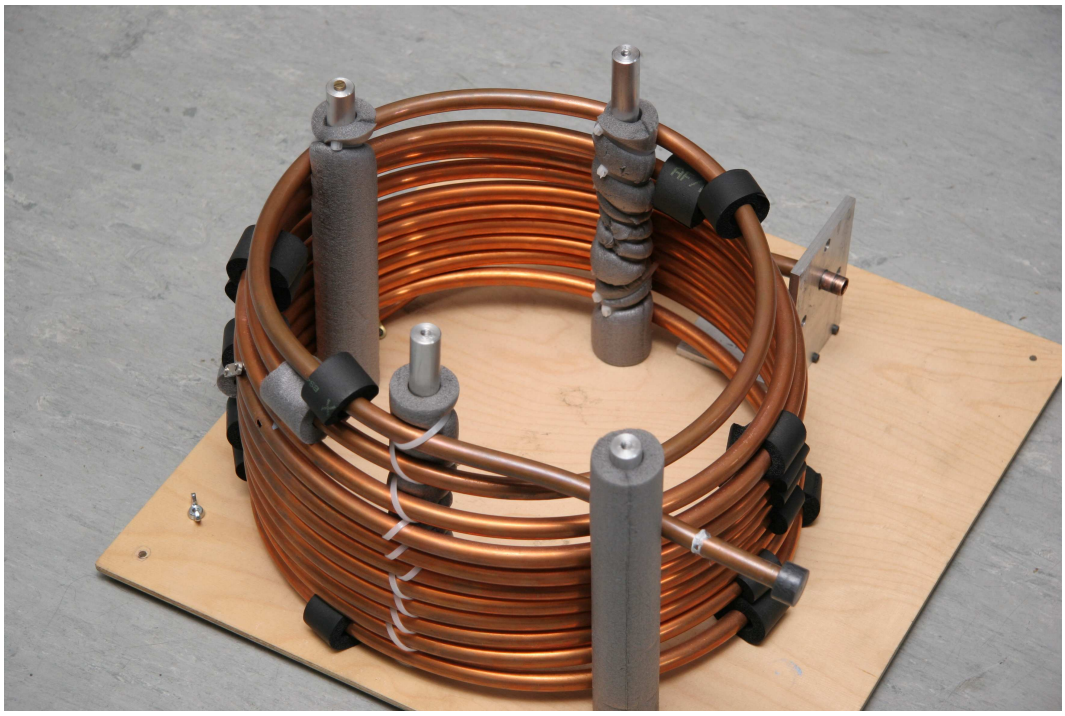

Figure 2.32: An example of the acoustic pulse reflectometer.

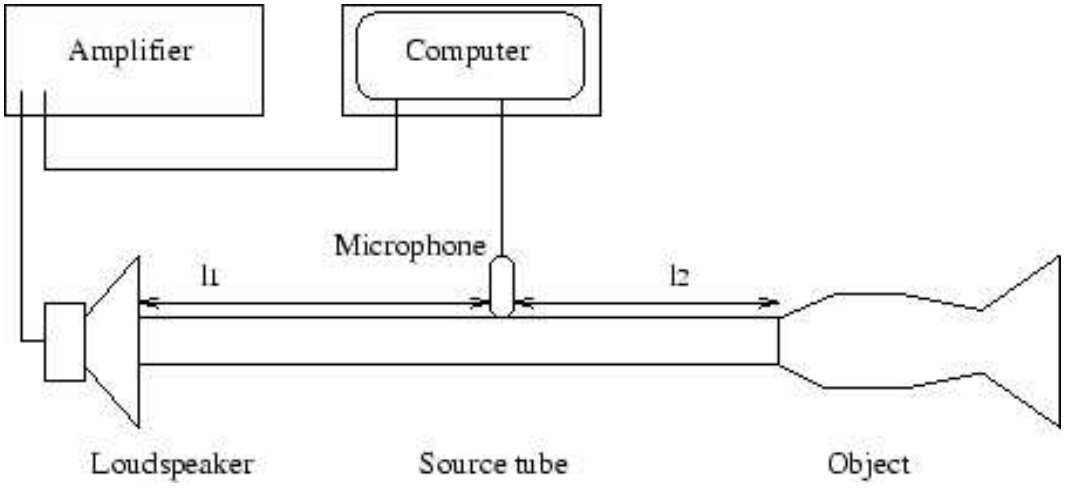

Figure 2.33: Schematic diagram of the acoustic pulse reflectometer.

2.15.2 Brass Instrument Analysis System

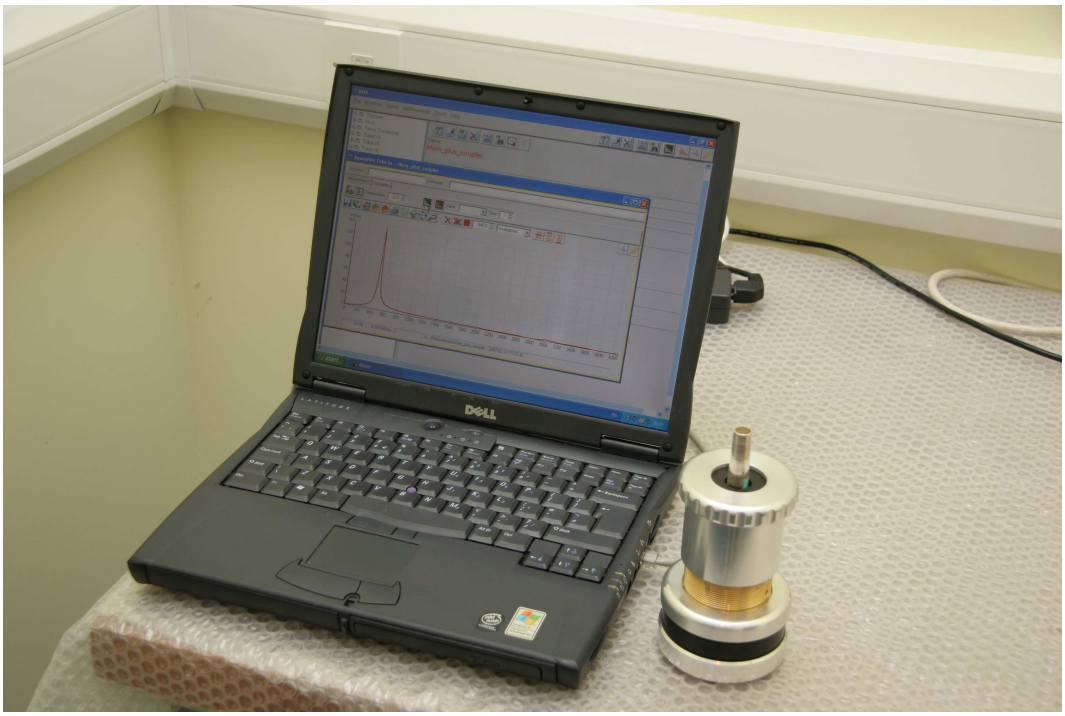

Figure 2.34: The Brass Instrument Analysis System (BIAS).

The BIAS system[76], like the TMFC is a frequency-domain technique and applies a sweeping sinusoidal pressure wave to the study object. The response of the object is monitored by a single microphone. A feedback mechanism helps the volume velocity to stabilise at a constant value throughout the sweep. The flow is produced by two high density capillaries in the head providing a high impedance to the flow. The input impedance of the study object is thus small in comparison. Since the particle velocity is constant the impedance becomes a monotonic function of the pressure measured by the microphone situated in the measurement head. The system is calibrated by measuring the impedance of two short closed tubes, for which the theoretical impedance is accurately known. The current system works over a frequency range of 20 Hz to 4 kHz.

2.16 Summary

The theory of sound wave propagation in various bore shapes has been examined by reviewing the wave equation in detail. From this knowledge the general expression for the input impedance of a cylinder in terms of the load impedance has been derived. The analogous case of electrical impedance has been discussed in an attempt to give an intuitive understanding of impedance, in particular the concept of capacitance and inductance. The reflection function - which is closely related to the impedance - has also been mentioned. The plane-wave input impedance of some simple cylindrically-symmetric objects for which a comparison can be made with experimental impedance results has been derived; the idea being that any instrument can be approximated as a series of cylinders of suitable length. Lossy and lossless propagation have been considered by modelling the propagation constant as either complex or real, respectively. Propagation is also assumed to be linear as only low-amplitude excitations are used for the experiments.

The impedance of a horn has been modelled using various methods including as a concatenation of cylinders, cones, and Bessel functions. It was found that modelling the horn as a single Bessel function gave an almost identical impedance curve to that obtained by using many concatenated cones, whereas the cylindrical element model gave a substantially different result. Two other important parameters have been described: the input impulse response, and bore reconstruction. Their relation to the impedance and details of how to obtain the other two parameters from knowledge of one has been demonstrated. A simple example has been given in which the theoretical plane-wave impedance is used as input for the reconstruction algorithm. It was found that the reconstructed profile fitted the true profile well; the reconstruction maintains a constant radius up to the closed end of the tube. Small over-predictions in the reconstruction at discontinuities is attributed to the Gibbs' phenomenon.

It was shown that the resolution of the impedance data determines the duration of the impulse response, but has no effect on the axial resolution of the bore reconstruction.

Chapter 3

The Two-Microphone-Four-Calibration System

In this chapter we will discuss the theory of operation of the Two-Microphone-Four-Calibration (TMFC) system which can be used for measuring the input impedance of an instrument. Other systems that have had success in bore reconstruction and impedance measurement, the acoustic pulse reflectometer and the brass instrument analysis system, will be briefly covered. Starting with a discussion of the experimental set up for the TMFC system, we will derive a general expression for the experimental input impedance to be compared with theory. This expression includes three complex coefficients. These coefficients can be obtained via a calibration procedure. The *full method* of calibration allows theory and experiment to be completely decoupled giving a comparison between the two. The *partial method* of calibration is used at the lower end of the frequency spectrum and involves the propagation constant being modelled by the plane wave theory covered in Chapter 2. The theory of higher modes is covered briefly and illustrated with an example in which the plane wave impedance is calculated for a relatively simple bore with a step. The step causes the generation of higher modes. These modes, when incorporated into the algorithm alter the yielded theoretical impedance curve. Singularity effects and calibration issues resulting from the usage of two microphones can potentially cause inaccurate results at specific frequencies. A strategic solution to this problem is elaborated on. We will discuss the upper frequency limit of the current system determined by such issues as the *cut-on frequency*, related

to the radius of the measurement duct, above which higher modes will propagate in the duct. The low frequency limit caused by the finite separation of the microphones (a result of their finite diameter) leading to 'singularities' will also be discussed. Then we will observe some typical impedance results obtained using both full and partial calibration methods which will be compared with the theoretical models derived in Chapter 2.

3.1 Experimental Set-up for the TMFC System

The TMFC method has built upon work by the likes of Dalmont et al[15, 16] and Gibiat et al[17] on the TMTC system described in Chapter 1 where three calibration measurements are made. However, this method requires knowledge of the propagation constant. It is found that at high frequencies the errors associated with modelling the propagation constant become large and the method breaks down. For this reason the TMFC system was developed by van Walstijn[18] which uses four calibration measurements and removes the need for calculating the propagation constant. This technique works well for frequencies between 1 kHz and 20 kHz but at frequencies below 1 kHz the length of the calibration objects become very large and it is desirable to avoid using them. Errors associated with modelling the propagation constant by plane-wave theory however are less severe at frequencies below 1 kHz[18] so a modification to the TMFC method has been implemented in this thesis whereby the propagation constant is modelled and a new calibration technique is used where excessively long straight tubes are not required.

The TMFC system is shown in Figure 3.1. A schematic diagram is shown in Figure 3.2. A sinusoidal excitation signal generated by the computer software is converted into an analogue signal by a data acquisition card (type National Instruments PCI 4452). The driver (type JBL 2426H) generates a plane wave which is sent along an aluminium measurement duct. The instrument to be studied is attached to this duct - in this case the study object is a brass tube which is closed at the far end so all of the wave is reflected at the closed end. These reflections returning back to the driver allow a wave pattern to be set up. The microphones (type Sennheiser KE4-211 condenser) generate the signals s_1 and s_2 by responding to this wave pattern i.e. by reacting to the

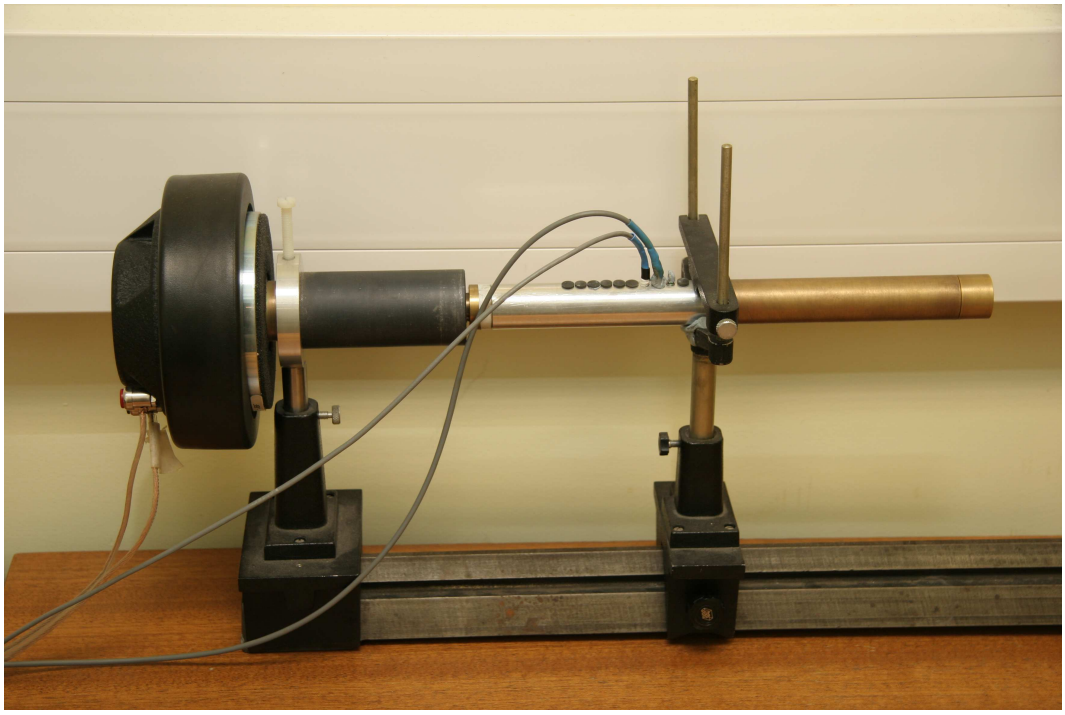

Figure 3.1: The TMFC system. The software controlled loudspeaker generates a pure sinusoidal excitation signal which propagates past the two microphones situated in the aluminium measurement duct and into the object to be studied (in this case a closed brass tube).

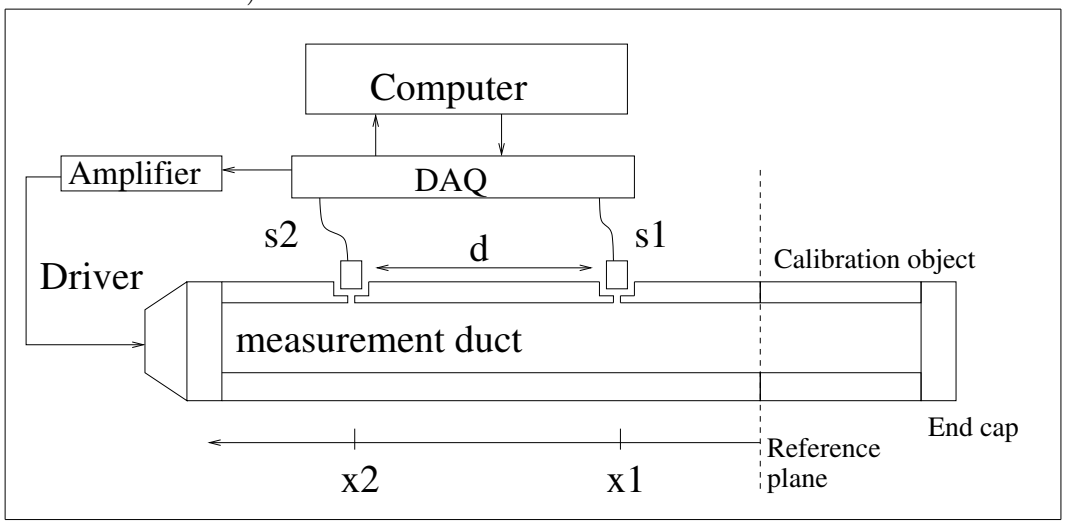

Figure 3.2: Schematic diagram of the Two-Microphone-Four-Calibration (TMFC) system used for measuring acoustic impedance.

change in air pressure in the duct. The time-domain microphone signals are Fourier transformed to obtain the amplitudes of the signals. To avoid complications when carrying out the Fourier transform the duration of the recorded microphone signal has to be an integer number of periods for a given frequency. There are ten microphone holes in the measurement duct allowing the distance between microphones to be adjusted. Unused holes are blocked with small plastic caps to ensure the measurement duct is flush at these points and that reflections are not created. The measurement duct is made sufficiently thick that its extent of vibration does not affect the measurements. It is desirable to have the microphones as close to the instrument under investigation as possible to minimise dissipative losses inside the tube. The system systematically runs over a range of discrete frequencies for which the initial and final frequency and frequency interval can be controlled by the software. There is enough of a delay between signals so that each result does not interfere with one another and remains discrete. This data is recorded by a data acquisition card (type National Instruments PCI 4451) which samples the microphone signals and stores the data in the computer memory. From the microphone signal ratio (sometimes referred to as the *transfer function* or the *standing wave ratio*) the impedance of the tubular object under study can be deduced.

We will now derive an expression for the input impedance as measured by the TMFC system in terms of the signals generated by the microphones and the propagation constant.

3.2 Experimental Expression for the Impedance

Observe Figure 3.3. Let us first derive expressions for the pressure and volume velocity at plane 1 in terms of the pressure and volume velocity at plane 2. The relation between the forward propagating wave at plane 1 p_1^+ and the forward propagating wave at plane 2 p_2^+ are given by

$$p_2^+ = \exp(-i\Gamma d)p_1^+ \tag{3.1}$$

where d is the distance between plane 1 and 2. The relation between the two backward propagating waves p_1^- and p_2^- is

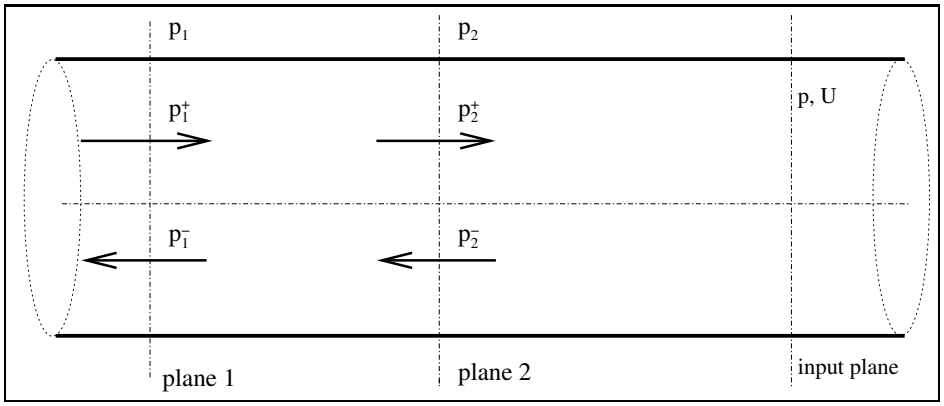

Figure 3.3: Expressions can be derived for the pressure and volume velocity at the input plane in terms of the pressure and volume velocity at plane 1 and plane 2.

$$p_2^- = \exp(i\Gamma d) p_1^- . \tag{3.2}$$

At plane 1 the following conditions hold

$$p_1 = p_1^+ + p_1^- \tag{3.3}$$

and

$$Z_c U_1 = p_1^+ - p_1^- \tag{3.4}$$

where p_1 is the total pressure at plane 1 and U_1 is the volume speed. Similarly at plane 2

$$p_2 = p_2^+ + p_2^- \tag{3.5}$$

and

$$Z_c U_2 = p_2^+ - p_2^- . \tag{3.6}$$

Adding together (3.3) and (3.4) eliminates p_1^- and gives

$$p_1 + Z_c U_1 = 2p_1^+ . \tag{3.7}$$

Subtracting (3.4) from (3.3) eliminates p_1^+ and gives

$$p_1 - Z_c U_1 = 2p_1^-. \tag{3.8}$$

Now we do the same procedure for the conditions at plane 2. Adding (3.5) and (3.6) eliminates p_2^- and gives

$$p_2 + Z_c U_2 = 2p_2^+. \tag{3.9}$$

Subtracting (3.6) from (3.5) eliminates p_2^+ and gives

$$p_2 - Z_c U_2 = 2p_2^-. \tag{3.10}$$

Using (3.1) and (3.7) in (3.9) we find that

$$p_2 + Z_c U_2 = (p_1 + Z_c U_1)\exp(-i\Gamma d). \tag{3.11}$$

Now we have an equation in terms of p_1, U_1, p_2, and U_2. The forward and backward propagating components have been eliminated. We do the same for (3.10) by substituting in the expression for p_2^- given by (3.2)

$$p_2 - Z_c U_2 = 2\exp(i\Gamma d)p_1^- \tag{3.12}$$

but using (3.8) we obtain

$$p_2 - Z_c U_2 = \exp(i\Gamma d)(p_1 - Z_c U_1). \tag{3.13}$$

Now, if we multiply (3.11) by $\exp(+i\Gamma d)$ and (3.13) by $\exp(-i\Gamma d)$ we get

$$(p_2 + Z_c U_2)\exp(i\Gamma d) = p_1 + Z_c U_1 \tag{3.14}$$

and

$$(p_2 - Z_c U_2)\exp(-i\Gamma d) = p_1 - Z_c U_1 \tag{3.15}$$

and then add them together

$$(p_2 + Z_c U_2)\exp(i\Gamma d) + (p_2 - Z_c U_2)\exp(-i\Gamma d) = 2p_1. \tag{3.16}$$

After a little re-arranging and usage of basic trigonometric relations we obtain

$$p_1 = p_2 \cos(\Gamma d) + iZ_c U_2 \sin(\Gamma d). \tag{3.17}$$

We now have an expression for the pressure at plane 1 in terms of the pressure and velocity at plane 2. If we subtract (3.15) from (3.14) and re-arrange a little we get

$$U_1 = i\frac{1}{Z_c} p_2 \sin(\Gamma d) + U_2 \cos(\Gamma d) \tag{3.18}$$

which is our desired expression for the volume velocity.

We can use (3.17) to find the impedance at an arbitrary distance from the two planes, for example the input plane. Let us denote the pressure and volume velocity at this plane p and U respectively.

We can write

$$p_1 = p\cos(\Gamma x_1) + iZ_c U \sin(\Gamma x_1) \tag{3.19}$$

and

$$p_2 = p\cos(\Gamma x_2) + iZ_c U \sin(\Gamma x_2) \tag{3.20}$$

where x_1 is the distance between plane 1 and the input plane and x_2 is the distance between plane 2 and the input plane, i.e.

$$x_1 - x_2 = d. \tag{3.21}$$

If the pressures p_1 and p_2 are measured by microphones that do not have an identical frequency response but have individual transducing properties denoted H_1 and H_2 respectively then we can account for this effect by modifying (3.19) and (3.20)

$$p_1 = H_1 p\cos(\Gamma x_1) + iH_1 Z_c U \sin(\Gamma x_1) \tag{3.22}$$

and

$$p_2 = H_2 p \cos(\Gamma x_2) + i H_2 Z_c U \sin(\Gamma x_2). \tag{3.23}$$

If we divide (3.22) by (3.23) and note that p_2/p_1 is just the microphone signal ratio denoted $\mathcal{Y}$ then after some re-arranging we find

$$\frac{Z}{Z_c} = \mathcal{A}\left(\frac{\mathcal{Y} - \mathcal{B}}{\mathcal{Y} - \mathcal{C}}\right) \tag{3.24}$$

where

$$\mathcal{A} = -i\left[\frac{\sin(\Gamma x_1)}{\cos(\Gamma x_1)}\right] \tag{3.25}$$

$$\mathcal{B} = G\left[\frac{\sin(\Gamma x_2)}{\sin(\Gamma x_1)}\right] \tag{3.26}$$

$$\mathcal{C} = G\left[\frac{\cos(\Gamma x_2)}{\cos(\Gamma x_1)}\right] \tag{3.27}$$

and $G = H_2/H_1$.

Notice the expressions for $\mathcal{A}$, $\mathcal{B}$, and $\mathcal{C}$ all have the propagation constant in them which can be modelled by the theory described in Chapter 2. Next we will outline the method used by van Walstijn[18] to calculate these coefficients purely in terms of the microphone signal ratios obtained from calibration measurements of four closed tubes of different length; this is referred to as the *full calibration method*.

3.3 Full Calibration

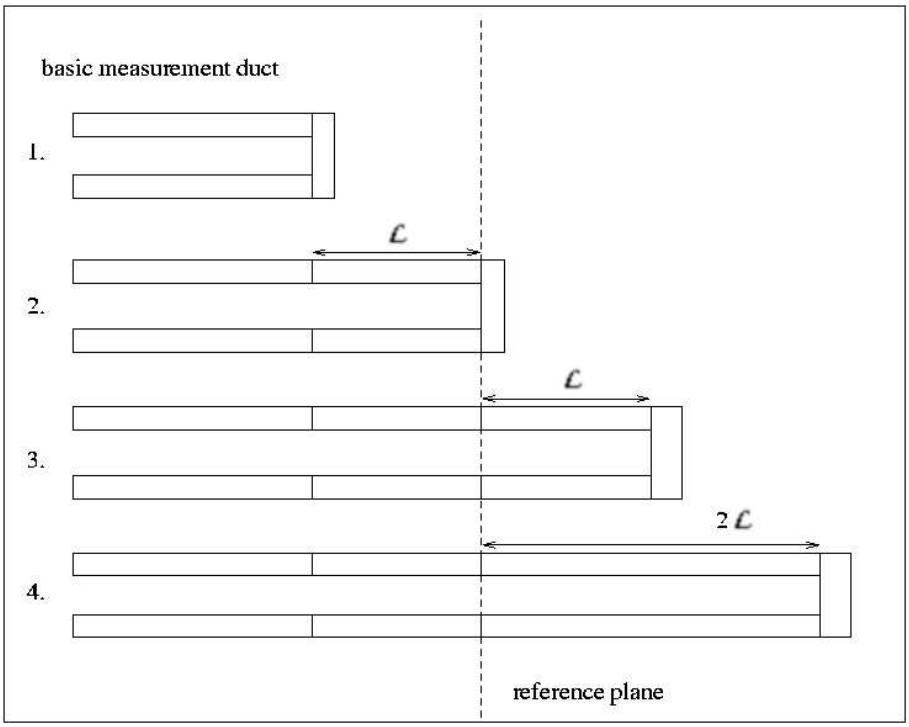

Figure 3.4: The full calibration method involves the measurement of four closed tubes of length $-\mathcal{L}$, 0, $+\mathcal{L}$, and $+2\mathcal{L}$.

The four calibration measurements used by van Walstijn[18] are shown in Figure 3.4 and are labelled 1, 2, 3, and 4. We define the reference plane to be a distance $\mathcal{L}$ beyond the physical end of the measurement duct. If we block the duct off, as shown in calibration 1, in a mathematical sense we have a calibration tube of length $-\mathcal{L}$ - the measured signal ratio for this calibration tube is defined as $\mathcal{Y}_{\text{neg}}$. In calibration 2 the duct is terminated at the reference plane - the signal ratio is labelled $\mathcal{Y}_0$. In calibration 3 and 4 the calibration tubes are of length $\mathcal{L}$ and $2\mathcal{L}$ respectively - the signal ratios are $\mathcal{Y}_{\text{pos}}$ and $\mathcal{Y}_{\text{2pos}}$ respectively. The simplest coefficient to obtain is the $\mathcal{C}$ coefficient.

3.3.1 The $\mathcal{C}$ Coefficient

Let us consider exciting the air at a particular frequency via the driver while coupling the duct to the calibration tube of length $\mathcal{L}$, closed at the far end i.e. the system is closed off at the reference plane as shown in Figure 3.4 calibration 2. Let the microphone

signal ratio measured during this calibration be denoted by $\mathcal{Y}_0$. At the closed end the particle velocity must be zero. This implies that the termination impedance is infinite. Since $\mathcal{B}$ and $\mathcal{Y}_0$ are finite the denominator in equation (3.24) must go to zero giving

$$\mathcal{C} = \mathcal{Y}_0. \tag{3.28}$$

Determination of the $\mathcal{B}$ coefficient requires a little more thought.

3.3.2 The $\mathcal{B}$ Coefficient

The theoretical expression for the input impedance of a closed tube of length $\mathcal{L}$ is given by

$$\frac{Z}{Z_c} = -i\cot(\Gamma\mathcal{L}). \tag{3.29}$$

Note also that the cotangent function is odd

$$\cot(-\Gamma\mathcal{L}) = -\cot(\Gamma\mathcal{L}). \tag{3.30}$$

If we have a positive length tube $+\mathcal{L}$ of impedance Z_{pos} and a negative length tube $-\mathcal{L}$ of impedance Z_{neg} then it follows that

$$\frac{Z_{\text{pos}}}{Z_c} + \frac{Z_{\text{neg}}}{Z_c} = 0. \tag{3.31}$$

Writing this out explicitly

$$\mathcal{A}\left[\left(\frac{\mathcal{Y}_{\text{pos}} - \mathcal{B}}{\mathcal{Y}_{\text{pos}} - \mathcal{C}}\right) + \left(\frac{\mathcal{Y}_{\text{neg}} - \mathcal{B}}{\mathcal{Y}_{\text{neg}} - \mathcal{C}}\right)\right] = 0. \tag{3.32}$$

Substituting expression (3.28) into the above and rearranging gives

$$\mathcal{B} = \frac{2\mathcal{Y}_{\text{pos}}\mathcal{Y}_{\text{neg}} - \mathcal{Y}_0(\mathcal{Y}_{\text{pos}} + \mathcal{Y}_{\text{neg}})}{(\mathcal{Y}_{\text{pos}} + \mathcal{Y}_{\text{neg}}) - 2\mathcal{Y}_0}. \tag{3.33}$$

3.3.3 The $\mathcal{A}$ Coefficient

The reflection coefficient was derived in Chapter 2 (2.56) and is given by

$$R = \frac{Z - Z_c}{Z + Z_c}. \tag{3.34}$$

For the positive length tube

$$Z_{\text{pos}} = -iZ_c \cot(\Gamma\mathcal{L}). \tag{3.35}$$

Substituting (3.35) into (3.34) and rewriting the trigonometric functions in terms of complex exponentials, we find the reflection function for the positive length tube

$$R_{\text{pos}} = \exp(-2\Gamma\mathcal{L}). \tag{3.36}$$

So for a tube of length $2\mathcal{L}$ this is

$$R_{2\text{pos}} = \exp(-4\Gamma\mathcal{L}) \tag{3.37}$$

and so

$$R_{2\text{pos}} = R_{\text{pos}}^2. \tag{3.38}$$

We can use equation (3.34) to rewrite the reflection coefficients in (3.38) in terms of impedance. After substantial rearranging we obtain

$$\bar{Z}_{\text{pos}}^2 - 2\bar{Z}_{\text{pos}}\bar{Z}_{2\text{pos}} + 1 = 0. \tag{3.39}$$

The 'bar' above Z_{pos} and $Z_{2\text{pos}}$ denotes that they have been normalised relative to the characteristic impedance. We can use equation (3.24) to write the above in terms of $\mathcal{A}$, $\mathcal{B}$, $\mathcal{C}$ and $\mathcal{Y}$. After some rearranging this gives

$$\mathcal{A} = \left[2\left(\frac{\mathcal{Y}_{\text{pos}} - \mathcal{B}}{\mathcal{Y}_{\text{pos}} - \mathcal{C}}\right)\left(\frac{\mathcal{Y}_{2\text{pos}} - \mathcal{B}}{\mathcal{Y}_{\text{pos}} - \mathcal{C}}\right) - \left(\frac{\mathcal{Y}_{\text{pos}} - \mathcal{B}}{\mathcal{Y}_{\text{pos}} - \mathcal{C}}\right)^2\right]^{-1/2}. \tag{3.40}$$

We have now derived expressions for the coefficients $\mathcal{A}$, $\mathcal{B}$, and $\mathcal{C}$ purely in terms

of signal ratios. No knowledge of the propagation constant is required and theory and experiment can be completely separated. The next step is to outline the technique that will be used for frequencies below 1 kHz. This is referred to as the *partial calibration technique*.

3.4 Partial Calibration

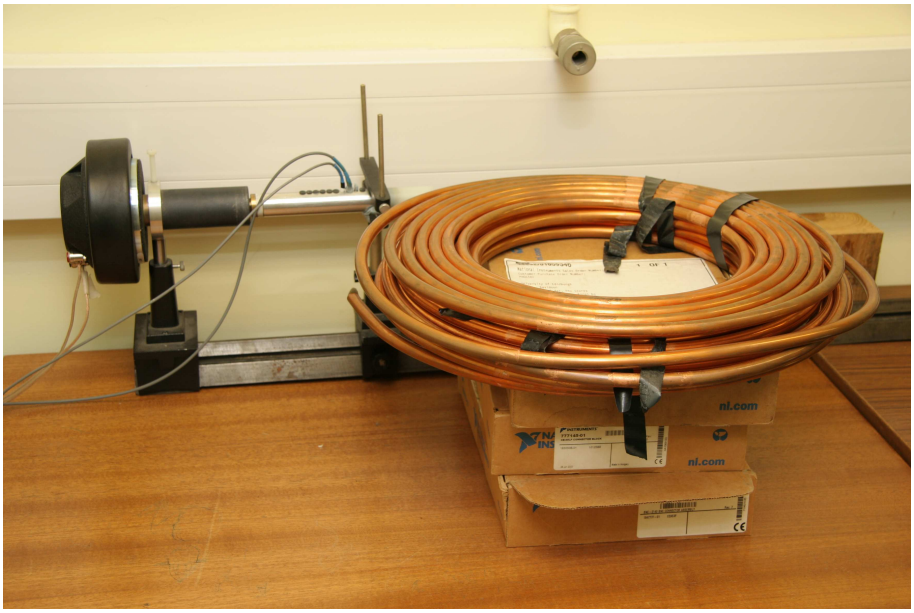

Figure 3.5: The TMFC system with an anechoic termination at the reference plane.

The set up for the partial TMFC method is shown in Figure 3.5. An anechoic measurement is made to obtain an expression for G. This is done by attaching a very long tube to the duct. A large fraction of the wave's energy is attenuated in traversing the tube. A foam wedge is placed at the end of the tube in an attempt to absorb the residual energy. In this procedure there are no reflections to consider and so the wave propagation is simple. The relation between the non-ideal microphone signals p_1 and p_2 takes the form similar to that of equation (3.1)

$$p_2 = \frac{H_2}{H_1} \exp(-i\Gamma d) p_1 \tag{3.41}$$

so

$$\mathcal{Y} = \frac{p_2}{p_1} = G\exp(-i\Gamma d). \tag{3.42}$$

To account for the individual characteristics of the microphones the anechoic measurement is performed and then repeated with the microphones switched in position. If we denote the first measurement of the signal ratio as $\mathcal{Y}_1$ then

$$\mathcal{Y}_1 = G\exp(-i\Gamma d). \tag{3.43}$$

If we repeat the measurement with the microphones switched in position, denoted $\mathcal{Y}_2$, then $H_1 \rightarrow H_2$ and $H_2 \rightarrow H_1$. This gives

$$\mathcal{Y}_2 = \frac{1}{G}\exp(-i\Gamma d). \tag{3.44}$$

Dividing (3.43) by (3.44) and rearranging gives

$$G = \sqrt{\frac{\mathcal{Y}_1}{\mathcal{Y}_2}}. \tag{3.45}$$

This expression for G can then be inserted into (3.26) and (3.27), x_1 and x_2 are known lengths and the propagation constant is modelled using theory from Chapter 2, equation (2.79). We now have expressions for the $\mathcal{A}$, $\mathcal{B}$, and $\mathcal{C}$ coefficients ready for substituting into (3.24). All we have to measure is the microphone signal ratio for the instrument under study.

3.5 Singularity Effects

In general, a complicated wave pattern is set up inside the measurement duct. One situation that can occur is that when the distance between the microphones is equal to half the wavelength, two pressure nodes can sit directly under both microphones. In this case the microphone signals tend to zero and the signal ratio becomes ill defined.

In fact, singularities occur whenever the distance between the microphones is equal to an integer number of half wavelengths

$$n\lambda = 2d, \qquad \text{where} \qquad n = 0, 1, 2, 3, ... \tag{3.46}$$

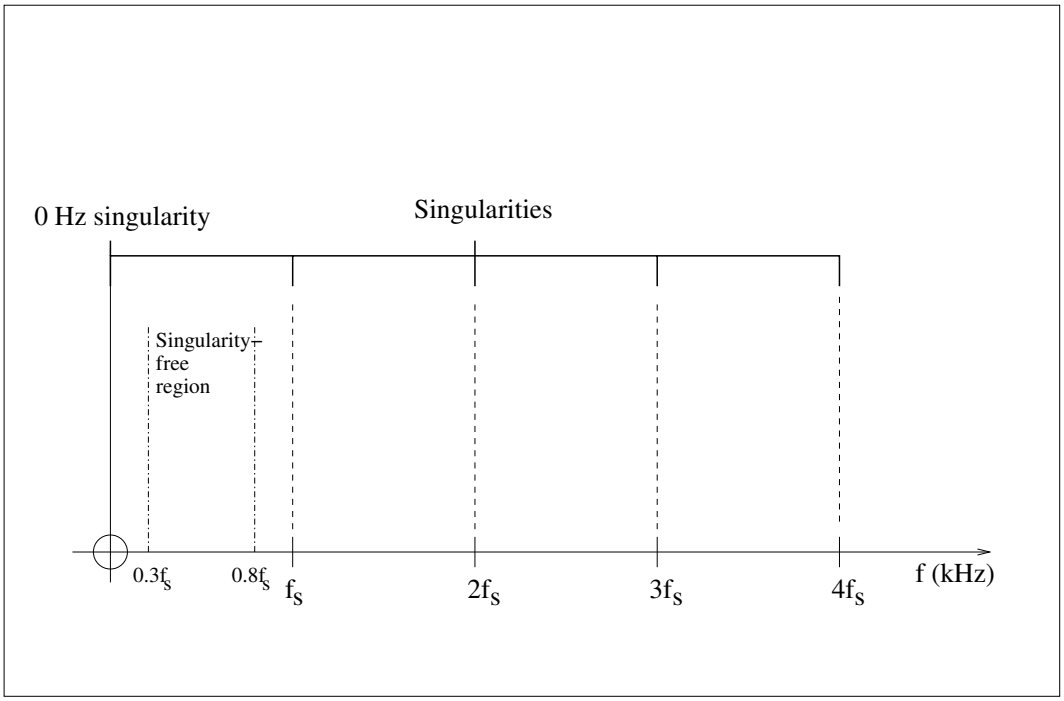

Figure 3.6: Schematic diagram showing singularities for a *fixed* value of microphone separation.

therefore

$$f = \frac{nc}{2d}. \tag{3.47}$$

The *first singular frequency* (not including $f = 0$ Hz) is denoted f_s and occurs when $n = 1$

$$f_s = \frac{c}{2d}. \tag{3.48}$$

In theory it is best to carry out measurements between zero frequency and f_s to ensure that singularities are avoided. However, empirically van Walstijn found the effective measurement bandwidth, referred to as the *suitable bandwidth (SBW)*[18], to be

$$\text{SBW} = [0.3 - 0.8]f_s. \tag{3.49}$$

Figure 3.6 shows a schematic diagram illustrating the singular frequencies occurring

at discrete values in frequency space for a *fixed* value of microphone separation.

For example, a microphone separation distance of 7 mm corresponds to a first singular frequency of about 25 kHz. This in turn gives a suitable bandwidth of 7 to 20 kHz. Observing lower frequencies requires a larger microphone separation.

Figure 3.7 shows the impedance of a closed tube of length 128 mm and radius 4.9 mm. A microphone separation of 49 mm was used giving a first singular frequency of 3.5 kHz. At this frequency the impedance magnitude is still fairly well behaved but the impedance phase has the incorrect sign.

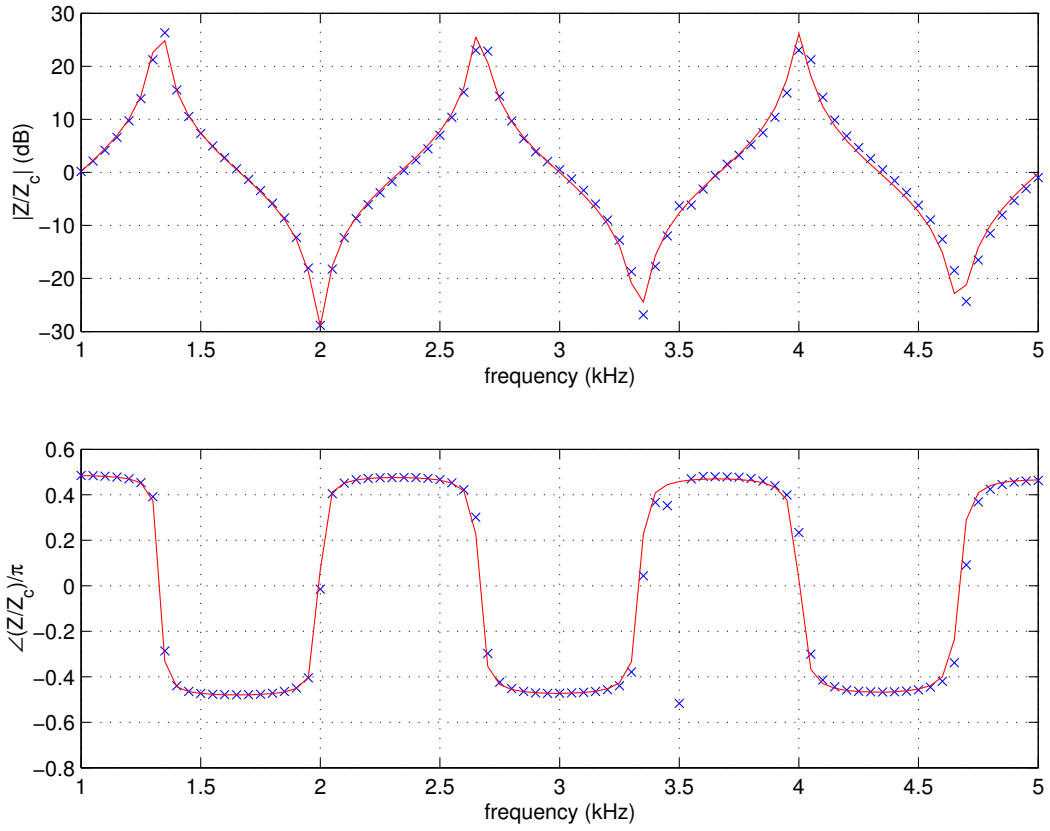

Figure 3.7: Singularity effect on the measured impedance.

3.5.1 Singularity Effects Dependent on the Length of Calibration Tube

Other singular effects occur due to the length of the calibration tubes used. Consider the calibration measurements involving the positive ($+\mathcal{L}$) and negative length ($-\mathcal{L}$) measurement. Singularities occur when the length $\mathcal{L}$ is an odd integer number of quarter wavelengths

$$f = \frac{nc}{4\mathcal{L}}, \qquad \text{where} \qquad n = 1, 3, 5, ... \tag{3.50}$$

This is because the impedances Z_{pos} and Z_{neg} are zero at these frequencies thus equation (3.31) is satisfied but the solution is trivial. For the positive and double positive ($+2\mathcal{L}$) measurement, singularities occur when the length $\mathcal{L}$ is an integer number of half wavelengths

$$f = \frac{nc}{2\mathcal{L}}, \qquad \text{where} \qquad n = 1, 2, 3, ... \tag{3.51}$$

This is because the impedances Z_{pos} and $Z_{2\text{pos}}$ will be equal at these frequencies thus presenting equivalent information[18]. Setting n to 1 in equation (3.50) and comparing with (3.48) we see that for the first singularity due to the calibration tube not to lie within the defined suitable bandwidth requires

$$\frac{c}{4\mathcal{L}} \geq \frac{c}{2d} \tag{3.52}$$

and so

$$\mathcal{L} \leq \frac{d}{2}. \tag{3.53}$$

Thus we use calibration tubes of length equal to half the microphone separation.

Figure 3.8 shows the current limitations of the TMFC system. The radius of the measurement duct is 4.9 mm. This radius determines the cut on frequency which is equal to 20.4 kHz. This frequency serves as an absolute upper limit for which plane wave data can be obtained. The smallest microphone separation was deliberately chosen as 7 mm since this gives a SBW of 7.4 kHz up to a round value of 20 kHz.

Li et al have shown that 50 Hz is the minimum frequency that must be measured in order to obtain a good reconstruction[26]. For that reason the largest microphone separation used was d =1.075 m since this corresponds to a first singular frequency of $f_s = 158$ Hz which in turn gives a SBW of 50 Hz to 125 Hz. All frequencies in between 50 Hz and 20 kHz can be obtained by using a microphone separation in between the two extremes of 7 mm and 1.075 m.

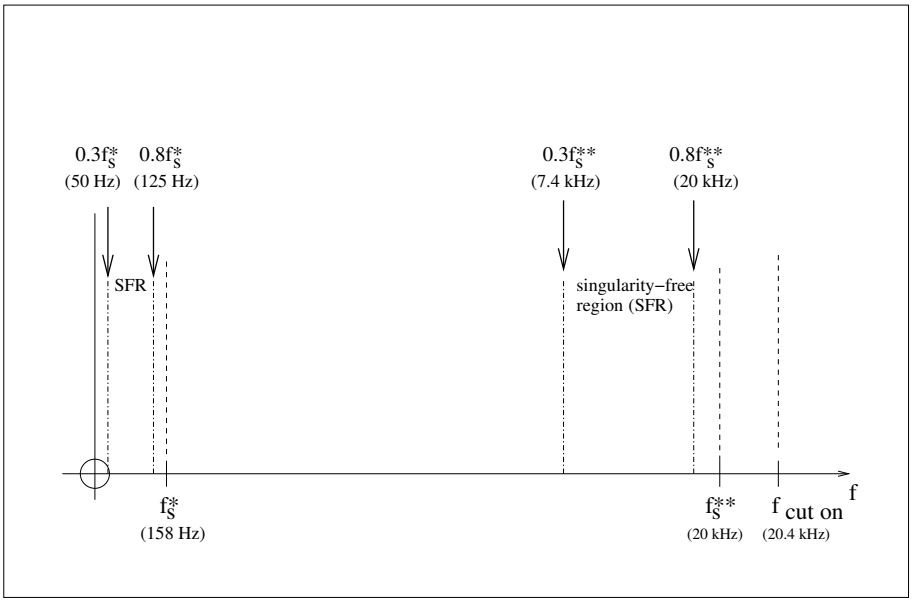

Figure 3.8: Effect of microphone separation on singular frequencies.

3.5.2 Strategy for Measuring Over a Large Bandwidth

Table 3.1 and 3.2 show how the 50 Hz to 20 kHz frequency spectrum can be divided into smaller overlapping suitable bandwidths governed by the separation of the microphones. The resulting data can then be combined to give the full range.

	d **(mm)**	f_s **(kHz)**	**SBW (kHz)**	$-\mathcal{L}$ (mm)	0 (mm)	$+\mathcal{L}$(mm)	$+2\mathcal{L}$ (mm)
I	7	24.6	7.4-20	-3.5	0	3.5	7
II	14	12.3	3.7-10	-7	0	7	14
III	28	6.1	2.0-5.0	-14	0	14	28
IV	49	3.5	1.0-2.9	-24.5	0	24.5	49

Table 3.1: Full calibration table. The possible microphone separation distances, their corresponding suitable bandwidths, and length of calibration tubes required are given.

	d (mm)	f_s (Hz)	SBW (Hz)
V	63	2,698	800-2,000
VI	141	1,206	400-900
VII	259	656	200-500
VIII	435	340	120-320
IX	1,075	158	50-125

Table 3.2: Partial calibration table. The possible microphone separation distances and corresponding suitable bandwidths are given.

3.6 Measurement of the $\mathcal{A}$, $\mathcal{B}$, and $\mathcal{C}$ coefficients

Figure 3.9, 3.10, and 3.11 show the $\mathcal{A}$, $\mathcal{B}$, and $\mathcal{C}$ coefficients as measured by the TMFC system. The frequency range is 1 to 2 kHz. From inspection of table 3.1 this requires a microphone separation of 49 mm. The reference plane is defined a distance 24.5 mm from the physical end of the measurement duct. By setting G to 1 we compare the results with plane-wave theory. We can see that there is close agreement in all three figures.

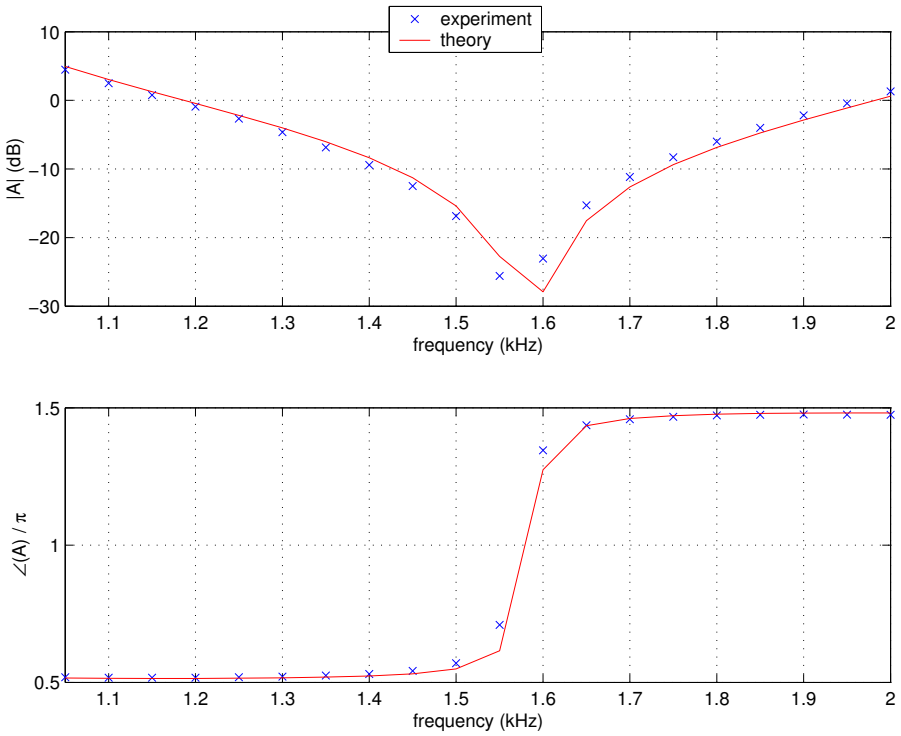

Figure 3.9: The $\mathcal{A}$ coefficient.

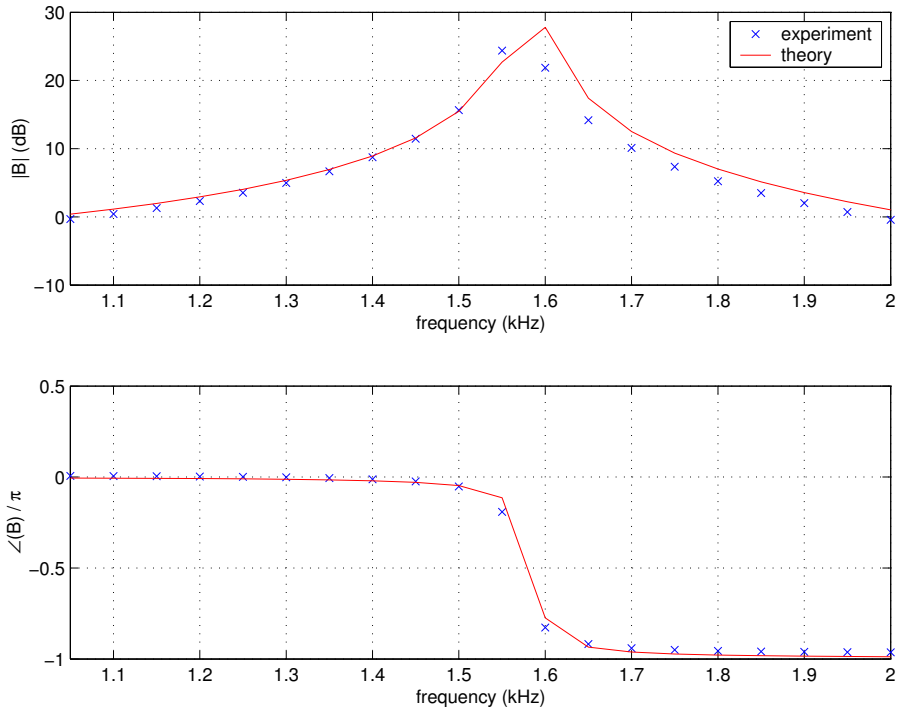

Figure 3.10: The $\mathcal{B}$ coefficient.

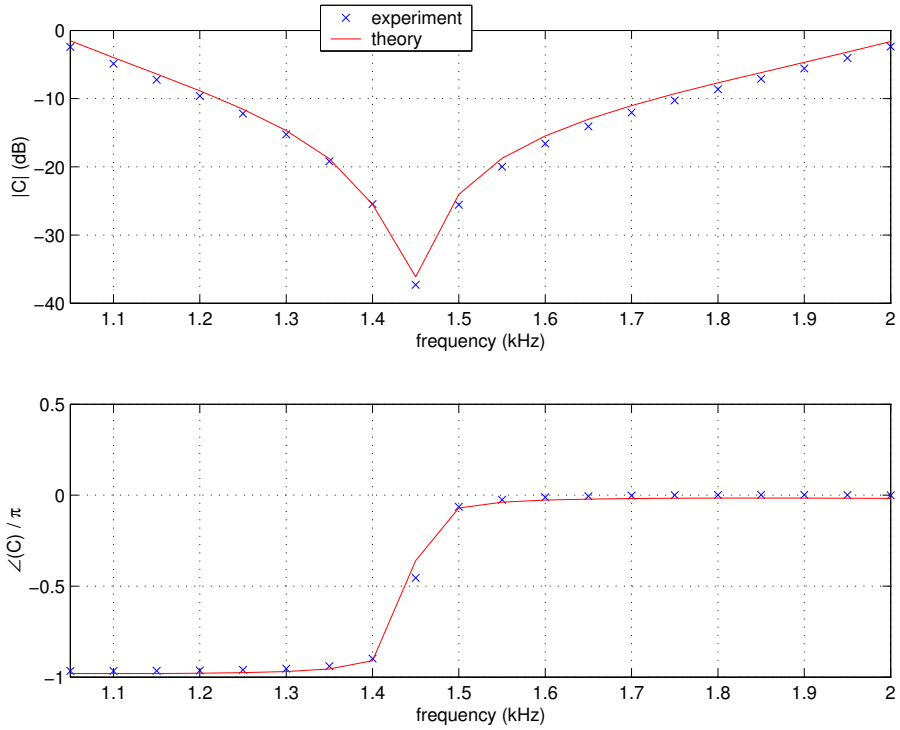

Figure 3.11: The $\mathcal{C}$ coefficient.

3.7 Example Impedance Results

3.7.1 The Closed Tube

The following figures show the impedance data obtained for a closed pipe of length 128 mm and constant radius 4.9 mm. Figures 3.12, 3.13, 3.14, and 3.15 correspond to the full calibration method. Figures 3.16, 3.17, 3.18, 3.19, and 3.20 correspond to the partial calibration method. The theoretical plane-wave impedance for a closed tube is simple and accurately known and is thus plotted in the figures for comparison.

Consider Figure 3.12 showing the impedance magnitude and phase obtained using set up I in table 3.1. The blue crosses are data obtained by the TMFC system. The continuous red line corresponds to the lossy plane wave theoretical model. A microphone separation d of 7 mm is used. This gives a first singular frequency of approximately 20.4 kHz. This in turn gives a suitable frequency range of 7.4 to 20 kHz. In this figure the data is taken in 50 Hz intervals. We see immediately that there is good agreement between theory and experiment - to within about one-tenth of a decibel. There are a total of 15 impedance maxima and 15 impedance minima for the tube over the 20 kHz range. The benefit of measuring high frequency data is the large bandwidth that can be achieved with one combination of microphones - since the suitable bandwidth is proportional to the first singular frequency. Seven of these impedance extrema lie in the 10 to 20 kHz region. The magnitude of the extrema of the impedance curve are very low since the measurement duct (and study object) have a small diameter (9.8 mm) resulting in large losses experienced by the excitation signal at the walls. The phase of the impedance is well behaved and there are no signs of singularity effects, as expected.

Now consider one of the partial calibration plots, for example Figure 3.18. We see the suitable bandwidth is so small we cannot observe a full impedance maxima or minima. This is because at lower and lower frequencies the suitable bandwidth becomes smaller. Again, the impedance magnitude agrees well with theory with a slight underprediction of 0.3 dB. This may well be due to the change in room temperature from the time it was noted to the time this frequency range was measured - the time to obtain a full data set is of the order of hours. This information, as we saw in Chapter 2, is a

required parameter for the theoretical model, as a perfectly feasible room temperature change of ± 0.5 degrees Celsius would be enough to make a visibly noticeable difference between the two data sets.

The impedance phase on first inspection appears to be largely different from theory, but a closer look at the scale of the phase axis reveals that there is a difference - at most - of about $0.003/\pi$ radians. This corresponds to an over-prediction of just over half a degree - a tiny amount.

For each experimental data point plotted, the corresponding theory point is plotted and connected via a straight line. For the large SBW figures the curve appears smooth and continuous, as it should do. For the low SBW figures - where there are few data points - the curve shows up its artificial discretisation.

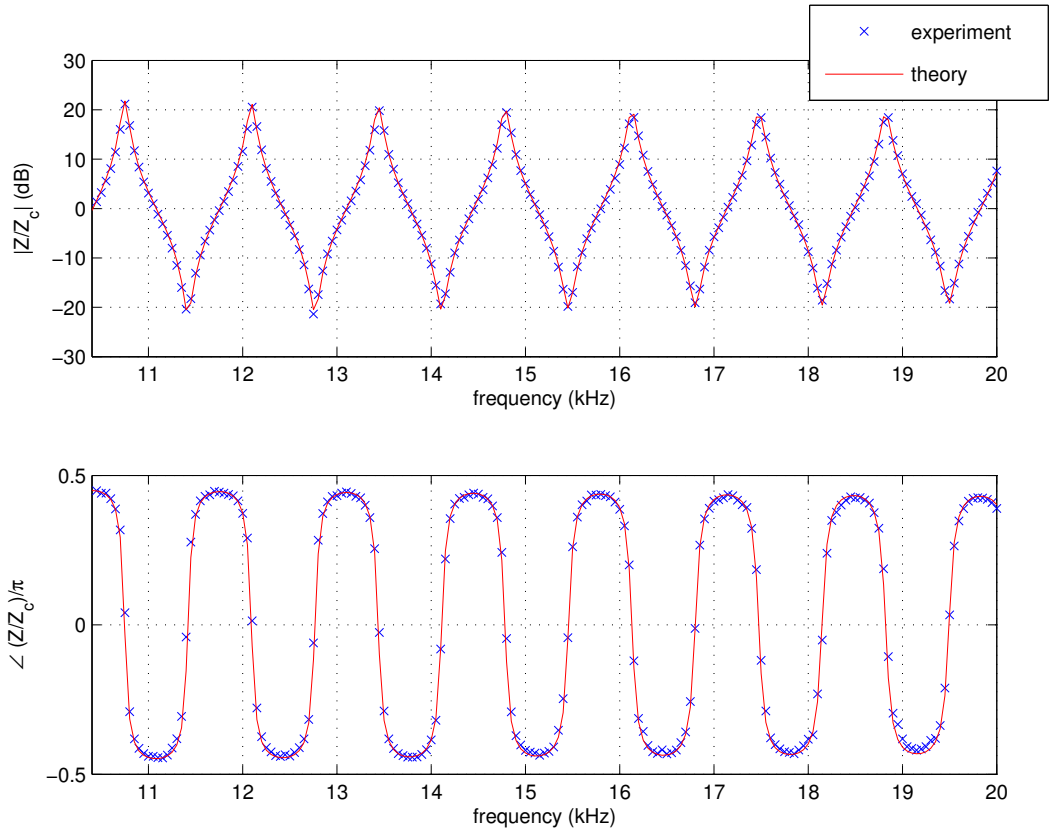

Figure 3.12: Full calibration using set up I, table 3.1.

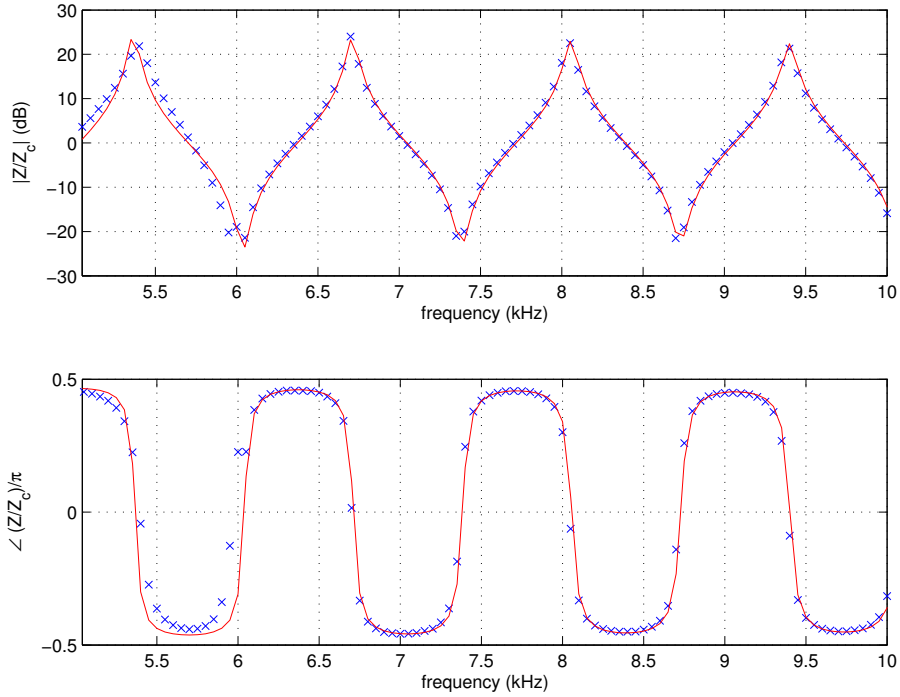

Figure 3.13: Full calibration using set up II, table 3.1.

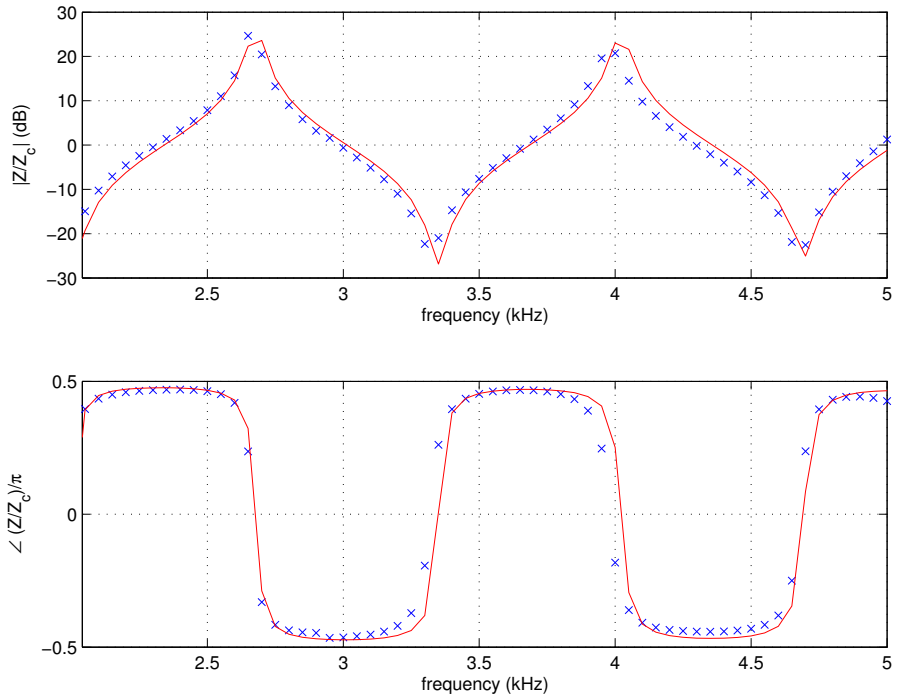

Figure 3.14: Full calibration using set up III, table 3.1.

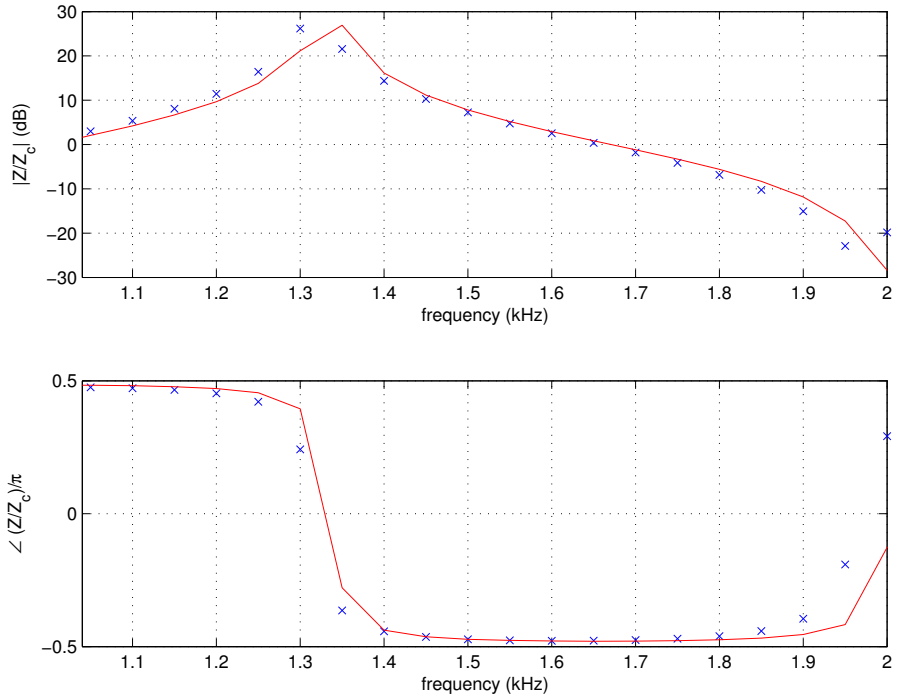

Figure 3.15: Full calibration using set up IV, table 3.1.

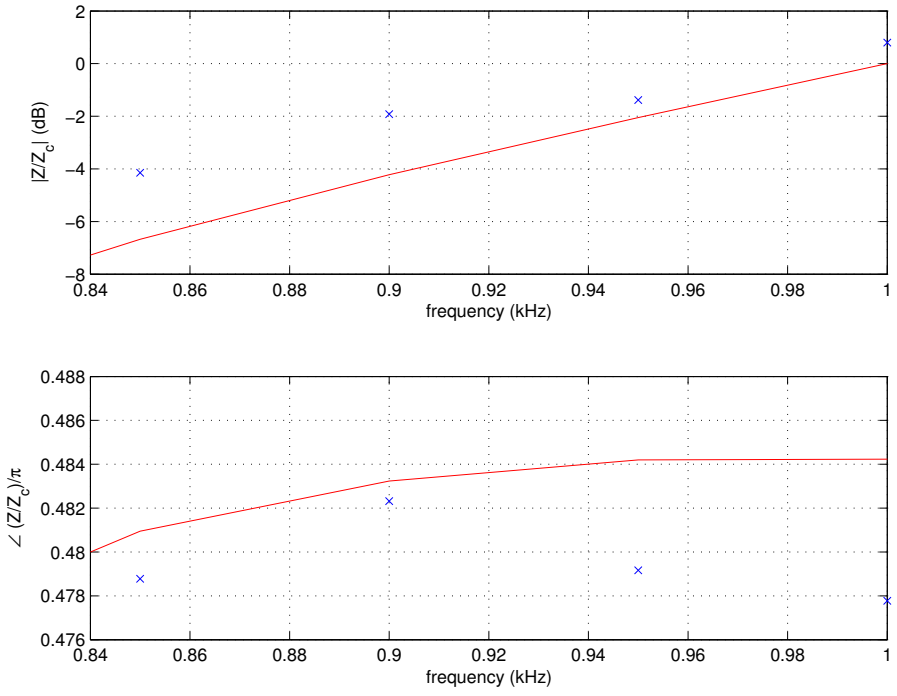

Figure 3.16: Partial calibration using set up V, table 3.2.

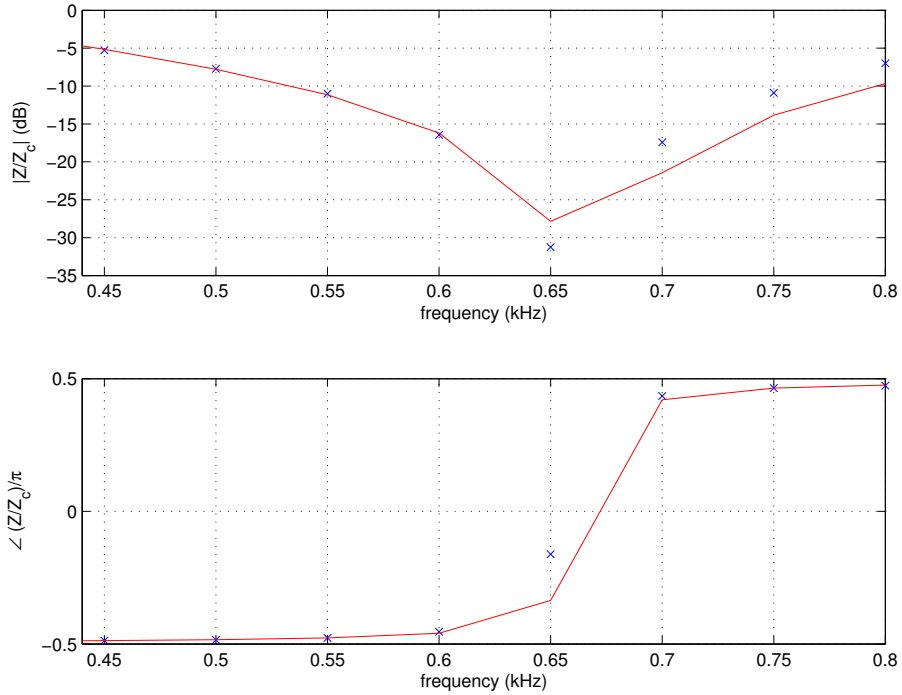

Figure 3.17: Partial calibration using set up VI, table 3.2.

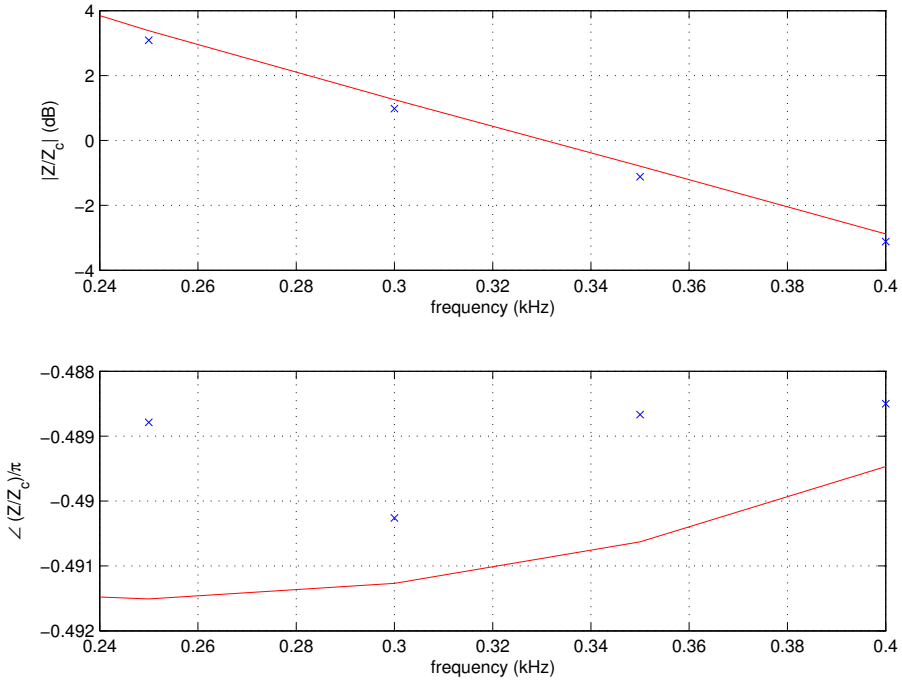

Figure 3.18: Partial calibration using set up VII, table 3.2.

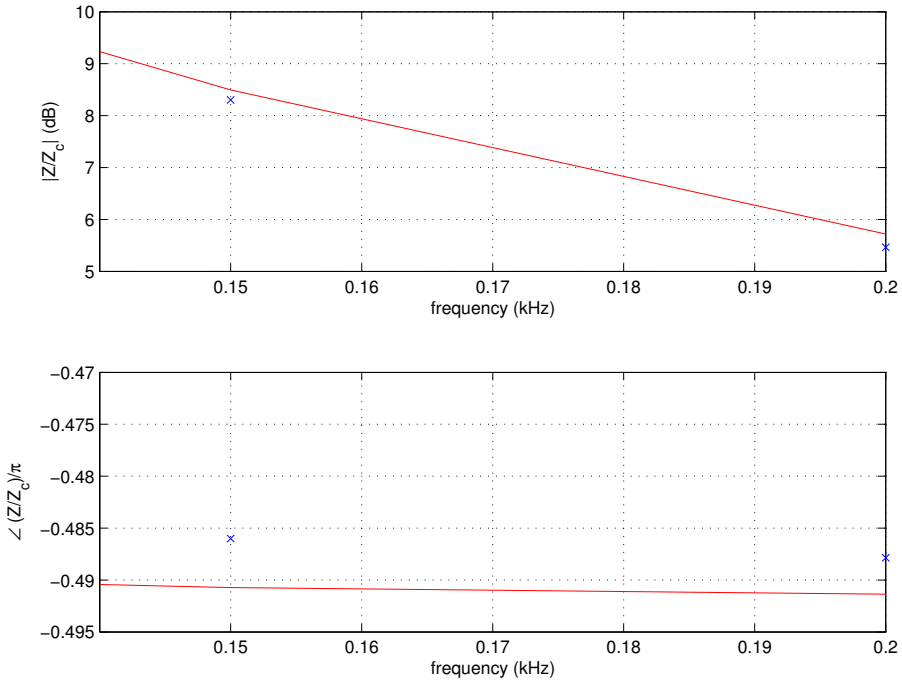

Figure 3.19: Partial calibration using set up VIII, table 3.2.

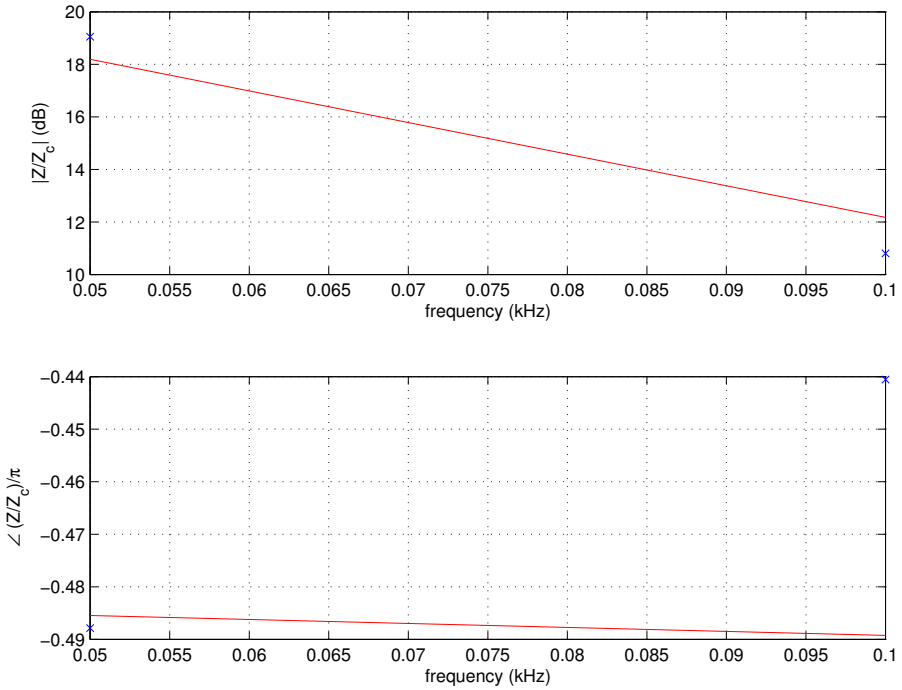

Figure 3.20: Partial calibration using set up IX, table 3.2.

3.7.2 The Closed Stepped Tube

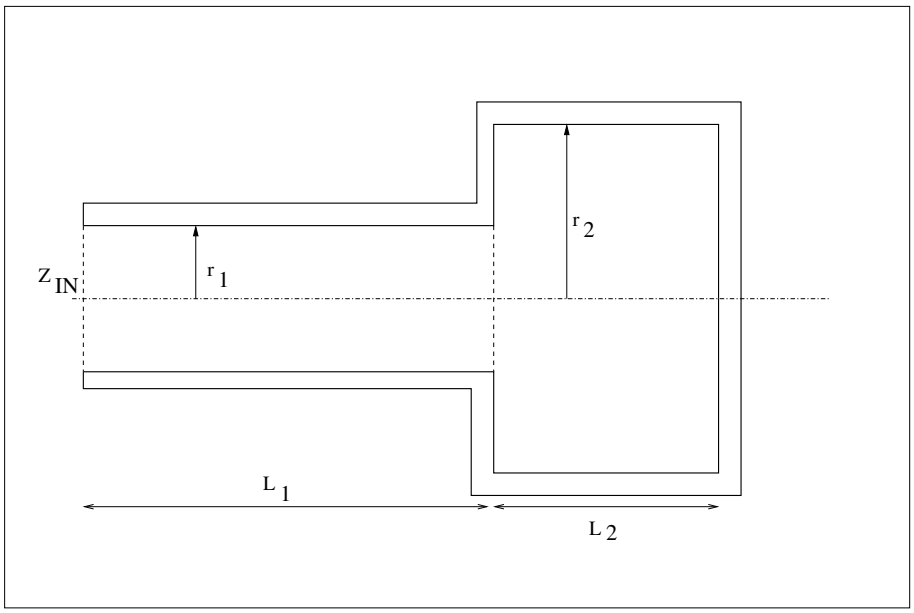

Figure 3.21: A closed stepped tube for which the impedance was measured using the TMFC system and compared to plane-wave theory.

Figure 3.21 shows the schematic for a closed stepped pipe with an initial radius of 4.9 mm and length 180 mm stepping up to a radius of 9.8 mm and length 64 mm.

The next step is to see if the system can accurately determine the impedance for an object with a change in cross section, which could potentially generate propagating higher modes, and this would make a difference between the experimental data and the plane-wave theory - which does not account for higher modes.

For the stepped tube the cut-on frequency for the first cylinder of radius 4.9 mm is 20.5 kHz. For the second cylinder, of double the radius, the cut-on frequency is half - 10.25 kHz. Higher modes will be excited at the step but should decay sufficiently fast so as to keep the propagation planar at the reference plane. Again, the first four figures correspond to the full calibration method and the last five figures correspond to the partial calibration method. As with the closed tube, there is good agreement between theory and experiment for the stepped tube above and below the cut-on frequency of 10.25 kHz for the second tube.

These results reassure us that we can obtain sensible impedance data over a large

frequency range. This also indicates that we should be able to obtain sensible bore profiles when we come to apply the reconstruction algorithm to TMFC data.

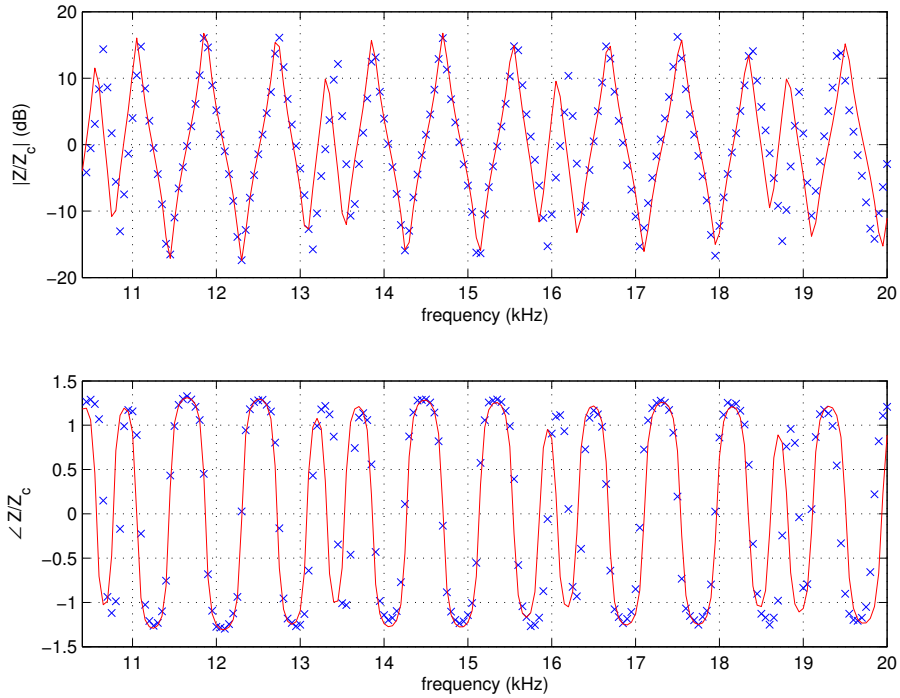

Figure 3.22: Full calibration using set up I, table 3.1.

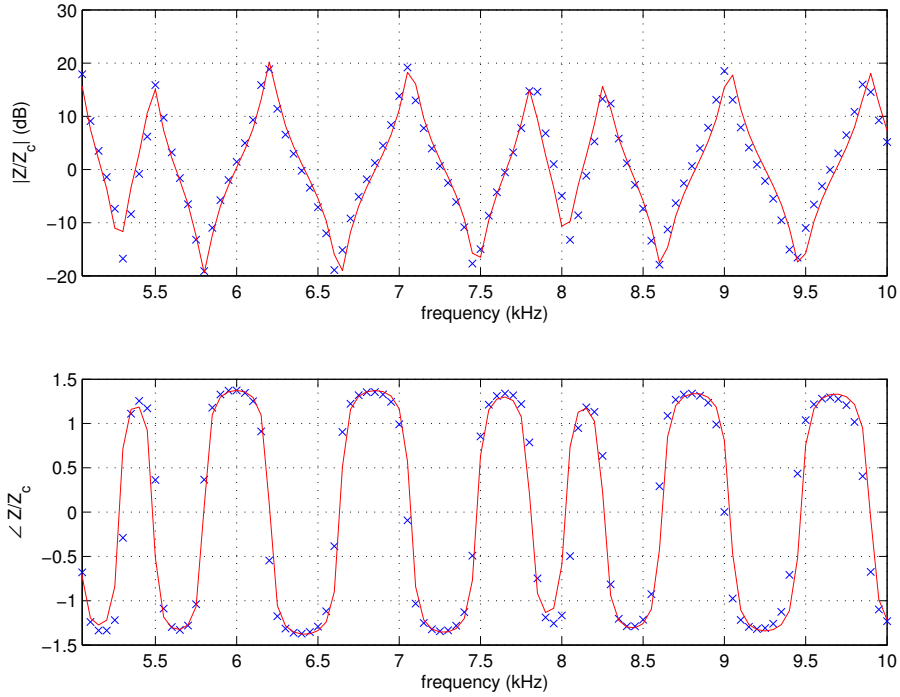

Figure 3.23: Full calibration using set up II, table 3.1.

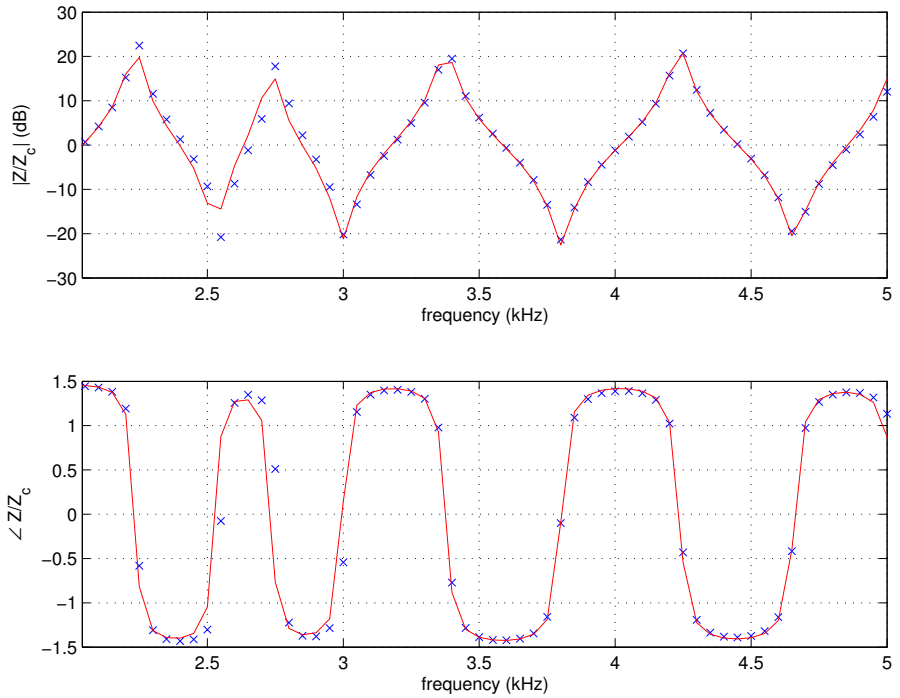

Figure 3.24: Full calibration using set up III, table 3.1.

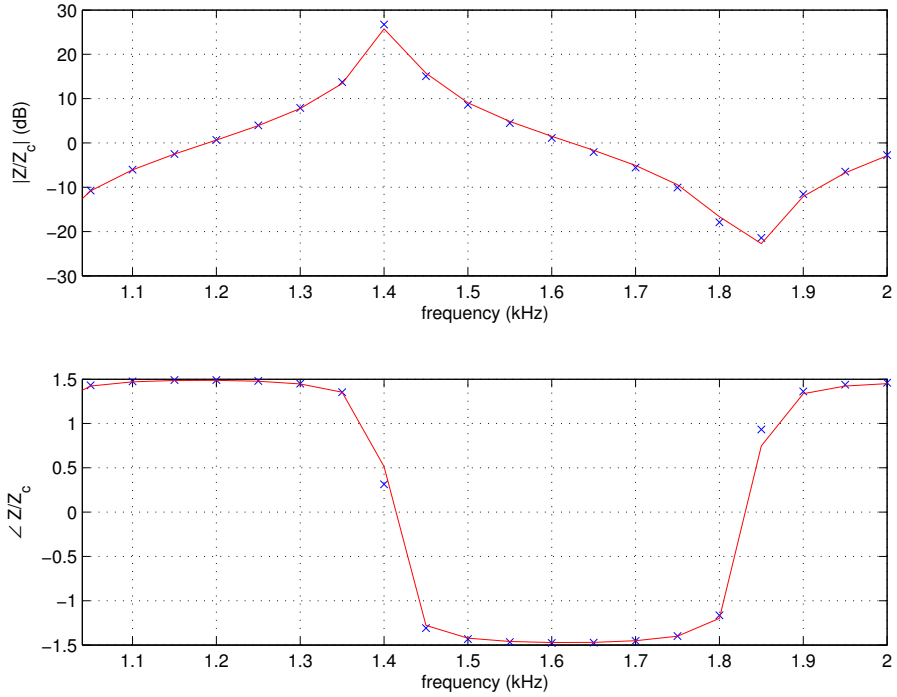

Figure 3.25: Full calibration using set up IV, table 3.1.

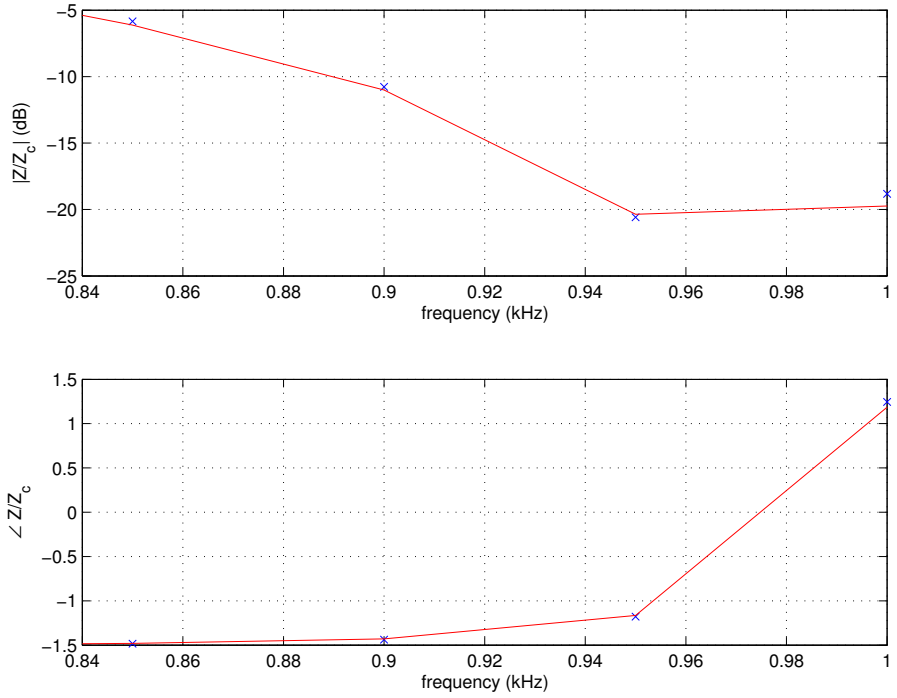

Figure 3.26: Partial calibration using set up V, table 3.2.

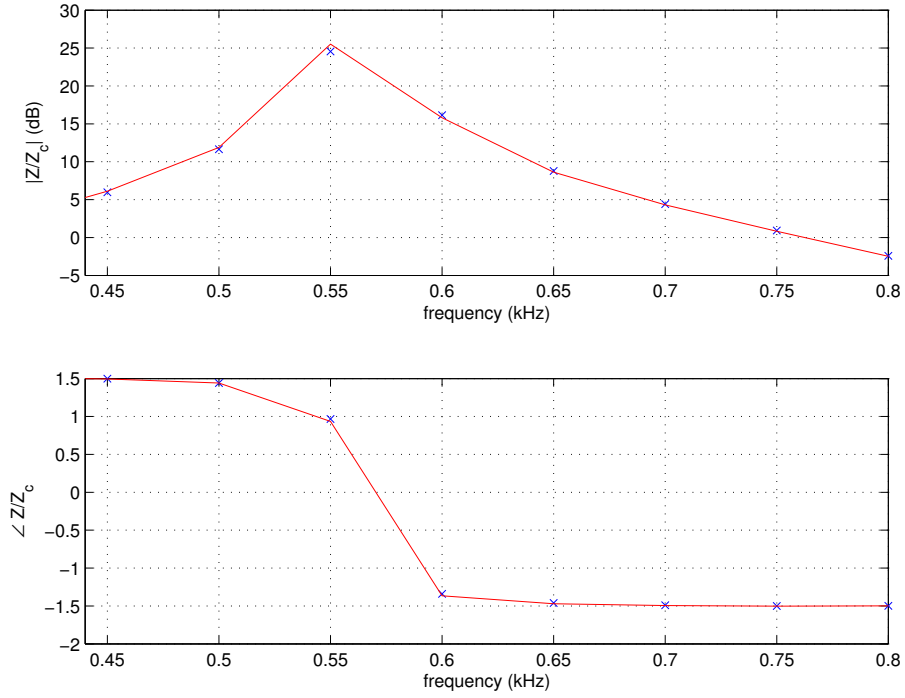

Figure 3.27: Partial calibration using set up VI, table 3.2.

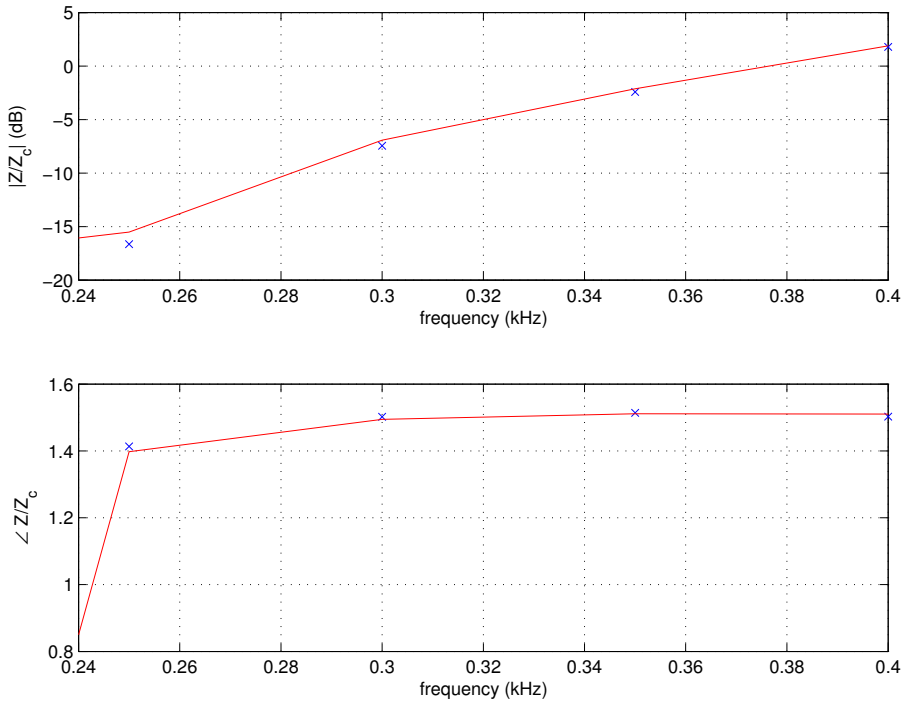

Figure 3.28: Partial calibration using set up VII, table 3.2.

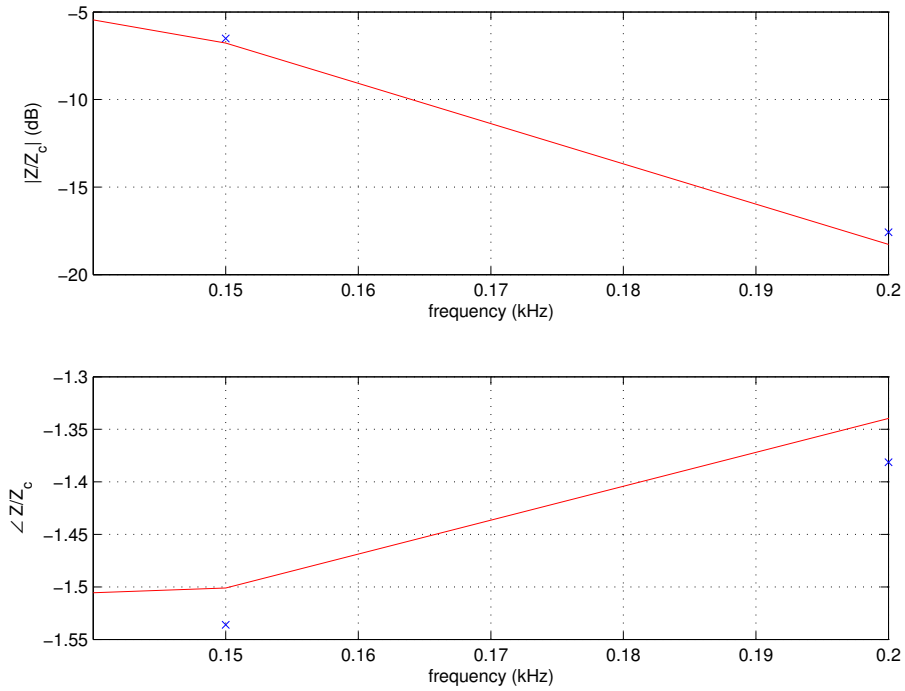

Figure 3.29: Partial calibration using set up VIII, table 3.2.

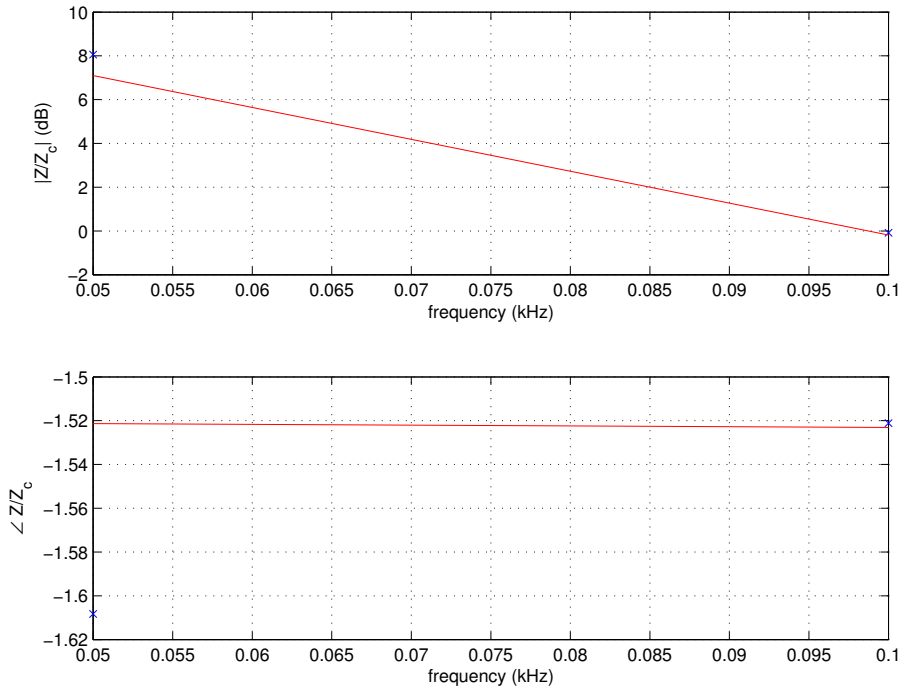

Figure 3.30: Partial calibration using set up IX, table 3.2.

3.8 Increasing the Frequency Range: Impedance Measurements Down to 10 Hz

The upper frequency for obtaining impedance data is limited by the cut-on frequency. The full calibration theory - in which experiment and theory are completely decoupled - says that the low frequency limit is governed by the microphone separation. However, at low frequencies - less than 1 kHz - we are using the partial calibration technique, not the full technique. We need to check the bandwidth over which accurate results can be obtained.

The magnitude and phase of the input impedance for a closed tube of length 1.408m over a frequency range of 10 Hz to 100 Hz using 10 Hz interval steps is shown in Figure 3.31. The microphone separation $d \approx 1$ m giving a first singular frequency of $f_s = c/2d \approx 170$ Hz. This in turn gives a suitable bandwidth of 50 Hz to 130 Hz. However, sensible results are still obtainable below 50 Hz, as far as 10 Hz. A good match between theory and experiment for the impedance magnitude is observed. A noticeable (but still acceptable) disagreement between theory and experiment for the phase is seen below 50 Hz. The effects of singularities can be seen more clearly in the reflection coefficient in Figure 3.32. A drastic disagreement between plane wave theory and experiment can be observed below 30 Hz due to the 0 Hz singularity.

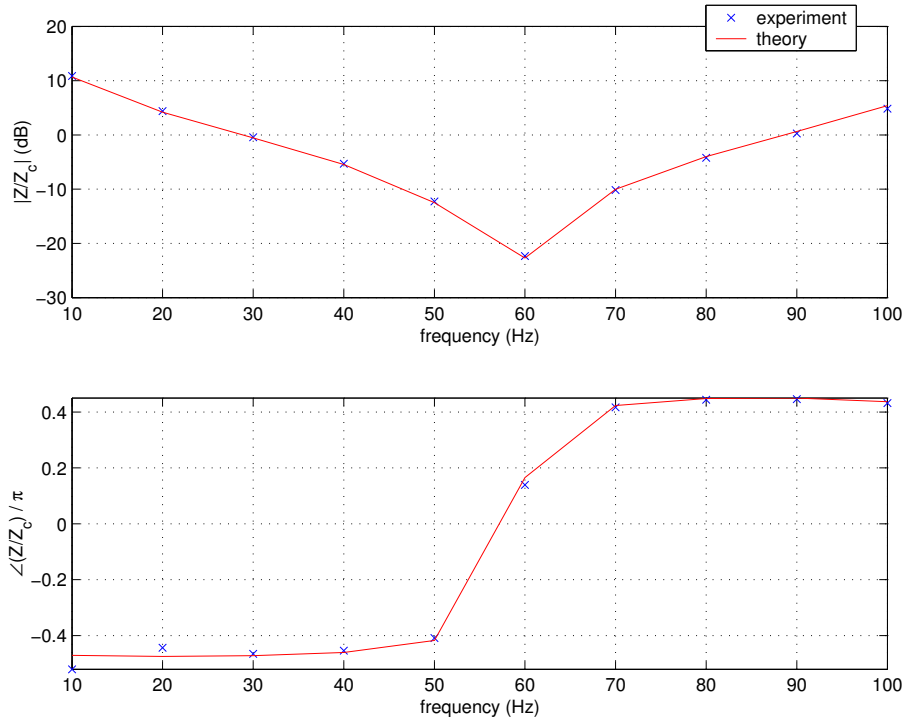

Figure 3.31: Magnitude and phase of the input impedance for a closed tube of length 1.408m over a frequency range of 10 Hz to 100 Hz using 10 Hz interval steps.

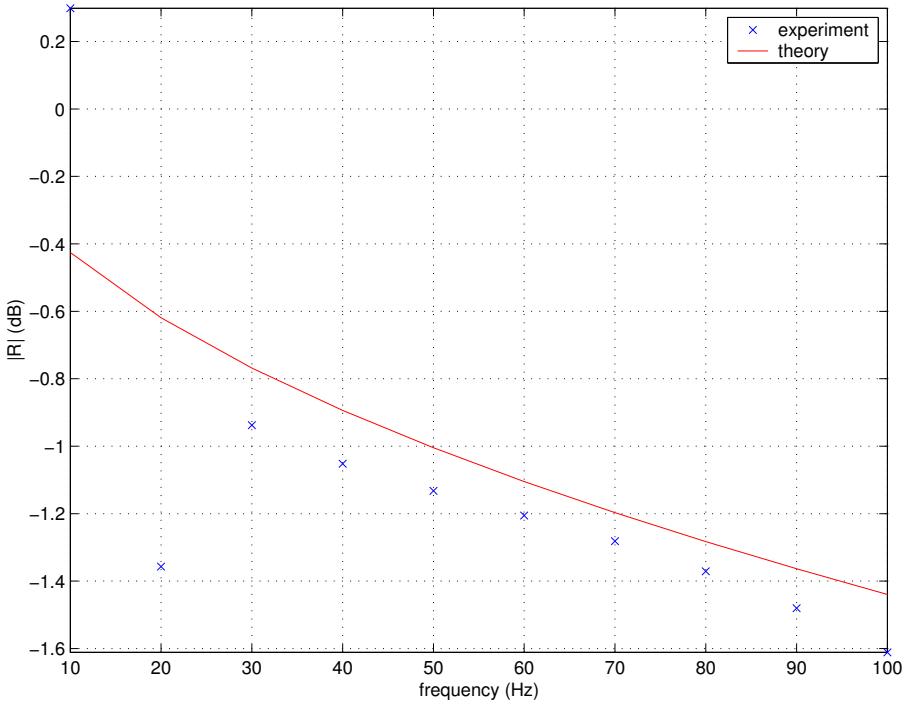

Figure 3.32: Reflection coefficient. A drastic disagreement between plane wave theory and experiment can be observed below 30 Hz due to the 0 Hz singularity.

3.9 Summary

It has been shown that an experimental expression for the input impedance of a cylindrically-symmetric study object can be obtained by measuring the pressure at two different points along the axial dimension of a cylindrical duct coupled to the study object. Calibration is achieved by measuring four calibration objects - closed tubes of differing length - of known impedance. This 'full' calibration procedure allows the determination of the three calibration coefficients $\mathcal{A}$, $\mathcal{B}$, and $\mathcal{C}$ purely in terms of microphone signal ratios, and so theory and experiment are completely separate, allowing a comparison between the two. This works well from 20 kHz down to 1 kHz. Below this frequency the microphone separation distance and length of calibration tubes become excessively large and impractical and so another method must be used. Below 1 kHz the calibration tubes are not used; $\mathcal{A}$, $\mathcal{B}$, and $\mathcal{C}$ are deduced by using a theoretical propagation constant, measuring the signal ratio for an anechoic termination, and then reversing the microphones and repeating the anechoic measurement. By strategic use of nine different microphone separations, singularities can be avoided, and a bandwidth of 50 Hz to 20 kHz can be achieved. It should be mentioned that the time taken to obtain a reconstruction is of the order of 5 hours since the relevant calibrations have to be carried out for each suitable bandwidth as well as measuring the study object. The system has been tested by measuring the impedance of two objects of known impedance: a closed tube and a closed stepped tube. A comparison with theory has been demonstrated. Good agreement has been observed.

In the next chapter we will use BIAS to obtain impedance data for the trumpet, after which we will return to the TMFC method.

Chapter 4

Impedance Measurement of Trumpets Using BIAS

This chapter is concerned with research on the Smith-Watkins trumpet. Expert trumpet players were invited to play a Smith-Watkins '464R-25' trumpet with: a 'symphonic' set-up consisting of a 1.5C mouthpiece and wide '36' Smith-Watkins leadpipe; and, a 'screamer' set-up consisting of a screamer mouthpiece and a narrow '12' Smith-Watkins leadpipe. Players found, as expected, that the two set-ups behaved in a similar manner - but with one noticeable exception: for the screamer set-up, there was a small, but definite 'slot' at approximately 2 kHz. This slot makes it easier to play a note. For the symphonic set-up there was no such observation. The purpose of this chapter is to use the Brass Instrument Analysis System (BIAS), which was outlined in Chapter two, to measure the impedance of the trumpet in different set-ups and either verify or contradict the results found by the players.

4.1 The Trumpet

Figure 4.1: A Smith-Watkins trumpet consisting of the main body, mouthpiece, and leadpipe. The mouthpiece fits into the leadpipe, which in turn, fits into the main bore of the instrument at the throat.

The modern trumpet is illustrated in Figure 4.1. The trumpet is a member of the brass family, which includes the trombone, French horn, tuba, euphonium, and baritone. The trumpet is highest in register relative to its family members. The main body is approximately cylindrical but flares out at the far end to form the radiating bell[101]. The cylindrical section is formed by a concatenation of tapers, which are small in length at the input end and become larger toward the bell end. The trumpet has three valves which, when depressed, deflect the airflow from their normal path through the main bore, into additional lengths of tubing. The extra length causes the pitch of the note to decrease. Depressing the first valve lowers the pitch by a tone, the second valve; a semitone, and the third valve; a minor third. The overall length of the trumpet is of the order of a metre but the instrument is shortest when no valves

are depressed and longest when all valves are depressed. The most common type of trumpet is built in the scale of B♭.

4.2 Mouthpiece and Leadpipe

The lips of the trumpet player rest against the rim of the mouthpiece. Behind this rim is a hemispherical volume (cup). The cup is connected to a conical section via a very small opening (the throat) which tapers out to the same diameter as that of the leadpipe, in which the mouthpiece sits. The leadpipe is located in the main bore of the trumpet at the input end. The leadpipe tapers out to match the main bore. The volume of the cup and the diameter of the throat are important parameters and have a significant effect on the impedance of the mouthpiece; the shape of the cup however, does not[86]. The impedance curve for a mouthpiece is generally a single, wide peak below 1 kHz; thus the mouthpiece has the effect of boosting the lower resonances of the trumpet.

Examples of mouthpieces and leadpipes are given in Figure 4.2 and Figure 4.3 respectively. The 1.5C mouthpiece is used with the 36 leadpipe to give - what is referred to by the manufacturers Smith-Watkins as - the symphonic set-up. The screamer mouthpiece and the 12 leadpipe give the screamer set-up. These set-ups are used in conjunction with a Smith-Watkins 464R-25 trumpet.

Figure 4.2: The screamer mouthpiece (left) used in the screamer set-up, and the 1.5C mouthpiece (right) used in the symphonic set-up.

Figure 4.3: The 12 leadpipe (top) used in the screamer set-up, and the 36 leadpipe (bottom) used in the symphonic set-up.

4.3 Results

4.3.1 Smith-Watkins 464 R-25 B♭ Trumpet

The BIAS was used to measure the trumpet in the symphonic and screamer set-up. Figure 4.4 shows the respective impedance curves where no valves were depressed during data acquisition. It can be seen that, indeed, there is a small impedance peak at about 2100 Hz. This is more easily observed in close-up around the 2 kHz region in Figure 4.5. It is also clear that above 2 kHz the impedance curve of the screamer set-up is approximately 50% higher than that of the the symphonic set-up.

The next logical question to ask is: Which component of the screamer set-up is causing the 2 kHz peak? Is it purely the mouthpiece, purely the leadpipe, or a combination of both?

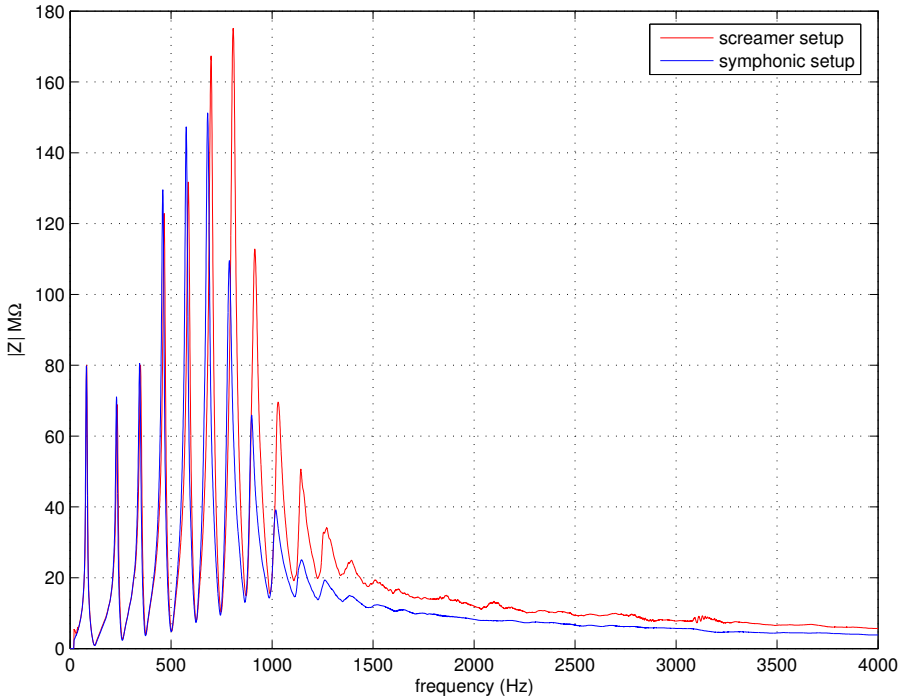

Figure 4.4: Impedance curves for the 'screamer' and 'symphonic' set-up.

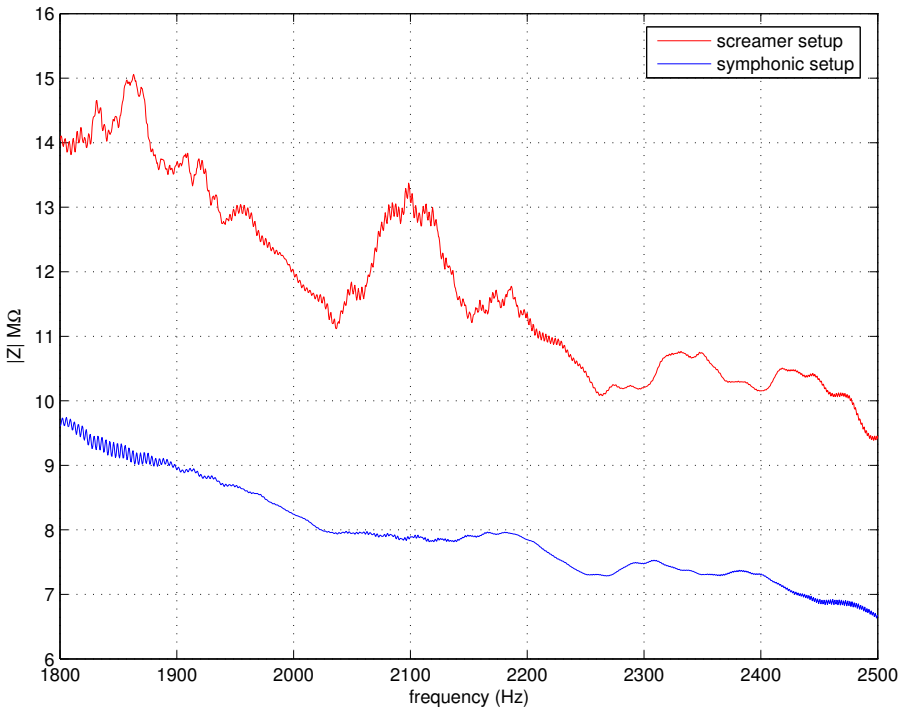

Figure 4.5: Close-up of the screamer and symphonic impedance curves at 2 kHz. A small but definite peak can be seen at 2,100 Hz.

4.3.2 Smith-Watkins 364-Trumpet

We wish to determine which component of the screamer set-up is causing the 2 kHz peak; is it purely the mouthpiece, purely the leadpipe, or a combination of both? To do this we have tried measuring the screamer mouthpiece with the 36 leadpipe (instead of the usual 12), and the symphonic mouthpiece with the 12 leadpipe (instead of the usual 36).

The other variable in the equation is, of course, the main body of the trumpet. For this reason we have repeated the BIAS tests on a different trumpet; a 364 trumpet, to see if the effect is still present.

All four possible combinations of mouthpiece and leadpipe are plotted in Figure 4.6: The screamer set-up (screamer mouthpiece and 12 leadpipe); the symphonic set-up (1.5C mouthpiece and 36 leadpipe); and the two possible cross-combinations (screamer mouthpiece and 36 leadpipe, and 1.5C mouthpiece and 12 leadpipe).

Consider first the screamer and symphonic set-ups (dark-blue, and green line respectively). We notice, as with the previous trumpet measurement, that the impedance above 2 kHz for the screamer set-up is approximately 50% higher than the impedance for the symphonic set-up. We also see some small peaks around the 2 kHz region in the close-up view in Figure 4.7. This indicates that the main body is not crucially responsible for observed differences and that it is due to either the mouthpieces and/or the leadpipes.

Observe the impedance curves in which the screamer mouthpiece is held constant and the leadpipe is varied (light-blue, and dark-blue line). We see that the two curves are almost identical; the tails of the impedance curves are the same in magnitude. This implies that the leadpipe has little or no effect on the magnitude of the impedance tail and is not responsible for the 50% difference. It is the screamer mouthpiece that is mostly, if not wholly, responsible for the difference.

This is further verified for the curves in which the 1.5C mouthpiece is held constant (red, and green line) and again, the leadpipes are varied; the two curves in this figure are almost indistinguishable.

Observe the two curves corresponding to the screamer mouthpiece in the close-up of the 2 kHz region in Figure 4.7. There is also a small impedance peak around 2

kHz, although it is not as convincing as the results for the 464R-25 trumpet. In this enhanced view, we see, as now expected, that using the 1.5C mouthpiece and changing the leadpipe has little or no effect on the flat impedance curve around 2 kHz. However, for the screamer mouthpiece the peaks around 2 kHz seem to be more pronounced when the 36 leadpipe is used, rather than the 12 leadpipe. This difference could possibly be explained due to lack of repeatability of the BIAS results. However, during test measurements the repeatability was found to be excellent, so this is unlikely.

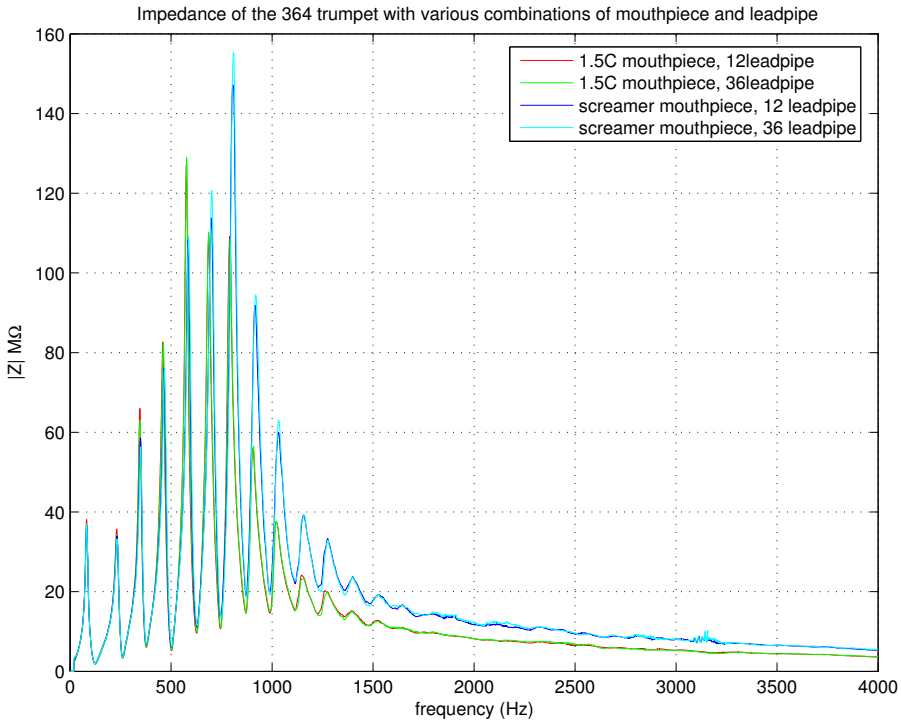

Figure 4.6: The four possible combinations of mouthpiece and leadpipe: the screamer set-up; the symphonic set-up; and the two cross-combinations.

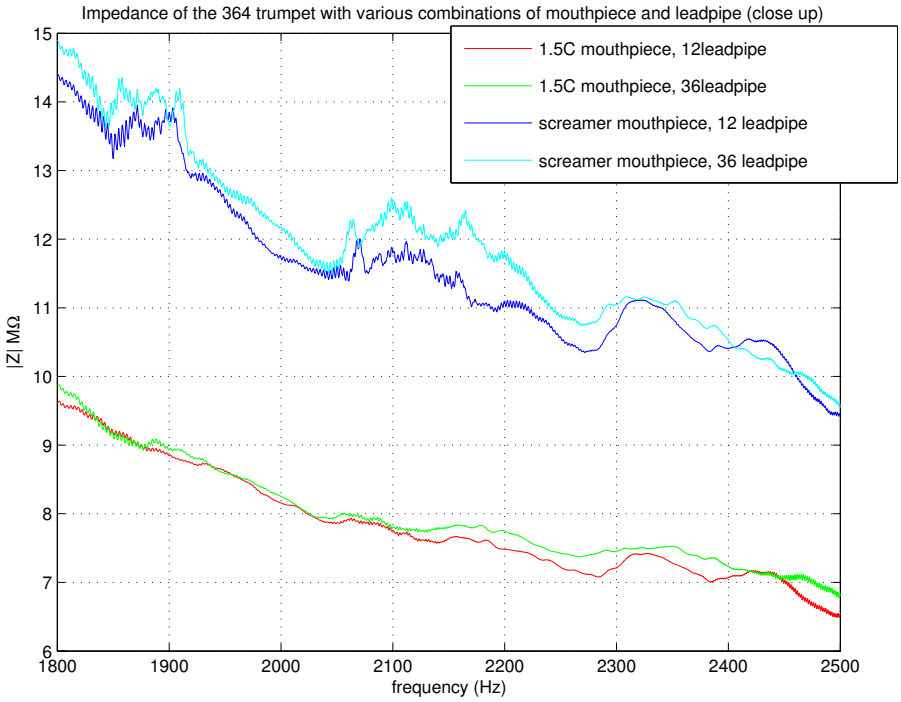

Figure 4.7: Four possible combinations of mouthpiece and leadpipe (close-up). A close-up around the 2 kHz region.

4.4 Summary

Playing tests indicated that there was a noticeable difference in the behaviour of the 464R-25 trumpet when the screamer - rather than symphonic - set-up was used; there was a small but noticeable slot at a frequency of 2 kHz where the note was relatively easy to play. This was verified by comparing the impedance curves of the two set-ups. The symphonic set-up had a relatively constant impedance around 2 kHz, whereas the screamer set-up revealed a small but definite impedance peak centred at 2100 Hz. It was also noticed that the tail of the impedance for the screamer set-up was about 50% higher than the tail for the symphonic set-up. This experiment was also conducted on a 364 trumpet to determine if the main body was an important factor in the production of the small impedance peak; and to deduce which component - screamer mouthpiece or 36 leadpipe - was important in producing the peak and the 50% difference. It was concluded that the main body is not responsible for the 50% difference or the 2 kHz peak; the screamer mouthpiece was mostly, if not wholly, responsible for the 50% difference and probably wholly responsible for the 2 kHz peak. This information was, however, only determined for the 364 trumpet. Future work would include repeating this analysis on the 464R-25 trumpet.

Chapter 5

Bore Reconstruction via the TMFC Method

In this chapter we will look at the impedance results obtained using the TMFC system, combining data obtained via the full and partial calibration techniques into a full spectrum of data over a bandwidth large enough to generate a suitable reconstruction. The resulting input impulse responses and bore reconstructions are then presented and discussed.

Possibilities for pushing the low frequency limits in the partial calibration regime closer to the 0 Hz singularity are shown.

A post-processing method for removing the effect of the coupler - necessary to ensure plane wave propagation at the reference plane - from the measured data is discussed. This is achieved by representing the impedance at selected points along the instrument as a 2×2 matrix. The impedance corresponding to the coupler can be removed by multiplying the experimentally measured impedance by the inverse of the matrix representing the coupler. This is referred to as transmission matrix theory.

Theoretical reconstructions in which plane-wave theory (which is a continuous function) is discretised and used as input for the reconstruction algorithm are given for comparison with the experimental findings. A comparison between the impedance determined by TMFC, plane-wave theory, and BIAS is then given.

An adaptor has been designed to accommodate instrument mouthpieces so that full instruments can be measured. An example measurement of a Dennis Wick 6BS

mouthpiece is given for illustration.

Finally an attempt is made to use the TMFC method to answer a physical question involving French horn crooks. An F-crook from the set is perceived to play poorly, and we wish to know why. To do this a bore reconstruction is obtained for the crook and compared with the profile of a quality F-crook. The crooks are also measured using pulse reflectometry for comparison.

5.1 Bore Reconstruction of a Closed Pipe

We will now calculate the bore reconstruction of a closed cylindrical tube - of length L and radius equal to that of the measurement duct - for which impedance result examples were given in the previous chapter[102, 103]. There are a total of fifteen impedance maxima below the cut-on frequency for the 128 mm tube. In an ideal case, these maxima are observed when an integer number, n, of half wavelengths fit inside the tube

$$f = \frac{nc}{2L}, \qquad n = 1, 2, 3, ... \tag{5.1}$$

There are also fifteen impedance minima frequencies. These occur when an odd integer number, m, of quarter wavelengths fit inside the tube

$$f = \frac{mc}{4L}, \qquad m = 1, 3, 5, ... \tag{5.2}$$

5.1.1 Impedance Results

When the magnitude of the input impedance is at a peak, this corresponds to a resonance. Note that the phase of the impedance is zero at these points i.e. p and U are in phase. The gradient of the phase is also negative. When the magnitude of the impedance is at a minimum this corresponds to anti-resonance. The phase of the impedance is also zero at antiresonance but the gradient is now positive. When the magnitude of the impedance is equal to that of the characteristic impedance, p and U are 180 degrees out of phase as observed in Figure 5.1. The extrema are not very sharp since the tubes used are very narrow and so the wall losses are very large. A much wider tube would reduce these losses and sharpen the peaks but, as mentioned before, this would reduce the cut-on frequency and leave us with a smaller possible frequency range to obtain plane-wave data.

The errors are difficult to observe from inspection of the impedance. To make the errors more obvious, the magnitude of the reflection coefficient, $R(\omega)$, defined in Chapter 2 equation (2.54), has been compared with the theoretical expression which, for a closed tube, is an exponentially decreasing function of frequency. Near points of

impedance maxima or minima the gradient of the curve is large. This means that any small discrepancies between theory and experiment caused by misalignment (say due to temperature or tube length inaccuracies) will cause the experimental reflection function to differ greatly from theory. Since the extrema occur at evenly spaced intervals, the discrepancies appear as small oscillations in the experimental reflection function.

Figure 5.1 shows the entire data collected for the magnitude and phase of the input impedance of the closed tube using the TMFC system. Results obtained via the full calibration (20 kHz down to 1 kHz) and partial calibration (1 kHz down to 50 Hz) techniques have been combined. The frequency range is 50 to 20,000 Hz with 50 Hz intervals between data points (blue crosses). The plane wave theoretical impedance prediction is represented by the continuous red line. We can see that there is good agreement between theory and experiment across the whole range. Figure 5.2 shows the real and imaginary parts of the impedance and Figure 5.3 shows the reflection coefficient calculated by transforming the impedance data using equation (2.56).

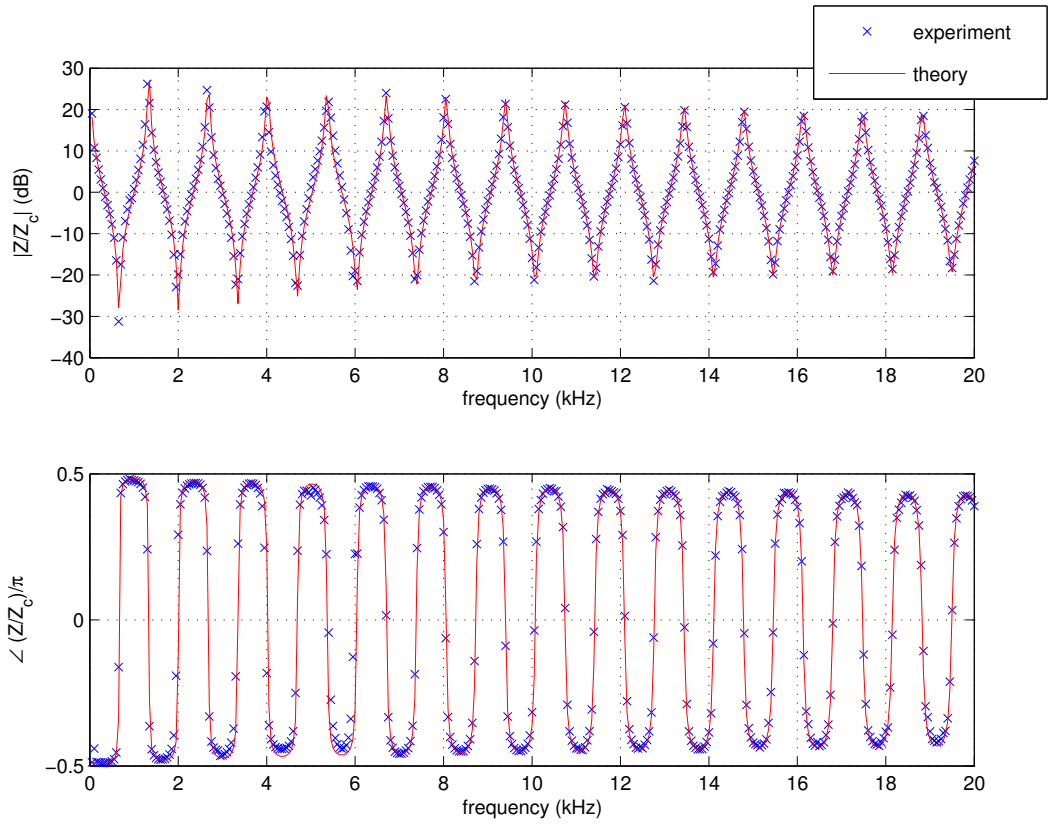

Figure 5.1: Full bandwidth impedance data for the closed tube.

5.1.2 Results: Input Impulse Response and Bore Reconstruction

The tube is closed so for the input impulse response we expect a large positive reflection to occur at a time $2L/c$ giving a value of approximately 0.8 ms. The impulse response - as described in Chapter 2, equation (2.122) - is calculated by inverse Fourier transforming the reflection function and taking the real part. This is shown in Figure 5.4 and more closely in Figure 5.5. The lowest frequency measured determines the length (in time) of the IIR signal; one is simply the reciprocal of the other. For 50 Hz the signal length, T_{IIR}, is 20 ms. This corresponds to a maximum reconstruction length of 3.45 m ($cT_{\mathrm{IIR}}/2$).

The result for the bore profile is shown in Figure 5.6. This has been obtained by applying the layer peeling algorithm - again outlined in Chapter 2, equation (2.124) - to the impulse response of Figure 5.4. Note that the starting radius must be defined in the reconstruction algorithm; this is just the radius of the measurement duct. Zero on the x-axis represents the position of the reference plane. Rather than remaining constant at 4.9 mm the reconstruction gradually expands as far as 6.4 mm - an increase of 30%. The point at which the profile drops to zero is accurately found as 128 mm, although it does not drop infinitely steeply - the drop is spread over approximately 4 mm, and it does not drop completely to zero but to 0.75 mm. After this initial drop the profile starts to increase again. We expect the profile to increase just before a large change in the profile - this is just the Gibbs' phenomenon. However, in this example the profile increases not only in the vicinity of the step but at all points where the profile should be continuous. This implies that it is not just the Gibbs' phenomenon that is causing the effect. To discover what is causing this problem consider the following argument. For a closed tube there should be only one reflection in the IIR. Sufficiently far after the peak we expect the IIR curve to drop to zero. However, it is found that rather than go to zero there is a constant small negative value i.e. the IIR is not centred on the $y = 0$ axis. Since a negative value for the IIR represents an expansion this explains the constant expansion on the x-axis. To remedy this, the small offset was calculated by taking the average value of the IIR after the main relection and subtracting it from each data point in an attempt to centre the IIR properly. The resulting reconstruction is given in Figure 5.7. The reconstruction now remains fairly constant at the correct radius up

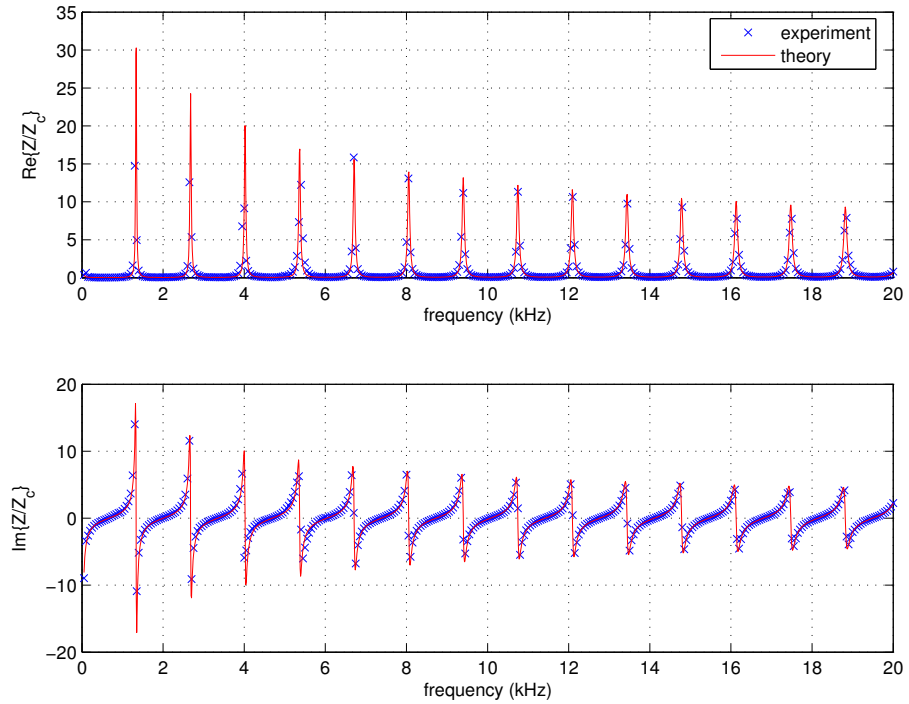

Figure 5.2: Real and imaginary part of the impedance for the closed tube.

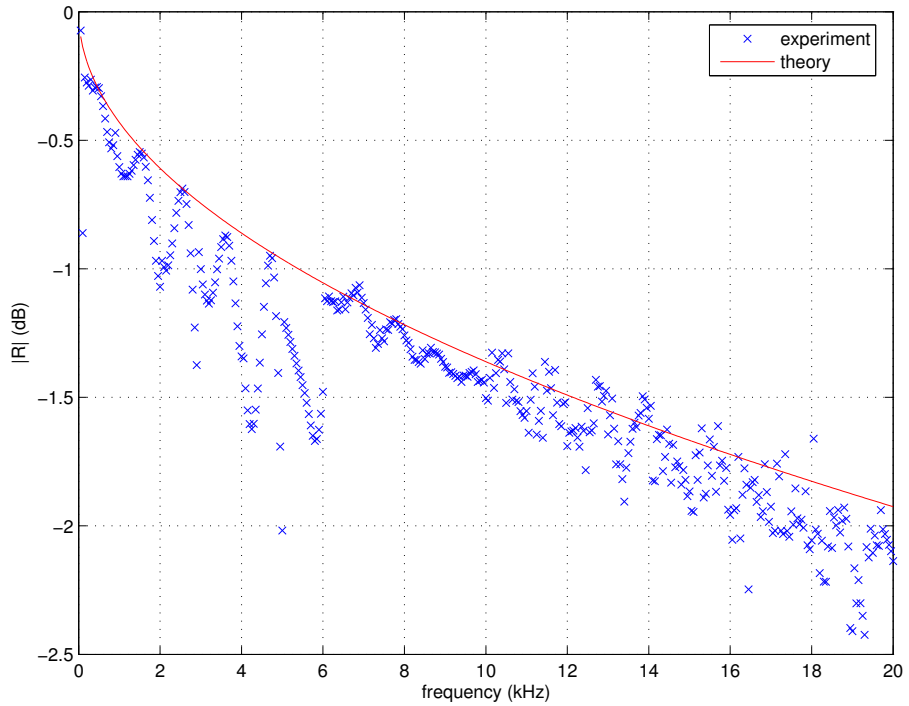

Figure 5.3: Reflection coefficient in dB for the closed tube.

to approximately 128 mm. There is still the small Gibbs' increase in the reconstructed radius just before the closed end giving a radius of 5.9 mm - an overprediction of 20% compared with the original 30%. The drop at the closed end is still spread over 4 mm but now it drops further to 0.63 mm comared with 0.75 mm. After this point the reconstruction remains fairly constant, rather than expanding, so it appears that the the effect indeed was due to the dc-level and has been adequately removed.

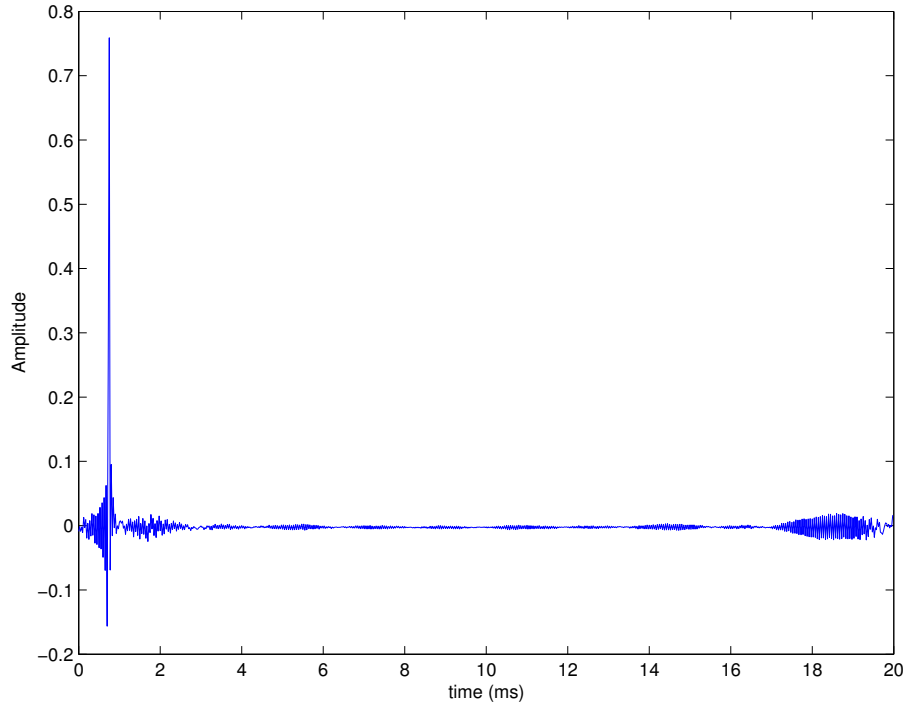

Figure 5.4: Input impulse response. For a closed tube this is simply a single peak due to the reflection at the closed end.

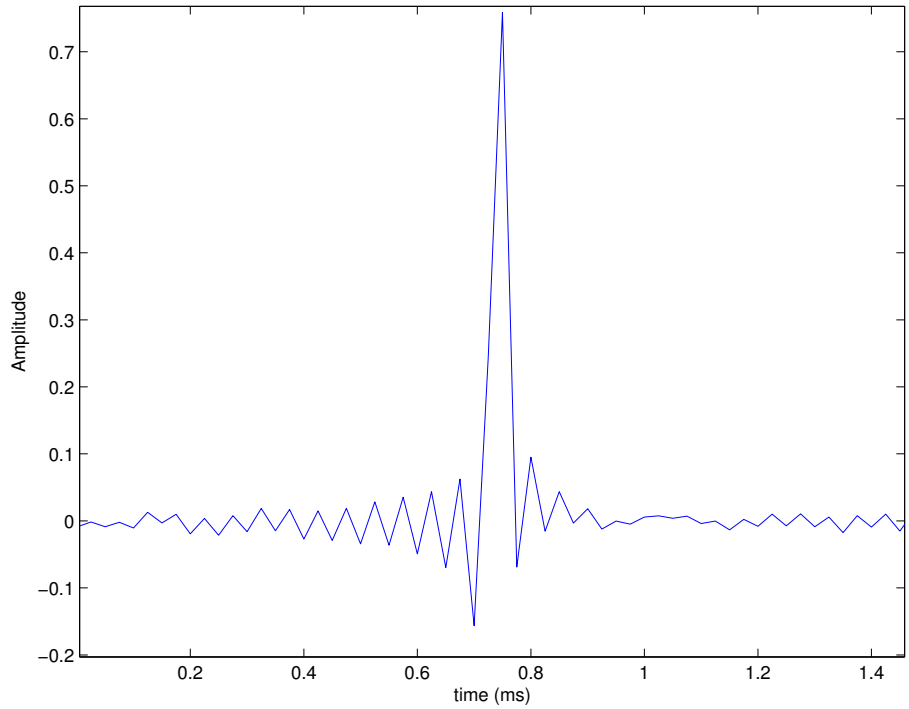

Figure 5.5: Close-up of the main peak in Figure 2.122. This peak occurs at a time $t = 2L/c$ which is roughly equal to 0.8 ms.

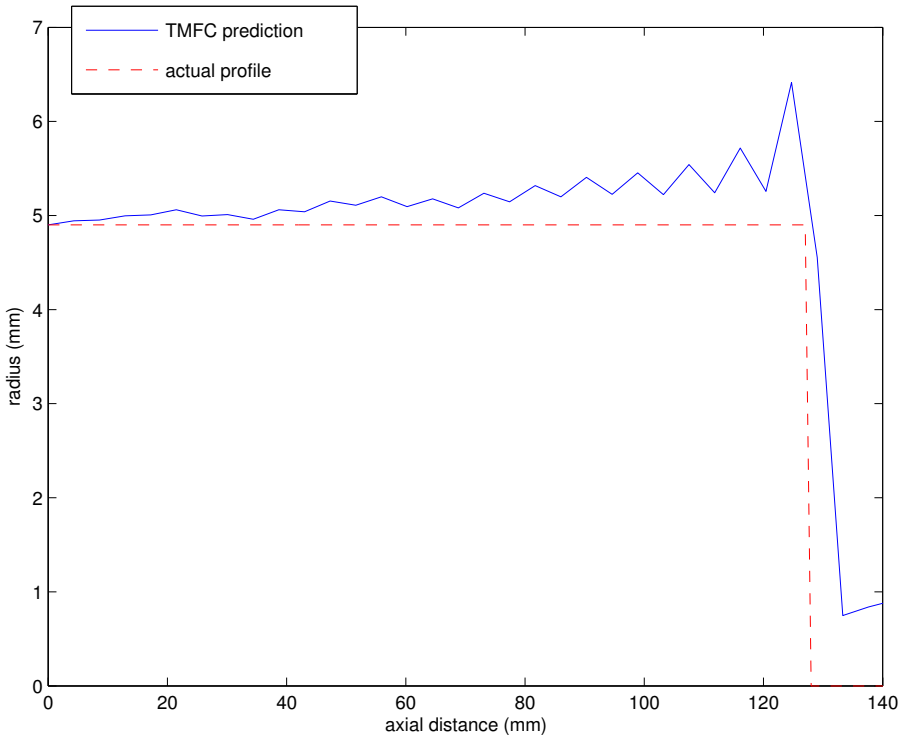

Figure 5.6: Bore reconstruction of the closed tube (dc offset present).

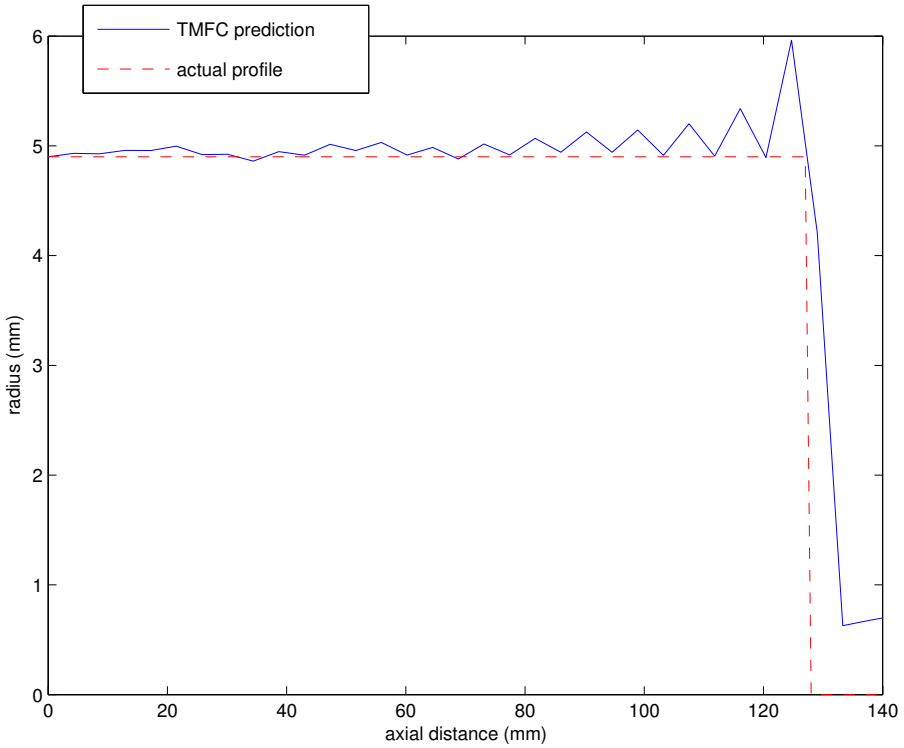

Figure 5.7: Bore reconstruction of the closed tube with the adjusted dc level.

5.1.3 Theoretical Bore Reconstruction

It is not surprising that there is an error in the dc value of the impulse response since the TMFC method never measures at 0 Hz. However, it could also be a problem of experimental nature - for example, the microphones generating a small amount of electrical noise. To investigate this last point further we can try a bore reconstruction using purely theoretical plane-wave data, removing the element of uncertainty caused by electrical noise etc.

The theoretical impedance for the tube has been discretised in the same manner as the experimental data and then inverse Fourier transformed to obtain the impulse response given in Figure 5.8. We see that the theoretical IIR has a much cleaner peak than the IIR derived from experiment. The reconstruction algorithm is then applied to this impulse response. So the theoretical reconstruction is the result we would get if there was perfect agreement between theory and experiment. This is given in Figure 5.10. The dc corrected experimental reconstruction is given by the blue line. The reconstruction generated by theory with no dc correction is given by the green line. If the offset was caused by electrical noise we would expect the theoretical profile to be better than the experimental. This is not the case. This implies the source of the dc-offset is not noise but related to the way the software has been implemented, possibly due to the harsh frequency resolution of 50 Hz.

To illustrate how the small discrepancies between theory and experimental impedance affects the reconstruction obtained, Figure 5.11 shows the theoretical profile with the dc value adjusted. We can see that the theoretical profile is now very similar to the experimental result, as we would expect since the agreement between the impedance curves was very good. However, we notice two main points. Firstly, the overshoot at the closed end is smaller - 5.3 mm compared with 5.9 mm. Just after the closed end the theoretical profile drops to 0.228 mm compared with 0.63 mm. After this initial drop the theoretical profile continues to drop towards zero whereas the experimental reconstruction remains constant.

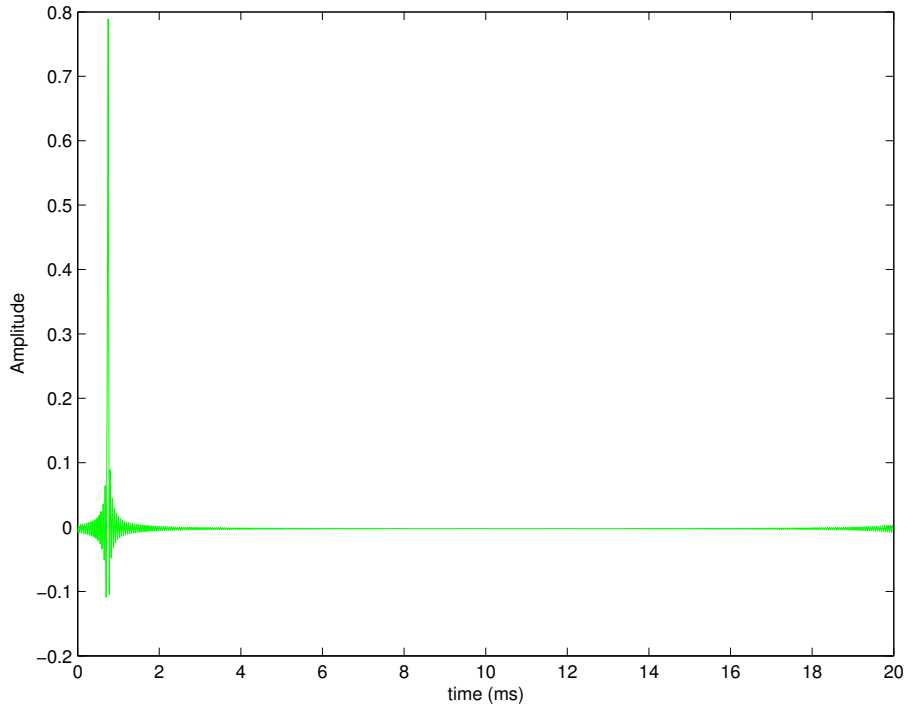

Figure 5.8: IIR for the closed tube using theoretical impedance data. The result is a clean peak at the expected value of 0.8 ms.

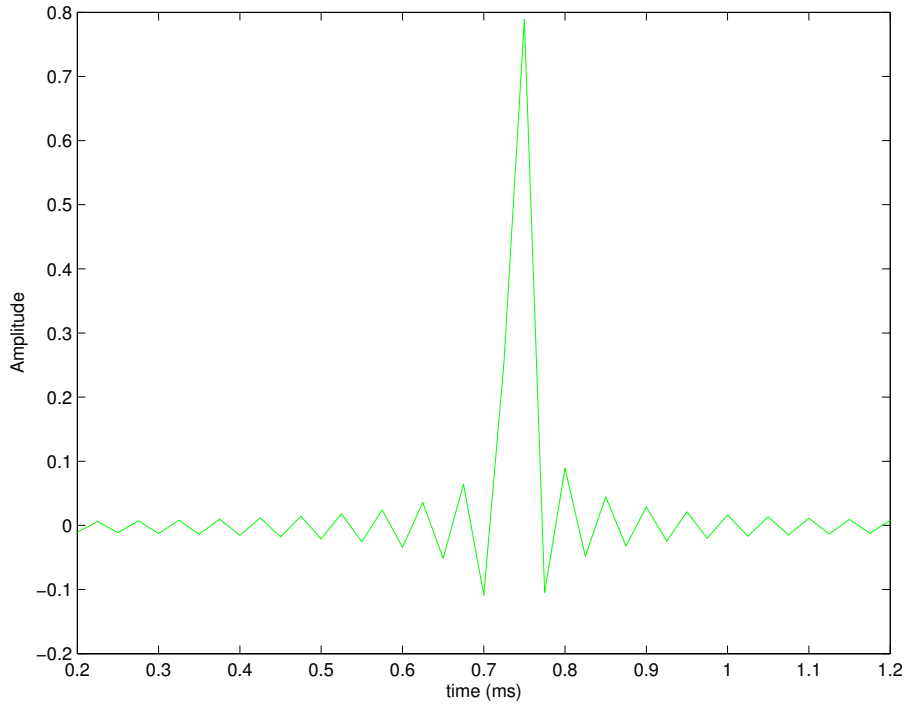

Figure 5.9: Close up of the single reflection from the closed end.

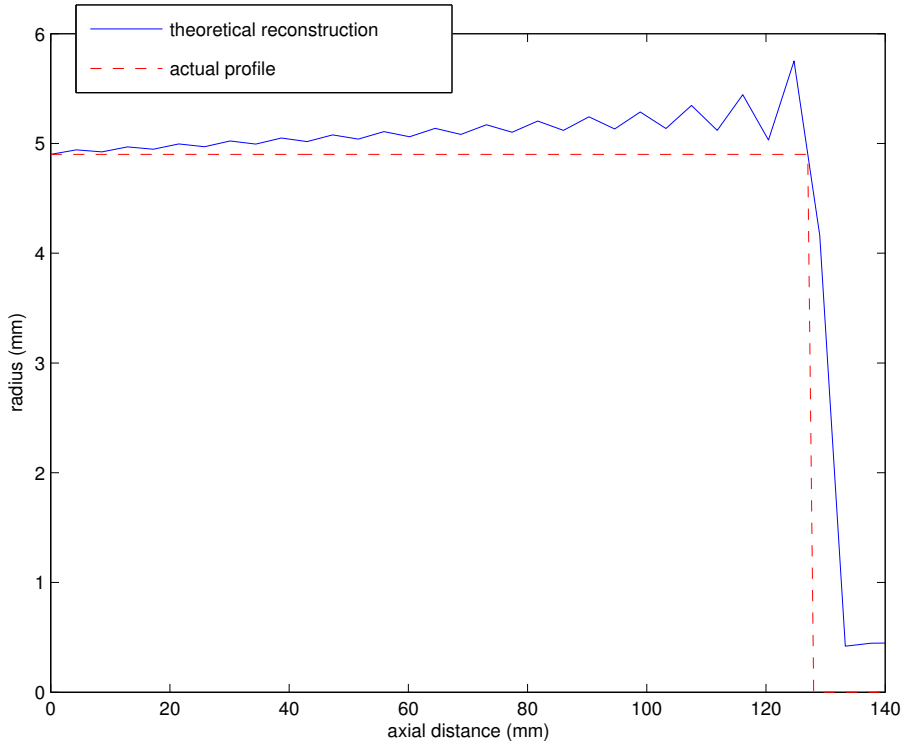

Figure 5.10: Reconstruction generated using plane-wave theory *with no dc adjustment.*

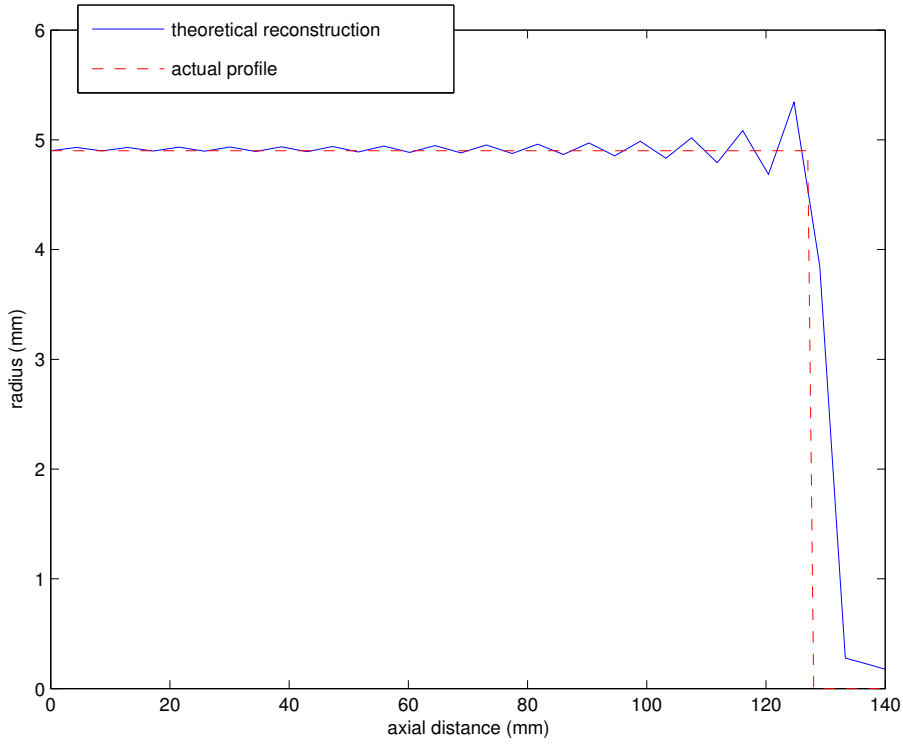

Figure 5.11: Theoretical reconstruction *with dc adjustment.*

5.1.4 Post-Processing Method: Transmission Matrix Theory

In the frequency-domain we can use what is known as transmission matrix theory. The impedance of the cylindrical coupler is represented by a 2×2 matrix, $\mathbf{H}$ - the coupler matrix . To calculate the impedance of the 80 mm tube alone, we multiply the inverse of the coupler matrix with the impedance of the 80 mm tube plus coupler (written in matrix form) for each frequency

$$Z_{\mathrm{IN}}^{\mathrm{new}} = \mathbf{H}_1^{-1} \begin{pmatrix} Z_{\mathrm{IN}} \\ 1 \end{pmatrix} \tag{5.3}$$

where $Z_{\mathrm{IN}}^{\mathrm{new}}$ is another 2×1 matrix and represents the impedance of the 80 mm tube, and Z_{IN} is the impedance of the 80 mm tube plus the coupler. The derivation of this formula is given in the appendices.

Figure 5.12 shows the TMT method applied to the impedance data for the 128 mm closed tube. In the previous section we subtracted a length of 48 mm from the tube by clipping the IIR. The TMT shows a much cleaner impedance curve which agrees exactly with theory. However, in the IIR method theory and experiment can be completely de-coupled whereas using TMT involves modelling the propagation constant.

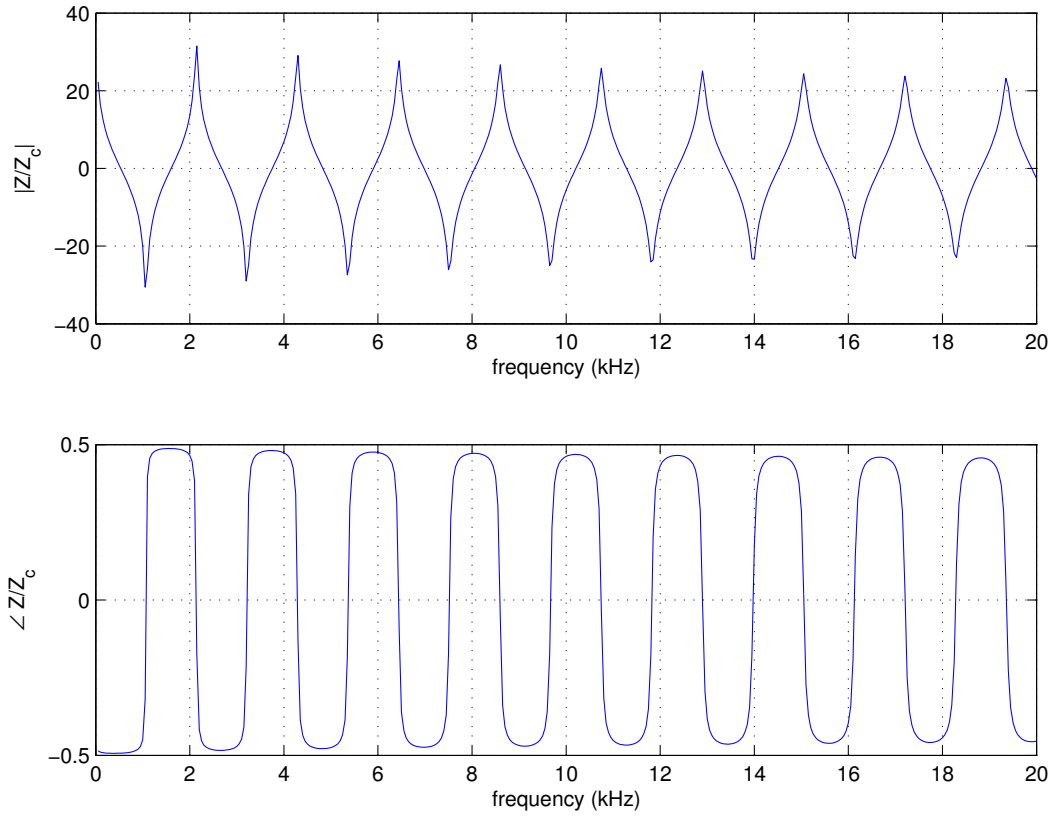

Figure 5.12: Impedance of 80 mm tube as calculated from full impedance using transmission matrix theory (TMT).

5.1.5 TMFC and BIAS Comparison

In Figure 5.13 we have the TMFC results for the closed tube compared with those obtained by the BIAS. The BIAS measures at a very high resolution - 0.5 Hz - and so a solid line is used for representation. The impedance magnitude is plotted in units of Megohms[1]. We see the agreement is good, but not perfect - between 3.5 kHz and 4 kHz BIAS consistently predicts a lower impedance than TMFC, and at approximately 1.3 kHz TMFC predicts a much higher value for the impedance maximum (a 20 MΩ difference). Figure 5.14 now shows the TMFC data compared with plane-wave theory. We see that the agreement is almost perfect. So although BIAS has the advantage of a much higher resolution it does not agree as well with theory as does the TMFC system.

[1] where $\Omega \equiv \mathrm{Pa} \cdot \mathrm{s/m}^3$

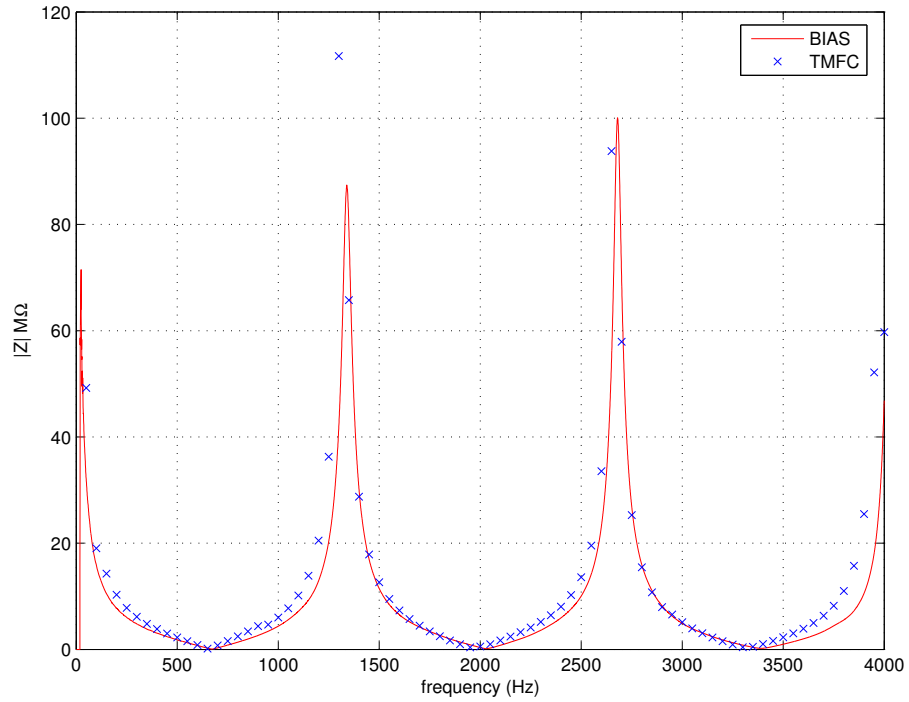

Figure 5.13: Comparison between TMFC and BIAS result for the 128 mm closed tube. We see that the agreement is quite good but not perfect.

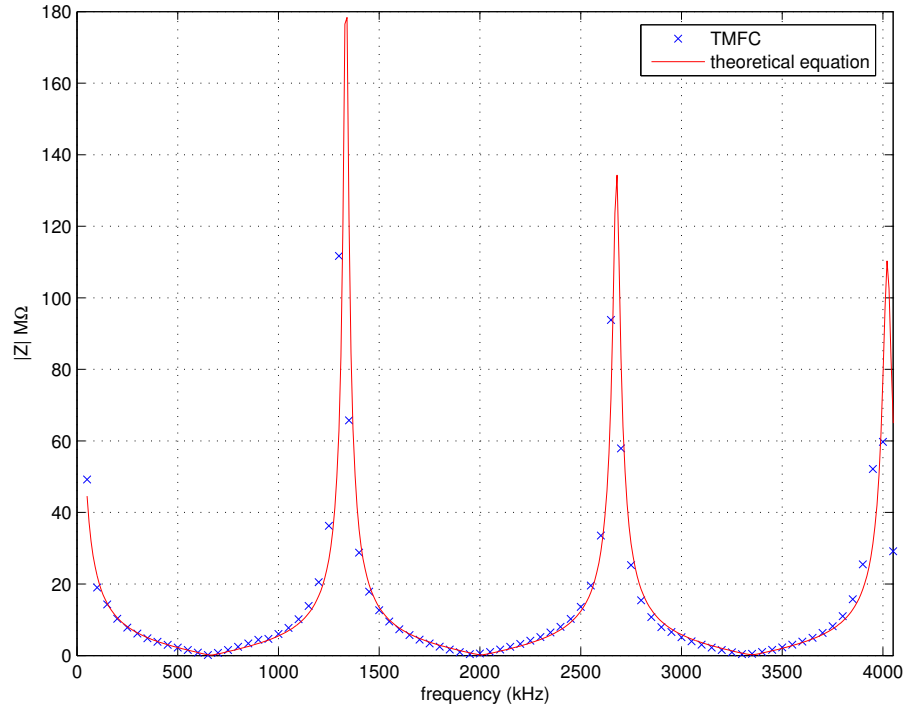

Figure 5.14: TMFC and plane-wave theory comparison. We see from inspection of both graphs that the agreement is better between theory and the TMFC results than between theory and the BIAS.

5.2 Bore Reconstruction for the Closed Stepped Tube

In this section we calculate the bore profile for the closed stepped tube which was described in the previous chapter. As discussed, the small sample of impedance results looked accurate for the stepped tube hinting that the TMFC method can reconstruct a change of radius without too many problems from higher modes. But how will the Gibbs' phenomenon affect it?

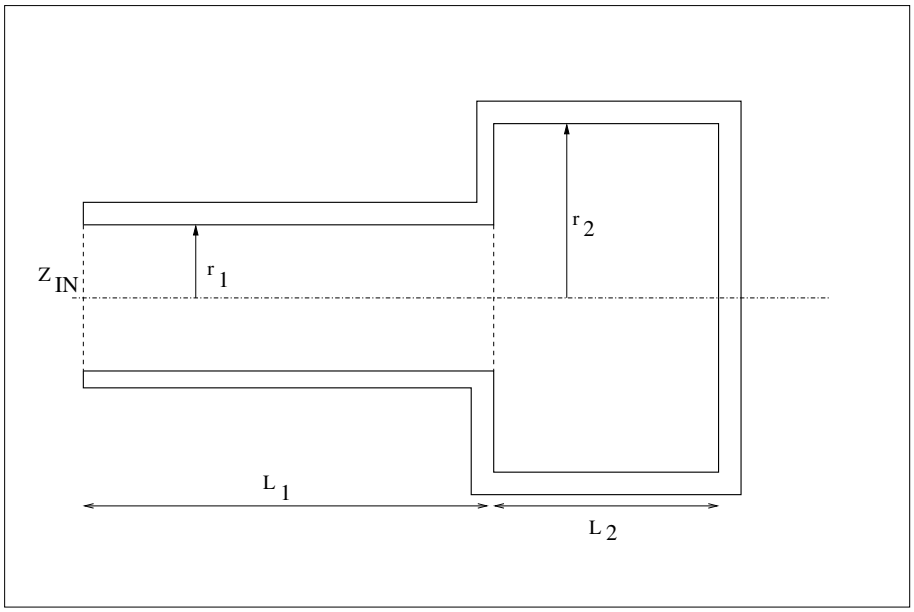

Figure 5.15: Schematic diagram of the closed stepped tube. The first cylinder has a radius $r_1 = 4.9$ mm and length $L_1 = 180$ mm. The second cylinder has a radius $r_2 = 9.8$ mm, a length $L_2 = 64$ mm and is stopped at the far end.

5.2.1 Impedance Results

Again, we see in Figure 5.16, very good agreement between plane-wave theory and experiment in both the magnitude and phase of the impedance over the whole frequency range. The reflection function for the stepped tube is now a little more elaborate than for the case of the closed tube as shown in Figure 5.18. Agreement is fairly good, especially at the lower frequencies.

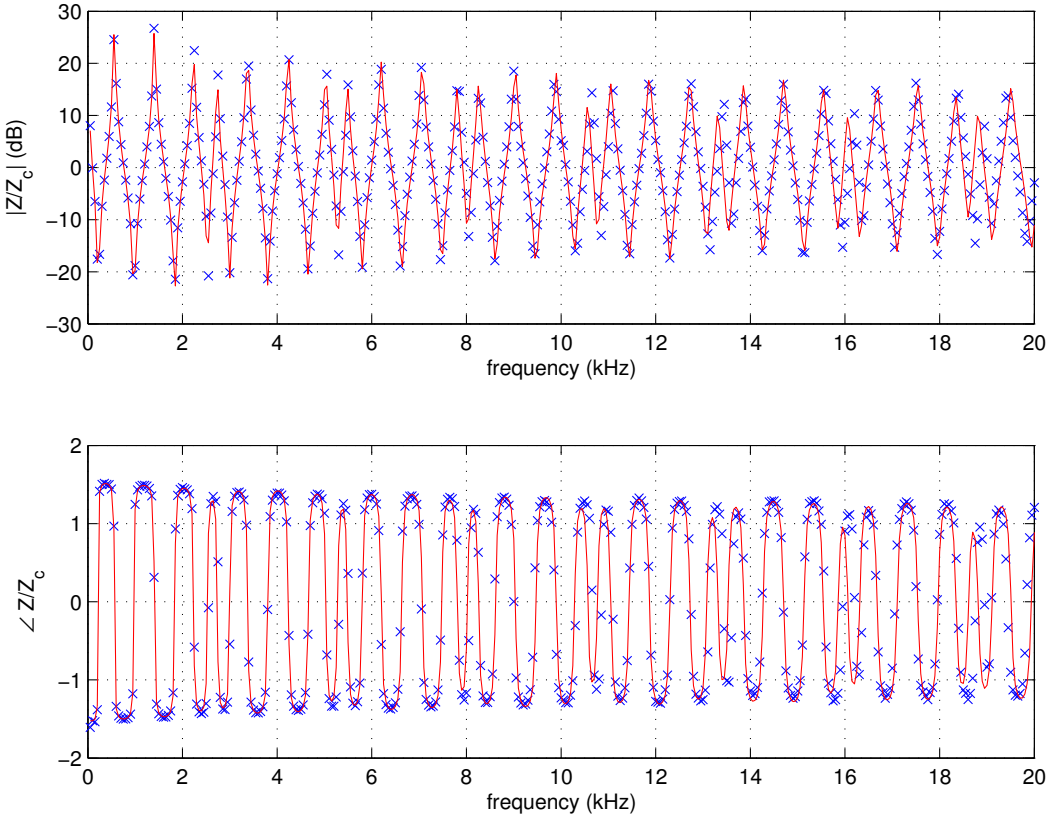

Figure 5.16: Input impedance magnitude and phase for the stepped pipe. Again there is good agreement between plane-wave theory and experiment.

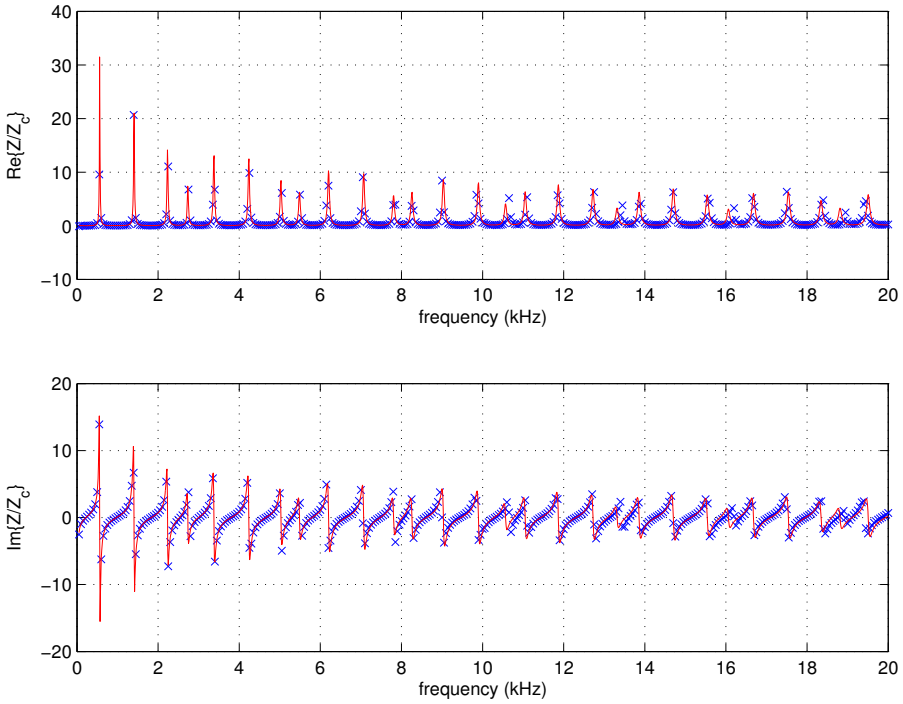

Figure 5.17: Real and imaginary part of the impedance for the closed stepped pipe.

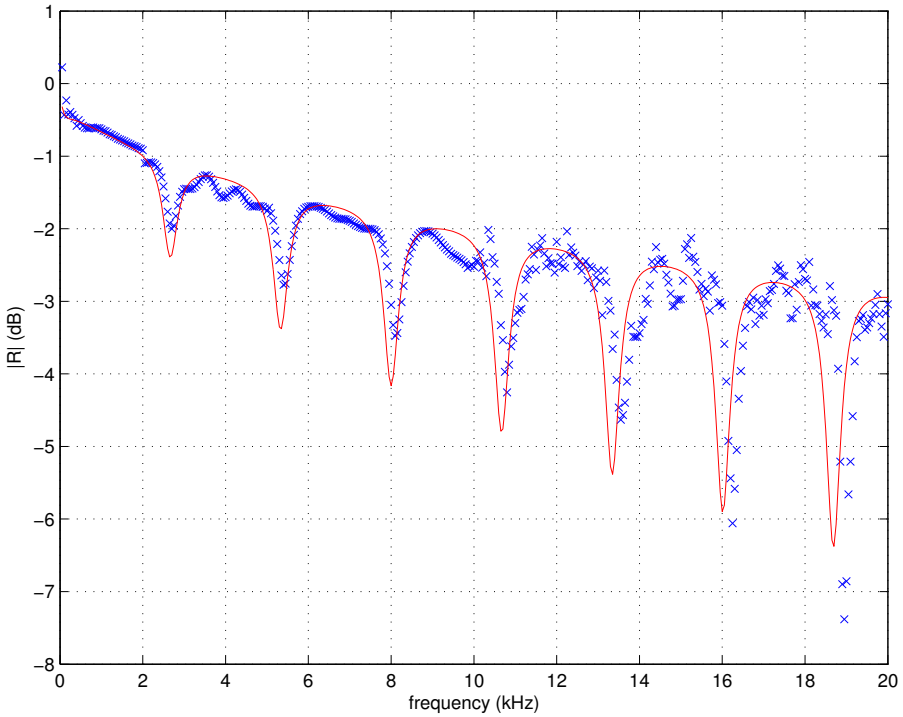

Figure 5.18: Reflection coefficient for the closed stepped pipe.

5.2.2 Results: Input Impulse Response and Bore Reconstruction

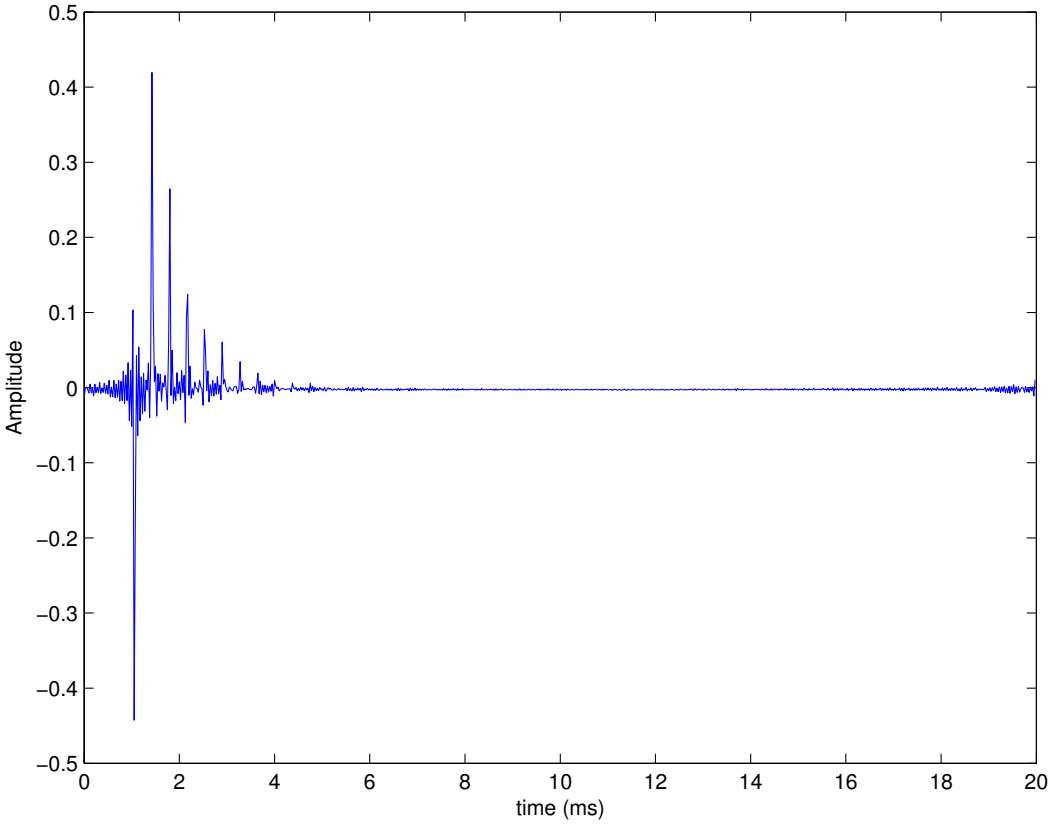

Figure 5.19: Input impulse response for the closed stepped pipe.

Consider the impulse response in Figure 5.19. We expect the first reflection to occur from the expansion at the interface of pipe 1 and pipe 2. This will reach the input plane after a time

$$t_1 = \frac{2L_1}{c} \approx 1\text{ms} \tag{5.4}$$

and will have a negative sign. The second reflection will be due to the fraction of the wave reflected at the closed end which corresponds to a large (infinite) contraction hence it should have an amplitude of opposite sign (positive) to that of the first reflection. It will occur at time

$$t_2 = \frac{2(L_1 + L_2)}{c} \approx 1.4\text{ms}. \tag{5.5}$$

These peaks are referred to as *primary reflections* since the wave endures only one reflection in each case. There will also be multiple peaks in the IIR for the fraction of the wave that encounters multiple reflections at the two changes in cross section. These are referred to as *secondary reflections*. The result of these reflections make up the IIR given in Figure 5.19. The bore reconstruction using the raw IIR is shown in Figure 5.20. We see the same problems as those found for the closed tube. The profile expands slightly for the profile of the first cylinder from 4.9 mm to 5.4 mm over the length of 180 mm. The jump point at 180 mm is correctly predicted but the second cylinder radius is over-predicted by about 1.5 mm. The second drop is predicted close to the true drop at 255 mm but only drops as far as 1 mm. Figure 5.21 shows the reconstruction obtained when the dc offset is adjusted by the same magnitude as that for the closed tube. We see the reconstruction is greatly improved. The reconstruction of the first cylinder is perfectly flat. It oscillates around the true value by approximately plus or minus 0.05 mm. The point at which the step occurs is still accurately obtained but spread over a 10 mm range, rather than infinitely sharp. The radius of the second cylinder is accurate, but not to the same degree as that of the first - to within an error of about 0.5 mm.

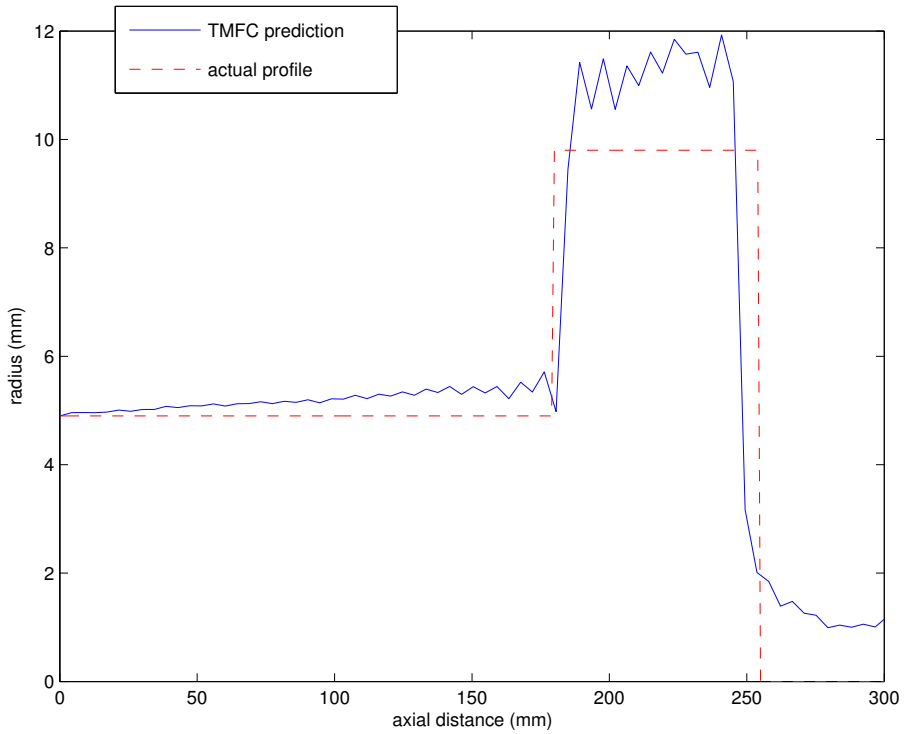

Figure 5.20: Bore reconstruction for a stepped pipe using raw TMFC data. Again the profile is found to expand gradually rather than remain constant.

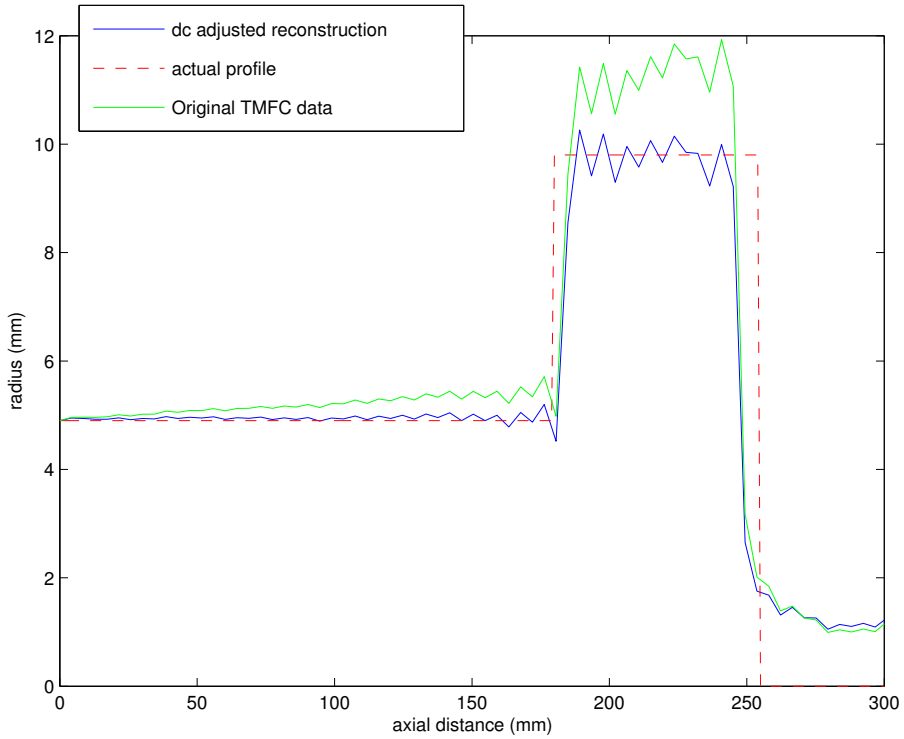

Figure 5.21: Bore reconstruction for the stepped pipe without dc adjustment (green line) and with dc adjustment (blue line).

5.3 Bore Reconstruction for the Horn

Now to measure an actual musical instrument. Results were obtained for the horn described in Chapter 2 attached to the TMFC system using a suitable coupler. The first cylindrical section of the coupler has a radius $r_1 = 4.9$ mm and length $L_1 = 128$ mm which then steps down to another cylinder of radius of $r_2 = 4.55$ mm and length $L_2 = 29$ mm. The horn has a length of $L_3 = 817$ mm, a bell end radius of $r_3 = 62.5$ mm and obeys a Bessel profile with a flare constant $m = 1.2$.

There are two main effects that a horn has on the sound production of an instrument. Firstly the bell will increase the length of the instrument. In turn, the resonance peaks and troughs will decrease in frequency hence lowering the pitch of the instrument. Secondly, the bell will allow closer impedance matching between the instrument and the surrounding environment. This means that more sound energy can be radiated. This leaves less energy resonating inside the instrument and so the amplitude of the resonance peaks and troughs will be weaker.

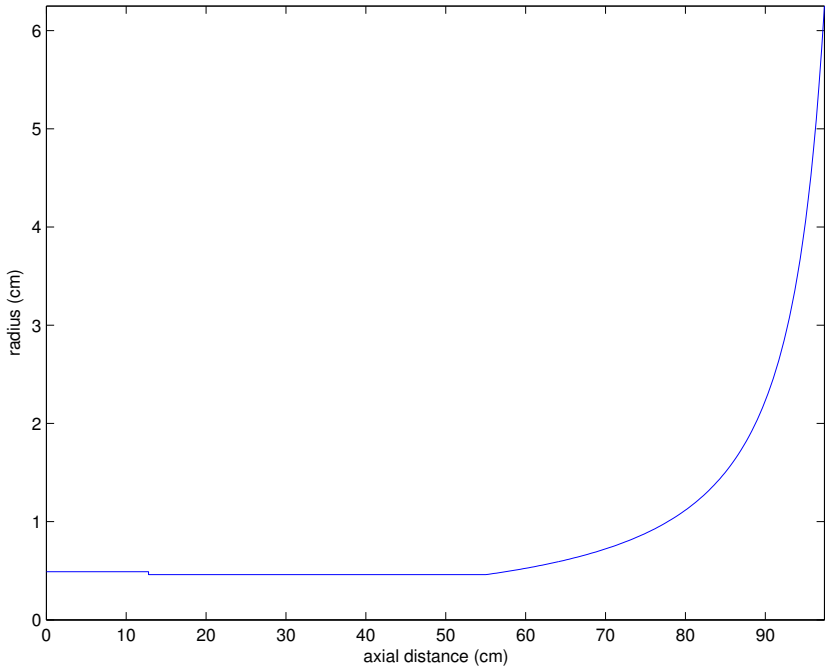

Figure 5.22: Approximated profile for the horn plus coupler in which the coupler is modelled as a stepped open tube and the horn has a Bessel profile with a flare constant of $m = 1.2$.

5.3.1 Impedance Results

Figure 5.23 shows the theoretical impedance for the horn plus coupler as calculated by the BIES based on the model profile given in Figure 5.22. Superimposed onto this is the TMFC data. Figure 5.24 shows a close-up over the 2kHz range.

From the theoretical result we see that frequency separation of the impedance peaks/troughs is 160 Hz. The frequency resolution of the data is 50 Hz so when we zoom in for detail we find that the resolution is not high enough.

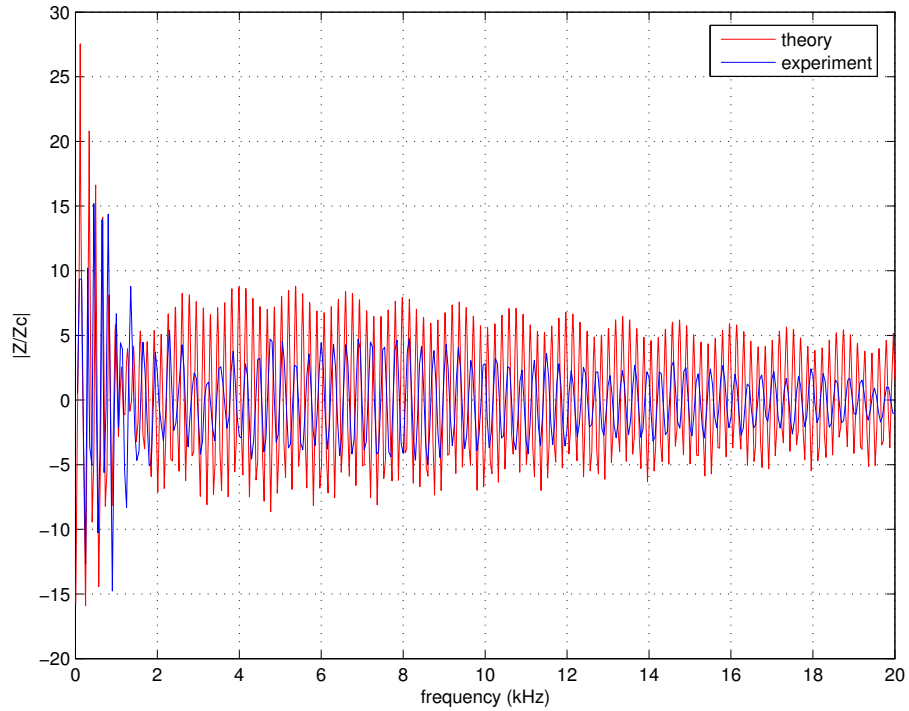

Figure 5.23: Theoretical plane wave and experimental impedance magnitude for the horn plus coupler assuming the bell has the profile of a Bessel function of flare constant $m = 1.2$.

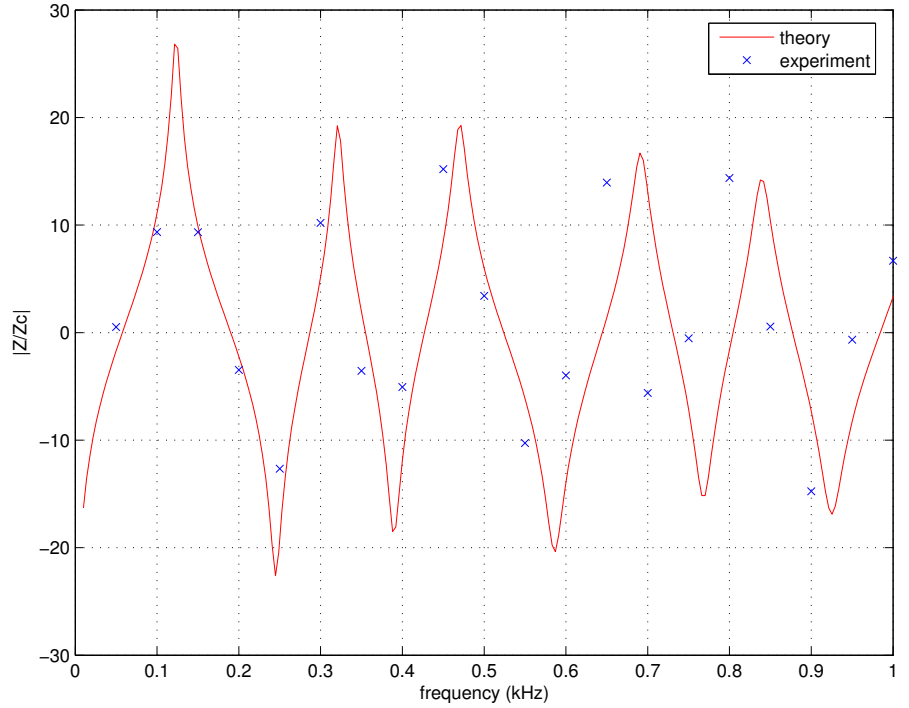

Figure 5.24: Theoretical plane wave and experimental impedance magnitude for the horn plus coupler assuming the bell has the profile of a Bessel function of flare constant $m = 1.2$.

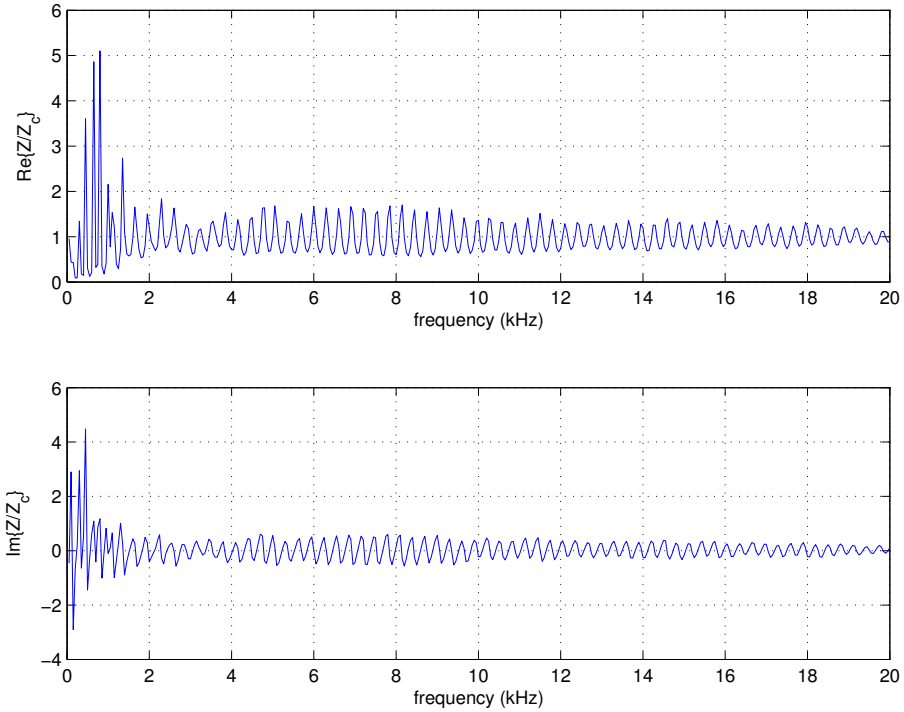

Figure 5.25: Real and imaginary part of the impedance for the horn plus coupler.

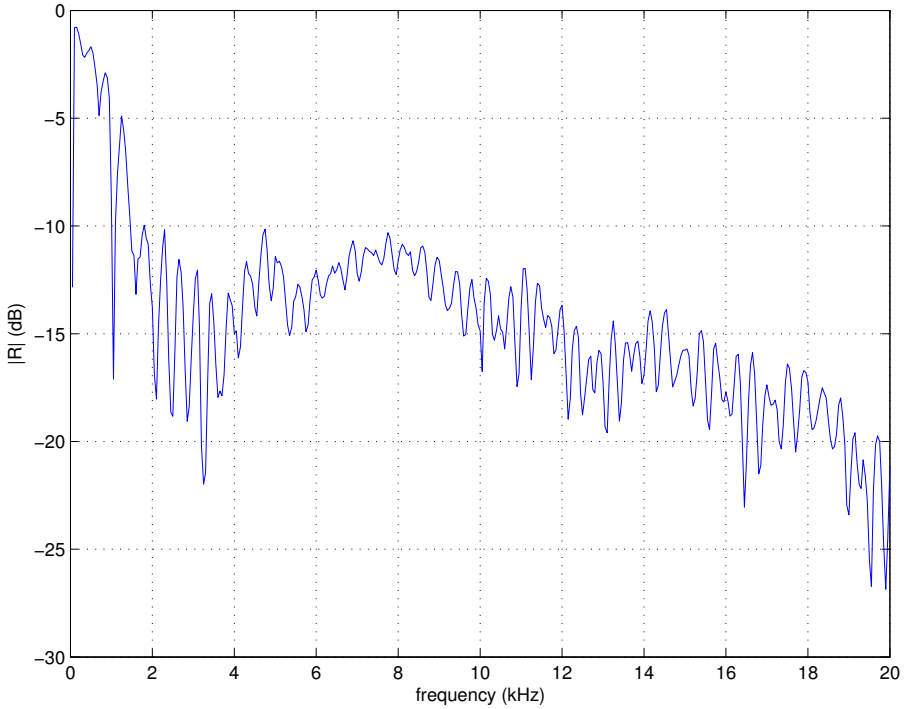

Figure 5.26: Reflection coefficient for the horn plus coupler.

5.3.2 Input Impulse Response and Bore Reconstruction

The IIR for the horn is given in Figure 5.27. The first peak at 1 ms corresponds to the step down in the coupler at 180 mm. The large negative peak at 3.2 ms corresponds to a length of 0.5 m. This is due to a join in the instrument since the horn is actually built as two separate parts: a roughly cylindrical section, and a bell section. The part of the IIR - around 5.5 to 7 ms - that resembles a negative sign curve is the reflection from the bell.

The resulting bore reconstruction is given in Figure 5.28. We see that the initial straight section of approximately 550 mm is well reconstructed. The rapidly flaring bell however is massively under-predicted.

Figure 5.29 shows the result when the dc level has been adjusted. Note this time that it is by a different value from that of the previous closed tube, +0.00275 compared with -0.0025. This value was found by taking the average value of the IIR amplitude in the first 0.5 milliseconds of the impulse response. The first half of the horn is approximately cylindrical and the true profile is represented by a dashed red line. There is agreement between theory and experiment to within 0.8 mm for this section of the instrument. The red crosses are calliper measurements of the horn at various points along its length. The step up at the axial length of around 570 mm is accurately determined by the TMFC and the general shape of the bell is well reconstructed. However, the reconstruction is slightly too slowly flaring for the first 360 mm of the bell. At an axial length of around 930 mm the TMFC and calliper-measured profile meet. After this point the reconstruction is slightly too rapidly flaring.

Figure 5.30 shows the theoretical impedance for the horn. The plane wave impedance is represented by the blue line, the impedance calculated by including the first two higher modes is given by the green line, and the impedance corresponding to the inclusion of the first six higher modes is given by the red line. At low frequencies, below 1 kHz, there is good agreement between all three impedance curve. Figure 5.31 shows a close up of the 0 to 300 Hz region where the TMFC impedance data has been included and is also in good agreement with the theoretical curves. The impedance corresponding to inclusion of the first two higher modes has been removed to avoid cluttering of the graph.

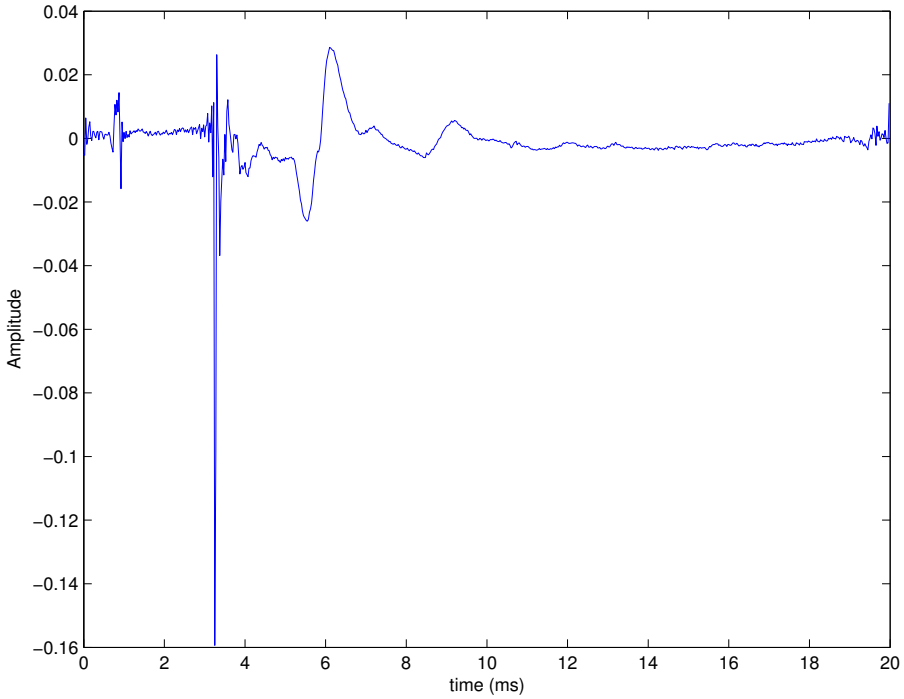

Figure 5.27: Input impulse response for the horn plus coupler.

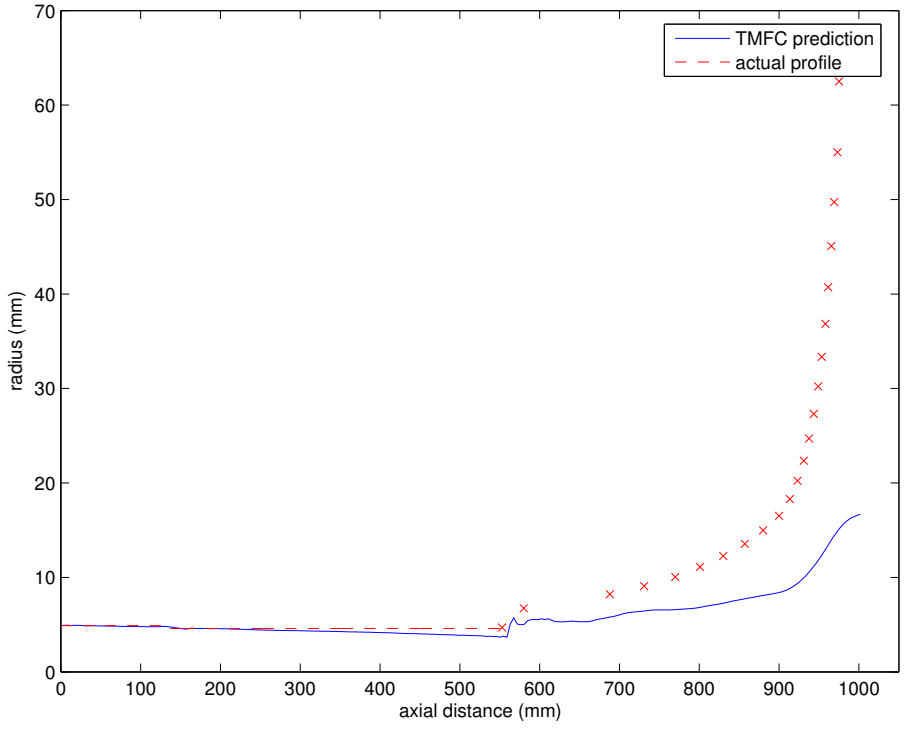

Figure 5.28: Bore reconstruction of the horn (dc offset present).

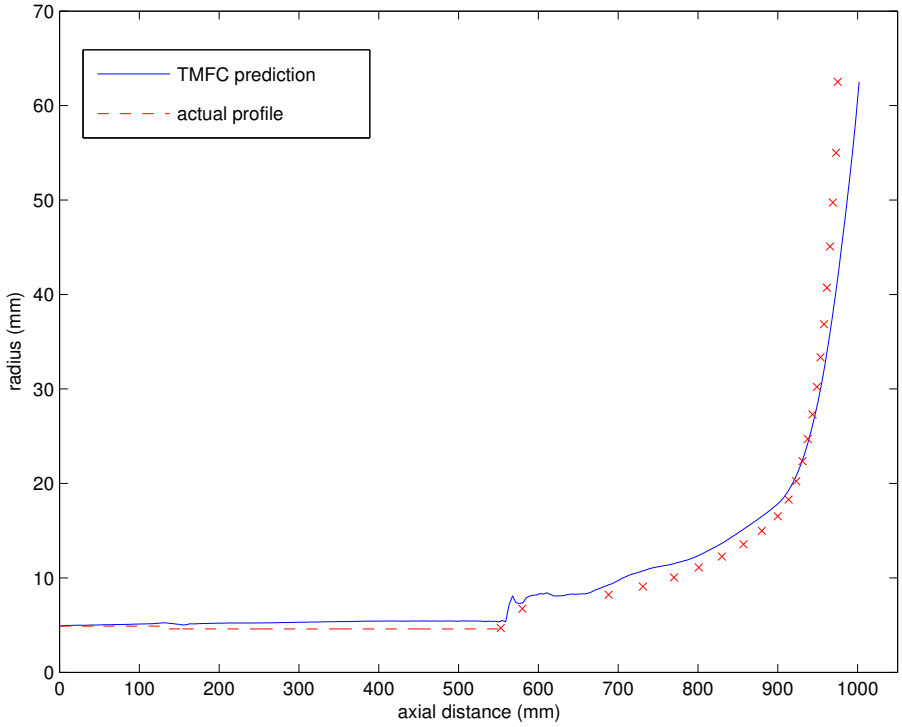

Figure 5.29: Bore reconstruction for the horn. The dc level has been adjusted by +0.00275.

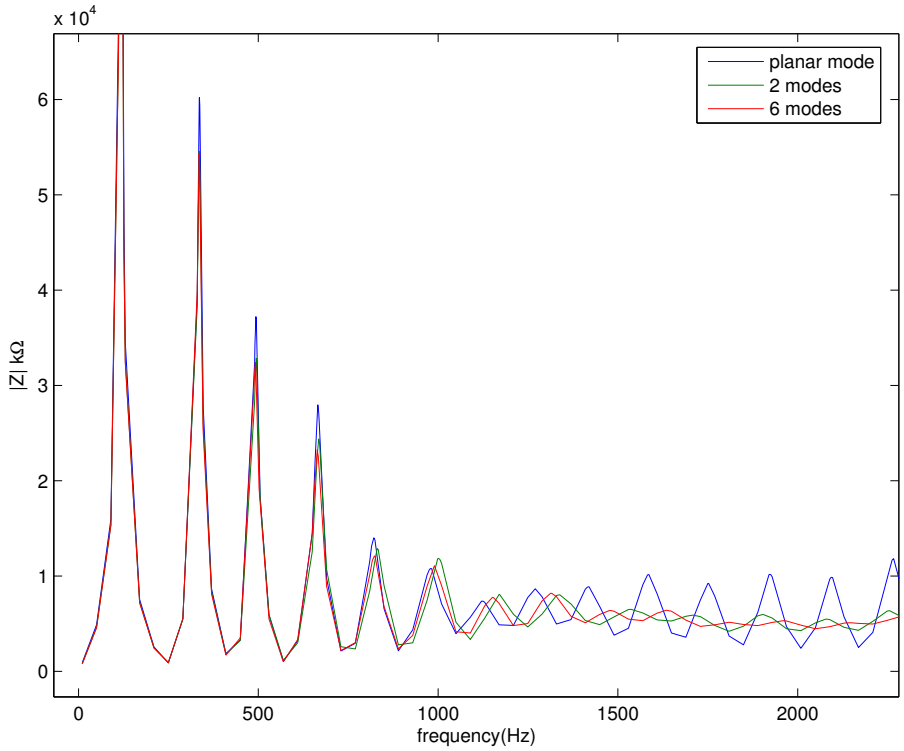

Figure 5.30: Impedance for the horn: Plane-wave and higher modal propagation.

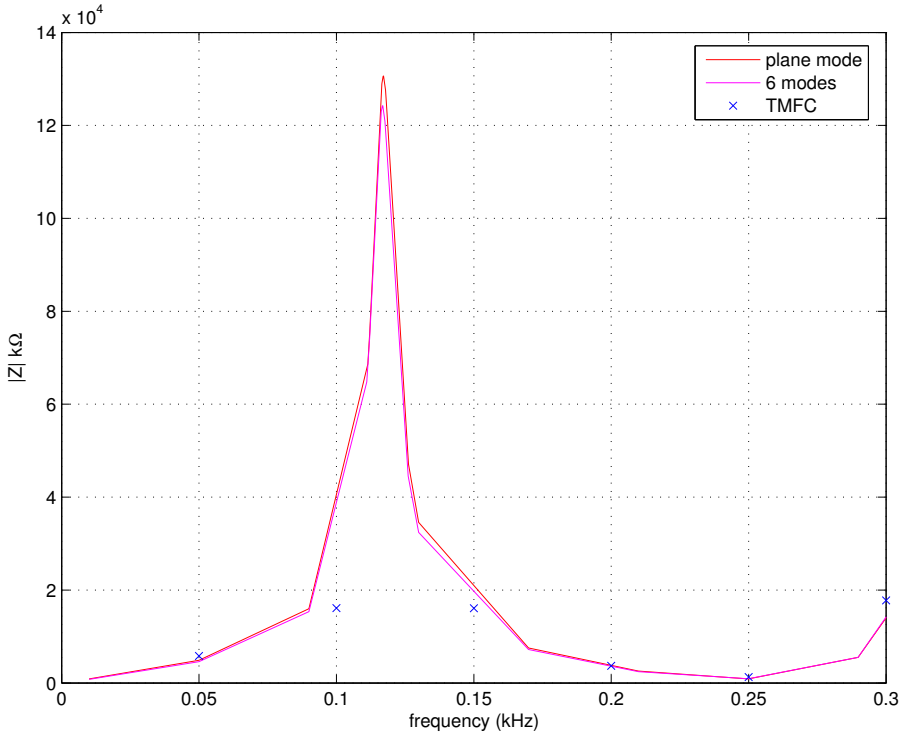

Figure 5.31: Comparison between plane-wave theoretical impedance, higher mode impedance, and TMFC data at low frequencies.

5.4 Measuring Instruments with Mouthpieces

For the system to have more versatility and to be able to measure a wider range of instruments, an adaptor was manufactured that would suitably couple a mouthpiece to the measurement duct. The adaptor must have a length of tube with a radius equal to that of the basic measurement duct since a discontinuity at the reference plane would cause the generation of higher modes and the equations on which the method is based would not apply. The length of this open cylinder is 18 mm but can easily be modified by attaching any number of open tubes to the adaptor. Figure 5.32 shows the main four components of the adaptor plus a Dennis Wick 6BS mouthpiece. Second from the left is the main component - with the open length of tube - which is screwed onto the basic measurement duct. The mouthpiece is pressed onto this component by the black cap (third from the left) and held in place by the aluminium outer-cylinder (left) and the screw-cap (right). Once the measurements are made the impedance corresponding to the small length of tube in the adaptor can be removed from the data using transmission matrix theory leaving the true impedance of the mouthpiece.

Figure 5.32: The various components of the 'BIAS-head replica' and a Dennis Wick 6BS mouthpiece.

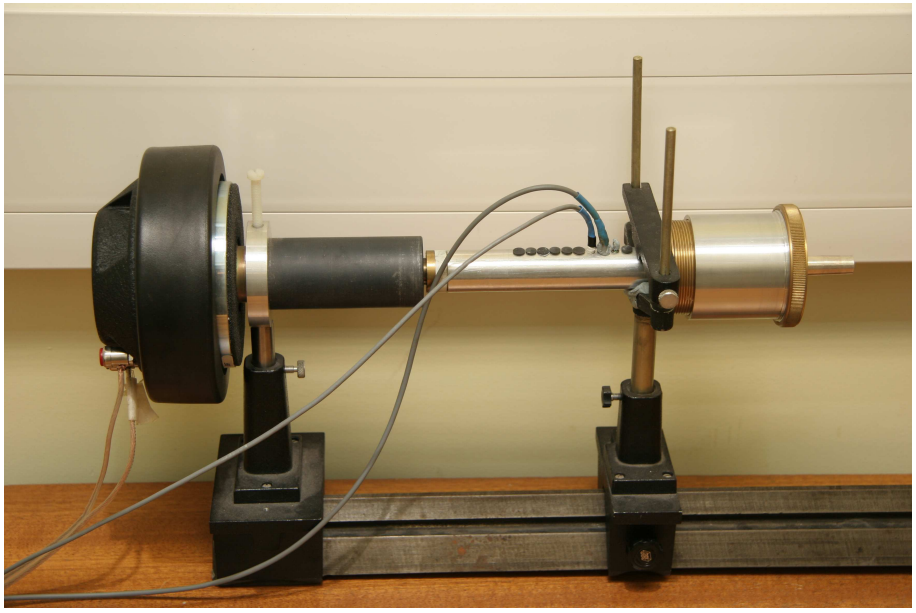

Figure 5.33: BIAS-head replica on TMFC apparatus.

5.4.1 Impedance Data

Figure 5.34 shows the measured impedance of the Dennis Wick 6BS mouthpiece. Figure 5.35 shows the real and imaginary part of the impedance and Figure 5.36 shows the reflection coefficient. Transmission matrix theory has been applied to the TMFC data to remove the impedance of the coupler and calculate the impedance of the mouthpiece alone. This is shown in Figure 5.37.

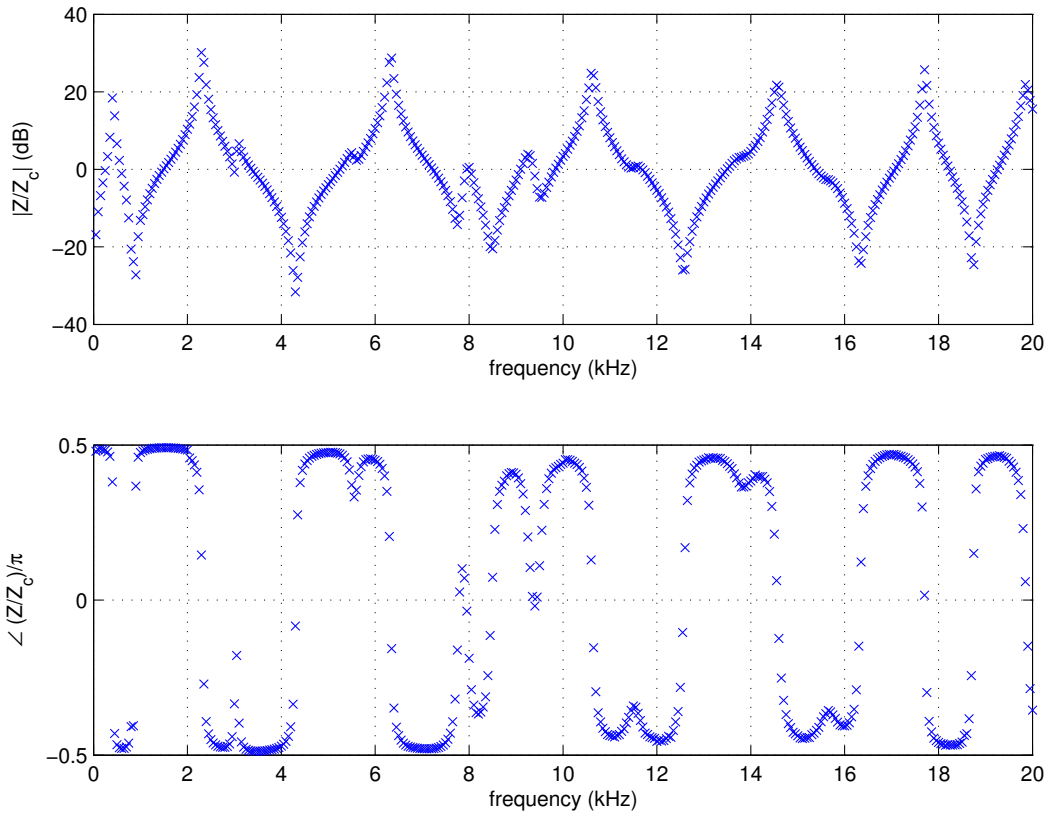

Figure 5.34: Impedance magnitude and phase for the Dennis Wick 6BS mouthpiece plus BIAS head replica.

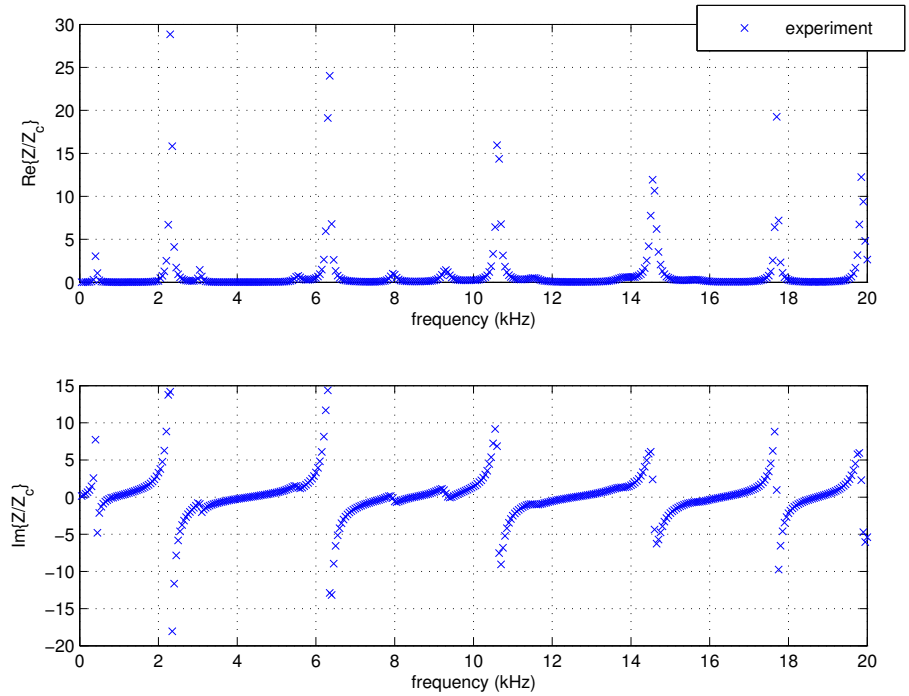

Figure 5.35: Real and imaginary part for the impedance of a Dennis Wick 6BS mouthpiece plus BIAS head replica.

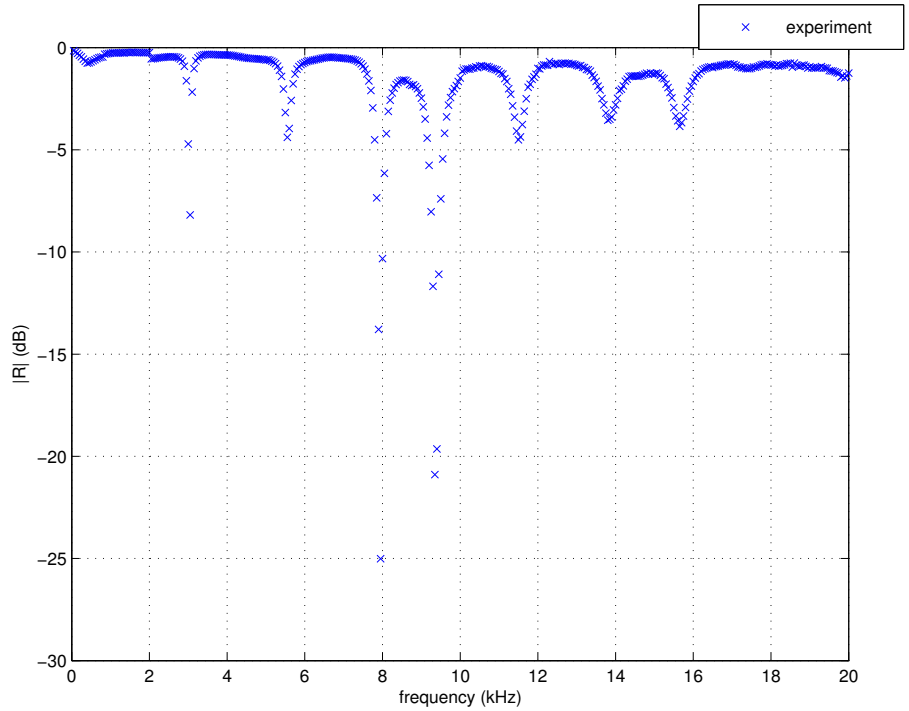

Figure 5.36: Reflection coefficient for the Dennis Wick 6BS mouthpiece plus BIAS head replica.

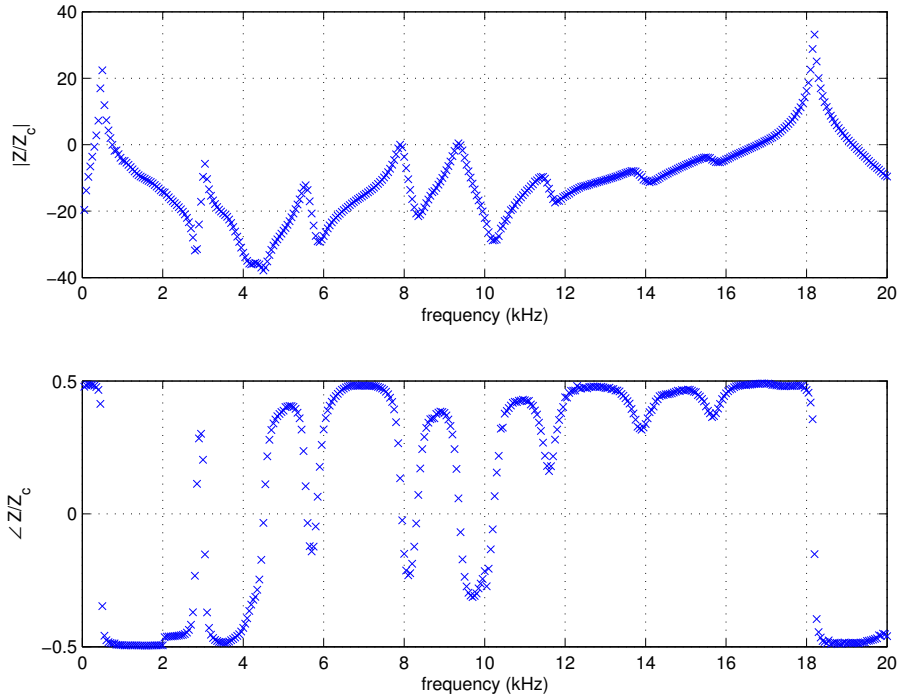

Figure 5.37: TMT applied to the impedance data for the Dennis Wick 6BS mouthpiece.

5.4.2 Input Impulse Response and Bore Reconstruction

The input impulse response and bore reconstruction for the coupler plus mouthpiece are given in Figure 5.38 and Figure 5.39 respectively. They have been calculated by transforming the impedance data given in Figure 5.34. Since a mouthpiece is very short - typically tens of centimetres - the IIR should be full of very closely spaced (in time) peaks. The first negative peak in the IIR corresponds to the expansion at the plane where the initial length of the adaptor - in this example 38 mm - meets the cup-face of the mouthpiece. Note that the length of the adaptor is not crucial and fairly arbitrary, provided it is long enough to ensure that higher modes from the instrument do not propagate to the reference plane. The total length of the adaptor plus mouthpiece is around 120 mm. This corresponds to the negative peak observed at 0.7 ms. The agreement between the reconstructed radius of the adaptor and the mechanically measured value is to within 0.08 mm. The general shape of the cup is reconstructed but to a very low resolution. The conical section of the mouthpiece is accurate to within 0.5 mm.

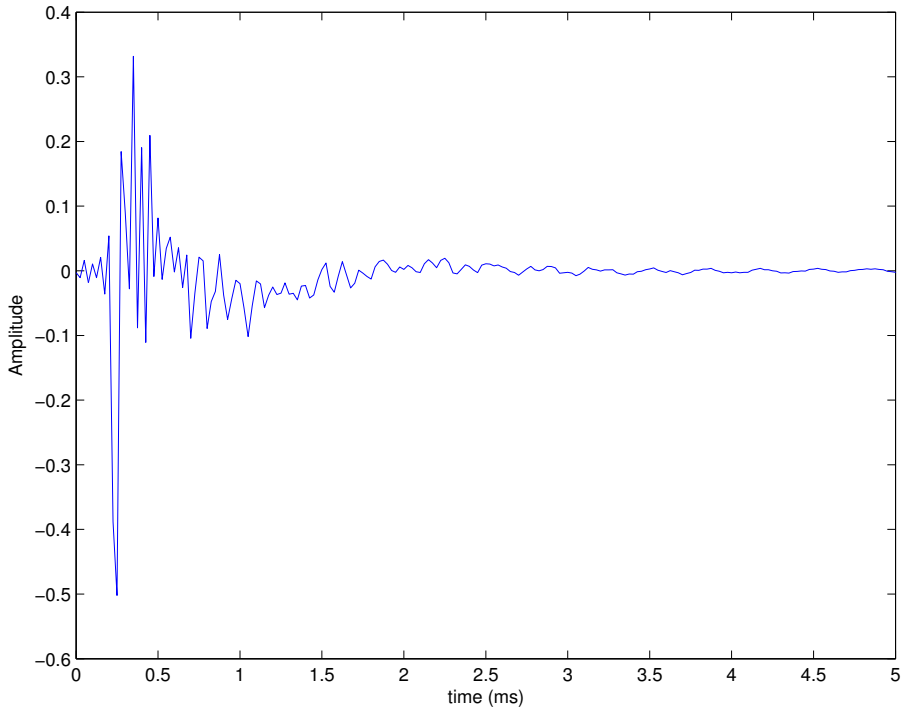

Figure 5.38: IIR for the Dennis Wick 6BS mouthpiece.

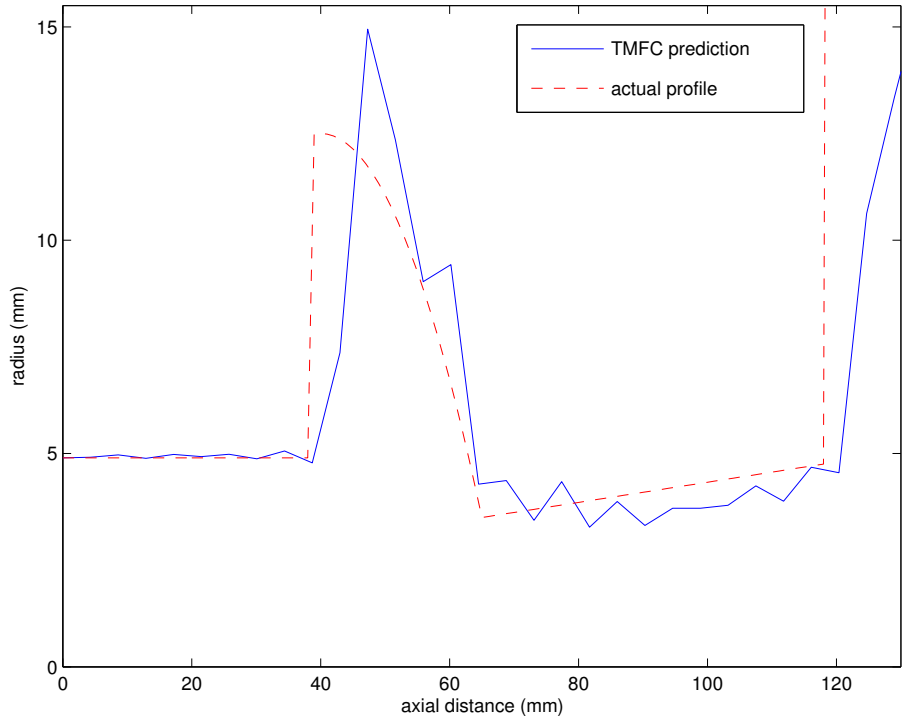

Figure 5.39: Bore reconstruction for the Dennis Wick 6BS mouthpiece.

5.5 Brass and Silver F-crook Comparison

In this section the TMFC has been used to answer a question of musical interest. An expert French horn player had discovered under playing tests that one of his F-crooks - a brass one - was perceived to play 'poorly'. He wanted to understand why. In an attempt to answer this question it was decided that a bore reconstruction of the brass crook would be obtained and compared with another F-crook in his collection - a silver one - which was considered to play 'well', to observe any physical differences. Both instruments were attached to the system via a suitable cylindrical-then-tapered coupler, measuring from the narrow end. The impulse response for both crooks is shown in Figure 5.40. The large negative peak in both graphs are from the expansion at the wide open end. We can see that both peaks are approximately the same in magnitude but there is a temporal separation of 0.425 ms; the brass crook is slightly longer than the silver crook. We notice also for the silver crook that, apart from the first 0.5 ms - which corresponds to the length of the coupler -and the open end reflection, the IIR is fairly flat; the profile is constant, whereas for the brass crook there is a definite positive peak at 4.5 ms. Figure 5.41 shows the resultant reconstructions. We see that the silver crook does have a very constant internal radius most of the way along its length and eventually tapers down at the wide end. The brass crook is longer and has a sudden step down in radius approximately two-thirds along its length which was not obvious from visual inspection. What was not apparent in the impulse responses was the other deviation near the input of the brass crook. To get an idea of how repeatable the results are we see in the close-up of the coupler, Figure 5.42 (which was used for both crook measurements and is of accurately known dimensions), that the two profiles are very similar - to within 0.015 mm - and are close to the true profile (within 0.15 mm) given by the red dashed line. So we now have some idea of why the instrument does not behave as expected. The next question to ask is: how much of the effect on the instrument musical performance can be attributed to the deviation at the input, and how much to the deviation at the open end?

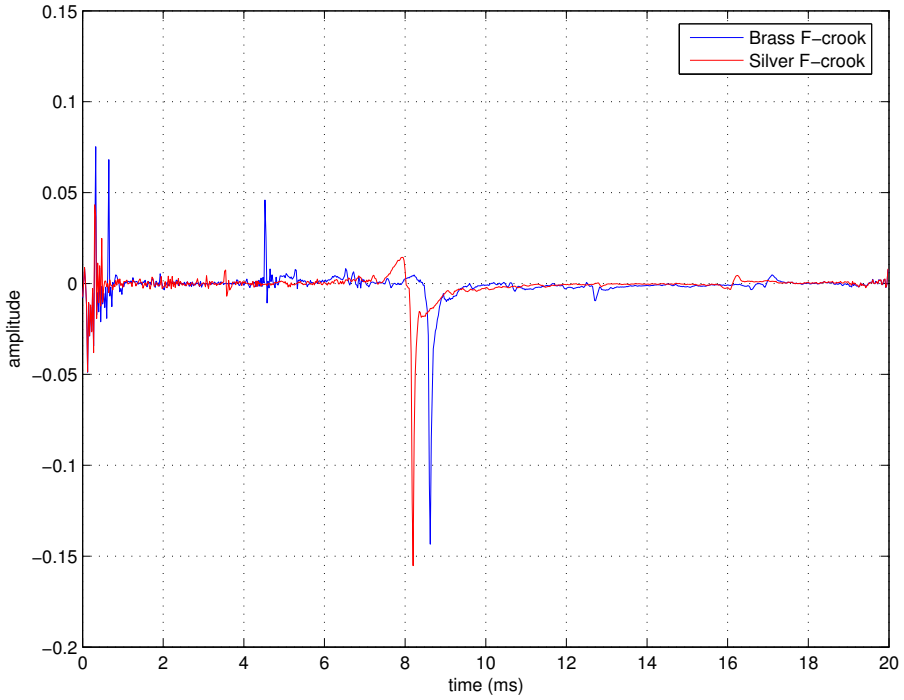

Figure 5.40: IIR for the brass, and silver, F-crook using the TMFC method.

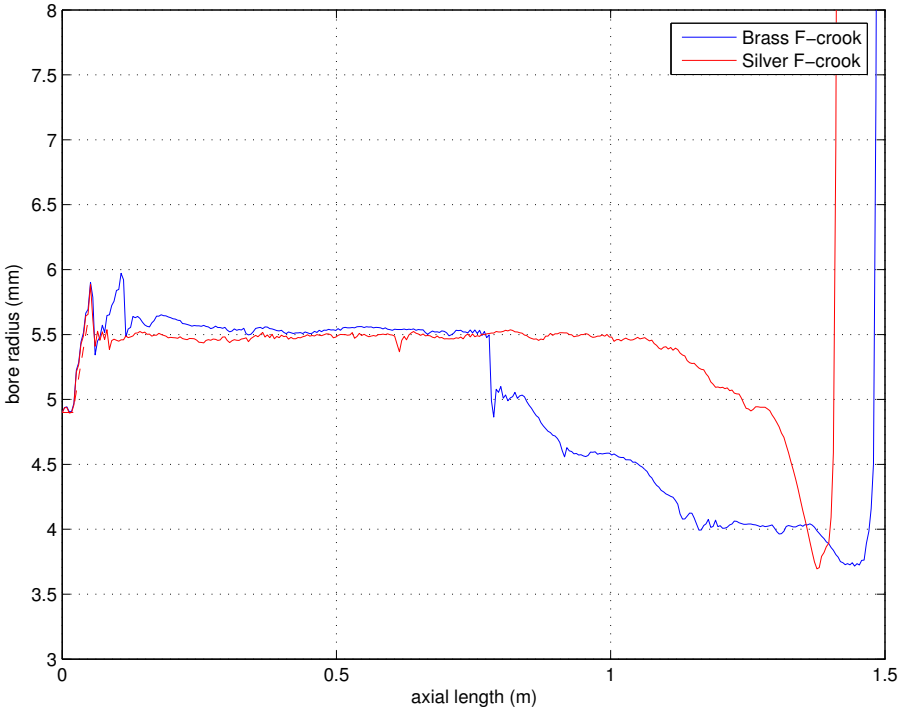

Figure 5.41: TMFC bore reconstruction for the brass, and silver, F-crook.

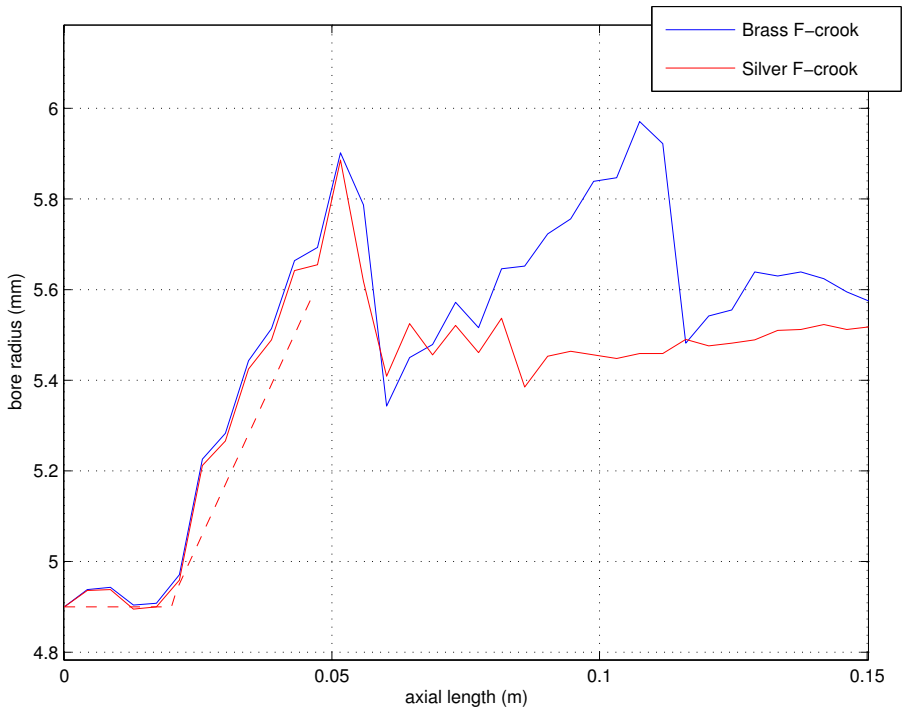

Figure 5.42: TMFC bore reconstruction for the brass, and silver, F-crook with a close-up on the coupler.

5.5.1 Simulation

Figure 5.43 shows the TMFC reconstruction for the silver crook compared with the profile of a simulated crook, 'Simulation1', which is the brass crook profile with the large deviation at the far end removed. The corresponding impedance curves in Figure 5.44 match very closely implying the small deviation at the input does not have much effect on the impedance i.e. it does not have a significant effect on the musicality of the instrument.

Figure 5.45 now shows the reconstruction for another simulated crook, 'Simulation2', which is the brass crook without the small deviation at the input end. The impedance curves in Figure 5.46 differ significantly implying that the deviation at the far end is mostly, if not entirely responsible for the difference in musicality between the silver and brass crooks.

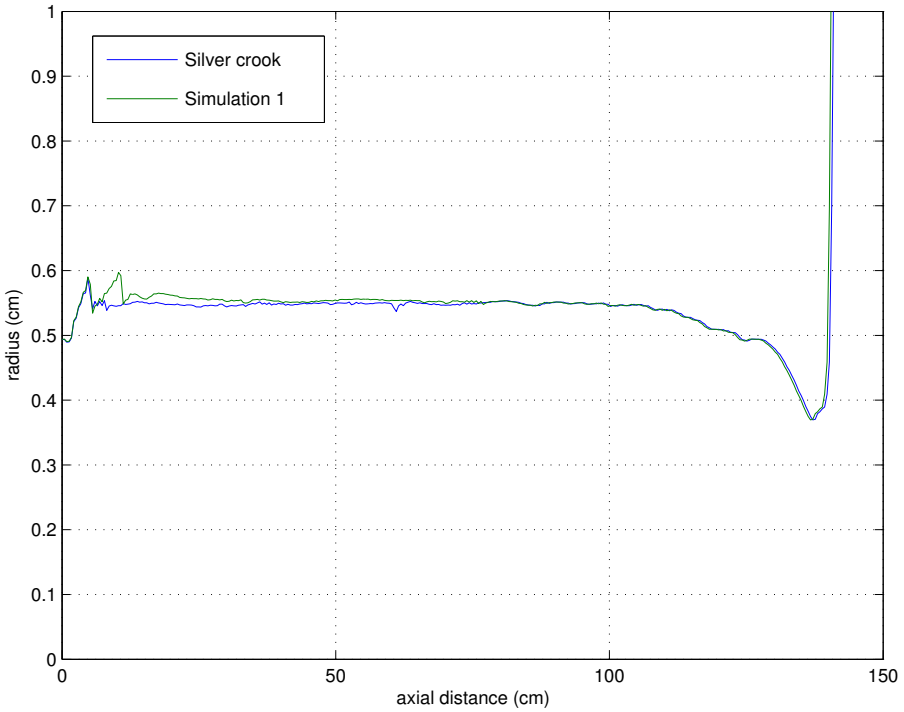

Figure 5.43: Bore profile of the silver crook compared to the profile of a simulated crook, 'Simulation1'.

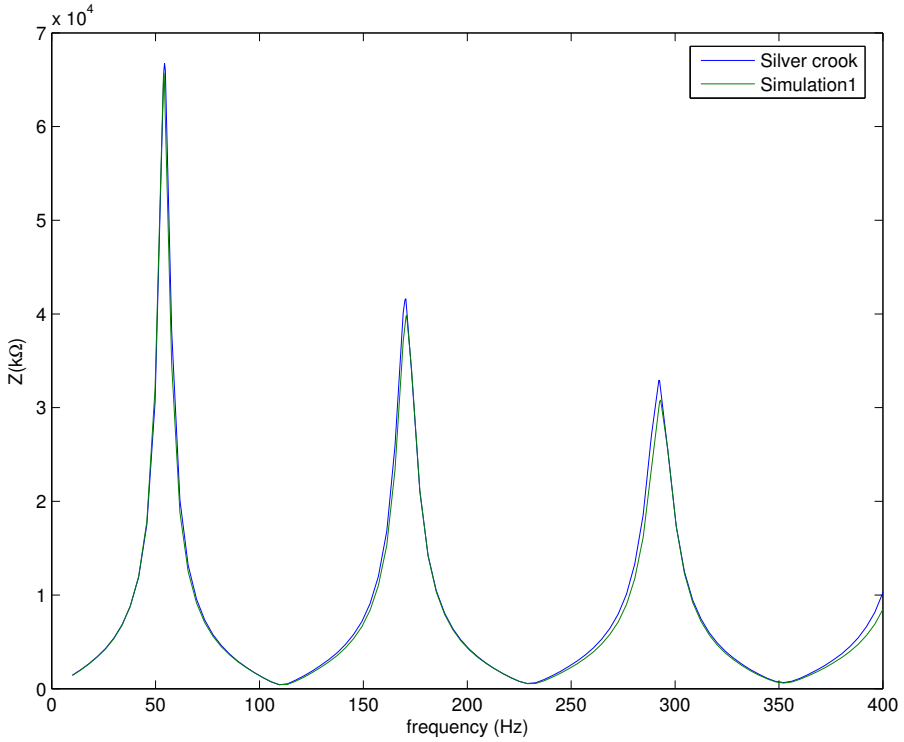

Figure 5.44: Impedance for the silver crook compared to the impedance of a simulated crook, 'Simulation1'.

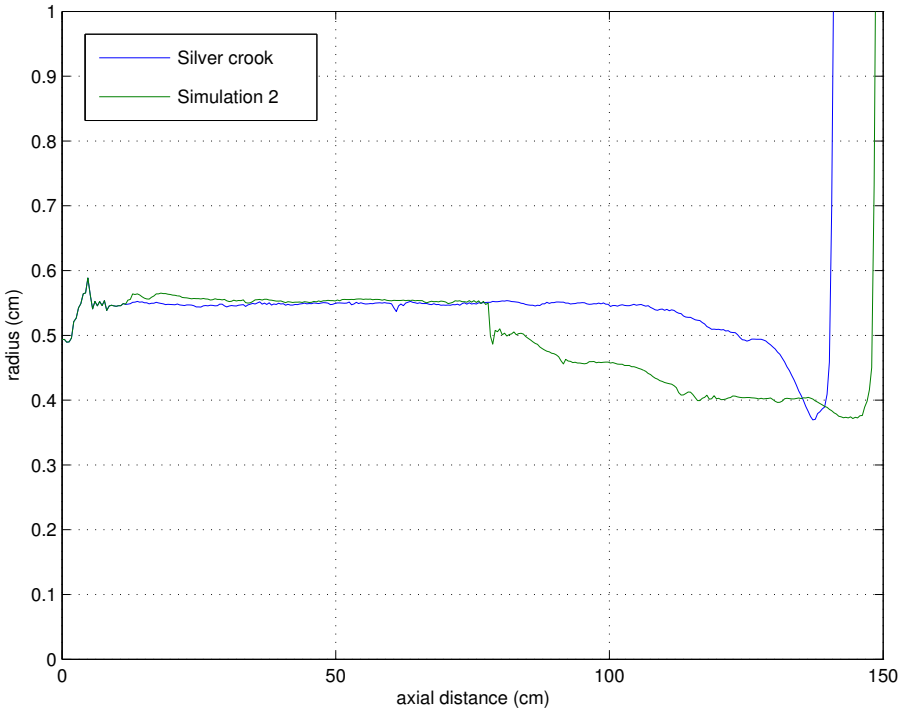

Figure 5.45: Bore profile of the silver crook compared to the profile of a simulated crook, 'Simulation2'.

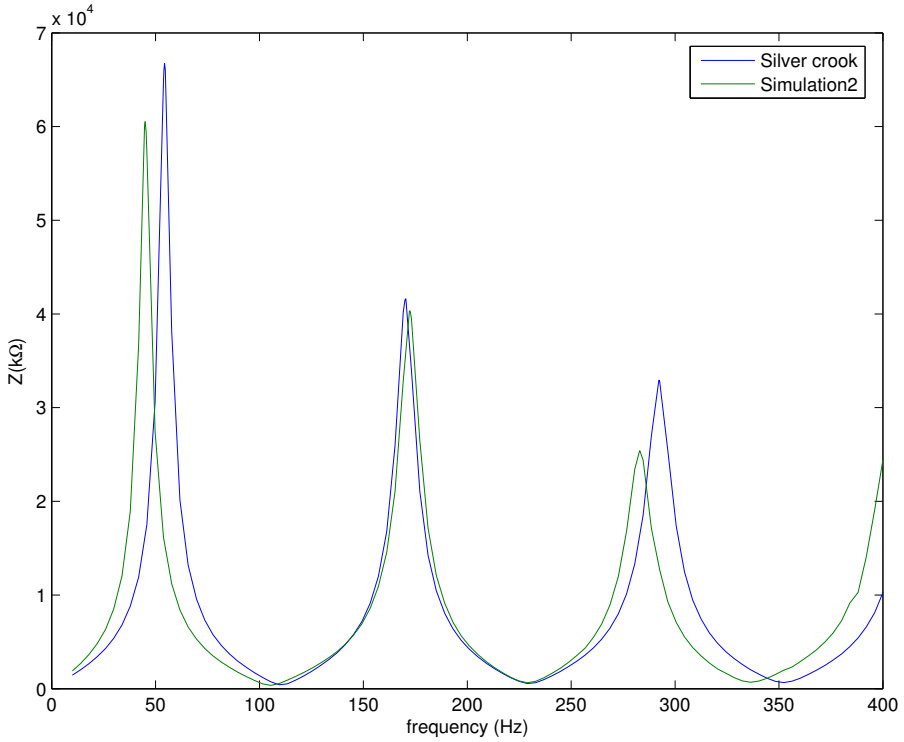

Figure 5.46: Impedance for the silver crook compared to the impedance of a simulated crook, 'Simulation2'.

5.5.2 Comparison with APR

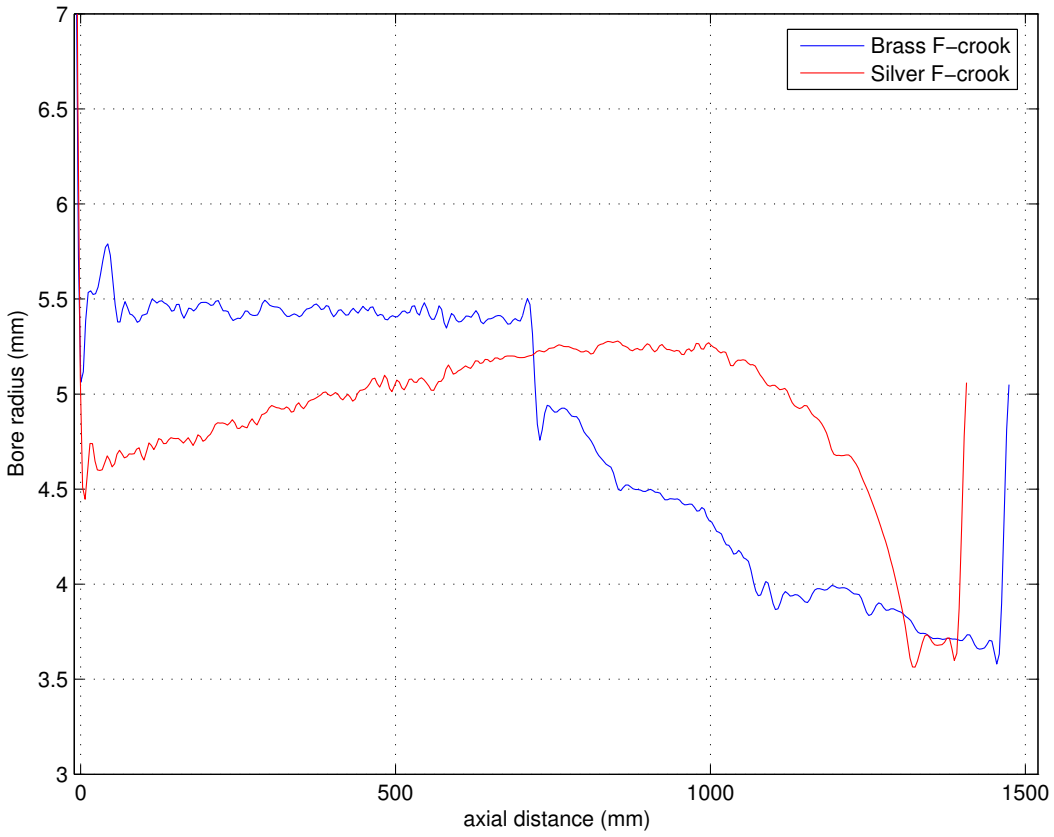

Figure 5.47: Brass and silver F-crook measured using APR. The TMFC result for the brass crook is verified; there is a step down approximately two-thirds along the instrument.

The same crooks were also measured with the pulse reflectometer for comparison and are shown in Figure 5.47. It should be noted that for the TMFC results the crooks were measured with the wide-end coupled to the system whereas for the APR results the narrow end was coupled to the system. If time had allowed, couplers would have been manufactured to allow the wide-end to be coupled to the APR system. To account for this the APR reconstruction profile data has been reversed and superimposed onto the TMFC data in some figures for comparison. We see that the pulse reflectometry result for the brass crook verifies the result from the TMFC; there is a step down approximately two-thirds along the crook's length. The result for the silver crook however is not in agreement with the TMFC result. For the TMFC result the silver

crook started off at the same radius as the brass crook - 5.5 mm - remained constant for the majority of its length and then tapered down at the far end. For the APR result this is not observed. The silver crook starts at a lower value of radius - 4.6 mm - increases to a maximum value of 5.28 mm at 860 mm along the axial distance and then tapers down to a value equal to that of the TMFC - 3.5 mm. This comparison is made clearer in Figure 5.48 which shows the TMFC and APR result for the brass crook on the same graph. This problem is believed to be caused by a lack of low frequency information in the APR data. Alterations to APR to correct this issue have been discussed by Kemp[41] whereby a two microphone technique akin to the TMFC set up is used to obtain impulse response data for the lowest two frequency bins. A similar comparison between the TMFC and APR systems has been done for the silver crook in Figure 5.49. We see that both methods obtain the same overall length for both crooks; the brass crook length is determined as 1.41 m; the silver crook - 1.33 m. For the brass crook we see that both methods display the deviation at the input and the step down two-thirds along the crook. They also give almost identical profiles - to within 0.2 mm discrepancy.

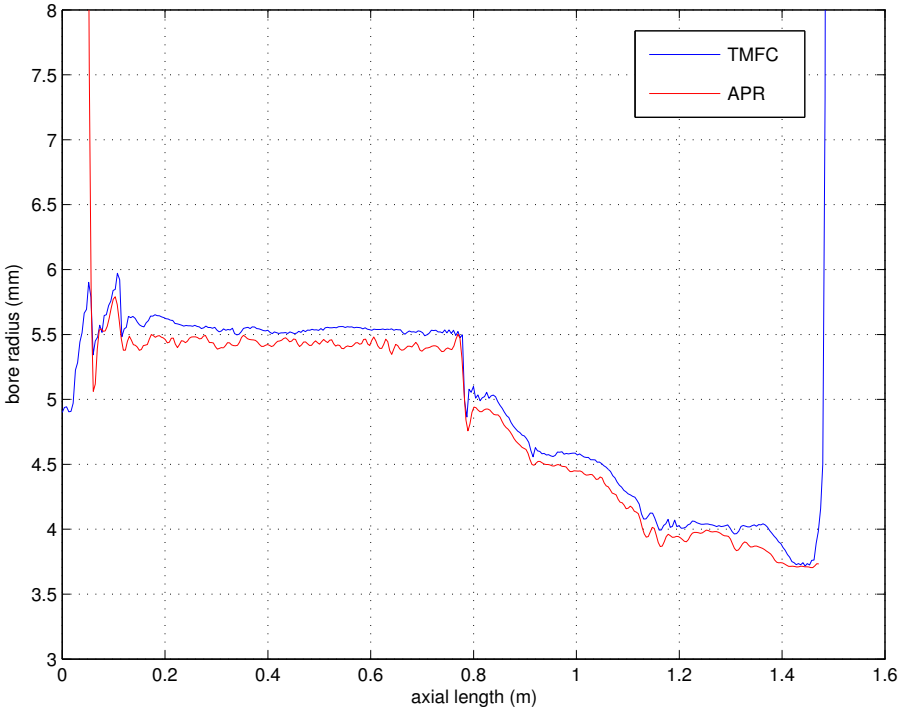

Figure 5.48: Brass F-crook as measured by APR and TMFC.

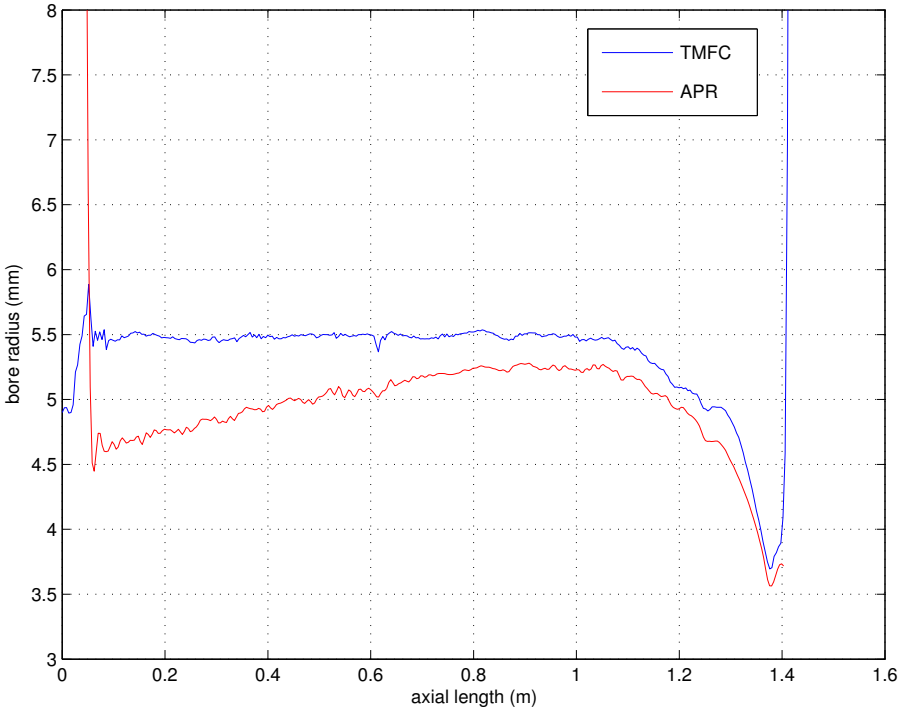

Figure 5.49: Silver F-crook as measured by APR and TMFC.

5.6 Summary

Bore reconstructions for some simple objects with well-known impedance curves were measured and compared with theory. In general, good agreement was found between the two. The resulting bore reconstructions were found to suffer from over-prediction problems; the profile was found to expand along the objects length rather than remain constant. This was found to be due to a constant positive value present in the IIR - the dc offset. Once the numerical value was identified it was subtracted from the IIR and a new result was obtained giving a reconstruction in much better agreement with theory. Exceptions were found close to sudden changes in cross-section where the Gibbs' phenomenon takes effect. It is also found that after a large step the reconstruction is never quite as accurate when compared to the profile before the step. A theoretical reconstruction was generated for the closed tube; theoretical plane-wave data was used as input for the reconstruction algorithms. Note that a dc adjustment was required for the theoretical data. The result was compared with the dc adjusted TMFC reconstruction and was found to be nearly identical. This tells us that the experimental results for the closed tube reconstruction was almost as good as it could possibly be, given the current range and resolution of impedance data and given that there is currently no known way of removing the Gibbs' effect.

Some comments have been made on a post-processing method. This involves the subtracting the impedance associated with the coupler using transmission matrix theory.

A modification to the TMFC system allowing the measurement of mouthpieces was described. This design was based on the BIAS hardware. A Dennis Wick 6BS trombone mouthpiece was measured as an example of usage.

The TMFC reconstructions have a good enough spatial resolution to identify the problem with the brass F-crook in which two major deviations were found when compared to the silver crook of the same type. These deviation were also verified by the pulse reflectometry system. It was deduced using simulation methods that the small deviation at the input has little effect on the performance of the instrument. The large deviation at the far end is almost all, if not fully, responsible for the problem.

Chapter 6

Bore Reconstruction of French Horn Crooks

This chapter investigates the usage and design of some traditional and contemporary horn crooks[41, 104, 105, 106, 107]. The bore profiles of three Courtois crooks of varying length - short, medium, and long - were derived from the TMFC method. Bore profiles for these crooks were also derived from time-domain pulse reflectometry measurements for comparison. Some comments are made on the limitations of the two reconstruction methods. Further pulse reflectometry measurements were made on the entire set of eight Courtois crooks. Further measurements were made on the F-crooks by five other manufacturers to observe how designs vary. A short comment is made on a peculiar result obtained for the Gautrot C-basso crook.

6.1 The Horn Crook: An Introduction

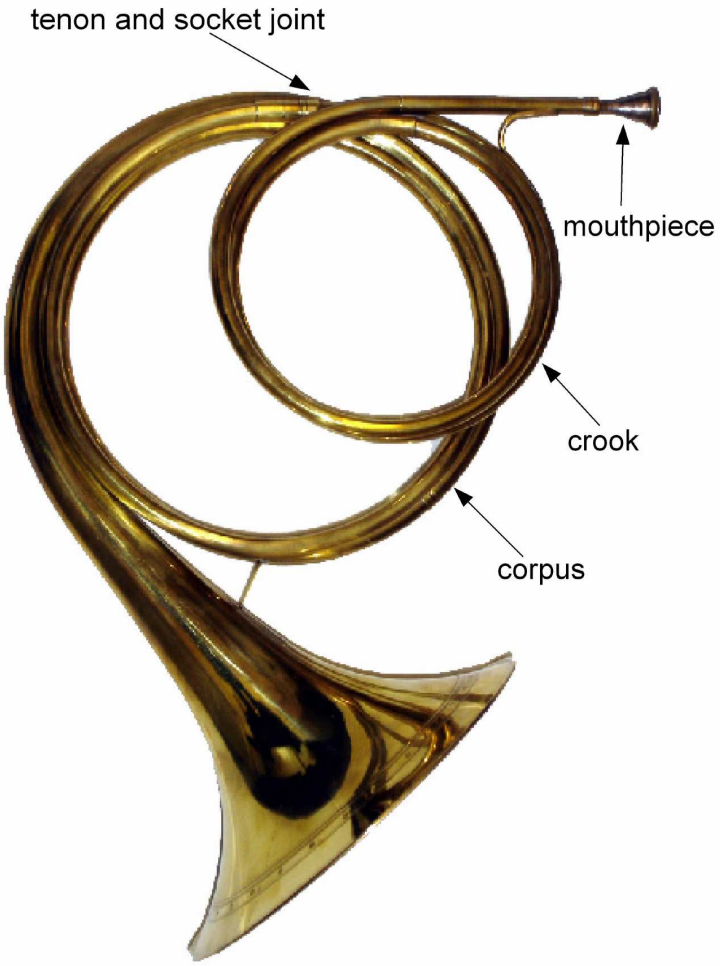

Figure 6.1: Main components of a natural horn. The crooks vary in length from tens of millimetres to more than three metres. For practical reasons, all but the shortest crooks are coiled with between 1 and 4 hoops.

Before the invention of valves, orchestral horns were generally equipped with a number of crooks of differing effective lengths to facilitate the use of the instrument in music of different tonalities. Even after the introduction of valves, some horns continued to be provided with detachable crooks. The experience of players is that the choice of crook critically affects the response of a horn, and that different crooks providing the same nominal pitch can have appreciably different playing properties.

The modern orchestral French horn is fully chromatic and can play in any key

through the use of valves which add or subtract lengths of tubing to or from the air column. Prior to the invention of valves, the 'natural horn', however, had no valves and could only play one key at a time through oscillating the lips at the different harmonic resonances of the air column. Natural horn players will therefore have a number of separate pipes called crooks which are of different lengths to set the instrument into different keys. These are normally designed such that the player's mouthpiece fits into one end and a tapered tenon at the other end is inserted into a socket on the main body, known as the corpus, of the instrument as shown in Figure 6.1.

The playing qualities of a natural horn are dependent on the design of the crooks and the corpus. In particular the resonances of the instrument's air column must be tuned close to a harmonic series for the instrument to have a satisfactory timbre, but also the bore profile can have an effect on the ease of starting a note, the intonation of the resonant modes and the ease with which the pitch can be 'bent' by the players lips for fine tuning[108]. For example, when a note is started, the reflections of the pressure oscillations produced by the players lips take several cycles to reflect from the bell of the instrument and return to the lips[108]. If the lips are vibrating close to a resonance frequency of the instrument then the reflections from the bell will arrive in phase to reinforce the resonances of the lips and the note should sound cleanly.

Dents and imperfections in crooks can lead to appreciable variations in their internal profile. The small reflections from these discontinuities in the internal bore profile will lead to small discrete reflections in the initial pressure oscillations and this may affect the playability of the instrument[109]. This also applies to discontinuities at the tenon and socket joint or joints.

This chapter will explore various techniques for measuring the internal profile of horn crooks and how sound reflects within them. Approximate measurements of the bore profile of crooks can be achieved by taking external measurements with callipers and then subtracting an estimate of the wall thickness. Internal measurements with callipers are only achievable near the open ends of coiled tubing in the instrument.

Acoustic pulse reflectometry is an effective method for crooks up to about 1.4 metres in length. The internal bore profile can then be reconstructed from this data. The TMFC method will also be used. Crooks of different length and of different ages (recent

and historical) will be measured and conclusions will be drawn on their construction, condition and playability.

6.2 History of the Horn Crook

Variations in design exist between different crooks made by different manufacturers and those made in different eras. Typically, British instruments built in the 18th Century would have used a relatively short tapered 'master crook' to which could be added one or more cylindrical couplers between the crook and corpus to achieve the desired length of horn. By the start of the 19th Century there was a certain level of standardisation amongst instrument makers and it had become more common to have separate crooks for almost all keys with the possible exception of B♭-basso which was normally achieved by adding a cylindrical coupler to the C-basso crook. Although there seems to be no standard taper for the tenon and socket joints on orchestral horns of the period, in many cases the crooks were interchangeable from one instrument to another, and it is likely that players would 'mix and match' the crooks to best meet their playing requirements.

The crook is constructed by first creating a solid shaft with the desired bore profile for the crook. This is known as a mandril. A metal washer is then used to drag a long piece of brass tubing onto the mandril forcing it to deform into the required shape. The straight crook is then filled with lead and bent and coiled around a solid wooden disk. The lead is used to prevent excessive 'crinkling' of the crook. Small imperfections are almost inevitable but these can be beaten out with a small mallet.

6.3 Results

All the horn crooks measured were designed to fit a standard horn mouthpiece at the input end and hence had internal diameters of 6 to 8 mm at the input. The tenons all had a standard internal diameter of around 11 mm making them interchangeable, although there was some small variation in the length of nominally similar crooks depending on manufacturer and variation in (historical) tuning systems. In some cases the different pitches were produced by the player piecing together up to four crooks. All crooks were measured mechanically with callipers.

While the internal dimensions of the bell of an instrument can be estimated directly using conventional calliper-style techniques, the internal dimension of tubing is much harder to determine, especially in coiled sections. Traditional techniques for estimating the bore profile involve measuring the external dimension, estimating the wall thickness and subtracting this from the external dimension. This generally works quite well but there will occasionally be uncertainties, for instance at overlapping joints and in the first section of the crook where there may be a reinforcing chemise at the mouthpiece receiver.

For the TMFC experiments, the crooks were measured by coupling the wide-end to the system's measurement duct. The crook sits inside the coupler and so the entire length of crook can be seen in the reconstruction. For the APR set-up, the narrow end was used. In this case the coupler sits inside the crook and so a tiny fraction - the order of a millimetre - of the crook is not present in the reconstruction. If time had allowed the crooks would have been measured by APR from the wide-end. In order for comparison, the TMFC bore profile data were reversed and superimposed onto the APR data. This introduces an uncertainty of ±3 mm in the axial positioning of the profile as it is not always clear from the reconstruction where the coupler ends and the crook starts.

6.3.1 APR and TMFC Comparison

The set of crooks made by Courtois consists of 8 crooks (giving nominal horn lengths for B♭, A, G, F, E, E♭, D, C-basso) and one coupler for extending the C-basso crook to B♭-basso. By way of comparing and validating the measurement techniques the Courtois A, F, and D-crooks were measured externally using callipers and internally using pulse reflectometry and the TMFC method. The results are shown in Figures 6.2, 6.3, and 6.4.

Figure 6.2 shows the reconstruction for the Courtois A-crook which has a mechanically measured length of about 700 mm. Good agreement is observed between the APR and TMFC method - within 0.5 mm for the first 570 mm. Both profiles remain below the external profile with the TMFC profile coming closest to the external profile at the large step at 620 mm. Both profiles also predict the overall length of the crook

accurately. The TMFC method predicts the correct internal exit diameter of 10.5 mm, whereas APR under-predicts its value at 9.8 mm. For the tapering section of the tenon the TMFC prediction for the inner profile has the same gradient as the outer profile - with a constant thickness of approximately 1.6 mm. The APR profile however has a much steeper gradient giving a variation in tenon thickness - 2.5 mm at the exit and 1.4 mm at 635 mm. For the reasons stated above it is suggested that for this particular result the TMFC method should be trusted over the APR method.

Figure 6.3 is the reconstruction for the Courtois F-crook with a calliper measured length of approximately 1.5 metres. Very good agreement is observed between the APR and TMFC - the reconstructed radii agree to within 0.07 mm for the first 500 mm along the axial length. There is then a significant dip in the TMFC reconstruction - differing from the APR result by 0.6 mm - at around 500 mm. This could be a genuine dent in the crook that APR has smoothed out due to its lower bandwidth. The TMFC method predicts the step at 700 mm which is reflected in the external calliper measurements. After this point both methods agree less well - within approximately 0.4 mm. The overall length is predicted accurately by both methods. Again the TMFC predicts a gradient for the tenon that closely matches the external gradient - with a thickness of 1.5 mm, and the APR predicts a much stepper gradient. However, neither method accurately determines the exit diameter mechanically measured as 10.5 mm $\pm$ 0.1 mm - APR states a value of 10.1 mm, and TMFC, a value of 10.7 mm.

Figure 6.4 is the reconstruction for the Courtois D-crook over 2 metres. This is now clearly too long for the TMFC to reconstruct as the profile is about 1 mm on average larger than the external measurement. This is most likely due to lack of low-frequency high-resolution data. Despite this obvious global over prediction the steps in external diameter at 700 mm and 1.5 m seem to appear in the reconstruction. The APR measurement still looks convincing. This is because of the two-microphone technique employed to obtain the two frequency components below 50 Hz - pulse reflectometry would usually stop working at around 1.4 m[41]. The APR method however underestimates the length of the crook by 4 cm. The exit diameter of this crook is 10.4 mm. Again, neither method obtains this value - TMFC is closest with 10.5 mm, whereas APR displays 10.0 mm. Once again, the TMFC method has produced a taper gradi-

ent that matches well with the gradient of the external profile of the tenon - giving a thickness of 2 mm - and again APR has produced a much steeper plot.

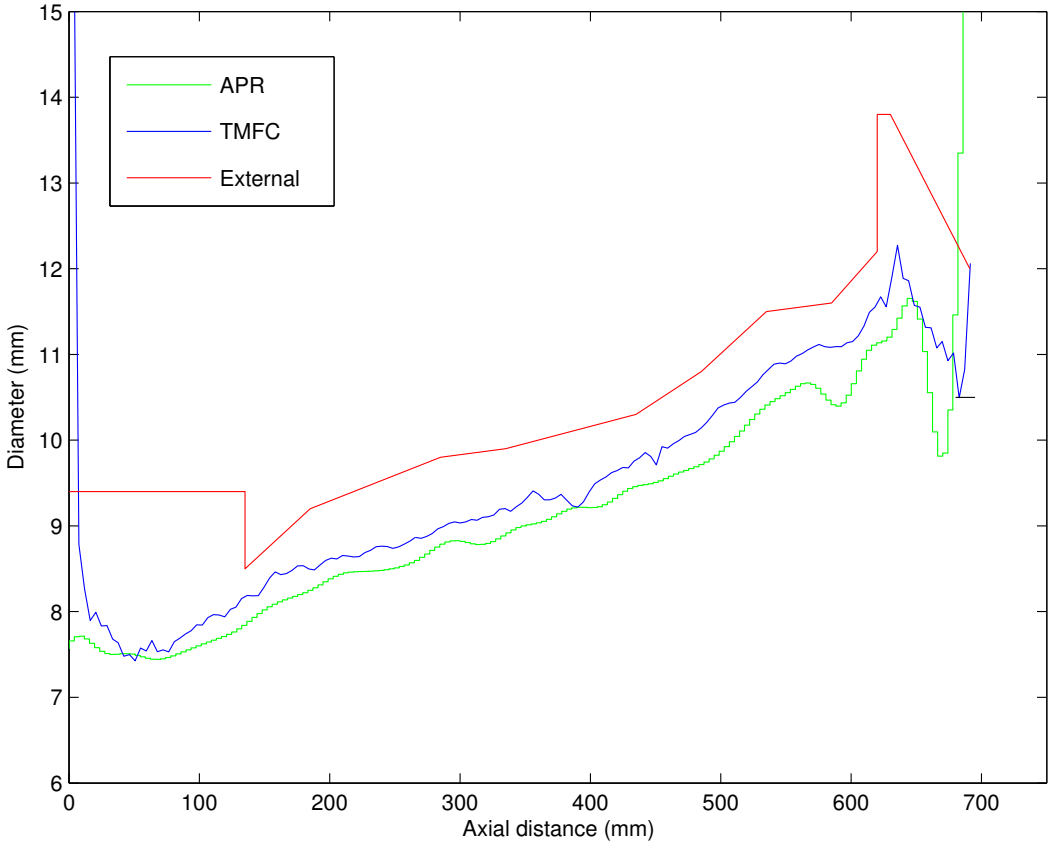

Figure 6.2: Comparison between measuring techniques for the Courtois A-crook: TMFC(blue); APR(green); and Calliper measurements of the external diameter(red).

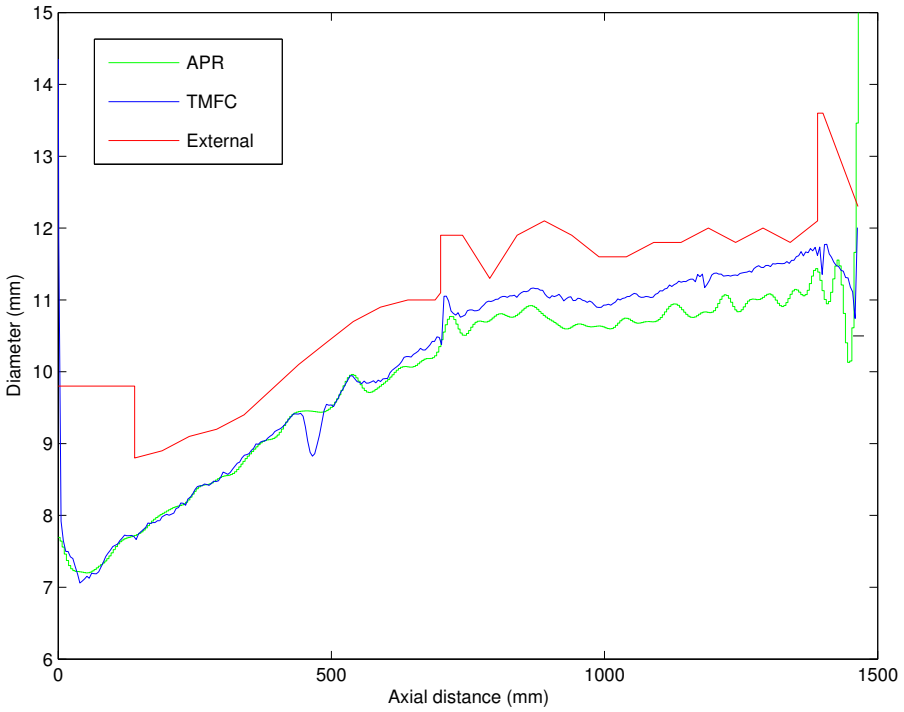

Figure 6.3: Comparison between measuring techniques for the Courtois F-crook: TMFC; APR; and Calliper measurements of the external diameter.

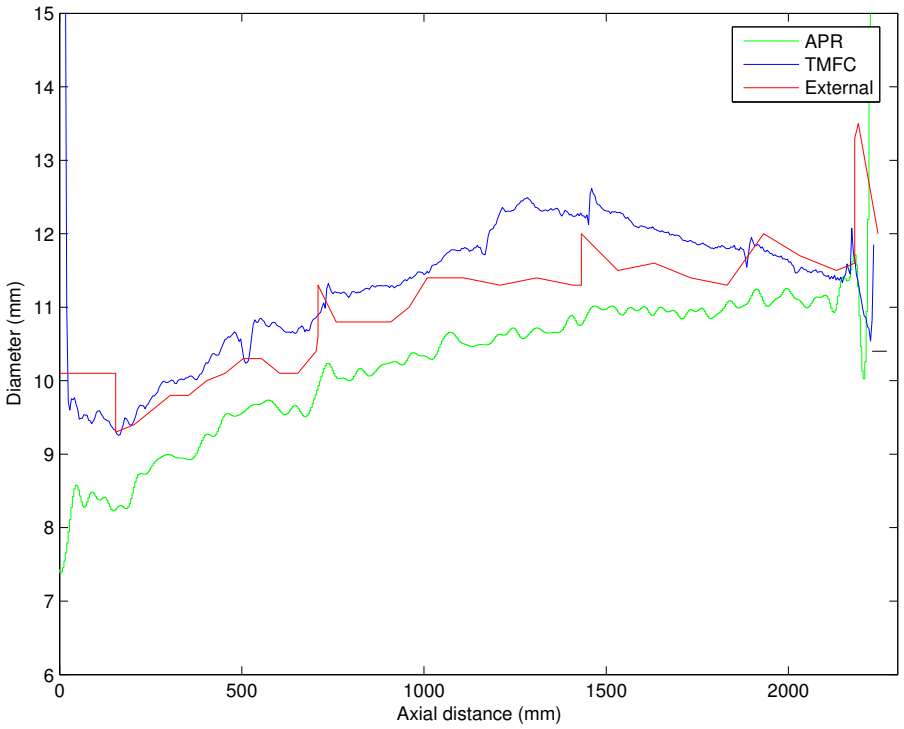

Figure 6.4: Comparison between measuring techniques for the Courtois D-crook: TMFC; APR; and Calliper measurements of the external diameter.

6.3.2 The Courtois Set

The following figures are the pulse reflectometry results for the Courtois set. Figure 6.5 shows again the Courtois F-crook reconstruction of Figure 6.3. The short black line is the internal exit diameter as measured with callipers. We can see that around this point that, despite the Gibbs ripple, the reconstruction passes through this line before increasing suddenly at the open end. The long dashed line is the averaged diameter of the G, F, E, E♭, D, and C crooks at a point just before the tenon.

Figure 6.6 shows the profiles of the Courtois G, F, E, E♭, D and C crooks. We see that all have a very similar profile. This implies that they have all come from the same mandril.

In Figure 6.7, profiles of the Courtois B♭ and A crooks are added. We observe that the crooks have very different profiles and are probably from two different mandrils.

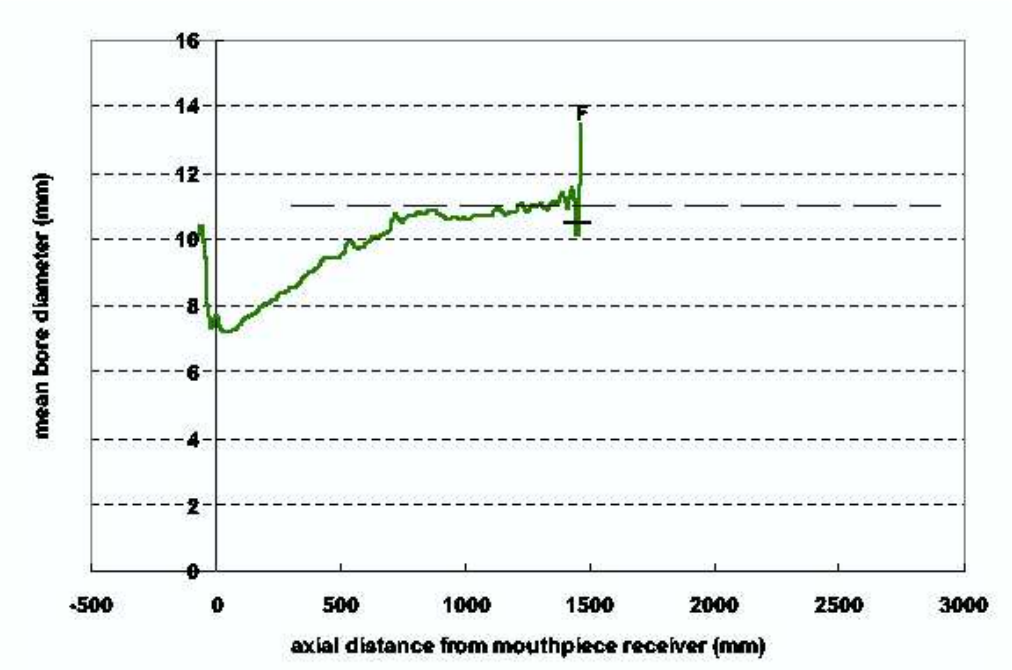

Figure 6.5: The Courtois F-crook as measured by APR.

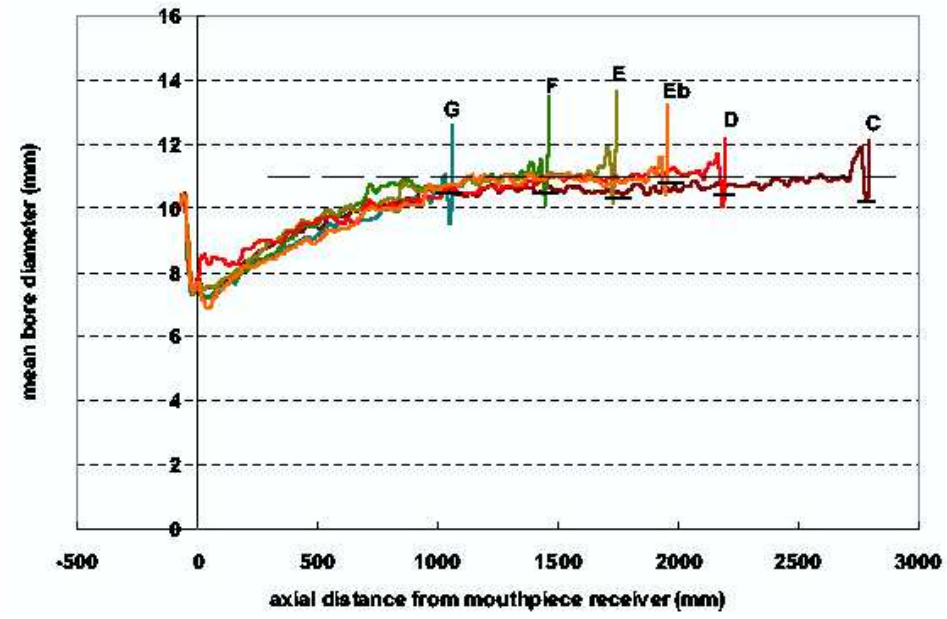

Figure 6.6: The Courtois G, F, E, E♭, D, and C as measured by APR.

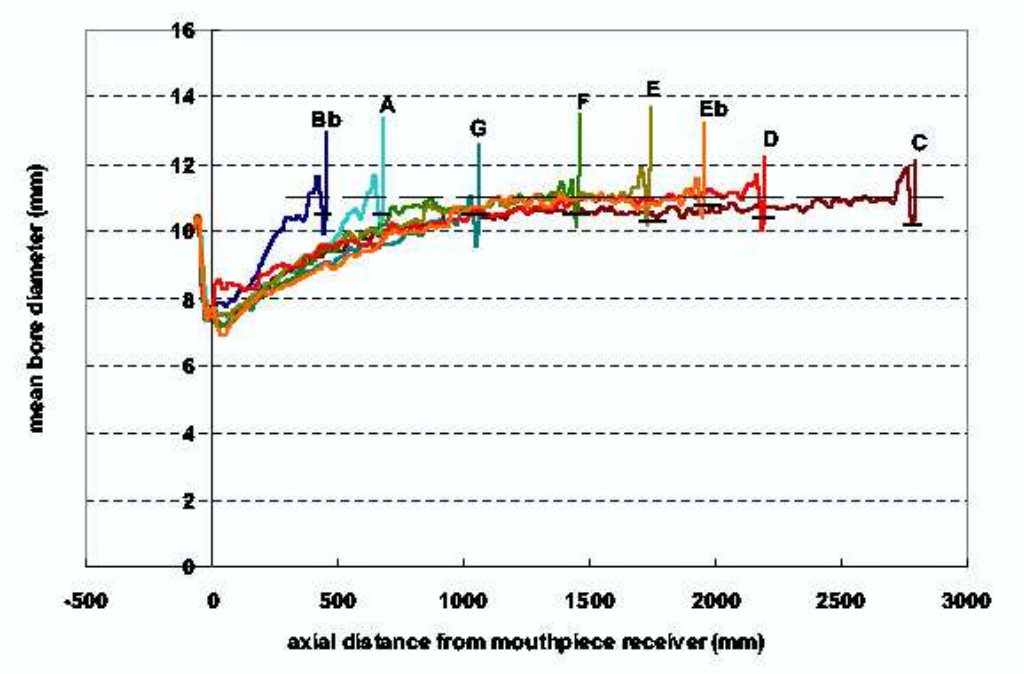

Figure 6.7: The Courtois G, F, E, E♭, D, C, B♭, and A crook as measured by APR.

6.3.3 Variations in Design

Figure 6.8 shows the Courtois F-crook compared with three other F-crooks by different makers: Besson, Gautrot, and Kretzschmann. We see that the Kretzschmann has a similar but smoother profile than that of the Courtois. There are no obvious joins and so this crook was probably made from one piece of tubing. The Besson is again similar to the Courtois but with a pronounced terraced joint at around 750 mm. The same can be said for the Gautrot which has a terraced joint at 700 mm. Apart from these minor details, all four crooks are fairly similar in profile.

Figure 6.9 shows the designs of the more modern-day crooks of Meinl and Boosey & Hawkes. We see that these crooks have a very different and more parabolic profile.

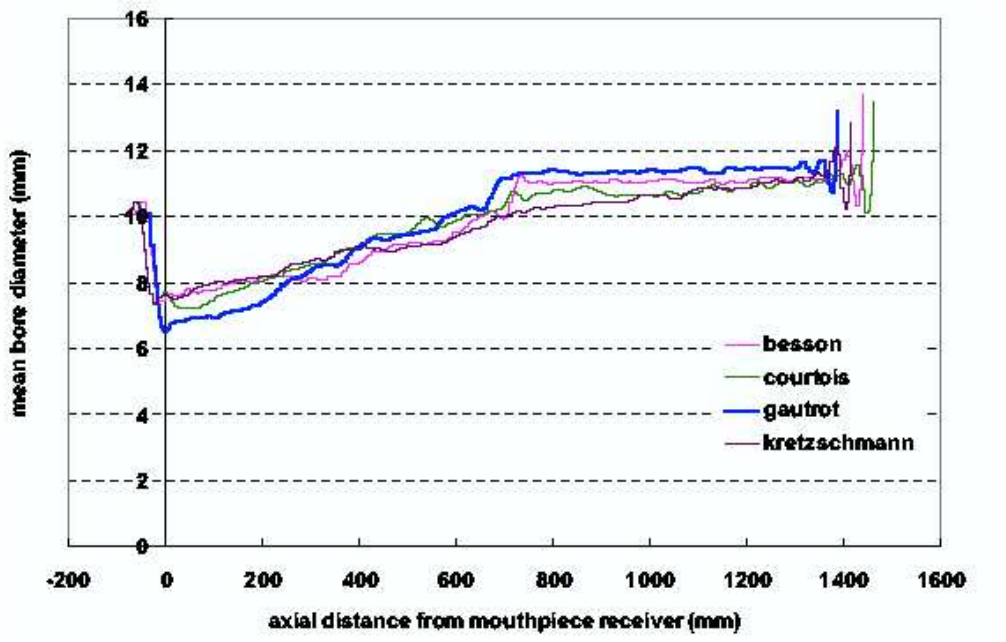

Figure 6.8: F-crooks by Besson, Courtois, Gautrot, and Kretzschmann as measured by APR.

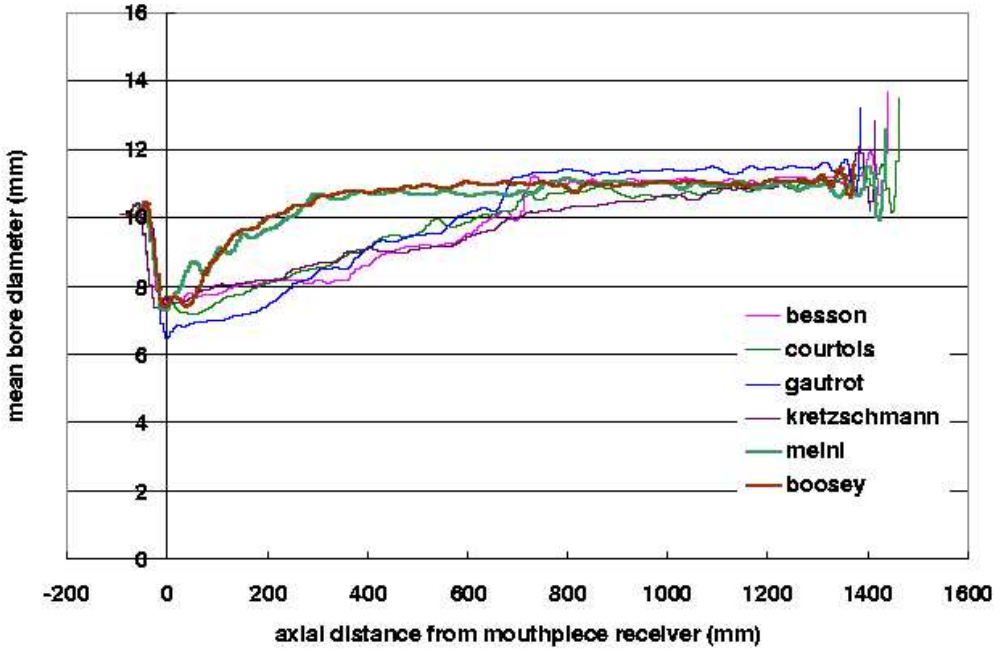

Figure 6.9: F-crooks by Besson, Courtois, Gautrot, and Kretzschmann, Meinl, and Boosey & Hawkes as measured by APR.

6.3.4 Gautrot C-Basso Crook

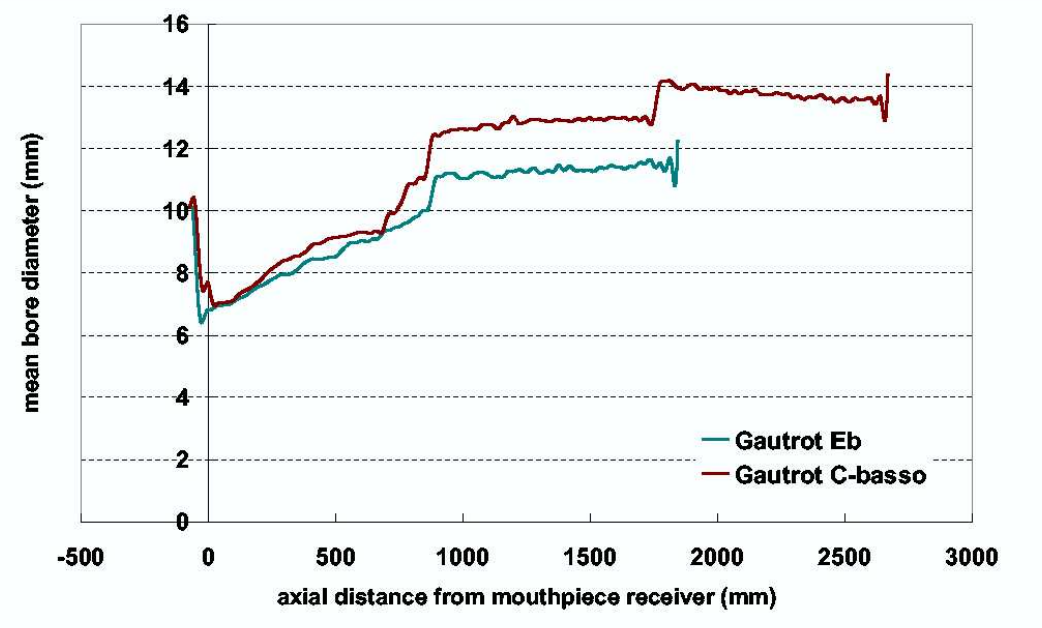

Figure 6.10: A Gautrot C-basso crook measured by APR with an air leak at 700 mm.

Figure 6.10 shows the reconstruction of a Gautrot C-basso crook as measured by pulse reflectometry. It was found that the pulse reflectometry reconstruction predicted two terraced joints for this crook crook. However, the internal diameter as measured by APR was found to be greater than the calliper measurements of the external diameter for the majority of the crook length. The figure also shows the profile of the C-basso crook compared with an E♭ Gautrot crook. The first terraced joint of the C-basso crook occurs at an axial distance of approximately 1 m, the second at about 1.8 m. The calliper measured external bore diameter between these two joints was an average of 12.3 mm. We can see from the figure that the internal bore diameter predicted by APR is greater than this value. From the second terraced joint to the wide end of the crook the calliper measurement of the external diameter was approximately 13.4 mm.

Again, APR predicts an internal diameter greater than this value - over 14 mm at the second terrace joint.

If we now compare the C-basso crook with the E♭ crook we see that both profiles are similar from the origin up to about 700 mm, then the profile of the C-basso increases rapidly. Work done by Sharp et al[57] demonstrates that when a leak occurs in a bore the profile before the point of the leak is reconstructed accurately. At any point after the leak the profile can expand spuriously leading to an overpredicted reconstruction, or worse, a reconstruction with no resemblance to the true profile. This indicates that a leak may be present in the C-basso crook at 700 mm. To verify this, the crook was placed it in a basin of water. One finger was placed over the wide end of the crook. Air was blown from the narrow end. Bubbles were seen to emerge from the predicted position. It should be noted that this leak was not visible to the naked eye.

6.4 Summary

The bore reconstructions of various crooks have been obtained via two different measurement techniques: the time-domain method of acoustic pulse reflectometry; and the frequency-domain TMFC method. For crooks of length less than 1.4 m, the TMFC system has delivered accurate, high-resolution, and promising results. Above 1.4 m however, the 'missing' low frequency data causes the reconstructions to over-predict the profile radii. Theoretically, the relatively new TMFC method should give better results than the well established APR method as the TMFC system measures over a much larger bandwidth than does APR. We hope to improve the results obtained via the TMFC method by reducing the lowest measured frequency from 50 Hz down to 10 Hz. We also hope to increase the frequency resolution of the data from 50 Hz intervals to 10 Hz intervals.

It has been demonstrated that of the Courtois set, the G, F, E, E♭, D, and C appear to have been constructed from the same mandril. The B♭ and A however are from two different mandrils.

Comparing the F-crooks of different makers we saw that the Courtois, Kretzschmann, Besson, and Gautrot (all 18th Century crooks) had a very similar profile. Subtle differences arose from the pronounced terrace joints in the Besson and Gautrot whereas the Kretzschmann had a much smoother profile and so is probably made from one piece of tubing.

On observing the modern crooks of Meinl and Boosey & Hawkes we saw that the profiles were very different and had a more parabolic shape.

Chapter 7

Conclusions and Future Work

7.1 Achievement of aims

The aims of this thesis outlined in Chapter 1 were:

7.1.1 Aim I.

To give a good foundation on the background theory of acoustics, in particular impedance theory, and to develop theoretical models with which to compare experimental results.

The theory of acoustic propagation has been highlighted in Chapter 2 by studying the linear wave equation. The theory of acoustic impedance has been covered in much detail. We start by calculating the input impedance of an object given that we know its internal profile. An expression for the input impedance in terms of a general termination impedance some distance from the reference plane has been derived. From this model the impedance of a complex instrument can be well approximated as a series of cylinders. An example is given where a horn is modelled as a concatenation of short cylinders and the impedance is calculated. Conical and Bessel elements are also used for modelling the horn.

The relation between the impedance and the input impulse response was defined and an analysis of how the quality of the bore reconstruction was related to the frequency range and resolution of the impedance data was given. The example of a closed tube was used to illustrate the method.

7.1.2 Aim II.

To develop a technique - known as the Two-Microphone-Four-Calibration (TMFC) method - capable of measuring the input impedance of musical instruments and instrument components at low frequencies.

This has been achieved by measuring, in general from 50 Hz up to 1 kHz using the partial calibration technique. At frequencies below 1 kHz the full calibration method was impractical due to the large length of calibration tubes needed. For this reason the partial calibration method was introduced to remove the need of these tubes, but at the expense of having to use theoretical plane-wave modelling for the propagation constant. As with the full calibration technique, strategic positioning of the microphones is required when using the partial calibration technique to avoid singular frequencies where the ratio of the two microphone signals is ill-defined. Some success was obtained by measuring as low as 10 Hz using the partial calibration technique; the limiting factor being the large microphone separation distance that is required. Generally, impedance data was collected using a 50 Hz interval.

7.1.3 Aim III.

To develop algorithms for the handling and post-processing of impedance data, involving the calculation of the input impulse response and bore reconstruction for musical instruments and their components.

A post-processing algorithm for removing the impedance corresponding to the coupler was developed. This method operated in the frequency-domain and implemented transmission matrix theory to remove the coupler-matrix from the impedance data. The simplest case of a closed tube of radius equal to that of the measurement duct was measured as propagation in the duct should be entirely planar in nature and show up any discrepancies between experiment and model - no significant discrepancy was observed over the entire bandwidth. The case of a stepped tube was used to see how well the system could predict a sudden change in profile; the point at which the jump occurs and the value of the new radius. It was found that a dc-offset as well as the

inevitable Gibbs' ripple had a detrimental effect on the reconstruction. Once the magnitude and sign of the offset was calculated and compensated for, the reconstructions were accurate to within a fraction of a millimetre.

7.1.4 Aim IV.

To use the TMFC technique, Acoustic Pulse Reflectometer (APR), and Brass Instrument Analysis System (BIAS) to solve design problems and investigate how instruments - historical and contemporary - have been manufactured. This will also involve giving a comparison between the three methods in terms of advantages/disadvantages and limitations.

A variety of instruments and instrument components have been investigated including horns, mouthpieces, trumpets, leadpipes, and French horn crooks. The length of these entities has varied from tens of millimetres to a few metres. The shorter of the instruments have proven a relative success. The longer instruments are still problematic. The measurement of longer instruments would thus require obtaining TMFC data at a higher frequency resolution.

At the end of Chapter 5, a study of two French horn F-crooks was carried out. The problem of why one was perceived to play poorly was revealed when a bore reconstruction of the crook was compared with a well playing crook. This showed that the poor crook had major deviations in its profile. These deviations are caused by small dents that the instrument has developed over the years.

From the point of view of historians and instrument makers, Chapter 6 displays valuable information that has been obtained regarding the design of various makes of crook. It has been demonstrated that most of the Courtois set were from the same mandril with the exception of B♭ and A. Of the 18th Century crooks measured most were found to have very similar profiles with the exception of various join and terrace patterns. The measurement of the Kretzschmann F-crook indicates that it is made from one piece of tubing. It was found that the more modern day crooks of Meinl and Boosey & Hawkes have a more parabolic profile compared with the straighter profiles of the earlier Courtois, Kretzschmann and such like.

A detailed description of the three acoustical systems - TMFC, APR, and BIAS - was given. APR was compared with TMFC in Chapter 6 when studying the French horn crooks. For the shorter crooks both methods gave sensible results. TMFC had a better resolution due to its superior bandwidth but the APR results are more reliable for the longer instruments due to improvements made by Kemp to obtain data at low frequencies[41]. The TMFC impedance result for a closed tube was compared with the BIAS result and plane-wave theory. It was found that TMFC agreed more closely with theory than BIAS did. The TMFC system's advantage over APR and BIAS is its high frequency range: 20 kHz compared with APR - 10 kHz[24], and BIAS - about 4 kHz. It was shown in Chapter 2 that the highest frequency component determines the axial resolution of the bore reconstruction. For the TMFC system this is a value of 4.3 mm compared with the APR value which is double this - 8.6 mm. The TMFC system can obtain higher frequency data than is possible with APR but lower frequency data is required for accurate reconstructions of long instruments.

Disadvantages of the TMFC system are that it is not as compact as the APR or BIAS system. It takes a long time to get full bandwidth data, four calibrations, calibration of microphones, and then finally measurement of the instrument. The time to obtain a full bandwidth of data for the TMFC system is typically of the order of hours compared with of the order of minutes for the APR and BIAS systems.

7.1.5 Aim V.

To suggest future work in terms of improvements to the TMFC method, algorithms to be developed, and instruments of interest to be studied.

This is outlined in the following section.

7.2 Future Work and Improvements to TMFC

7.2.1 Leak Detection

One suggestion for post-doctoral and postgraduate research includes developing algorithms for the measurement of narrow diameter bores (comparable to that of the current

measurement duct) with multiple leaks[57, 60, 61]. Both the layer-peeling and optimisation techniques of bore reconstruction have been successful for non-leaking bores. However, when a bore contains one or more leaks, only the profile before the point of the leak is accurately reconstructed. After the leak, the profile wildly expands, bearing no resemblance to the true profile. It is hoped that both the layer-peeling and optimisation method can be modified to calculate accurately the length of a leaking duct, the position, and diameter of the holes. Providing this proves successful, non-cylindrical ducts may also be studied.

7.2.2 Wide Diameter Bores: Higher Modes

As well as narrow bores, wide diameter non-leaking bores is a proposed avenue of study. As discussed, when the study object has a diameter equal to that of the measurement duct, the wave inside the system can be assumed to be planar- also assuming that the highest frequency component used as an excitation signal is *less* than the cut-on frequency of the duct. This frequency is inversely proportional to the diameter of the duct, so as the diameter is increased, the cut-on frequency decreases and higher modal propagation becomes more and more significant. Proposed work includes the experimental measurement of the first higher mode of excitation in the measurement duct. Since the first higher mode encountered is the anti-symmetric (1,0) mode, this could be done by placing a small microphone at 90 degrees to the main row of microphone positions used for planar mode measurements. This would allow the impedance information containing the plane and higher mode component to be decoupled. Then the plane component could be used with the standard reconstruction algorithm. One complication that arises is that some energy will have been lost from the plane waves component to the higher modes. Alternatively, some computational and theoretical work could be carried out to incorporate higher modes, but this has so far proven to be a challenge as it is mathematically complex and includes the added problem of the Gibbs' phenomenon inherently present in all reconstructions due to their Fourier nature.

7.2.3 Signal-to-Noise-Ratio and Distortion Control

A problem encountered during measurements is the variation in loudness within the duct during excitation. This can cause distortion in one or both of the microphones, which will require that particular phase of the experiment to be repeated. Alternatively, the volume at a microphone can become very low and noise can become an issue. It is not a requirement that the source volume remain constant for the duration of the measurement of the study object, only during calibration of the microphones. Therefore a possible improvement to the system to avoid unnecessary repetition of measurements would be to write a piece of software with a feedback loop to control the loudspeaker volume and avoid particularly loud or quiet signals at the microphones.

7.2.4 Wall Vibrations

Other work that was considered included investigating the effect of wall vibrations on the impedance/musicality of a brass instrument[110, 111, 112]. The method involves measuring the impedance for a selected instrument, allowing it to vibrate freely as normal, and then repeating the experiment with the instrument packed in sandbags to damp out the wall vibrations as much as possible. Care needs to be taken near the bell of the instrument as the presence of the bags could significantly adjust the radiation impedance of the instrument.

7.2.5 Radiation Impedance

The radiation impedance of a flaring bell is rather difficult to measure by acoustic means. For this reason it is suggested that the TMFC system could be modified for measuring radiation impedance as well as input impedance. This could be achieved as follows. As we saw in the section on transmission matrix theory, the input impedance is given as

$$Z_{\text{IN}} = \frac{aZ_r + b}{cZ_r + d}. \tag{7.1}$$

At the flaring end of the bell the load impedance, $Z_{\mathcal{L}}$, has been replaced by the radiation impedance, Z_r. We have four unknowns a, b, c, and d to determine. We can

do this by removing the bell, leaving the relatively straight section, and attaching four open tubes of different lengths with known radiation impedance and measuring the input impedance for each case. Once we have the entries for the transmission matrix the radiation impedance is found by re-arranging equation (7.1)

$$Z_r = -\frac{b - dZ_{\text{IN}}}{a - cZ_{\text{IN}}} \tag{7.2}$$

and then measuring the input impedance of the instrument with the bell attached.

7.2.6 The French Horn

French horn players sometimes put their hand in the bell to adjust, or bend, the pitch of the note they are playing. An interesting question to ask is: does the presence of a hand in the bell have a significant effect at higher frequencies as well as at low frequencies. TMFC is a good possible candidate for answering this question due to its ability to measure at higher frequencies than possible with APR or BIAS. Again, to notice small differences in the impedance curve of the bell on its own compared with a hand in the bell would require high resolution data.

Appendix A

Mathematical Formulae and Physical Constants

The following operators, functions, and trigonometric identities are used throughout this thesis and are provided here as a quick reference.

Euler Identity

$$\exp(i\theta) = \cos\theta + i\sin\theta \tag{A.1}$$

Double-angle formulae

$$\sin(\theta \pm \phi) = \sin\theta\cos\phi \pm \cos\theta\sin\phi \tag{A.2}$$

$$\cos(\theta \pm \phi) = \cos\theta\cos\phi \mp \sin\theta\sin\phi \tag{A.3}$$

Hyperbolic identities

$$\cosh\theta = \frac{1}{2}[\exp(i\theta) + \exp(-i\theta)] \quad , \quad \sinh\theta = \frac{1}{2}[\exp(i\theta) - \exp(-i\theta)] \tag{A.4}$$

$$\sinh(i\theta) = i\sin(\theta) \quad , \quad \sin(i\theta) = i\sinh(\theta) \tag{A.5}$$

$$\cosh(i\theta) = \cos(\theta) \quad , \quad \cos(i\theta) = \cosh(\theta) \tag{A.6}$$

Gradient operator

$$\nabla \equiv \hat{x}\frac{\partial}{\partial x} + \hat{y}\frac{\partial}{\partial y} + \hat{z}\frac{\partial}{\partial z} \tag{A.7}$$

Divergence operator

$$\nabla\cdot \equiv \frac{\partial}{\partial x} + \frac{\partial}{\partial y} + \frac{\partial}{\partial z} \tag{A.8}$$

The Laplacian operator

Rectangular coordinates (x, y, z)

$$\nabla^2 \equiv \frac{\partial^2}{\partial x^2} + \frac{\partial^2}{\partial y^2} + \frac{\partial^2}{\partial z^2} \tag{A.9}$$

Spherical-polar coordinates (r, θ, ϕ)

$$\nabla^2 \equiv \frac{1}{r^2}\frac{\partial}{\partial r}\left(r^2\frac{\partial}{\partial r}\right) + \frac{1}{r^2\sin\theta}\frac{\partial}{\partial\theta}\left(\sin\frac{\partial}{\partial\theta}\right) + \frac{1}{r^2\sin^2\theta}\frac{\partial^2}{\partial\phi^2} \tag{A.10}$$

Cylindrical coordinates (r, ϕ, z)

$$\nabla^2 \equiv \frac{1}{r}\frac{\partial}{\partial r}\left(r\frac{\partial}{\partial r}\right) + \frac{1}{r^2}\frac{\partial^2}{\partial\phi^2} + \frac{\partial^2}{\partial z^2} \tag{A.11}$$

Bessel function of the first kind

$$J_\alpha(x) = \sum_{m=0}^{\infty}\frac{(-1)^m}{m!\Gamma(m+\alpha+1)}\left(\frac{x}{2}\right)^{2m+\alpha} \tag{A.12}$$

where

$$\Gamma(z) = \int_0^\infty t^{z-1}\exp(-t)\mathrm{d}t \tag{A.13}$$

Commonly used values

c	speed of sound in air at room temperature	345 m/s
$\mathcal{R}$	ideal gas constant	8.31 J/K/mol
γ	adiabatic constant	1.4
$\mathcal{B}_\mathcal{M}$	bulk modulus	1.42105 Pa
ρ_0	density of air	1.292 kg/m^3

Appendix B

Transmission Matrix Theory

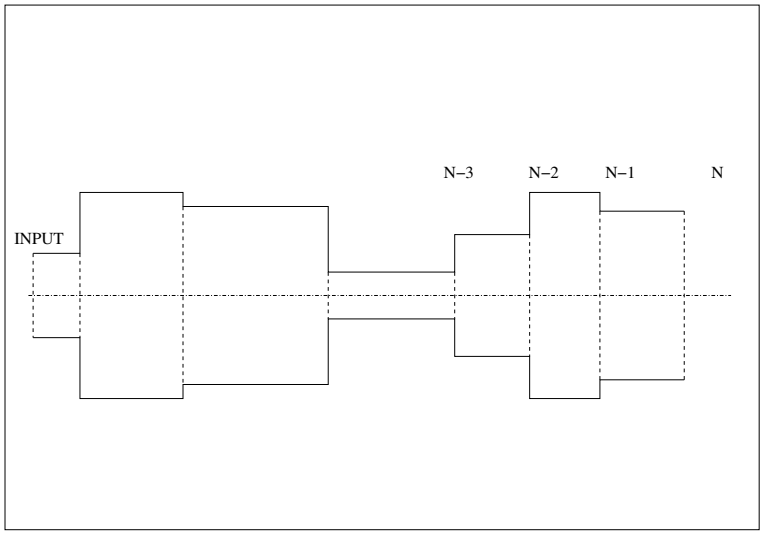

Figure B.1: Transmission matrix theory (TMT). The impedance at each interface can be represented by a 2×2 matrix. If the input impedance of the N cylinder object is known, the input impedance of the $N-1$ cylinder object can be derived.

Thus far we have used equation (2.53) to derive the impedance of some simple cylindrical objects by starting with the load impedance and working back to the input impedance by nesting the equations. As a reminder, this equation has the form

$$Z_{\text{IN}} = Z_c \left[\frac{Z_{\mathcal{L}} \cos(\Gamma \mathcal{L}) + i Z_c \sin(\Gamma \mathcal{L})}{i Z_{\mathcal{L}} \sin(\Gamma \mathcal{L}) + Z_c \cos(\Gamma \mathcal{L})} \right]. \tag{B.1}$$

It is sometimes more useful to represent each change in cross-section by a 2×2 transmission matrix $\mathbf{H}$. This strategy is known as *transmission matrix theory (TMT)*. Here we will outline how this theory works. We can rewrite equation (B.1) as

$$Z_{\text{IN}} = \frac{a Z_{\mathcal{L}} + b}{c Z_{\mathcal{L}} + d} \tag{B.2}$$

where

$a = \cos(\Gamma\mathcal{L})$, $b = iZ_c \sin(\Gamma\mathcal{L})$, $c = \frac{1}{Z_c} i \sin(\Gamma\mathcal{L})$, and $d = \cos(\Gamma\mathcal{L})$. These entries form the transmission matrix

$$\mathbf{H} = \begin{pmatrix} a & b \\ c & d \end{pmatrix}. \tag{B.3}$$

For the general case, as shown in Figure B.1, consisting of N sections where the object is terminated by a load impedance $Z_{\mathcal{L}}$, the input impedance is the product of the matrices that represent each interface

$$Z_{\text{IN}} = \prod_{k=1}^{N} \mathbf{H}_k \begin{pmatrix} Z_{\mathcal{L}} \\ 1 \end{pmatrix} \tag{B.4}$$

where k is a dummy index,

$$\mathbf{H}_k = \begin{pmatrix} \cos(\Gamma\mathcal{L}_k) & iZ_c \sin(\Gamma\mathcal{L}_k) \\ i\frac{1}{Z_c} \sin(\Gamma\mathcal{L}_k) & \cos(\Gamma\mathcal{L}_k) \end{pmatrix} \tag{B.5}$$

and $\mathcal{L}_k$ is the length of section between plane k and plane $k+1$. Note that the input impedance here is rewritten in a 2×1 matrix form

$$\begin{pmatrix} Z_{\text{IN}} \\ 1 \end{pmatrix}. \tag{B.6}$$

So we know the input impedance of the N section object. Suppose we wish to remove the first cylinder ($k = 1$) closest to the input. The new impedance $Z_{\text{IN}}^{\text{new}}$ - which is also a 2×1 matrix - can be expressed in terms of the original impedance

$$Z_{\text{IN}}^{\text{new}} = \prod_{k=2}^{N} \mathbf{H}_k \begin{pmatrix} Z_{\mathcal{L}} \\ 1 \end{pmatrix}, \tag{B.7}$$

$$= \mathrm{H}_1^{-1} \prod_{k=1}^{N} \mathbf{H}_k \begin{pmatrix} Z_{\mathcal{L}} \\ 1 \end{pmatrix}, \tag{B.8}$$

$$Z_{\text{IN}}^{\text{new}} = \mathbf{H}_1^{-1} \begin{pmatrix} Z_{\text{IN}} \\ 1 \end{pmatrix}. \tag{B.9}$$

So, in words, the new input impedance, $Z_{\text{IN}}^{\text{new}}$, of the $N-1$ cylinder object is equal to the original input impedance, Z_{IN}, of the N cylinder object multiplied by the inverse of the transmission matrix representing the removed first cylinder, $\mathbf{H}_1^{-1}$. As stated, $Z_{\text{IN}}^{\text{new}}$ is in 2×1 matrix form

$$Z_{\text{IN}}^{\text{new}} = \begin{pmatrix} \alpha \\ \beta \end{pmatrix}. \tag{B.10}$$

To express the impedance as a 1-D vector we divide α by β.

Appendix C

Gibbs' Phenomenon

Fourier's theorem states that any signal $f(t)$ for which $f(t+T) = f(t)$ is said to be periodic and can be represented by a summation of sines and cosines with frequencies equal to an integer multiple of the fundamental, $f = 1/T$.

As the number of terms used in the series increases, the representation of the signal is improved in accuracy. However, close to a jump (discontinuity) there is a small overshoot which, rather than tending to zero, approaches a finite limit of approximately 18%. This is demonstrated in the following example. For a square wave the Fourier expression has the form

$$f(t) = \sum_{j=2}^{\infty} \frac{1}{j-1} \sin[(j-1)x]. \tag{C.1}$$

where the dummy index j is even. If we approximate this expression using a summation of N terms we obtain the following figures where $N = 8$, 16, 32, and 64 respectively. As the number of terms used increases it can be clearly seen that the profile is exaggerated slightly at each discontinuity. This is the Gibbs' phenomenon.

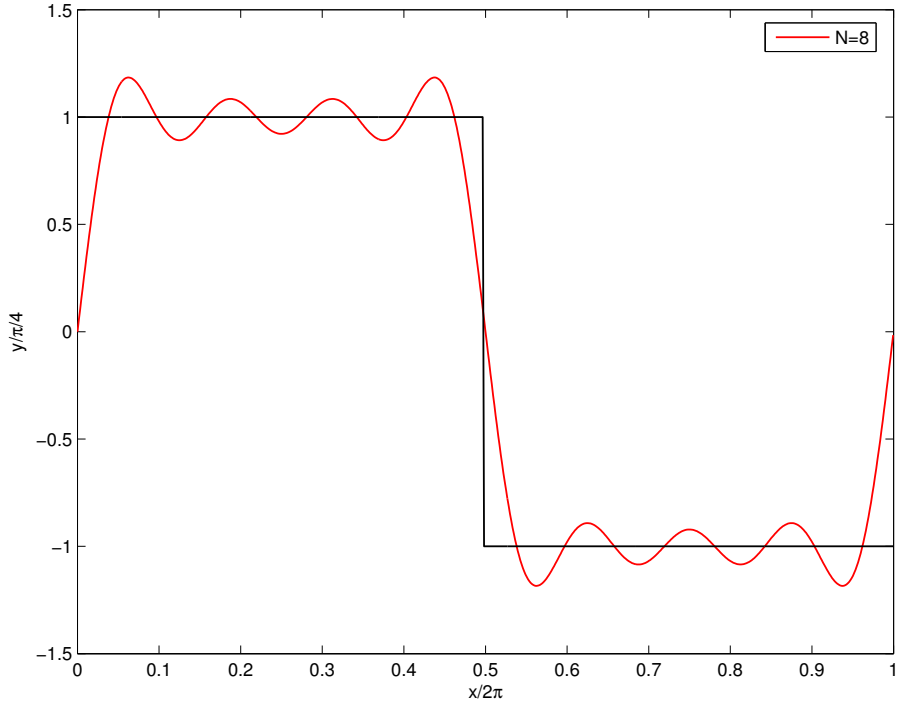

Figure C.1: Fourier representation of a square wave; 8 terms.

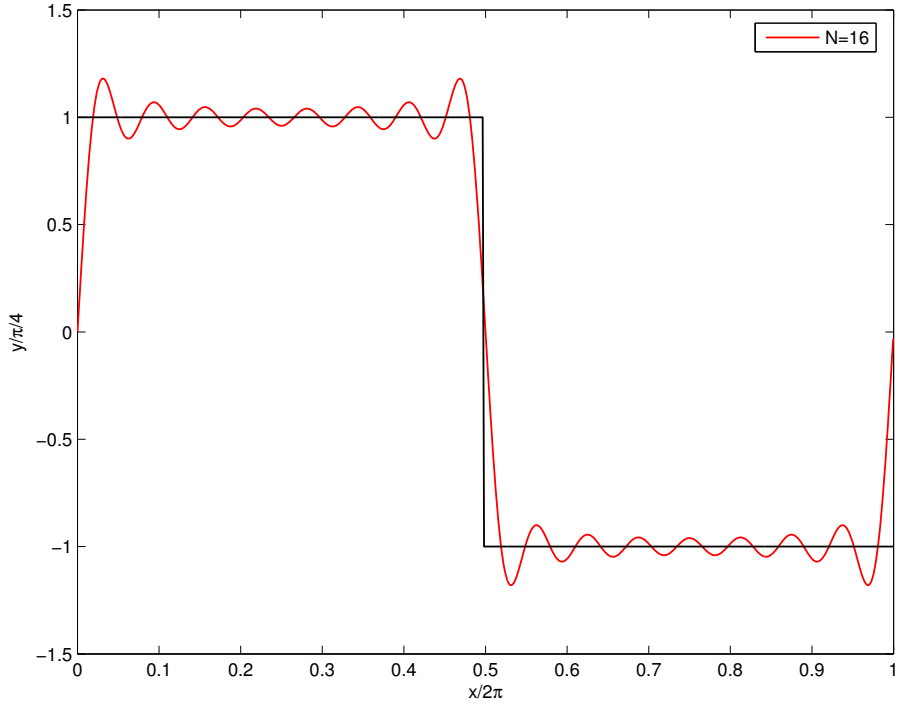

Figure C.2: Fourier representation of a square wave; 16 terms.

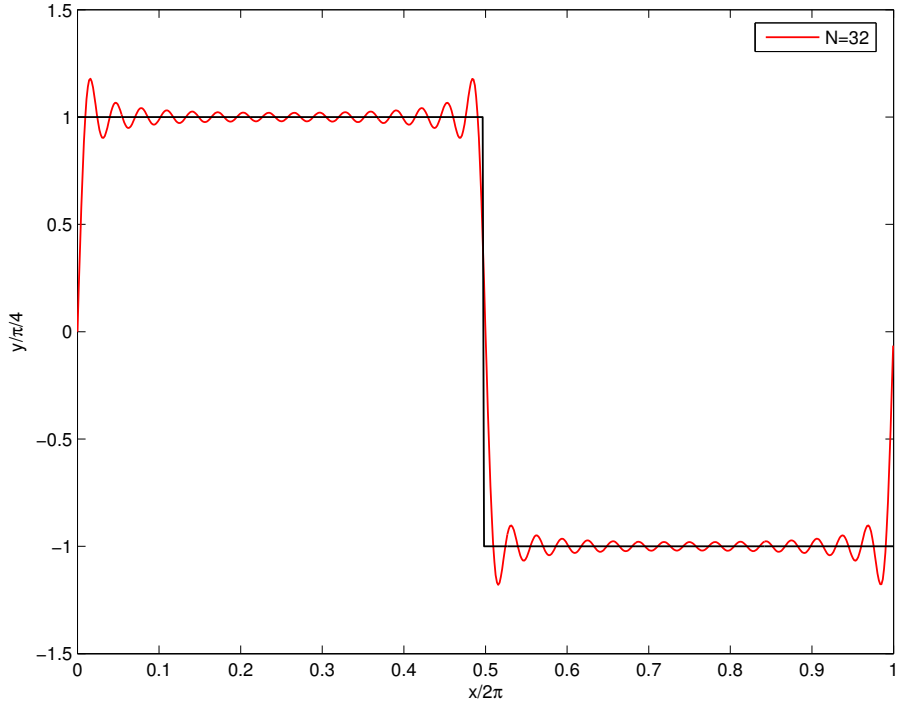

Figure C.3: Fourier representation of a square wave; 32 terms .

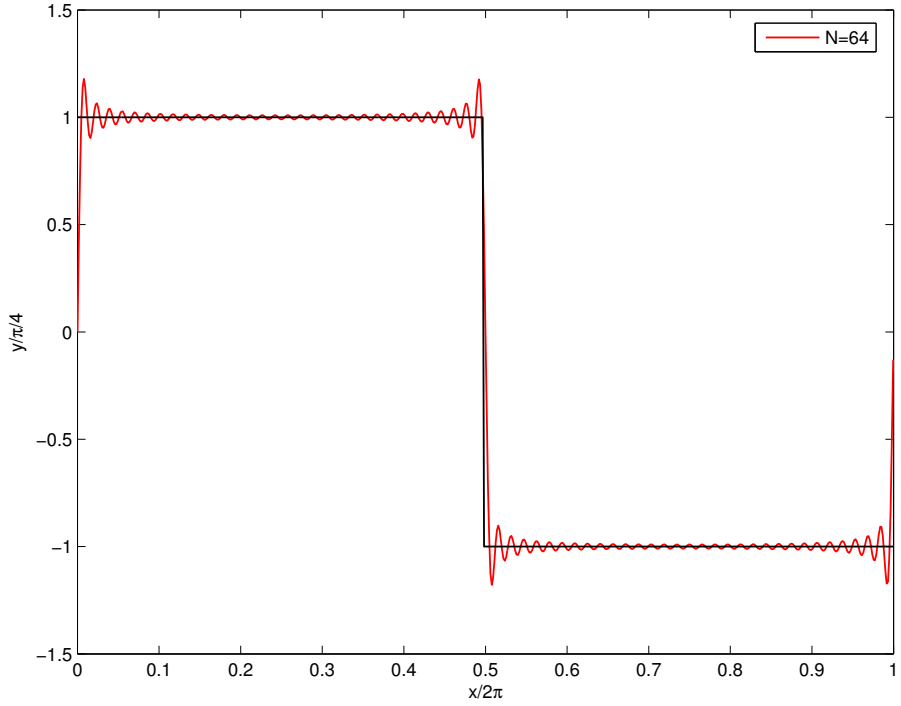

Figure C.4: Fourier representation of a square wave; 64 terms.

Appendix D

Courtois crooks

The following figures show the input impulse response and bore reconstruction for the set of Courtois crooks.

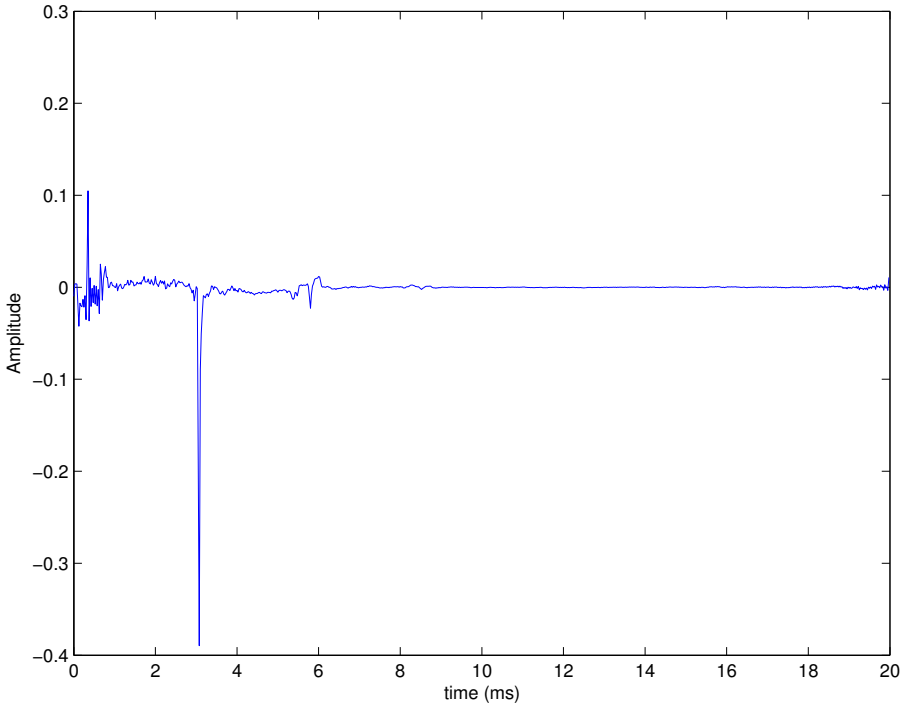

Figure D.1: IIR for the Courtois B♭ crook.

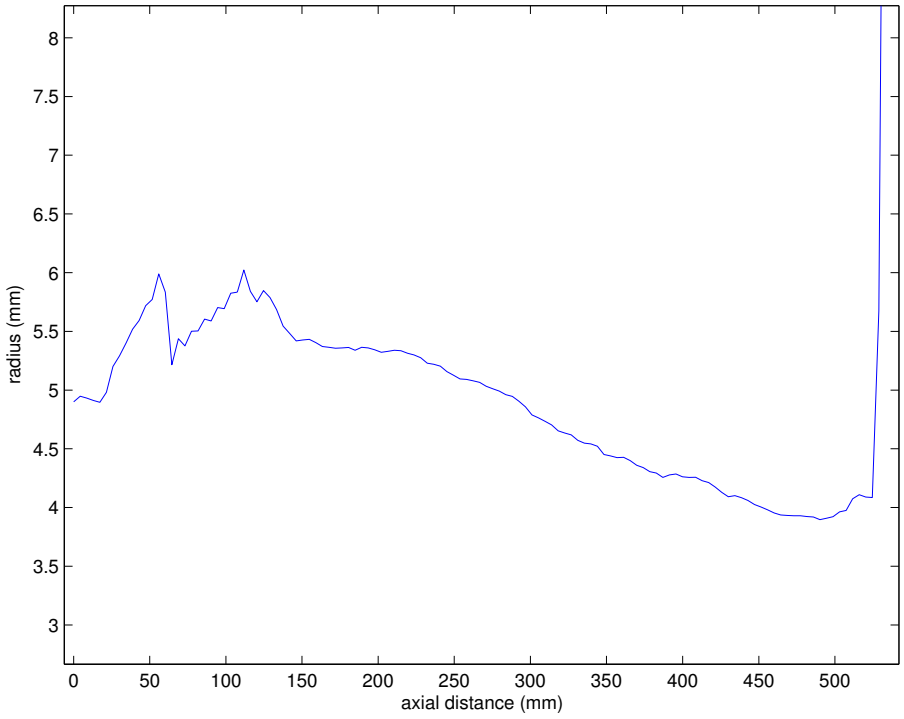

Figure D.2: Bore reconstruction for the Courtois B♭ crook.

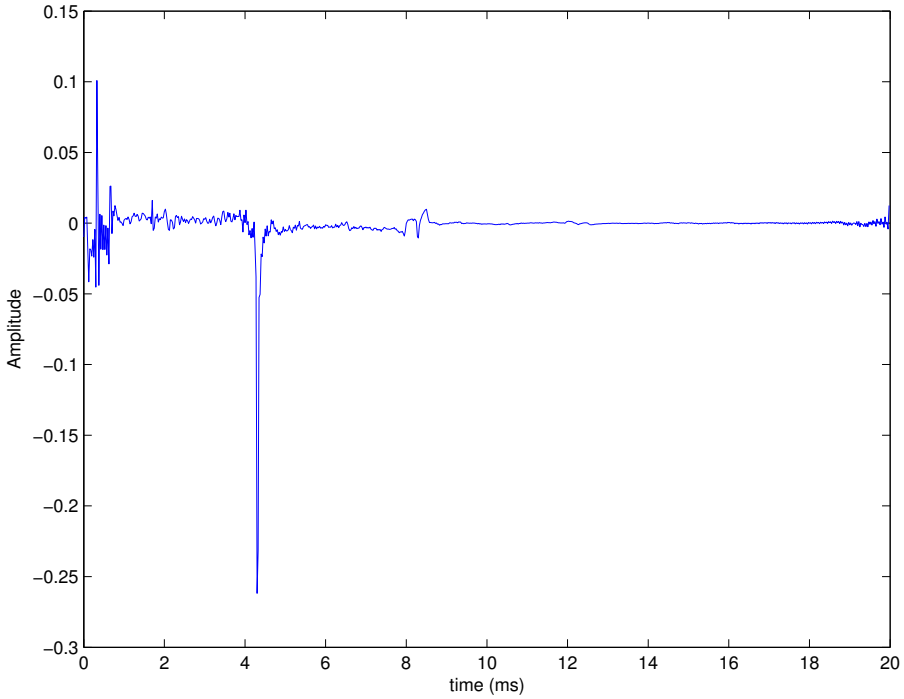

Figure D.3: IIR for the Courtois A crook.

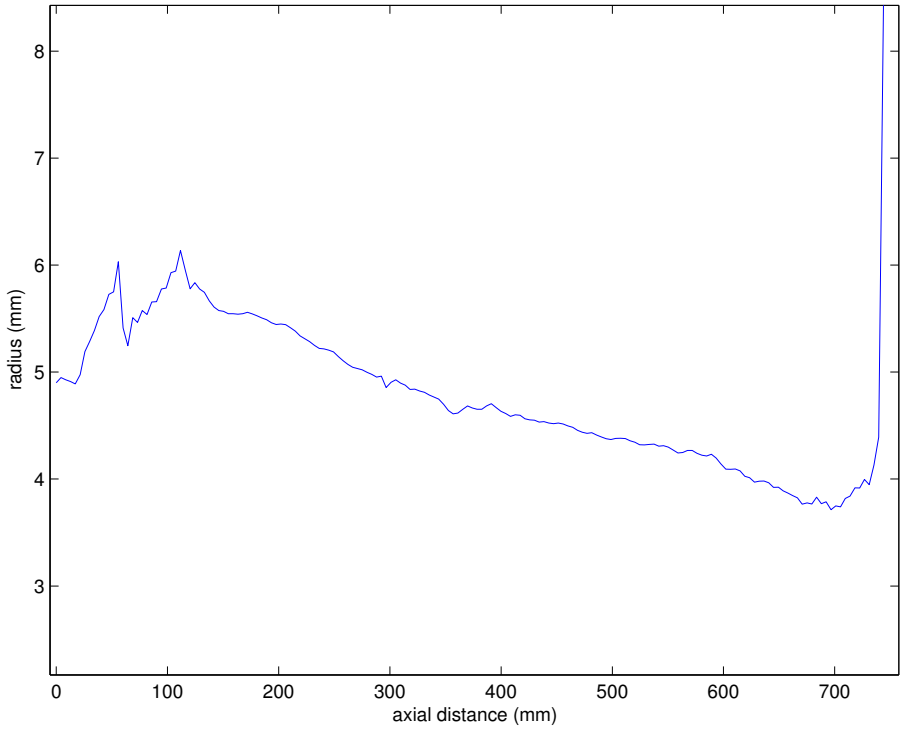

Figure D.4: Bore reconstruction for the Courtois A crook.

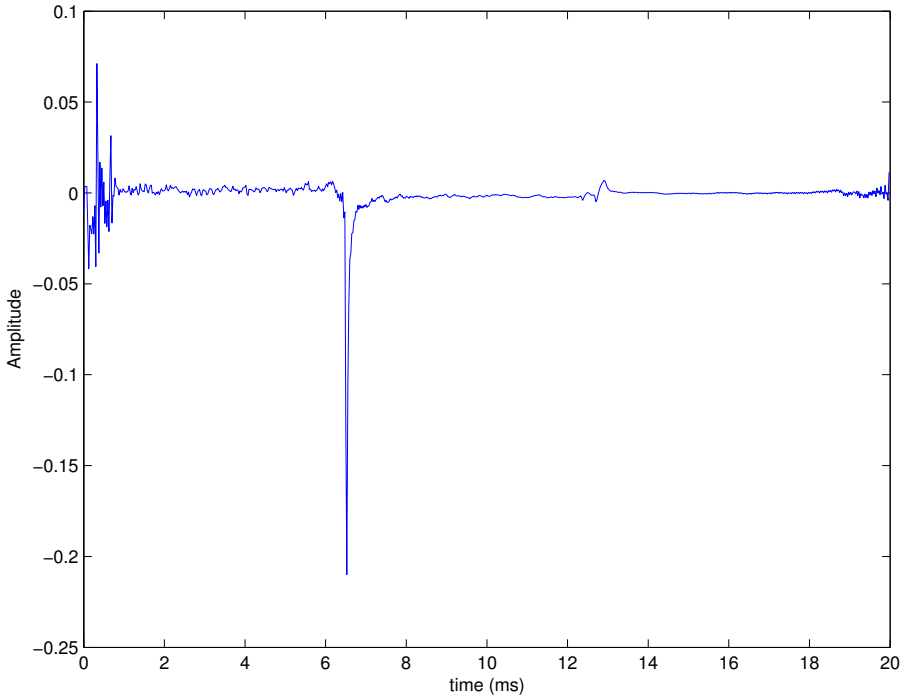

Figure D.5: IIR for the Courtois G crook.

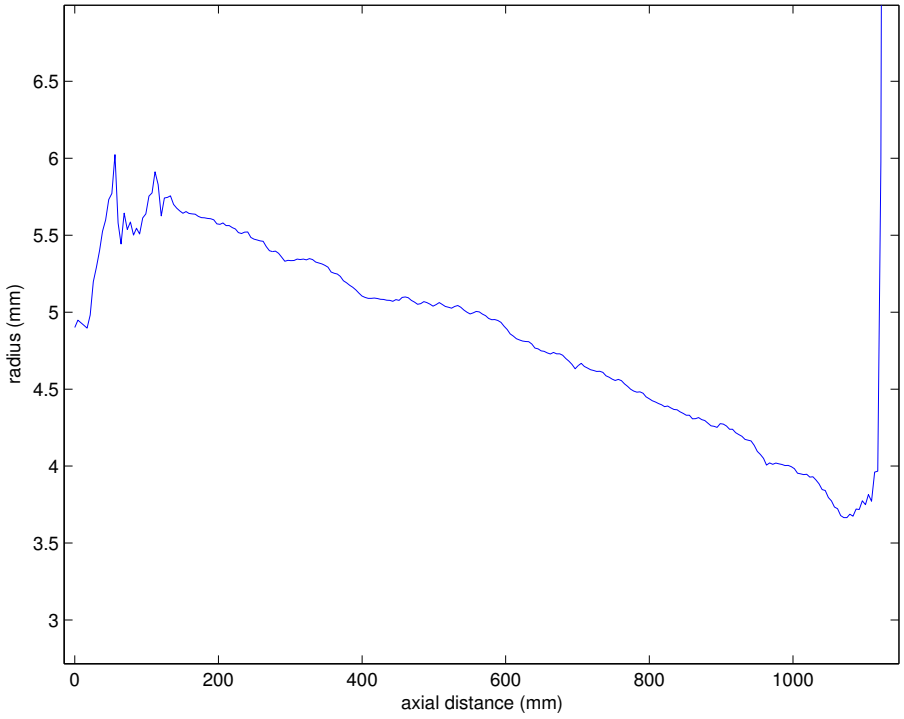

Figure D.6: Bore reconstruction for the Courtois G crook.

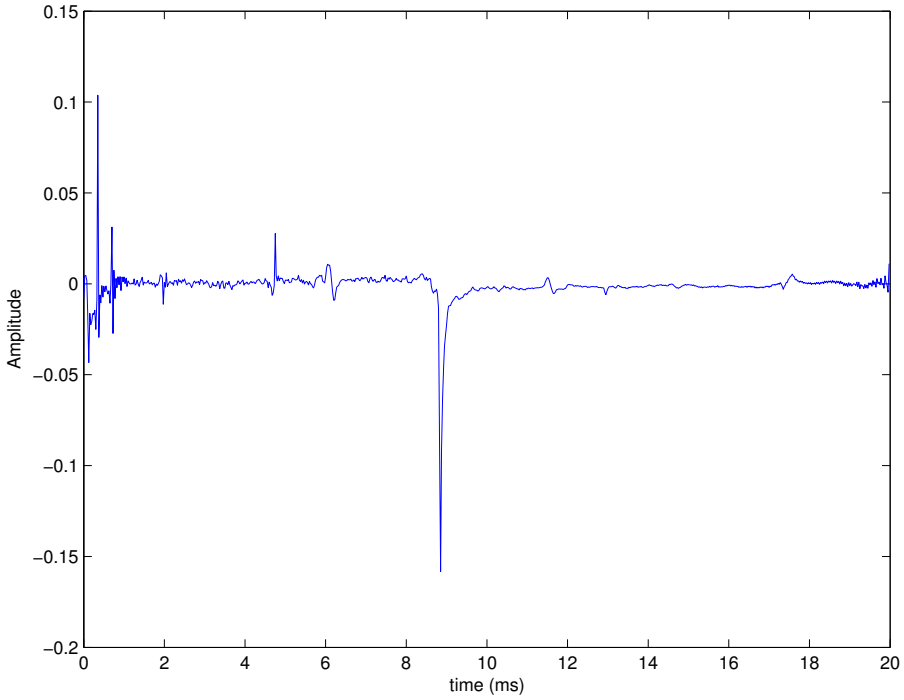

Figure D.7: IIR for the Courtois F crook.

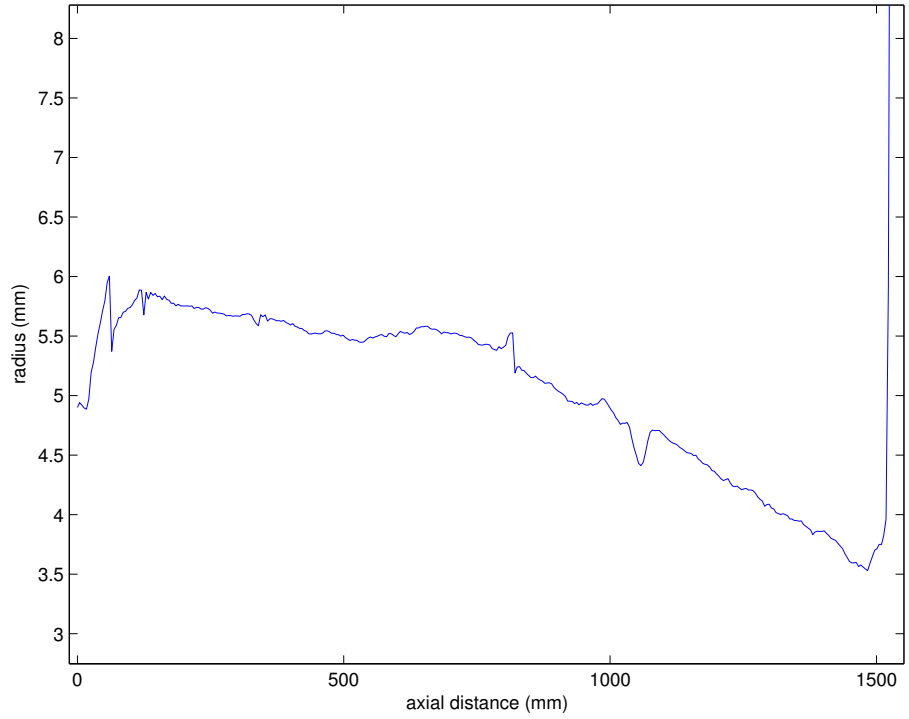

Figure D.8: Bore reconstruction for the Courtois F crook.

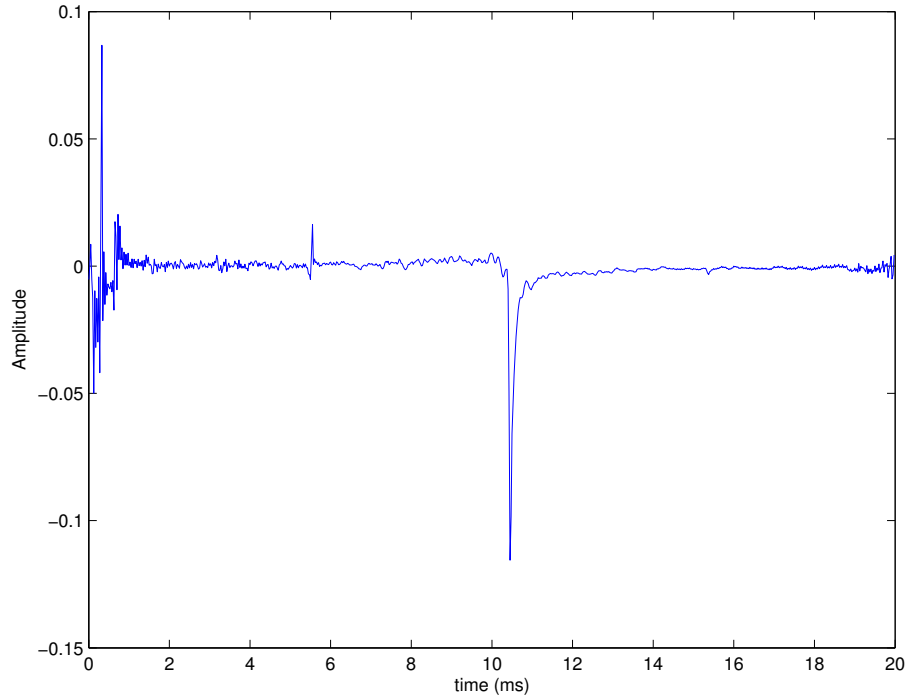

Figure D.9: IIR for the Courtois E crook.

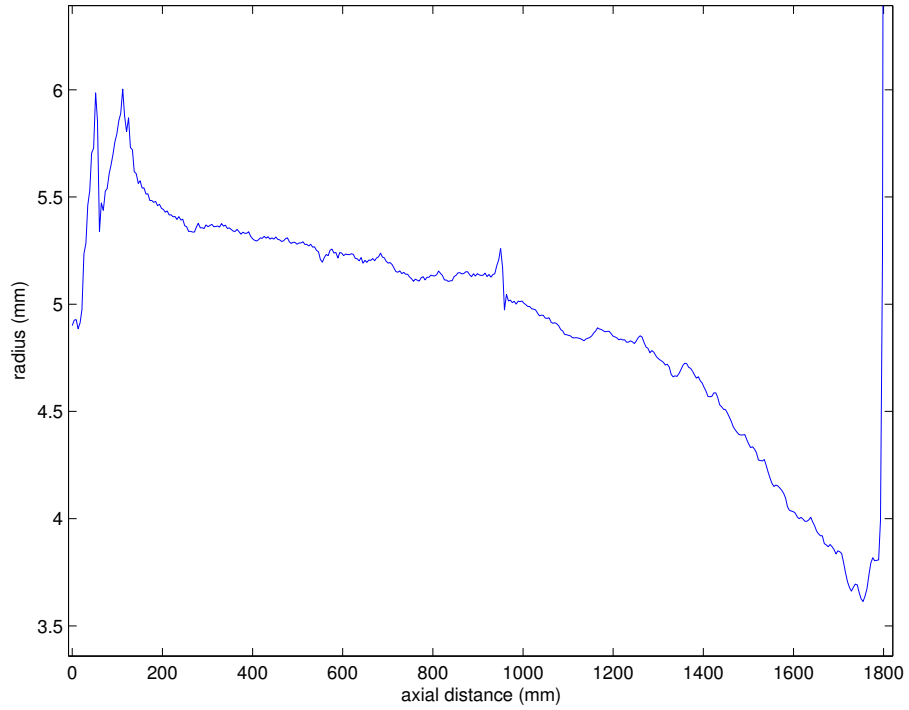

Figure D.10: Bore reconstruction for the Courtois E crook.

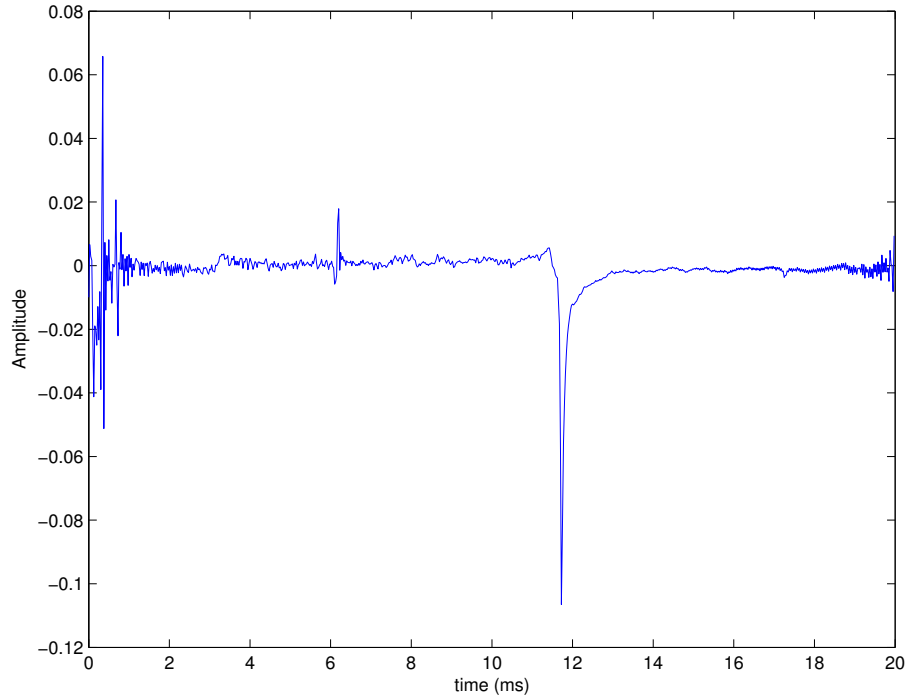

Figure D.11: IIR for the Courtois E♭ crook.

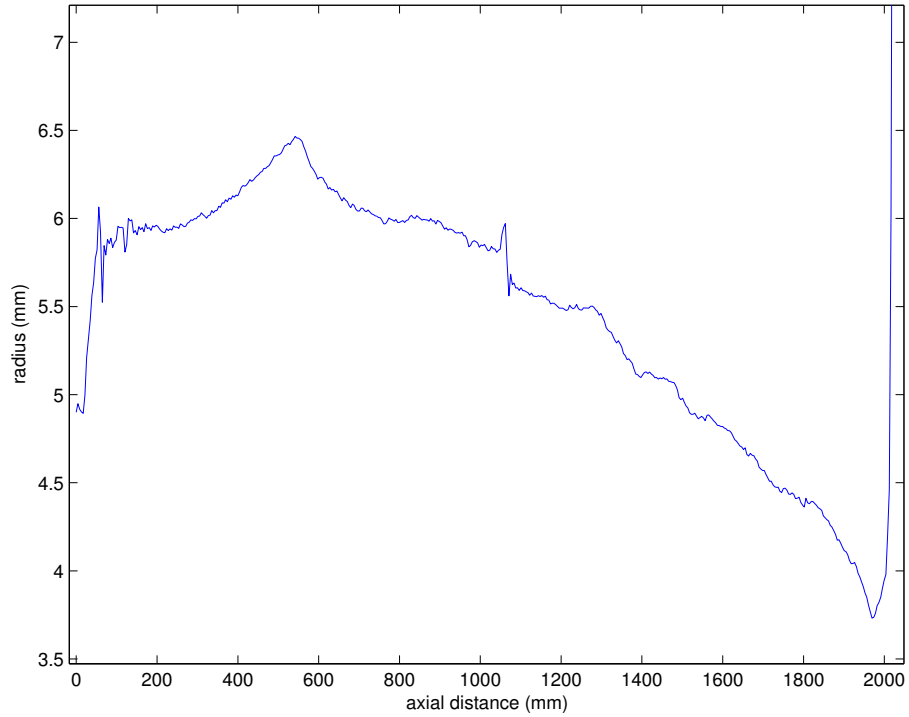

Figure D.12: Bore reconstruction for the Courtois E♭ crook.

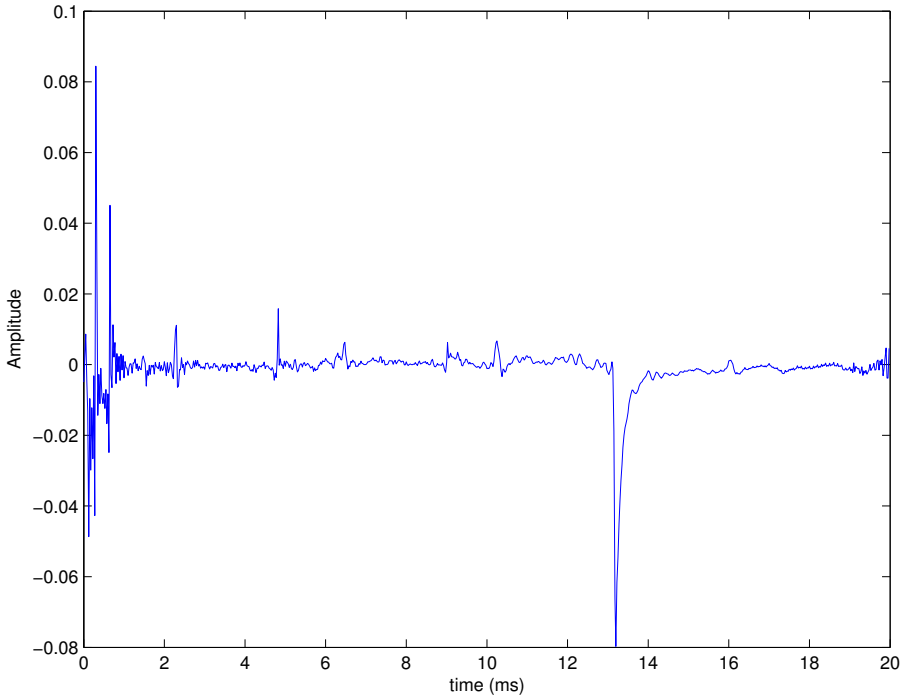

Figure D.13: IIR for the Courtois D crook.

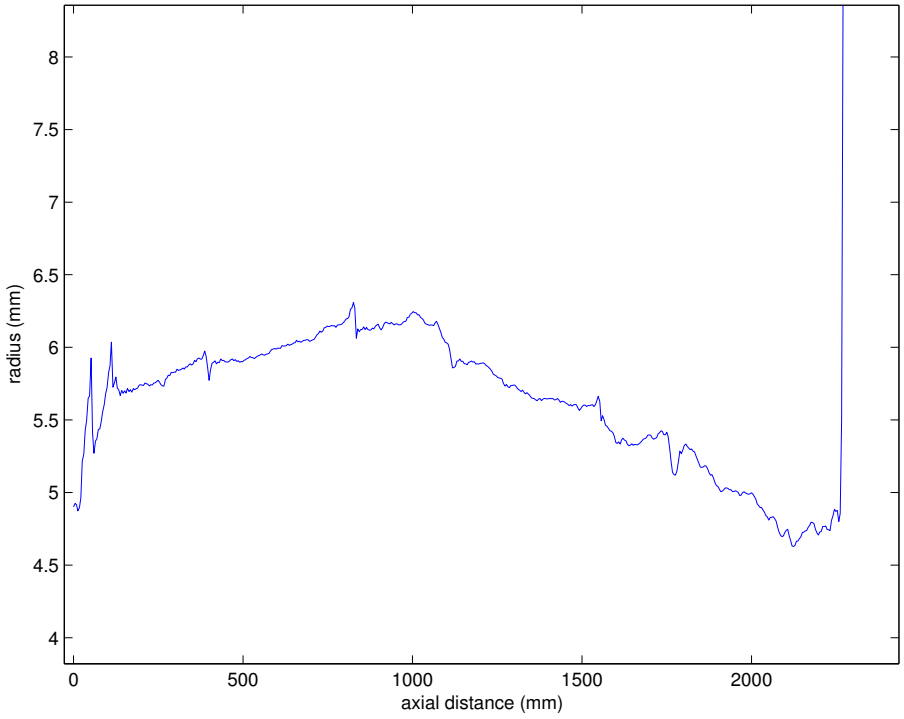

Figure D.14: Bore reconstruction for the Courtois D crook.

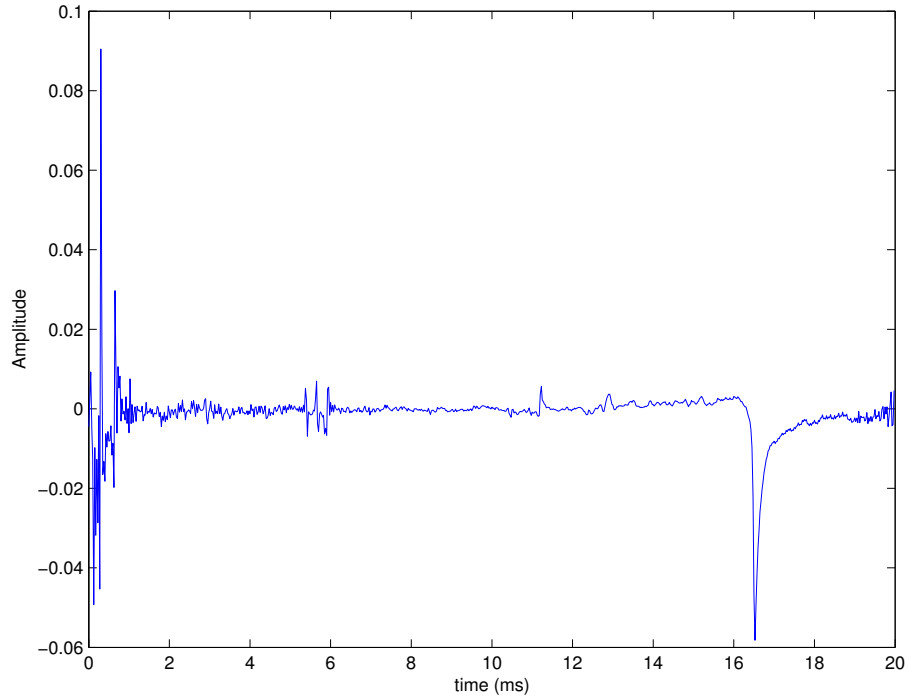

Figure D.15: IIR for the Courtois C crook.

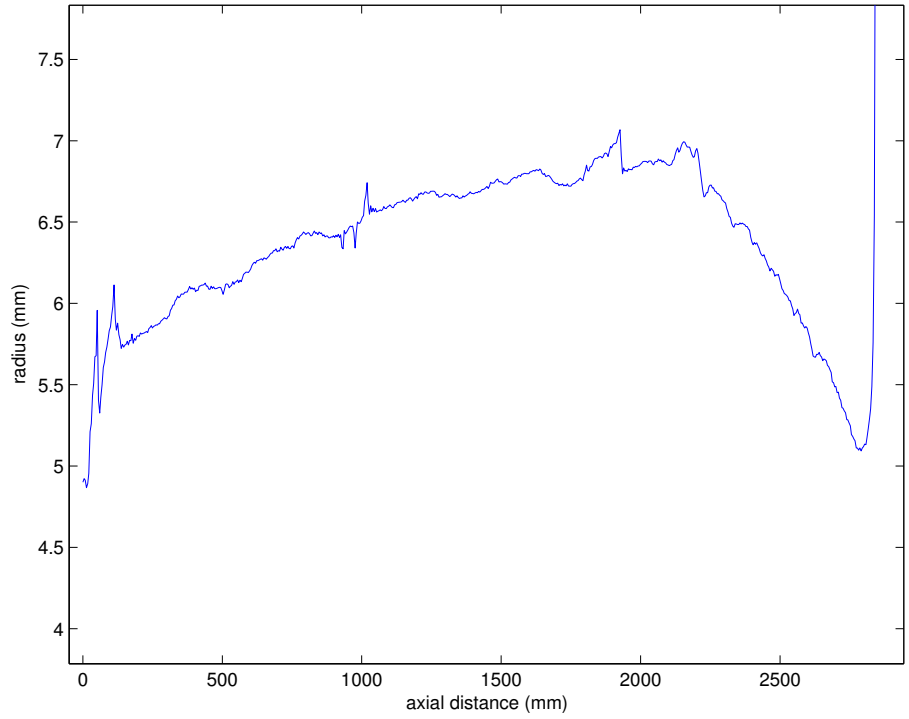

Figure D.16: Bore reconstruction for the Courtois C crook.

Appendix E

Algorithms

E.1 Transmission Matrix Theory Test Program

```
%%%%%TRANSMISSION_MATRIX_THEORY_FOR_THE_THREE_CYLINDER_STEPPED_PIPE.M%%%%%
%%%%DARREN HENDRIE%%%%%%%%%%%%%%%%%%%%%%%%%%%%%%%%%%%%%%%%%%%%%%%%%%%%%%%
%THIS TEST PROGRAM CALCULATES THE INPUT IMPEDANCE OF AN OPEN THREE CYLINDER
%STEPPED PIPE USING PLANE WAVE THEORY. IT THEN CALCULATES THE IMPEDANCE%%%%
%WITH THE FIRST CYLINDER REMOVED. THE SAME IS DONE USING TRANSMISSION%%%%%
%MATRIX THEORY.%%%%%%%%%%%%%%%%%%%%%%%%%%%%%%%%%%%%%%%%%%%%%%%%%%%%%%%%%

%%%VARIABLES%%%%%%%%%%%%%%%%%%%%%%%%%%%%%%%%%%%%%%%%%%%%%%%%%%%%%%%%%%%%
%%%%%%%%%%%%%%%%%%%%%%%%%%%%%%%%%%%%%%%%%%%%%%%%%%%%%%%%%%%%%%%%%%%%%%%%

i = sqrt(-1);   % imaginary unit
c = 345;        % speed of sound
rho = 1.2;      % density of air

r1 = 4.9e-3;      % radius of first cylinder
r2 = 4.9e-3;      % radius of second cylinder
r3 = 4.9e-3;      % radius of third cylinder

L1 = 20e-3;       % Length of first cylinder 64 +128
L2 = 8e-3;        % Length of second cylinder
L3 = 100e-3;        % Length of third cylinder

Z_c1 = (rho*c)/(pi*r1^2);  % characteristic impedance of the first cylinder
Z_c2 = (rho*c)/(pi*r2^2);  % characteristic impedance of the second cylinder
Z_c3 = (rho*c)/(pi*r3^2);  % characteristic impedance of the third cylinder

f = 50 : 50 : 200;                          % frequency range
omega = 2*pi*f;                      % angular frequency of propagating wave
v = c*(1 - (1.65e-3*(1/r1)*(1./sqrt(f))));    % velocity in pipe

k = 2*pi*f/c;                                 %lossless case
```

```
alpha = 3e-5*sqrt(f)./r1;                    % attenuation constant
Gamma = (omega./v) - i*alpha;                %lossy case
%Gamma = 2*pi*f/c;

%%%alpha and Gamma models by Fletcher and Rossing, page 196 of The Physics
%%%of Musical Instruments%%%%%%%%%%%%%%%%%%%%%%%%%%%%%%%%%%%%%%%%%%%%%%%%

%%%RADIATION IMPEDANCE%%%%%%%%%%%%%%%%%%%%%%%%%%%%%%%%%%%%%%%%%%%%%%%%%%

real_part = 0.25*Z_c3*k.^2*r3^2;  %Real part for unflanged open end
imag_part = 0.6*Z_c3*k*r3;        %Imaginary part for unflanged open end

%Zr = real_part + i*imag_part; % Complex radiation impedance
%for non-ideal unflanged open end

%Zr = 0*f; %Ideal open end

Zr=zeros(1,length(f));
for j = 1 : 1 : length(f)  %Radiation impedance for closed end (infinite)
Zr(j) = 1e+10;
end

%%%INPUT IMPEDANCE OF AN OPEN PIPE WITH RADIATION IMPEDANCE ZR%%%%%%%%%%%%

Z_open_pipe = Z_c3*(Zr + i*Z_c3*tan(Gamma*L3))./(Z_c3 + i*Zr.*tan(Gamma*L3));
%Z_c3

%%%%INPUT IMPEDANCE OF TWO CYLIDER PIPE%%%%%%%%%%%%%%%%%%%%%%%%%%%%%%%%%

Z_open_stepped_pipe = Z_c2*(Z_open_pipe + i*Z_c2*tan(Gamma*L2))./(Z_c2 + i*Z_ope
n_pipe.*tan(Gamma*L2));  %Z_c2

%%%%INPUT IMPEDANCE OF THREE CYLINDER PIPE%%%%%%%%%%%%%%%%%%%%%%%%%%%%%%%%

Z_IN_3 = (Z_open_stepped_pipe + i*Z_c1*tan(Gamma*L1))./(Z_c1 + i*Z_open_stepped_
pipe.*tan(Gamma*L1)); %Normalised relative to Z_c1

%%%IN dB%%%%%%%%%%%%%%%%%%%%%%%%%%%%%%%%%%%%%%%%%%%%%%%%%%%%%%%%%%%%%%%%

Z_IN_3_dB = 20*log10(abs(Z_IN_3)); % Input impedance in dB

%%%PLOTTING%%%%%%%%%%%%%%%%%%%%%%%%%%%%%%%%%%%%%%%%%%%%%%%%%%%%%%%%%%%%%%
%%%%%%%%%%%%%%%%%%%%%%%%%%%%%%%%%%%%%%%%%%%%%%%%%%%%%%%%%%%%%%%%%%%%%%%%

figure(1);
subplot(2,1,1)
plot(f/1000, Z_IN_3_dB, 'r-')
```

```
xlabel('frequency (kHz)');
ylabel(' |Z/Z_c| (dB)');
%ylim([-60 60]);
title('Impedance of the three cylinder open pipe (theory)');
grid;
subplot(2,1,2)
plot(f/1000, angle(Z_IN_3)/pi, 'r-')
xlabel('frequency (kHz)');
ylabel('\angle (Z/Z_c)/\pi');
ylim([-0.6 0.6]);
grid;

%%%REMOVE FIRST CYLINDER r1=0, L1=0%%%%%%%%%%%%%%%%%%%%%%%%%%%%%%%%%%%%%%%%%%%%
%%%INPUT IMPEDANCE FOR AN OPEN STEPPED PIPE%%%%%%%%%%%%%%%%%%%%%%%%%%%%%%%%%%%%
%%%%%%%%%%%%%%%NEW EQUATIONS%%%%%%%%%%%%%%%%%%%%%%%%%%%%%%%%%%%%%%%%%%%%%%%%%%

Z_LOAD = Z_c3*(Zr + i*Z_c3*tan(Gamma*L3))./(Z_c3 + i*tan(Gamma*L3).*Zr);

Z_IN_2 = (Z_LOAD + i*Z_c2*tan(Gamma*L2))./(Z_c2 + i*Z_LOAD.*tan(Gamma*L2));
% Normalised relative to Z_c2

%%%dB%%%%%%%%%%%%%%%%%%%%%%%%%%%%%%%%%%%%%%%%%%%%%%%%%%%%%%%%%%%%%%%%%%%%%%%%

Z_IN_2_dB = 20*log10(abs(Z_IN_2)); % Input impedance in dB

%%%%%%%%%%%%%%%PLOTTING%%%%%%%%%%%%%%%%%%%%%%%%%%%%%%%%%%%%%%%%%%%%%%%%%%%%%%
%%%%%%%%%%%%%%%%%%%%%%%%%%%%%%%%%%%%%%%%%%%%%%%%%%%%%%%%%%%%%%%%%%%%%%%%%%%%

figure(2);
subplot(2,1,1)
plot(f/1000, Z_IN_2_dB, 'r-')
xlabel('frequency (kHz)');
ylabel(' |Z/Z_c| (dB)');
%ylim([-50 50]);
title('Impedance of the two cylinder open pipe (theory)');
grid;
subplot(2,1,2)
plot(f/1000, angle(Z_IN_2)/pi, 'r-')
xlabel('frequency (kHz)');
ylabel('\angle (Z/Z_c)/\pi');
ylim([-0.6 0.6]);
grid;

%%%%%%%%%%%%%%%%%%%%%%%%%%%%%%%%%%%%%%%%%%%%%%%%%%%%%%%%%%%%%%%%%%%%%%%%%%%%%%%
%%%%%%%%%%%%%%%%%%%%%%%%%%%%%%%%%%%%%%%%%%%%%%%%%%%%%%%%%%%%%%%%%%%%%%%%%%%%%%%
%%%TRANSMISSION MATRIX THEORY%%%%%%%%%%%%%%%%%%%%%%%%%%%%%%%%%%%%%%%%%%%%%%%%%%
%%%%%%%%%%%%%%%%%%%%%%%%%%%%%%%%%%%%%%%%%%%%%%%%%%%%%%%%%%%%%%%%%%%%%%%%%%%%%%%
```

```
%%%%%%%%%%%%%%%%%%%%%%%%%%%%%%%%%%%%%%%%%%%%%%%%%%%%%%%%%%%%%%%%%%%%%%%%%%%%

Zrad=zeros(2,1,length(f));
for j = 1 : 1 : length(f)        %Radiation impedance for an ideal open end
    Zrad(:,:,j) = [Zr(:,j);1];   %[0;1] ideal
end

%%%COEFFICIENTS FOR TRANSMISSION MATRICES%%%%%%%%%%%%%%%%%%%%%%%%%%%%%%%%%%%%
%%%COEFFICIENT FOR H1
a1 = cos(Gamma*L1);
b1 = Z_c1*i*sin(Gamma*L1);
c1 = (1/Z_c1)*i*sin(Gamma*L1);
d1 = cos(Gamma*L1);

%%%COEFFICIENT FOR H2
a2 = cos(Gamma*L2);
b2 = Z_c2*i*sin(Gamma*L2);
c2 = (1/Z_c2)*i*sin(Gamma*L2);
d2 = cos(Gamma*L2);

%%%COEFFICIENTS FOR H3
a3 = cos(Gamma*L3);
b3 = Z_c3*i*sin(Gamma*L3);
c3 = (1/Z_c3)*i*sin(Gamma*L3);
d3 = cos(Gamma*L3);

%%%FOR LOOPS GENERATING TRANSMISSION MATRICES%%%%%%%%%%%%%%%%%%%%%%%%%%%%%%%

H1=zeros(2,2,length(f));
for j = 1 : 1 : length(f)                              %Generate H1 matrix
H1(:,:,j) = [a1(j), b1(j); c1(j), d1(j)];
end

H2=zeros(2,2,length(f));
for j = 1 : 1 : length(f)                              %Generate H2 matrix
H2(:,:,j) = [a2(j), b2(j); c2(j), d2(j)];
end

H3=zeros(2,2,length(f));
for j = 1 : 1 : length(f)
H3(:,:,j) = [a3(j), b3(j); c3(j), d3(j)];               %Generate H3 matrix
end

%%%CALCULATE IMPEDANCE%%%%%%%%%%%%%%%%%%%%%%%%%%%%%%%%%%%%%%%%%%%%%%%%%%%%%

Z_IN_3T=zeros(2,1,length(f));
for j = 1 : 1 : length(f)
```

```
Z_IN_3T(:,:,j) = H1(:,:,j)*H2(:,:,j)*H3(:,:,j)*Zrad(:,:,j);
%Multiply matrices to obtain p and U
end

Z_TMT_3=zeros(1,1,length(f));
for j = 1 : 1 : length(f)
%Divide p by U for each frequency to obtain impedance
Z_TMT_3(:,:,j) = Z_IN_3T(1,1,j)/Z_IN_3T(2,1,j);
end

impedance_3=zeros(1,length(f));
for j = 1 : 1 : length(f)
%Generate 1-D impedance vector and normalise
impedance_3(j) = Z_TMT_3(j)./Z_c1;
end

impedance_3_dB = 20*log10(abs(impedance_3)); % Input impedance in dB

%%%PLOTTING%%%%%%%%%%%%%%%%%%%%%%%%%%%%%%%%%%%%%%%%%%%%%%%%%%%%%%%%%%%%%%%%%%%%
%%%%%%%%%%%%%%%%%%%%%%%%%%%%%%%%%%%%%%%%%%%%%%%%%%%%%%%%%%%%%%%%%%%%%%%%%%%%%%

figure(3)
subplot(2,1,1)
plot(f/1000, impedance_3_dB, 'r-')
title('Impedance of the three cylinder open pipe (TMT)')
xlabel('frequency (kHz)')
ylabel('|Z/Z_c|')
grid;
subplot(2,1,2)
plot(f/1000, angle(impedance_3)/pi, 'r-')
xlabel('frequency (kHz)')
ylabel('\angle Z/Z_c')
ylim([-0.6 0.6]);
grid;

%%%%%%%%%%%%%%%%%%%%%%%%%%%%%%%%%%%%%%%%%%%%%%%%%%%%%%%%%%%%%%%%%%%%%%%%%%%%%%

%%%TWO CYLINDER PIPE USING TMT%%%%%%%%%%%%%%%%%%%%%%%%%%%%%%%%%%%%%%%%%%%%%%%
%%%%%%%%%%%%%%%%%%%%%%%%%%%%%%%%%%%%%%%%%%%%%%%%%%%%%%%%%%%%%%%%%%%%%%%%%%%%%%

invH1=zeros(2,2,length(f));
for j = 1 : 1 : length(f)
invH1(:,:,j) = inv(H1(:,:,j));                %Generate inverse of H1 matrix
end

Z_IN_2T=zeros(2,1,length(f));
for j = 1 : 1 : length(f)
```

```
Z_IN_2T(:,:,j) = invH1(:,:,j)*Z_IN_3T(:,:,j); %Multiply matrices to obtain
%impedance
end

Z_TMT_2=zeros(1,1,length(f));
for j = 1 : 1 : length(f)      %Divide p by U for each frequency to obtain
%impedance
Z_TMT_2(:,:,j) = Z_IN_2T(1,1,j)/Z_IN_2T(2,1,j);
end

impedance_2=zeros(1,length(f));
for j = 1 : 1 : length(f)              %Generate 1-D impedance vector
impedance_2(j) = Z_TMT_2(j)./Z_c2;
end

impedance_2_dB = 20*log10(abs(impedance_2)); % Input impedance in dB

%%%PLOTTING%%%%%%%%%%%%%%%%%%%%%%%%%%%%%%%%%%%%%%%%%%%%%%%%%%%%%%%%%%%%%%%%%%%%
%%%%%%%%%%%%%%%%%%%%%%%%%%%%%%%%%%%%%%%%%%%%%%%%%%%%%%%%%%%%%%%%%%%%%%%%%%%%%%

figure(4)
subplot(2,1,1)
plot(f/1000, impedance_2_dB, 'r-')
title('Impedance of the two cylinder open pipe (TMT)')
xlabel('frequency (kHz)')
ylabel('|Z/Z_c|')
grid;
subplot(2,1,2)
plot(f/1000, angle(impedance_2)/pi, 'r-')
xlabel('frequency (kHz)')
ylabel('\angle Z/Z_c')
ylim([-0.6 0.6]);
grid;
```

E.2 Transmission Matrix Theory Program

```
%%%%%TRANSMISSION_MATRIX_THEORY_FOR_SUBTRACTING_COUPLER.M%%%%%%%%%%%%%%%%
%%%%DARREN HENDRIE%%%%%%%%%%%%%%%%%%%%%%%%%%%%%%%%%%%%%%%%%%%%%%%%%%%%%%
%THIS PROGRAM READS THE IMPEDANCE FILE FOR THE INSTRUMENT PLUS COUPLER. IT
%THEN CALCULATES THE IMPEDANCE WITH THE COUPLER IMPEDANCE REMOVED USING
%TRANSMISSION MATRIX THEORY.%%%%%%%%%%%%%%%%%%%%%%%%%%%%%%%%%%%%%%%%%%%%

%%%VARIABLES%%%%%%%%%%%%%%%%%%%%%%%%%%%%%%%%%%%%%%%%%%%%%%%%%%%%%%%%%%%
%%%%%%%%%%%%%%%%%%%%%%%%%%%%%%%%%%%%%%%%%%%%%%%%%%%%%%%%%%%%%%%%%%%%%%%

i = sqrt(-1);   % imaginary unit
c = 345;        % speed of sound
rho = 1.2;      % density of air

r1 = 4.9e-3;       % radius of first cylinder

L1 = 40e-3;       % Length of first cylinder

Z_c1 = (rho*c)/(pi*r1^2);  % characteristic impedance of the first cylinder

f = 50 : 50 : 20000;                            % frequency range
omega = 2*pi*f;          % angular frequency of propagating wave
v = c*(1 - (1.65e-3*(1/r1)*(1./sqrt(f))));    % velocity in pipe

k = 2*pi*f/c;                                   %lossless case
alpha = 3e-5*sqrt(f)./r1;                       % attenuation constant
Gamma = (omega./v) - i*alpha;                   %lossy case
%Gamma = 2*pi*f/c;

%%%alpha and Gamma models by Fletcher and Rossing, page 196 of The Physics
%%%of Musical Instruments%%%%%%%%%%%%%%%%%%%%%%%%%%%%%%%%%%%%%%%%%%%%%%%

%OPEN EXPERIMENTAL IMPEDANCE FILE
%fid1=fopen('impedance_data_128mm_closed_tube.txt', 'r');
fid1=fopen('impedance_data_Dennis_Wick_mouthpiece.txt', 'r');
experimental=fscanf(fid1, '%f  %f',[2 inf]);

%MAKE X1 THE TIME DATA AND Y1 THE AMPLITUDE DATA FOR THE INPUT PULSE
%frequency=experimental(1,:);
expreal=experimental(1,1:length(f));
expimag=experimental(2,1:length(f));
expcomplex=expreal+sqrt(-1)*expimag;

Zexp_dB = 20*log10(abs(expcomplex));
```

```
%%%PLOTTING%%%%%%%%%%%%%%%%%%%%%%%%%%%%%%%%%%%%%%%%%%%%%%%%%%%%%%%%%%%%%%%%%%%

figure(1)
subplot(2,1,1)
plot(f/1000, Zexp_dB, 'r-');
xlabel('frequency (kHz)');
ylabel('|Z/Z_c| (dB)');
%xlim([0 4050]);
title('Original impedance data');
%legend('')
grid;
subplot(2,1,2)
plot(f/1000, angle(expcomplex)/pi, 'r-');
xlabel('frequency (kHz)');
ylabel('\angle (Z/Z_c)/\pi');
%xlim([0 4050]);
%legend('')
grid;

%%%RADIATION IMPEDANCE%%%%%%%%%%%%%%%%%%%%%%%%%%%%%%%%%%%%%%%%%%%%%%%%%%%%%%%%

%real_part = 0.25*Z_c3*k.^2*r3^2;  %Real part for unflanged open end
%imag_part = 0.6*Z_c3*k*r3;        %Imaginary part for unflanged open end

%Zr = real_part + i*imag_part; % Complex radiation impedance for non-ideal
%unflanged open end

%Zr = 0*f; %Ideal open end

% Zr=zeros(1,length(f));
% for j = 1 : 1 : length(f) %Radiation impedance for closed end (infinite)
% Zr(j) = 1e+10;
% end

%%%%%%%%%%%%%%%%%%%%%%%%%%%%%%%%%%%%%%%%%%%%%%%%%%%%%%%%%%%%%%%%%%%%%%%%%%%%%%
%%%%%%%%%%%%%%%%%%%%%%%%%%%%%%%%%%%%%%%%%%%%%%%%%%%%%%%%%%%%%%%%%%%%%%%%%%%%%%
%%%TRANSMISSION MATRIX THEORY%%%%%%%%%%%%%%%%%%%%%%%%%%%%%%%%%%%%%%%%%%%%%%%%%
%%%%%%%%%%%%%%%%%%%%%%%%%%%%%%%%%%%%%%%%%%%%%%%%%%%%%%%%%%%%%%%%%%%%%%%%%%%%%%
%%%%%%%%%%%%%%%%%%%%%%%%%%%%%%%%%%%%%%%%%%%%%%%%%%%%%%%%%%%%%%%%%%%%%%%%%%%%%%

% Zrad=zeros(2,1,length(f));
% for j = 1 : 1 : length(f)        %Radiation impedance for an ideal open end
%     Zrad(:,:,j) = [Zr(:,j);1];   %[0;1] ideal
% end

expcomplex_new=zeros(2,1,length(f));
for j = 1 : 1 : length(f)        %Modify vector structure of impedance
```

```
    expcomplex_new(:,:,j) = [Z_c1*expcomplex(:,j);1];   %[0;1] ideal
end

%%%COEFFICIENTS FOR TRANSMISSION MATRICES%%%%%%%%%%%%%%%%%%%%%%%%%%%%%%%%%%%%
%%%COEFFICIENT FOR H1
a1 = cos(Gamma*L1);
b1 = Z_c1*i*sin(Gamma*L1);
c1 = (1/Z_c1)*i*sin(Gamma*L1);
d1 = cos(Gamma*L1);

%%%FOR LOOPS GENERATING TRANSMISSION MATRICES%%%%%%%%%%%%%%%%%%%%%%%%%%%%%%%%

H1=zeros(2,2,length(f));
for j = 1 : 1 : length(f)                                   %Generate H1 matrix
H1(:,:,j) = [a1(j), b1(j); c1(j), d1(j)];
end

%%%TWO CYLINDER PIPE USING TMT%%%%%%%%%%%%%%%%%%%%%%%%%%%%%%%%%%%%%%%%%%%%%%
%%%%%%%%%%%%%%%%%%%%%%%%%%%%%%%%%%%%%%%%%%%%%%%%%%%%%%%%%%%%%%%%%%%%%%%%%%%%

invH1=zeros(2,2,length(f));
for j = 1 : 1 : length(f)
invH1(:,:,j) = inv(H1(:,:,j));              %Generate inverse of H1 matrix
end

Z_IN_2T=zeros(2,1,length(f));
for j = 1 : 1 : length(f)
Z_IN_2T(:,:,j) = invH1(:,:,j)*expcomplex_new(:,:,j); %Multiply matrices to
%obtain impedance
end

Z_TMT_2=zeros(1,1,length(f));
for j = 1 : 1 : length(f) %Divide p by U for each frequency to obtain impedance
Z_TMT_2(:,:,j) = Z_IN_2T(1,1,j)/Z_IN_2T(2,1,j);
end

impedance_2=zeros(1,length(f));
for j = 1 : 1 : length(f)              %Generate 1-D impedance vector
impedance_2(j) = Z_TMT_2(j)./Z_c1;
end

impedance_2_dB = 20*log10(abs(impedance_2)); % Input impedance in dB

%%%PLOTTING%%%%%%%%%%%%%%%%%%%%%%%%%%%%%%%%%%%%%%%%%%%%%%%%%%%%%%%%%%%%%%%%%
%%%%%%%%%%%%%%%%%%%%%%%%%%%%%%%%%%%%%%%%%%%%%%%%%%%%%%%%%%%%%%%%%%%%%%%%%%%%

figure(2)
```

```
subplot(2,1,1)
plot(f/1000, impedance_2_dB, 'bx')
%title('Impedance of the instrument minus coupler (TMT)')
xlabel('frequency (kHz)')
ylabel('|Z/Z_c|')
grid;
subplot(2,1,2)
plot(f/1000, angle(impedance_2)/pi, 'bx')
xlabel('frequency (kHz)')
ylabel('\angle Z/Z_c')
%ylim([-0.6 0.6]);
grid;
```

E.3 Courtois Crooks: APR and TMFC Comparison

```
%%%%%%%%COURTOIS_AFD_APR_TMFC_COMPARISON.M%%%%%%%%%%%%%%%%%%%%%%%%%%%%%%%%%%%%
%%WRITTEN BY DARREN HENDRIE%%%%%%%%%%%%%%%%%%%%%%%%%%%%%%%%%%%%%%%%%%%%%%%%%%
%%THIS PROGRAM DISPLAYS THE BORE RECONSTRUCTIONS FOR THE COURTOIS CROOKS%%%
%%OBTAINED BY THE APR AND TMFC METHOD%%%%%%%%%%%%%%%%%%%%%%%%%%%%%%%%%%%%%%%%

%OPEN 1st (A crook) APR RECONSTRUCTION FILE
fid1=fopen('courtois4668ba08e-05-07_ins.rec', 'r');
%courtois4668ba08e-05-07_ins.rec
%courtois4668df08e-05-07_ins.rec
%courtois4668gd08e-05-07_ins.rec

APR_reconstruction_A_crook=fscanf(fid1, '%f  %f',[2 inf]); %identifies the
%two columns in impresp.txt as impresp
fclose(fid1);

%FIRST COLUMN IS AXIAL DISTANCE AND SECOND COLUMN IS BORE RADIUS
axial_distance_A_crook=APR_reconstruction_A_crook(1,:); %takes column one
%(related to time parameter) and names it iirx.
bore_radius_A_crook=APR_reconstruction_A_crook(2,:); %takes column two
%(related to IIR amplitude) and names it iiry.

%%%%%%%%%%%%%%%%%%%%%%%%%%%%%%%%%%%%%%%%%%%%%%%%%%%%%%%%%%%%%%%%%%%%%%%%%%%%%

%OPEN 2nd (F crook) APR RECONSTRUCTION FILE
fid1=fopen('courtois4668df08e-05-07_ins.rec', 'r');
%courtois4668ba08e-05-07_ins.rec
%courtois4668df08e-05-07_ins.rec
%courtois4668gd08e-05-07_ins.rec

APR_reconstruction_F_crook=fscanf(fid1, '%f  %f',[2 inf]); %identifies the
%two columns in impresp.txt as impresp
fclose(fid1);

%FIRST COLUMN IS AXIAL DISTANCE AND SECOND COLUMN IS BORE RADIUS
axial_distance_F_crook=APR_reconstruction_F_crook(1,:); %takes column one
%(related to time parameter) and names it iirx.
bore_radius_F_crook=APR_reconstruction_F_crook(2,:); %takes column two
%(related to IIR amplitude) and names it iiry.

%%%%%%%%%%%%%%%%%%%%%%%%%%%%%%%%%%%%%%%%%%%%%%%%%%%%%%%%%%%%%%%%%%%%%%%%%%%%%

%OPEN 3rd (D crook) APR RECONSTRUCTION FILE
fid1=fopen('courtois4668gd08e-05-07_ins.rec', 'r');
%courtois4668ba08e-05-07_ins.rec
```

```
%courtois4668df08e-05-07_ins.rec
%courtois4668gd08e-05-07_ins.rec

APR_reconstruction_D_crook=fscanf(fid1, '%f  %f',[2 inf]); %identifies the
%two columns in impresp.txt as impresp
fclose(fid1);

%FIRST COLUMN IS AXIAL DISTANCE AND SECOND COLUMN IS BORE RADIUS
axial_distance_D_crook=APR_reconstruction_D_crook(1,:); %takes column one
%(related to time parameter) and names it iirx.
bore_radius_D_crook=APR_reconstruction_D_crook(2,:); %takes column two
%(related to IIR amplitude) and names it iiry.

%%%%%%%%%%%%%%%%%%%%%%%%%%%%%%%%%%%%%%%%%%%%%%%%%%%%%%%%%%%%%%%%%%%%%%%%%%%

%PLOT APR RECONSTRUCTION
figure(1);
plot(axial_distance_A_crook*1000, 2*bore_radius_A_crook*1000,
'r-', axial_distance_F_crook*1000, 2*bore_radius_F_crook*1000,
'b-', axial_distance_D_crook*1000, 2*bore_radius_D_crook*1000, 'g-');
%convert time to miliseconds
xlabel('axial distance (mm)');
ylabel('Bore diameter (mm)');
legend('A crook', 'F crook', 'D crook');
title('Bore reconstruction for the A, F, and D Courtois crooks using the
APR method');

%fclose(fid1);

%%%%%%%%%%%%%%%%%%%%%%%%%%%%%%%%%%%%%%%%%%%%%%%%%%%%%%%%%%%%%%%%%%%%%%%%%%%
%%%%%%%%%%%%%%%%%%%%%%%%%%%%%%%%%%%%%%%%%%%%%%%%%%%%%%%%%%%%%%%%%%%%%%%%%%%

%OPEN 1st (A crook) TMFC RECONSTRUCTION FILE
fid2=fopen('recons_4668b.txt', 'r');
%recons_4668b.txt
%recons_4668d.txt
%recons_4668g.txt

TMFC_reconstruction_A_crook=fscanf(fid2, '%f  %f',[2 inf]);
%fclose(fid1);

%FIRST COLUMN IS AXIAL DISTANCE AND SECOND COLUMN IS BORE RADIUS
axial_A_crook=TMFC_reconstruction_A_crook(1,:); %takes column one
%(related to time parameter) and names it iirx.
bore_A_crook=TMFC_reconstruction_A_crook(2,:); %takes column two
%(related to IIR amplitude) and names it iiry.
```

```
fclose(fid2);

%%%%%%%%%%%%%%%%%%%%%%%%%%%%%%%%%%%%%%%%%%%%%%%%%%%%%%%%%%%%%%%%%%%%%%%%%%%%

%OPEN 2nd (F crook) TMFC RECONSTRUCTION FILE
fid2=fopen('recons_4668d.txt', 'r');
%recons_4668b.txt
%recons_4668d.txt
%recons_4668g.txt

TMFC_reconstruction_F_crook=fscanf(fid2, '%f  %f',[2 inf]);
%fclose(fid1);

%FIRST COLUMN IS AXIAL DISTANCE AND SECOND COLUMN IS BORE RADIUS
axial_F_crook=TMFC_reconstruction_F_crook(1,:); %takes column one
%(related to time parameter) and names it iirx.
bore_F_crook=TMFC_reconstruction_F_crook(2,:); %takes column two
%(related to IIR amplitude) and names it iiry.

fclose(fid2);

%%%%%%%%%%%%%%%%%%%%%%%%%%%%%%%%%%%%%%%%%%%%%%%%%%%%%%%%%%%%%%%%%%%%%%%%%%%%

%OPEN 3rd (D crook) TMFC RECONSTRUCTION FILE
fid2=fopen('recons_4668g.txt', 'r');
%recons_4668b.txt
%recons_4668d.txt
%recons_4668g.txt

TMFC_reconstruction_D_crook=fscanf(fid2, '%f  %f',[2 inf]);
%fclose(fid1);

%FIRST COLUMN IS AXIAL DISTANCE AND SECOND COLUMN IS BORE RADIUS
axial_D_crook=TMFC_reconstruction_D_crook(1,:); %takes column one
%(related to time parameter) and names it iirx.
bore_D_crook=TMFC_reconstruction_D_crook(2,:); %takes column two
%(related to IIR amplitude) and names it iiry.

fclose(fid2);

%%%%%%%%%%%%%%%%%%%%%%%%%%%%%%%%%%%%%%%%%%%%%%%%%%%%%%%%%%%%%%%%%%%%%%%%%%%%

 %PLOT TMFC RECONSTRUCTION
 figure(2);
 plot(axial_A_crook*1000, 2*bore_A_crook*1000, 'r-', axial_F_crook*1000,
2*bore_F_crook*1000, 'b-', axial_D_crook*1000, 2*bore_D_crook*1000, 'g-');
 xlabel('axial distance (mm)');
```

```
 ylabel('Bore diameter (mm)');
 xlim([0 2500]);
 ylim([0 20]);
 legend('A crook', 'F crook', 'D crook');
 title('Bore reconstruction for the A, F, and D Courtois crooks using
the TMFC method');

%fclose(fid2);

%%%%%%%%%%%%%%%%%%%%%%%%%%%%%%%%%%%%%%%%%%%%%%%%%%%%%%%%%%%%%%%%%%%%%%%%%%%%
%%%%%%%%%%%%%%%%%%%%%%%%%%%%%%%%%%%%%%%%%%%%%%%%%%%%%%%%%%%%%%%%%%%%%%%%%%%%

fid1=fopen('recons_4668b_reversed.txt', 'w');

%REVERSE 1st (A crook) TMFC RECONSTRUCTION FILE
for j=1:372
   fprintf(fid1, '%f  %f\n', axial_A_crook(373-j), bore_A_crook(373-j));
end

fclose(fid1);

%%OPEN REVERSED TMFC RECONSTRUCTION FILE
fid2=fopen('recons_4668b_reversed.txt', 'r');

TMFC_reconstruction_A_crook_REVERSED=fscanf(fid2, '%f  %f',[2 inf]);
%fclose(fid1);

%FIRST COLUMN IS AXIAL DISTANCE AND SECOND COLUMN IS BORE RADIUS
axial_A_crook_reversed=TMFC_reconstruction_A_crook_REVERSED(1,:); %takes column
%one (related to time parameter) and names it iirx.
bore_A_crook_REVERSED=TMFC_reconstruction_A_crook_REVERSED(2,:); %takes column
%two (related to IIR amplitude) and names it iiry.

%%%%%%%%%%%%%%%%%%%%%%%%%%%%%%%%%%%%%%%%%%%%%%%%%%%%%%%%%%%%%%%%%%%%%%%%%%%%

fid1=fopen('recons_4668d_reversed.txt', 'w');

%REVERSE 2nd (F crook) TMFC RECONSTRUCTION FILE
for j=1:518
   fprintf(fid1, '%f  %f\n', axial_F_crook(519-j), bore_F_crook(519-j));
end

fclose(fid1);

%%OPEN REVERSED TMFC RECONSTRUCTION FILE
fid2=fopen('recons_4668d_reversed.txt', 'r');
```

```
TMFC_reconstruction_F_crook_REVERSED=fscanf(fid2, '%f  %f',[2 inf]);
%fclose(fid1);

%FIRST COLUMN IS AXIAL DISTANCE AND SECOND COLUMN IS BORE RADIUS
axial_F_crook_reversed=TMFC_reconstruction_F_crook_REVERSED(1,:); %takes
%column one (related to time parameter) and names it iirx.
bore_F_crook_REVERSED=TMFC_reconstruction_F_crook_REVERSED(2,:); %takes
%column two (related to IIR amplitude) and names it iiry.

%%%%%%%%%%%%%%%%%%%%%%%%%%%%%%%%%%%%%%%%%%%%%%%%%%%%%%%%%%%%%%%%%%%%%%%%%%%%

fid1=fopen('recons_4668g_reversed.txt', 'w');

%REVERSE 3rd (D crook) TMFC RECONSTRUCTION FILE
for j=1:800
   fprintf(fid1, '%f  %f\n', axial_D_crook(801-j), bore_D_crook(801-j));
end

fclose(fid1);

%%OPEN REVERSED TMFC RECONSTRUCTION FILE
fid2=fopen('recons_4668g_reversed.txt', 'r');

TMFC_reconstruction_D_crook_REVERSED=fscanf(fid2, '%f  %f',[2 inf]);
%fclose(fid1);

%FIRST COLUMN IS AXIAL DISTANCE AND SECOND COLUMN IS BORE RADIUS
axial_D_crook_reversed=TMFC_reconstruction_D_crook_REVERSED(1,:); %takes
%column one (related to time parameter) and names it iirx.
bore_D_crook_REVERSED=TMFC_reconstruction_D_crook_REVERSED(2,:); %takes
%column two (related to IIR amplitude) and names it iiry.

%PLOT REVERSED TMFC RECONSTRUCTION
figure(3);
plot(axial_A_crook*1000, 2*bore_A_crook_REVERSED*1000,
'r-', axial_F_crook*1000, 2*bore_F_crook_REVERSED*1000,
'b-', axial_D_crook*1000, 2*bore_D_crook_REVERSED*1000, 'g-');
xlabel('axial distance (mm)');
ylabel('Bore diameter (mm)');
xlim([0 3500]);
ylim([0 20]);
legend('A crook', 'F crook', 'D crook');
title('Bore reconstruction for the A, F, and D Courtois crooks using the
TMFC method (REVERSED)');

%%%%%%%%%%%%%%%%%%%%%%%%%%%%%%%%%%%%%%%%%%%%%%%%%%%%%%%%%%%%%%%%%%%%%%%%%%%%
%%%%%%%%%%%%%%%%%%%%%%%%%%%%%%%%%%%%%%%%%%%%%%%%%%%%%%%%%%%%%%%%%%%%%%%%%%%%
```

```
%%%A CROOK TMFC TRIM%%%%%%%%%%%%%%%%%%%%%%%%%%%%%%%%%%%%%%%%%%%%%%%%%%%%%%%%
axial_A_crook = axial_A_crook(1:359);
bore_A_crook_REVERSED = bore_A_crook_REVERSED(1:359);

%%%F CROOK TMFC TRIM%%%%%%%%%%%%%%%%%%%%%%%%%%%%%%%%%%%%%%%%%%%%%%%%%%%%%%%%
axial_F_crook = axial_F_crook(1:504);
bore_F_crook_REVERSED = bore_F_crook_REVERSED(1:504);

%%%D CROOK TMFC TRIM%%%%%%%%%%%%%%%%%%%%%%%%%%%%%%%%%%%%%%%%%%%%%%%%%%%%%%%%
axial_D_crook = axial_D_crook(1:788);
bore_D_crook_REVERSED = bore_D_crook_REVERSED(1:788);

%%%F CROOK APR TRIM%%%%%%%%%%%%%%%%%%%%%%%%%%%%%%%%%%%%%%%%%%%%%%%%%%%%%%%%%
 axial_distance_F_crook = axial_distance_F_crook(1:980);
 bore_radius_F_crook = bore_radius_F_crook(1:980);

%PLOT APR AND TMFC (REVERSED) RECONSTRUCTION
figure(4);
plot(axial_distance_A_crook*1000, 2*bore_radius_A_crook*1000, 'r-',
axial_A_crook*1000-850, 2*bore_A_crook_REVERSED*1000, 'b-',
axial_distance_F_crook*1000, 2*bore_radius_F_crook*1000, 'g-',
axial_F_crook*1000-700, 2*bore_F_crook_REVERSED*1000, 'y-',
axial_distance_D_crook*1000, 2*bore_radius_D_crook*1000, 'c-',
axial_D_crook*1000-1150, 2*bore_D_crook_REVERSED*1000, 'm-');
xlabel('axial distance (mm)');
ylabel('Bore diameter (mm)');
xlim([-50 2400]);
ylim([6 15]);
legend('A crook (APR)', 'A crook (TMFC)', 'F crook (APR)', 'F crook (TMFC)',
'D crook (APR)', 'D crook (TMFC)');
title('Bore reconstruction for the A, F, and D Courtois crooks using
the APR and TMFC method');

%%%%%%%%%%%%%%%%%%%%%%%%%%%%%%%%%%%%%%%%%%%%%%%%%%%%%%%%%%%%%%%%%%%%%%%%%%%%
%%%%%%%%%%%%%%%%%%%%%%%%%%%%%%%%%%%%%%%%%%%%%%%%%%%%%%%%%%%%%%%%%%%%%%%%%%%%
%%%INDIVIDUAL COMPARISONS%%%%%%%%%%%%%%%%%%%%%%%%%%%%%%%%%%%%%%%%%%%%%%%%%%%
%%%%%%%%%%%%%%%%%%%%%%%%%%%%%%%%%%%%%%%%%%%%%%%%%%%%%%%%%%%%%%%%%%%%%%%%%%%%

%%%EXTERNAL DIAMETER%%%%%%%%%%%%%%%%%%%%%%%%%%%%%%%%%%%%%%%%%%%%%%%%%%%%%%%
fid2=fopen('external_Courtois_A_crook.txt', 'r');

external_profile=fscanf(fid2, '%f  %f',[2 inf]);
%fclose(fid1);

%FIRST COLUMN IS AXIAL DISTANCE AND SECOND COLUMN IS BORE RADIUS
external_length=external_profile(1,:); %takes column one.
```

```
external_diameter=external_profile(2,:); %takes column two.

%%%%%%%%%%%%%%%%%%%%%%%%%%%%%%%%%%%%%%%%%%%%%%%%%%%%%%%%%%%%%%%%%%%%%%%%%%%%%%%

y_equation = 10.5*ones(length(axial_distance_A_crook));
x_equation = 680:695;

%A CROOK PLOT APR AND TMFC (REVERSED) RECONSTRUCTION
figure(5);
plot(axial_distance_A_crook*1000, 2*bore_radius_A_crook*1000,
'g-', axial_A_crook*1000-848, 2*bore_A_crook_REVERSED*1000,
'b-', external_length, external_diameter,
'r-', x_equation, y_equation(680:695), 'k-' )
xlabel('Axial distance (mm)');
ylabel('Diameter (mm)');
xlim([0 750]);
ylim([6 15]);
legend('APR', 'TMFC', 'External')
%title('Bore reconstruction for the A Courtois crook using the APR and TMFC
%method');

%%%%%%%%%%%%%%%%%%%%%%%%%%%%%%%%%%%%%%%%%%%%%%%%%%%%%%%%%%%%%%%%%%%%%%%%%%%%%%%
%%%%%%%%%%%%%%%%%%%%%%%%%%%%%%%%%%%%%%%%%%%%%%%%%%%%%%%%%%%%%%%%%%%%%%%%%%%%%%%

%%%EXTERNAL DIAMETER%%%%%%%%%%%%%%%%%%%%%%%%%%%%%%%%%%%%%%%%%%%%%%%%%%%%%%%%%%
fid2=fopen('external_Courtois_F_crook.txt', 'r');

external_profile_F=fscanf(fid2, '%f  %f',[2 inf]);
%fclose(fid1);

%FIRST COLUMN IS AXIAL DISTANCE AND SECOND COLUMN IS BORE RADIUS
external_length_F=external_profile_F(1,:); %takes column one.
external_diameter_F=external_profile_F(2,:); %takes column two.

y_equation_F = 10.5*ones(length(axial_distance_A_crook));
x_equation_F = 1455:1475;

%F CROOK PLOT APR AND TMFC (REVERSED) RECONSTRUCTION
figure(6);
plot(axial_distance_F_crook*1000, 2*bore_radius_F_crook*1000,
'g-', axial_F_crook*1000-700, 2*bore_F_crook_REVERSED*1000,
'b-', external_length_F, external_diameter_F,
'r-', x_equation_F, y_equation_F(1455:1475), 'k-')
xlabel('Axial distance (mm)');
ylabel('Diameter (mm)');
xlim([-0 1500]);
ylim([6 15]);
```

```
legend('APR', 'TMFC', 'External');
%title('Bore reconstruction for the F Courtois crook using the APR and TMFC
%method');

%%%%%%%%%%%%%%%%%%%%%%%%%%%%%%%%%%%%%%%%%%%%%%%%%%%%%%%%%%%%%%%%%%%%%%%%%%%%%%%%
%%%%%%%%%%%%%%%%%%%%%%%%%%%%%%%%%%%%%%%%%%%%%%%%%%%%%%%%%%%%%%%%%%%%%%%%%%%%%%%%

%%%EXTERNAL DIAMETER%%%%%%%%%%%%%%%%%%%%%%%%%%%%%%%%%%%%%%%%%%%%%%%%%%%%%%%%%%%
fid2=fopen('external_Courtois_D_crook.txt', 'r');

external_profile_D=fscanf(fid2, '%f  %f',[2 inf]);
%fclose(fid1);

%FIRST COLUMN IS AXIAL DISTANCE AND SECOND COLUMN IS BORE RADIUS
external_length_D=external_profile_D(1,:); %takes column one.
external_diameter_D=external_profile_D(2,:); %takes column two.


y_equation_D = 10.4*ones(length(axial_distance_A_crook));
x_equation_D = 2230:2270;

%D CROOK PLOT APR AND TMFC (REVERSED) RECONSTRUCTION
figure(7);
plot(axial_distance_D_crook*1000, 2*bore_radius_D_crook*1000,
'g-', axial_D_crook*1000-1150, 2*bore_D_crook_REVERSED*1000,
'b-', external_length_D, external_diameter_D,
'r-', x_equation_D, y_equation_D(2230:2270), 'k-' );
xlabel('Axial distance (mm)');
ylabel('Diameter (mm)');
xlim([-0 2300]);
ylim([6 15]);
legend('APR', 'TMFC', 'External');
%title('Bore reconstruction for the D Courtois crook using the APR and TMFC
%method');
```

Bibliography

[1] D. Smith and T. L. Parrott, "Comparison of three methods for measuring acoustic properties of bulk materials", J. Acoust. Soc. Am. **74**, 1577–1582 (1983).

[2] S. L. Yaniv, "Impedance tube measurement of propagation constant and characteristic impedance of porous acoustical material", J. Acoust. Soc. Am. **54**, 1138–1142 (1973).

[3] L. L. Beranek, "Acoustical properties of homogeneous, isotropic rigid tiles and flexible blankets", J. Acoust. Soc. Am. **19**, 556–568 (1947).

[4] B. H. Song and J. S. Bolton, "A transfer-matrix approach for estimating the characteristic impedance and wave numbers of limp and rigid porous materials", J. Acoust. Soc. Am. **107**, 1131–1152 (2000).

[5] R. T. Muehleisen and C. W. Beamer, "Comparison of errors in the three- and four-microphone methods used in the measurement of the acoustic properties of porous materials", Acoustical Society of America **3**, 112–117 (2002).

[6] Y. Champoux and M. R. Stinson, "Measurement of the characteristic impedance and propagation constant of materials having high flow resistivity", J. Acoust. Soc. Am. **90**, 2182–2191 (1991).

[7] L. L. Beranek, "Acoustic impedance of commercial materials and the performance of rectangular rooms with one treated surface", J. Acoust. Soc. Am. **12**, 14–23 (1940).

[8] W. T. Chu, "Transfer function technique for impedance and absorption measurements in an impedance tube using a single microphone", J. Acoust. Soc. Am. **108**, 555–560 (1986).

[9] B. F. G. Katz, "Method to resolve microphone and sample location errors in the two-microphone measurement method", J. Acoust. Soc. Am. **108**, 2231–2237 (2000).

[10] D. H. Keefe, "Woodwind air column models", J. Acoust. Soc. Am. **88**, 35–51 (1990).

[11] A. P. Watson and J. M. Bowsher, "Impulse measurements on brass musical instruments", Acustica - Acta Acustica **66**, 170–174 (1988).

[12] B. Gazengel, J. Gilbert, and N. Amir, "Time domain simulation of single reed wind instrument. from the measured input impedance to the synthesis signal. where are the traps?", Acustica - Acta Acustica **3**, 445–472 (1995).

[13] M. E. McIntyre, R. T. Schumacher, and J. Woodhouse, "On the oscillations of musical instruments", J. Acoust. Soc. Am. **74**, 1325–1345 (1983).

[14] R. D. Ayers, "Impulse responses for feedback to the driver of a musical wind instrument", J. Acoust. Soc. Am. **100**, 1190–1198 (1996).

[15] J. P. Dalmont, "Acoustic impedance measurement, part i: A review", Journal of Sound and Vibration **243**, 427–439 (2001).

[16] J. P. Dalmont, "Acoustic impedance measurement, part ii: A new calibration method", Journal of Sound and Vibration **243**, 441–459 (2001).

[17] V. Gibiat and F. Laloe, "Acoustical impedance measurements by the two-microphone-three-calibration (tmfc) method", J. Acoust. Soc. Am. **88**, 2533–2544 (1990).

[18] M. O. van Walstijn, D. M. Campbell, J. A. Kemp, and D. B. Sharp, "Wideband measurement of the acoustic impedance of tubular objects", Acustica - Acta Acustica **91**, 590–604 (2005).

[19] M. O. van Walstijn, D. M. Campbell, and D. B. Sharp, "Measurement of input impedance of an acoustic bore with application to bore reconstruction", in *Proc. of the Institute of Acoustics Meeting* (2002).

[20] M. O. van Walstijn and D. M. Campbell, "Large bandwidth measurement of acoustic response of tubular objects", in *Proc. of the Forum Acusticum Meeting* (2002).

[21] M. O. van Walstijn, "Acoustic bore reconstruction using the layer-peeling algorithm: signal processing aspects and future development involving the inclusion of higher modes", in *Poster presentation at the International Congress on Acoustics, Rome* (2001).

[22] A. F. Seybert and D. F. Ross, "Experimental determination of acoustic properties using a two-microphone random-excitation technique", J. Acoust. Soc. Am. **61**, 1362–1370 (1997).

[23] D. B. Sharp, "Acoustic pulse reflectometry for the measurement of musical wind instruments", Ph.D. thesis, The University of Edinburgh (1996).

[24] J. A. Kemp, "Theoretical and experimental study of wave propagation in brass musical instruments", Ph.D. thesis, The University of Edinburgh (2002).

[25] D. B. Sharp, "Acoustic pulse reflectometry: A review of the technique and some future possibilities", in *Proc. of the 8th International Congress on Sound and Vibration* (2001).

[26] A. Li and D. B. Sharp, "The problem of offset in measurements made using acoustic pulse reflectometry", Acustica - Acta Acustica **91**, 789–796 (2005).

[27] A. Li, "Improvements to the acoustic pulse reflectometry technique for measuring duct dimensions", Ph.D. thesis, Open University (2004).

[28] A. Li, D. Sharp, and B. Forbes, "Increasing the axial resolution of bore profile measurements made using acoustic pulse reflectometry", Meas. Sci. Technol **16**, 2011–2019 (2005).

[29] A. Li, D. Sharp, and B. Forbes, "Improving the high frequency content of the input signal in acoustic pulse reflectometry", in *Proc. of the International Symposium on Musical Acoustics* (2001).

[30] A. Li and D. Sharp, "Reducing the source tube to improve the bandwidth of acoustic pulse reflectometry", in *Proc. of the Stockholm Music Acoustics Conference* (2003).

[31] D. B. Sharp, A. Myers, R. Parks, and D. Campbell, "Bore reconstruction by pulse reflectometry and its potential for the taxonomy of brass instruments", in *Proc. of the 15th International Congress on Acoustics* (1995).

[32] D. B. Sharp, D. M. Campbell, and A. Myers, "Input impedance measurements on wind instruments using pulse reflectometry", in *Proc. of the International Symposium on Musical Acoustics* (1995).

[33] D. B. Sharp, "Increasing the length of tubular object that can be measured using acoustic pulse reflectometry", Measurement Science and Technology **9**, 1469–1479 (1998).

[34] D. B. Sharp, "Have you ever found an oboe and wondered where it came from?", in *Proc. of the International Symposium on Musical Acoustics*, 205–208 (2001).

[35] D. B. Sharp, "Acoustic pulse reflectometry for the non-invasive monitoring of ducts", Proc. of the Institute of Acoustics. Spring Conference **24** (2002).

[36] D. B. Sharp, A. Myers, and D. M. Campbell, "Improvements in the resolution of bore reconstruction of brass musical instruments by pulse reflectometry", in *Proc. of the Institute of Physics Annual Congress* (1996).

[37] D. B. Sharp, A. Myers, and D. M. Campbell, "Using pulse reflectometry to compare the evolution of the cornet and the trumpet in the 19th and 20th centuries", in *Proc. of the Institute of Acoustics* (1997).

[38] D. B. Sharp and J. Buick, "Measurement of musical wind instruments using acoustic pulse reflectometry", in *Proc. of the Institute of Acoustics* (1999).

[39] J. A. Ware and K. Aki, "Continuous and discrete inverse-scattering problems in a stratified elastic medium. i. plane waves at normal incidence", J. Acoust. Soc. Am. **45**, 911–921 (1969).

[40] N. Harrop and K. Attenborough, "On the reliability of acoustic-to-seismic coupling ratio measurements", in *Proc. 3rd Symposium, Bouyoucos Conference on Agroacoustics* (1998).

[41] J. A. Kemp, J. Chick, D. M. Campbell, D. A. Hendrie, , and A. Myers, "Measurement techniques and the playability of terminal horn crooks", in *International Congress on Acoustics* (2007).

[42] D. B. Sharp and D. M. Campbell, "Measuring longer tubular objects using acoustic pulse reflectometry", in *Proc. of the 16th International Congress on Acoustics and the 135th Meeting of the Acoustical Society of America* (1998).

[43] D. H. Keefe, R. Ling, and J. C. Bulen, "Method to measure acoustic impedance and reflection coefficient", J. Acoust. Soc. Am. **91**, 470–485 (1992).

[44] M. R. Schroeder, "Determination of the geometry of the human vocal tract by acoustic measurements", J. Acoust. Soc. Am. **41**, 1002–1010 (1967).

[45] P. Mermelstein, "Determination of the vocal-tract shape from measured formant frequencies", J. Acoust. Soc. Am. **41**, 1283–1294 (1967).

[46] M. M. Sondhi and J. R. Resnick, "The inverse problem for the vocal tract: Numerical methods, acoustical experiments, and speech synthesis", J. Acoust. Soc. Am. **73**, 985–1002 (1983).

[47] M. M. Sondhi and B. Gopinath, "Dermination of vocal-tract shape from impulse response at the lips", J. Acoust. Soc. Am. **49**, 1867–1873 (1971).

[48] J. J. Fredberg, M. E. B. Wohl, G. M. Glass, and H. L. Dorkin, "Airway area by acoustic reflections measured at the mouth", J. Appl. Physiol. **48**, 749–758 (1980).

[49] J. J. Fredberg, M. E. B. Wohl, G. M. Glass, and H. L. Dorkin, "Reproducibility and accuracy of airway area by acoustic reflection", J. Appl. Physiol. **57**, 777–787 (1984).

[50] I. Rubinstein, R. B. P. A. Mclean, N. Zamel, J. J. Fredberg, and V. Hoffstein, "Effect of mouthpiece, noseclips, and head position on airway area measured by acoustic reflections", J. Appl. Physiol. **63**, 1469–1474 (1987).

[51] V. Hoffstein, R. G. Castile, C. R. O'Donnel, G. M. Glass, D. J. Strider, M. E. B. Wohl, and J. J. Fredberg, "In vivo estimation of tracheal distensibility and hysteresis in normal adults", J. Appl. Physiol. **63**, 2482–2489 (1987).

[52] D. T. Raphael, "Acoustic reflectometry profiles of endotracheal and esophageal intubation", American Society of Anesthesiologists **92**, 1293–1299 (2000).

[53] A. C. Jackson, J. P. Butler, E. J. Millet, F. G. H. JR., and S. V. Dawson, "Airway geometry by analysis of acoustic pulse response measurements", J. Appl. Physiol. **43**, 523–536 (1977).

[54] A. C. Jackson and D. E. Olson, "Comparison of direct and acoustical area measurements in physical models of human central airways", J. Appl. Physiol. **48**, 896–902 (1980).

[55] C. D. Gray, "Acoustic pulse reflectometry for measurement of the vocal tract with application in voice synthesis", Ph.D. thesis, The University of Edinburgh (2005).

[56] C. D. Gray, D. Campbell, and C. Greated, "Acoustic pulse reflectometry for vocal tract measurement", in *Proc. of the Stockholm Musical Acoustics Conference* (2003).

[57] D. B. Sharp and D. M. Campbell, "Leak detection in pipes using acoustic pulse reflectometry", Acustica - Acta Acustica **83**, 560–566 (1997).

[58] D. B. Sharp, D. M. Campbell, and A. Myers, "Pulse reflectometry as a method of leak detection in historical brass instruments", in *Proc. of Forum Acusticum* (1996).

[59] D. B. Sharp and V. Chilekwa, "An optimisation approach to the location and sizing of multiple leaks in a duct", in *Proc. of the Institute of Acoustics Spring Conference* (2006).

[60] V. Chilekwa, D. Sharp, and T. J. W. Hill, "Leak detection in musical wind instruments using acoustic pulse reflectometry", in *Proc. of the Stockholm Music Acoustics Conference* (2003).

[61] D. S. V. Chilekwa and T. J. W. Hill, "Detection, location and sizing of multiple leaks in a duct", in *Proc. of Forum Acusticum* (2005).

[62] W. Kausel, "Bore reconstruction of tubular ducts from its acoustic impedance curve", in *IEEE Transactions of Instrumentation and Measurement*, volume 53 (2004).

[63] W. Kausel, "Computer optimization of brass wind instruments", in *Unpublished paper.*

[64] B. J. Forbes, E. R. Pike, D. B. Sharp, and T. Aktosun, "Inverse potential scattering in duct acoustics", J. Acoust. Soc. Am. **119**, 65–73 (2006).

[65] B. J. Forbes, E. R. Pike, and D. B. Sharp, "The acoustical klein-gordon equation: The wave-mechanical step and barrier potential functions", J. Acoust. Soc. Am. **114**, 1291–1302 (2003).

[66] B. J. Forbes, D. B. Sharp, and J. A. Kemp, "Acoustic pulse reflectometry: Singular system analysis and regularisation of the inverse problem", in *Proc. of the Institute of Acoustics* (2002).

[67] B. J. Forbes, J. A. Kemp, and D. B. Sharp, "Pulse reflectometry as an acoustical inverse problem: Regularisation of the bore reconstruction", in *Proc. of the First Pan-American/Iberian Meeting on Acoustics incorporating the 144th Meeting of the Acoustical Society of America* (2002).

[68] B. J. Forbes, "Acoustical impedance defined by wave-function solutions of the reduced webster equation", in *Physical Review E* (2005).

[69] B. J. Forbes, "Acoustical klein-gordon equation: A time-independent perturbation analysis", in *Physical Review Letters* (2004).

[70] B. J. Forbes, D. B. Sharp, J. A. Kemp, and A. Li, "Singular system methods in acoustic pulse reflectometry", Acustica - Acta Acustica **89**, 743–753 (2003).

[71] P. Dickens, R. France, J. Smith, and J. Wolfe, "Clarinet acoustics: Introducing a compendium of impedance and sound spectra", Acoustics Australia **35**, 17–24 (2007).

[72] J. Wolfe and J. Smith, "Cutoff frequency and cross fingerings in baroque, classical, and modern flutes", J. Acoust. Soc. Am. **114**, 2263–2272 (2003).

[73] P. Dickens, J. Smith, and J. Wolfe, "Improved precision in measurements of acoustic impedance spectra using resonance-free calibration loads and controlled error distribution", J. Acoust. Soc. Am. **121**, 1471–1481 (2007).

[74] J. Wolfe, J. Smith, J. Tann, and N. H. Fletcher, "Acoustic impedance spectra of classical and modern flutes", Journal of Sound and Vibration **243**, 127–144 (2001).

[75] N. H. Fletcher, J. Smith, A. Z. Tarnopolsky, , and J. Wolfe, "Acoustic impedance measurements - correction for probe geometry mismatch", J. Acoust. Soc. Am. **117**, 2889–2895 (2005).

[76] A. C. P. Braden, "Bore optimisation and impedance modelling of brass musical instruments", Ph.D. thesis, The University of Edinburgh (2006).

[77] A. C. P. Braden, "Input impedance of bent waveguides", in *Proc. of Institute of Acoustics Spring Conference* (2006).

[78] A. C. P. Braden, "Optimisation techniques for solving design problems in modern trombones", in *Proc. of Forum Acusticum* (2005).

[79] A. C. P. Braden, "Higher modes and the input impedance of trombones", in *Proc. of Vienna Talk on the Future of Wind Instruments* (2005).

[80] A. C. P. Braden, "Brass instrument evolution software tutorial", in *Unpublished paper.*

[81] D. M. Campbell and M. O. van Walstijn, "Intonation of cornetti", Poster.

[82] D. M. Campbell and C. A. Greated, *The musician's guide to acoustics* (Oxford University Press) (2001).

[83] F. M. White, *Fluid mechanics* (McGraw-Hill International Editions) (1994).

[84] A. P. French, *Vibrations and waves* (Stanley Thornes) (1965).

[85] L. E. Kinsler, A. R. Frey, A. B. Coppens, and J. V. Sanders, *Fundamentals of acoustics* (John Wiley and Sons) (2000).

[86] N. H. Fletcher and T. Rossing, *The physics of musical instruments* (Springer-Verlag) (1998).

[87] D. J. Tritton, *Physical fluid dynamics* (Oxford Science Publications) (1988).

[88] M. O. van Walstijn, "Discrete-time modelling of brass and reed woodwind instruments with application to musical sound synthesis", Ph.D. thesis, The University of Edinburgh (2002).

[89] M. F. Hamilton and D. T. Blackstock, *Nonlinear acoustics* (Academic Press) (1998).

[90] G. Woan, *The Cambridge Handbook of Physics Formulas* (Cambridge University Press) (2000).

[91] D. Halliday, R. Resnick, and J. Walker, *Fundamentals of physics* (Wiley inernational edition) (2001).

[92] D. M. Campbell and C. A. Greated, "Acoustics 4", Unpublished lecture notes.

[93] J. Martinez and J. Agullo, "Conical bores. part i: reflection functions associated with discontinuities", J. Acoust. Soc. Am. **84**, 1613–1619 (1988).

[94] J. Martinez and J. Agullo, "Conical bores. part ii: multiconvolution", J. Acoust. Soc. Am. **84**, 1620–1627 (1988).

[95] J. Agullo, A. Barjau, and J. Martinez, "Alternatives to the impulse response $h(t)$ to describe the acoustical behaviour of conical ducts", J. Acoust. Soc. Am. **84**, 1606–1612 (1988).

[96] J. A. Kemp, N. Amir, and D. M. Campbell, "Calculation of input impedance including higher modes: circular and rectangular cross-section", in *Proc. of the 5th French Congress on Acoustics* (2000).

[97] J. A. Kemp, N. Amir, D. M. Campbell, and M. O. van Walstijn, "Multimodal propagation in acoustic horns", in *Proc. of the International Symposium on Musical Acoustics (ISMA)* (2001).

[98] V. Pagneux, N. Amir, and J. Kergomard, "A study of wave propagation in varying cross-section waveguides by modal decomposition. part i: Theory and validation", J. Acoust. Soc. Am. **100**, 2034–2048 (1996).

[99] A. M. Bruckstein, B. C. Levy, and T. Kailath, "Differential methods in inverse scattering", SIAM Journal on Applied Mathematics **45**, 312–335 (1985).

[100] N. Amir, G. Rosenhouse, and U. Shimony, "A discrete model for tubular acoustic systems with varying cross-section - the direct and inverse problems. parts 1 and 2: thoery and experiment", Acustica - Acta Acustica **81**, 450–474 (1995).

[101] J. Backus and T. C. Hundley, "Harmonic generation in the trumpet", J. Acoust. Soc. Am. **49**, 509–519 (1971).

[102] D. A. Hendrie and D. M. Campbell, "Input impedance measurement of musical wind instruments using a two microphone system", in *IoA* (2006).

[103] D. A. Hendrie and D. M. Campbell, "Musical wind instrument analysis", in *Forum Acusticum* (2005).

[104] D. B. Sharp, T. J. MacGillivray, W. Ring, J. M. Buick, and D. Campbell, "Acoustical comparison of bassoon crooks", in *Proc. of the International Symposium on Musical Acoustics* (1998).

[105] D. B. Sharp, H. A. K. Wright, and W. Ring, "The effect of crook profile on the perceived playing properties of the bassoon", in *Proc. of Forum Acusticum* (1999).

[106] D. B. Sharp, H. A. K. Wright, and W. Ring, "An acoustical investigation into the effect of the crook profile on the sound produced by the bassoon", Acustica - Acta Acustica **89**, 137–144 (2003).

[107] T. J. W. Hill and D. B. Sharp, "Acoustical and psychoacoustical investigations of the effect of crook bore profile on the playability of bassoons", in *Proc. of the Stockholm Music Acoustics Conference* (2003).

[108] A. H. Benade, "Effect of dispersion and scattering on the startup of brass instrument tones", J. Acoust. Soc. Am. **45**, 296–297 (1969).

[109] J. M. Buick, J. A. Kemp, D. B. Sharp, M. O. van Walstijn, D. M. Campbell, and R. A. Smith, "Distinguishing between similar tubular objects using pulse reflectometry: a study of trumpet and cornet leadpipes", Meas. Sci. Technol **13**, 750–757 (2002).

[110] T. R. Moore, E. T. Shirley, I. E. W. Codrey, and A. E. Daniels, "The effect of bell vibrations on the sound of the modern trumpet", Acustica - Acta Acustica **91**, 578–589 (2005).

[111] J. W. Whitehouse, D. B. Sharp, and T. J. W. Hill, "Wall vibrations in wind instruments", IOA Acoustics Bulletin **28**.

[112] S. Dorn, J. Whitehouse, and D. B. Sharp, "The effect of wall material on the structural vibrations excited when lip-reed instruments are blown", in *Proc. of the Institute of Acoustics Spring Conference* (2006).

Publications

Conference Papers

1. Darren Hendrie and Murray Campbell. Musical Wind Instrument Analysis. *Forum Acusticum, Budapest 29th August-2nd September 2005, 4th European Congress on Acoustics*, page 49. Hungary. Acustica - Acta Acustica.

2. Darren Hendrie and Murray Campbell. Input Impedance Measurement of Musical Wind Instruments Using a Two Microphone System. *Institute of Acoustics, Spring Conference 2006, 3rd-4th April*, Southampton, England.

3. J. Kemp, J. Chick, D. M. Campbell, D. Hendrie, and A. Myers. Measurement Techniques and the Playability of Terminal Horn Crooks. *International Congress on Acoustics 2007, 2nd-7th September*, Madrid, Spain.